ELECTROCHROMIC DEVICES INCORPORATING CONJUGATED POLYMERS AND CELLULOSE: NEW OPPORTUNITIES FOR ORGANIC ELECTRONICS

A Dissertation
Presented to
The Academic Faculty

by

Augustus William Lang

In Partial Fulfillment
of the Requirements for the Degree
Doctor of Philosophy in the
School of Materials Science and Engineering

Georgia Institute of Technology
December 2020

ELECTROCHROMIC DEVICES INCORPORATING CONJUGATED POLYMERS AND CELLULOSE: NEW OPPORTUNITIES FOR ORGANIC ELECTRONICS

Approved by:

Dr. John R. Reynolds, Advisor
School of Chemistry and Biochemistry
Georgia Institute of Technology

Dr. Elsa Reichmanis
School of Chemical and Biomolecular Engineering
Georgia Institute of Technology

Dr. Lars Berglund
Department of Fiber and Polymer Technology
KTH Royal Institute of Technology

Dr. Natalie Stingelin
School of Materials Science and Engineering
Georgia Institute of Technology

Dr. Robert Moon
School of Materials Science and Engineering
Georgia Institute of Technology

Date Approved: August 21, 2020

For my family

ACKNOWLEDGEMENTS

First and foremost, I would like to thank Dr. John Reynolds, my graduate advisor who welcomed me into the group as the first student from Materials Science and Engineering. Dr. Reynolds' endless kindness and optimism have made my graduate experience more rewarding than I could have imagined. Dr. Reynolds has enabled both my scientific and personal development throughout graduate school and has shown me what it means to be a scientist and a mentor! I feel extremely fortunate to have been part of such a collaborative and stimulating research group these past five years.

In several ways, I would not be writing this dissertation without Dr. Anna Österholm and Dr. Eric Shen. They assembled the RBI proposal that funded the majority of my graduate work, and more importantly, have served as incredible mentors helping me improve my thinking, writing, and presenting. My scientific development and experience of Atlanta certainly would certainly have suffered without the opportunity to work with Anna and Eric.

I would also like to thank the rest of the Reynolds group members and the visiting scientists, both past and present. To Abigail Advincula, Austin Bassett, Dr. Dylan Christiansen, Dr. Graham Collier, Anna Dillon, Dr. Jeff Hernandez, Dr. Kin Lo, Dr. Austin Jones, Linda Nhon, Dr. Javier Padilla, Dr. Ian Pelse, Dr. Sandra Pitteli, Dr. James Ponder, Josh Rhinehart Dr. Brian Schmatz, Dr. Zach Siebers, Dr. Erdal Uzunlar, and Dr. Rylan Wolfe, thank you making the Reynolds group what it is. The countless small discussions with group members add up to a tremendous amount of guidance. A special thanks goes to Brandon DiTullio and Lisa Savagian for an unforgettable trip to Sweden and for always

being willing to think deeply about science and life. I'd also like to thank Dr. Ray Bulloch, in whose shoes I stepped into when I joined the group and who was kind enough to serve as my mentor as I was just starting out.

One of the most rewarding parts of graduate school has been the opportunities to collaborator with diverse set of scientists and engineers. I would like to thank Dr. Lars Berglund and Dr. Yuanyuan Li for introducing me to engineered-wood materials, for so graciously hosting me at KTH in 2017, and for their collegial nature as we worked together on the transparent wood project. I would also like to thank Dr. Robert Moon both for being a part of my committee and for advising the CN@GT group which has consistently led to interesting discussions and collaborations over the years in the area of nanocellulose. Many thanks to Dr. Chinmay Satam and Dr. Carson Meredith with who a collaboration grew out of this group and continues through Yue Ji and Dr. Zeyang Yu.

I would like to thank Dr. Lars Berglund, Dr. Robert Moon, Dr. Elsa Reichmanis and Dr. Natalie Stingelin for serving on my committee. Input from these committee members has come directly at program milestones as well as indirectly through group members and has served to guide my thinking in preparing this dissertation. Thank you to the committee members for your time given for my scientific development.

My ability to perform research at Georgia Tech has been greatly enabled by the Institute of Electronics and Nanotechnology (IEN) facilities through their organic clean room and materials characterization facility and a seed grant back in 2016. Many thanks go to the scientists who support research in this center – Dr. David Gottfried, Dr. Eric Woods, Dr. Walter Henderson, Rathi Monikandan. These facilities have been a major

enabler for my research and have given me the freedom to explore a wide variety of topics. The Center for the Science and Technology of Advanced Materials and Interfaces (STAMI) has also played a huge role in my research development through a graduate fellowship, the STAMI shared lab space, and most importantly through the network of researchers in polymer science.

I owe a huge thanks to everyone I've had the chance to work with at Grand Challenges and LEAD. I want to thank Dr. Wes Wynens and Dr. Jeff Davis for constantly thinking differently and running such a great program. Many thanks to the rest of the team- Stacey Doremus, Alison Southern, Caroline Dyess, and Ashton Bettis for showing me what developing others really looks like. I would also like to thank Dr. Aaron Bivins for leading our co-teaching duo of the second-year course in 2019 and for bringing intensity, light sarcasm, and humor in right proportions.

Through the MSE department, I've been fortunate to cross paths a with many talented and interesting people. Thanks goes to Dr. Chris Perini and Dr. Alex Lohse who did their part in convincing me to come to the Georgia Tech. I am especially grateful for Travis Voorhees who's been an incredible kind friend and roommate throughout graduate school. Thank you for making Atlanta a home away from home.

Without the guidance and support of mentors prior to graduate school, I certainly would not have ended up on this path in life. Thank you to my undergraduate mentors Dr. Steven Nutt, Dr. Andrea Armani, and Dr. Deniz Armani who invested in my early development and opened my eyes to scientific research. In addition to all of the mentors listed above, I've been lucky to have many wonderful teachers over the past 20+ years that

I've been in school. I can only hope to pay this gift forward to the next generation of young people as I progress through my career.

Finally, I thank my friends and family for supporting me and enhancing life so greatly. Thanks to the Denver team – Conner, Nick, and Sam, I've grown tremendously alongside you three. A million thanks to my partner, Leslie Blackshear for the love, thoughtfulness, and endless adventure. Last but certainly not least, I must thank my parents and my twin sister, Kate. It is the ultimate gift to have such a supportive family. To you, I owe it all.

TABLE OF CONTENTS

LIST OF TABLES

LIST OF FIGURES

LIST OF SYMBOLS AND ABBREVIATIONS

AIBN	2,2'azobis(2-methylpropionitrile)
AFM	Atomic Force Microscope
CA	Cellulose acetate
C_d	Double-layer capacitance
C_D	Diffusional pseudocapacitance
ChNF	Chitin Nanofiber
CNC	Cellulose Nanocrystal
CNF	Cellulose Nanofibril
CPE	Constant phase element
CV	Cyclic voltammetry
$Đ$	Dispersity
Δ%T	Change in transmittance
ΔE^*	Change in colorimetric $L^*a^*b^*$ coordinates
DI	Deionized
DMSO	Dimethyl sulfoxide
ECD	Electrochromic Device
ECP	Electrochromic Polymer
EDOT	3,4-ethylenedioxythiophene
EG	Ethylene glycol
EIS	Electrochemical impedance spectroscopy
EMI	1-ethyl-3-methyl imidazolium
$FeCl_3$	Iron (III) chloride

$Fe(Tos)_3$	Iron (III) *p*-toluene sulfonate
FTB	3M flexible transparent barrier film
GPC	Gel permeation chromatography
HOMO	Highest occupied molecular orbital
I-V	Current-voltage
IR	Infrared
ITO	Tin-doped indium oxide
LUMO	Lowest unoccupied molecular orbital
µPAD	Microfluidic paper-based analytical device
MALDI	Multiple-angle-assisted laser desorption/ionization
MCCP	Minimally color changing polymer
M_n	Number-average molecular weight
M_w	Weight-average molecular weight
NMP	N-methyl-2-pyrollidone
NMR	Nuclear magnetic resonance
ω	Angular frequency (radians second^{-1})
OECT	Organic electrochemical transistor
OFET	Organic field effect transistor
OPV	Organic photovoltaics
P3HT	Poly(3-hexylthiophene)
PC	Propylene carbonate
PEDOT	Poly(3,4-ethylenedioxythiophene)
PEG	Poly(ethylene glycol)
PET	Poly(ethylene terephthalate)
PMMA	Poly(methyl methacrylate)

PPBT	Poly[3-(potassium-4- butanoate) thiophene-2,5-diyl]
PPG	Poly(propylene glycol)
P(ProDOP)	Poly(3,4-ethylenedioxypyrrole-*N*-octadecyl)
P(ProDOT)	Poly(3,4-ethylenedioxypyrrole-*N*-octadecyl)
PSS	Poly(styrene sulfonate)
*p*TSA	*para*-toluene sulfonate
SEM	Scanning electron microscopy
τ_D	Diffusional time constant
$TBAPF_6$	Tetrabutylammonium hexafluorophosphate
THF	Tetrahydrofuran
trans-$(CH)_x$	*trans*-poly(acetylene)
TFSI	Bis(trifluoromethyl sulfonyl)imide
TW	Transparent wood
UV	Ultraviolet
XPS	X-ray photoelectron spectroscopy
Z	Impedance

SUMMARY

Electrochromic devices (ECDs) enable on-demand light modulation for use in dimmable windows, mirrors, eyewear, and printed color-changing displays. Conventionally, these devices have been constructed using glass or petroleum-derived-plastics which represent the majority of the device mass. Considering the environmental burden of processing and disposal of these materials, this dissertation explores the use of renewable alternatives for the next generation of printable electrochromic devices based on redox-active conjugated polymers.

Chapter 1 introduces the field printed electronics with a focus on the developments of conjugated polymer active materials, in particular, poly(3,4-ethylendioxythiophene) (PEDOT). The unique structure and properties of wood-based materials are introduced along with a discussion of the prior work in combining cellulose with conducting polymers. Chapter 2 covers the experimental methods used in processing poly(3,4-ethylenedioxythiophene): poly(styrene sulfonate) (PEDOT:PSS)-based electrodes and electrochromic polymer films using materials developed previously in the Reynolds group. Electrochromic device assembly and characterization techniques are then outlined as the experimental bases for the projects contained in Chapters 3, 4 and 5.

Chapter 3 presents a relatively benign acid post-treatment used to generate highly conductive poly(3,4-ethylenedioxythiophene): poly(styrene sulfonate) (PEDOT:PSS) electrodes. These electrode films were applied to transparent wood composites developed in Prof. Lars Berglund's group at KTH to generate lab-scale window-type electrochromic devices. The redox-properties of the PEDOT:PSS films were investigated, finding an

expansion of the conductive potential window and emergence of new redox-active species following the post treatment. ECDs based on transparent wood were successfully demonstrated, showing a particularly color-neutral bleached state attributed to the high haze of the transparent wood substrates.

Chapter 4 details the translation the mild acid post treatment to inkjet-printed PEDOT:PSS electrodes on paper substrates. These color-neutral, printed electrodes were effective for reversibly cycling cyan-to-clear, magenta-to-clear, and yellow-to-clear, and black-to-clear electrochromic polymers thus providing access to the full color gamut. Switching kinetics were assessed using video analysis to shed insight into the speed of the electrochromic moving front and the material parameters governing switching speed.

In Chapter 5, lateral ECD geometry was used again to investigate the photodegradation of the devices encapsulated with a renewable barrier film developed in Prof. Carson Meredith's lab based on cellulose and chitin. These barrier films showed comparable performance to petroleum-derived poly(ethylene terephthalate) each generating a 10x improvement in photostability over the unencapsulated devices. The photodegradation was found to proceed more rapidly when the ECP was set in its bleached state prior to irradiation despite lower photochemical oxidation observed by X-ray photoelectron spectroscopy.

These studies demonstrate the potential for cellulose-based, printed electrochromic devices capable of reaching practical device lifetimes. A perspective on future studies involving electrochromic devices and photostability is presented in Chapter 6. This chapter covers some current limitations of paper-based electronics more generally and concludes

with a discussion of some fundamental questions related to the study of new materials accessible using the three-dimensional structure of delignified wood.

CHAPTER 1. INTRODUCTION

1.1 Overview of Low-Cost, Disposable Electronics

Semiconductor technology has experienced remarkable exponential growth since the 1970s. Rapid increases in transistor density in integrated circuits (doubling roughly every two years per Moore's Law) has led not only to massive improvements in computational power, but also to a continually declining cost and availability of computing power for the masses.[1] While continued downscaling of transistor dimensions is now reaching a major technological hurdle for the highest-performing computer chips, there exists a growing opportunity for the field of printed, disposable electronics.[2] The development of solution-processible conductors, semiconductors, and dielectrics has enabled the use of conventional printing methods to pattern electronic circuitry through an additive means with device performance approaching that of amorphous silicon.[3,4] While printed circuitry comes with the inherent tradeoff between feature resolution and throughput, printed devices with coarse feature sizes are attractive for a number of applications in sensing, labeling, and environmental monitoring where their ultra-low cost promises to be impactful.

The concept of printing electronic circuitry is by no means new. The German scientist, Albert Hanson postulated on this possibility as early as 1903, and industrially relevant printed electronics have been developed commercially for the past 20 years.[5,6] Many large corporations have developed business sectors dedicated to printed electronics (BASF, DuPont) and several smaller companies have grown over the past decade driven solely through printed electronics (Acreo, VTT, Ynvisible). IDTechX research, the flexible

and printed electronics market was estimated to be 37.1 Billion USD in 2019, dominated by displays (OLED, electrophoretic, etc.), but with significant contributions from conductive inks, printed logic, and printed sensors. While the field of printed semiconducting oxides has made great advancements in terms of processing requirements,[7] organic materials for electronics have been studied extensively in this area as synthetic modifications offer nearly limitless opportunities for tuning solubility (solution processability), electronic configuration, and phase behavior as solid thin films, all with important implications for the resulting properties (more on this in Section 1.2.2).

Research and development efforts have advanced technology geared toward a number of applications in a few key areas: (1) organic field effect transistors for driving large-area displays, (2) printable solar cells and thermoelectrics, (3) and printed conductors for antennae capable of receiving and transmitting information. Each of these device components can be integrated to develop a wide variety of printed devices, in particular for environmental monitoring using printed sensors. Low-cost sensing now seems ripe for adoption in a number of industries from agriculture to healthcare to logistics pushed by our desire for ever-more-granular information (and potential control) of our surroundings.

1.1.1 Applications in smart packaging, environmental and biomedical sensing

Printed electronics have been considered ideal for low-power devices with minimal computational needs. Smart labels on packages, for instance, could relay inventory data via printed RFID tags running off of power from printed batteries. Dynamic labeling has been an attractive area of aesthetic packaging where a color-changing display could relay product information. The area of active packaging has also grown in recent years for food

packaging that can prevent spoilage and notify the user via optical readout to consume the contents before they go bad. Printed electrochemical sensors have also gained popularity in their ability to analyze metabolites and electrolyte concentrations in sweat as an application for wearable electronics.[8] The expansion of sensor capabilities in printable devices promises to give a window into biology even beyond sweat analysis in the future.

In terms of low-cost sensors, point-of-care diagnostics have emerged as a promising tool for providing better care to remote and under-resourced populations. Microfluidic paper analytical devices (μPADs) patterned through wax printing, leverage the capillary action of fluids on paper as a means to transport analytes to detection zones. This field of research has seen significant development academically, largely focused on colorimetric assays of pertinent biomolecules such as glucose).[9–11] The library of biological sensing approaches has also benefited from tools developed by the synthetic biology community where freeze-dried cellular machinery deposited onto paper provided colorimetric detection of genetic material, specifically from the Ebola virus.[12] These studies highlight the exciting possibility for integrating printed electronic components (particularly redox-active materials) with the tools developed by biologists for greater breadth and performance in sensing.

1.1.2 Advances in bioderived and biodegradable materials for electronics

As the next generation of printed electronics are deployed, there is a desire to mitigate the environmental consequences of single-use plastic packaging by seeking renewable and recyclable materials as substrates and other inactive device components.[13,14] While an emphasis is often placed on biodegradability as the key metric for reducing

environmental impact, serving this priority limits thinking to the disposal of new materials and may in fact raise CO_2 emissions from the degradation process. Therefore, considering new materials more holistically in terms of their source, processing (energy, solvents, etc.), and their disposal will be of paramount importance moving forward. It is important to recognize that merely substituting a renewable material for one that is petroleum derived will not necessarily produce benefits in terms of the environmental footprint of the product. Well-defined principles exist for guiding green chemistry and life cycle assessments quantifying features such as greenhouse gas emissions, energy consumption, and material inputs for a product from cradle to grave are necessary considerations for the future of disposable electronics.[15]

Consistent with this thinking is the use of bioderived materials, already recycled at high rates (70% in the US). Cellulose papers have been sought after for printed electronics as the ultimate low-cost substrate. While the rough and porous nature of standard office paper makes it incompatible with printed electronic materials (typically 100s of nm thick), a variety of specialty papers have been published in the literature[16,17] and have been commercialized by the company Arjo Wiggins. These papers typically include much smoother surfaces (10s of nm of roughness) and barrier layers to prevent the inks from soaking through the substrate.

In order to achieve both low roughness and porosity, nanocellulose papers have been studied extensively over the past decade.[18,19] By utilizing nanofibrillated cellulose (Section 1.3) these substrates also optically transparent, making them ideal bioderived materials upon which to deposit transparent conductors and subsequently, optoelectronic devices.[20,21] The challenges for these materials is the high energy required to generate the

nanofibrils as well as batch-to-batch variation in the fibril suspensions. Commercial development of nanocellulose promises to tackle these challenges to make nanocellulose a viable material in the future. In addition to cellulose, other biopolymers have received significant attention for advantageous properties for incorporating into future electronics. Silk fibroin, for instance exhibits extremely high toughness, barrier properties, and optical transparency inspiring its use to make tough and conductive composites. It's versatility in terms of accessible microstructure as attracted significant research attention.[22,23]

While not yet derived from biomass, conjugated polymers represent a class of active materials for printed electronics that can be rendered water-soluble,[24–27] and even degradable[28] making them ideal candidates for the green electronics future. They offer advantageous properties in their ability to convert and store electrical energy and can be easily derivatized to sense various molecules.[29] The following section will give a brief history of these materials and their relevant properties as electroactive materials.

1.2 A Brief History of π-Conjugated Polymers

With the 2000 Nobel Prize in chemistry awarded to Alan Heeger, Alan MacDiarmid, and Hideki Shirakawa "for the discovery and development of conducting polymers", this class of materials cemented its place in scientific history among the many other Nobel Prizes in polymer science: Staudinger (1953), Natta & Ziegler (1963), Flory (1974), de Gennes (1991), Fenn, Tanaka, & Wüthrich (2002) and Grubbs, Schrock, & Chauvin (2005). For some context into this field and thus, this dissertation, this section will briefly explore the roots of π-conjugated polymer science, especially in the understanding of conductivity, redox properties, and optical properties.

Two scientists deserve credit for the earliest chemistry performed in the early 1800s to prepare what is now known to be poly(aniline): Friedlib Ferndinand Runge and Carl Fritzsche.[30] As a chemist working for the Königliche Seedhadlungs Societät (Royal Sea Trade Society), Runge isolated aniline as well as other relevant conjugated polymer precursors such as pyrrole and phenol from coal tar. He then prepared a green-black dye for cotton by the electrochemical oxidation of aniline in 1834 (poly(aniline)). Fritzche further described the isolation of aniline from indigo, giving the compound its modern name. Fritzche became the first to determine the chemical composition of the emeraldine salt in 1840 as $C_{24}H_{40}N_4Cl_2O$ (close!). While electrical conductivity remained unknown, and the concept of a "polymer" was still 80 years out for these chemists, their work laid the chemical groundwork for the efforts to prepare conducting macromolecules in the 1960s and 1970s.

Although it wasn't the first polymer synthesized for electrical conductivity[31] (or even the first poly(acetylene) synthesized[32]), *trans*-polyacetylene prepared in 1977 and doped to metallic conductivities proved to be the pivotal development kickstarting the field of research for years to come.[32–34] The conceptual simplicity of a one-dimensional polymer conductor combined with metallic conductivity of 10^5 S cm^{-1} in *trans*-$(CH)_x$ sparked the imagination for a future of polymer transmission lines, electronics, even superconductors.[35] As Alan Heeger described in his Nobel lecture, this class of materials opened up exciting opportunities for research at the boundary of polymer chemistry and condensed-matter physics, exemplified by the instructive work to bridge the two fields' terminology.[36,37] Conducting polymers offered a new way to study extended π-conjugation with the immense toolbox available to synthetic organic chemists. Beautiful experiments showed a degenerate ground state and soliton formation in *trans*-$(CH)_n$ opening up the field to the possibilities for tuning electronic structure easily via molecular structure. Physical models such as the Su-Schrieffer-Heeger (SSH) model served to capture the interesting charge-transport properties in this material.[38] The early work in the 1980's focused largely on understanding conductivity and charge carriers in these materials with the major "parent" polymers, poly(pyrrole), poly(aniline), poly(thiophene), and poly(*para*-phenylene) receiving much of the attention.[36] The electrochemical properties of poly(aniline), poly(pyrrole), and poly(thiophene) derivatives were studied in depth for their ability to be doped electrochemically, conducting both ions and electrons.[39,40]

The ability to solubilize these materials led to a new wave of research in "plastic" electronics promising to dramatically reduce the cost of many electronic devices assuming performance improvements could render these materials comparable to amorphous silicon

electronics. Organic field-effect transistors, taking advantage of the semiconducting properties of conjugated polymers were studied at Bell Laboratories in 1990s[41] and continue to be an active area of research, particularly in the investigation of new n-type materials.[42,43] Organic light emitting devices, first demonstrated for a polymer emitter in 1990 using poly(*p*-phenylene vinylene), which sparked the imagination for the future of printable displays.[44] True technological impact has been realized through the development of organic light-emitting diodes now popular as televisions, computer, and smartphone displays based on phosphorescent emitters.[45,46] These materials have reached-near unity quantum efficiencies owing to the high degree of mixing of singlet and triplet excited states (thus improving upon the 25% efficiency ceiling of singlet-emitting conducting polymer devices).

The mid-2000s brought an explosion of research into the field for the development of organic solar cells which has continued to this day as a result of the consistent improvement of power conversion efficiencies, especially in the post-fullerene era (17.3%).[47] For indoor lighting conditions, organic solar cells remain the top performers.[48] The past few years have also seen a resurgence of interest into the redox properties of these materials as mixed ionic-electronic conductors for bioelectronics including electrochemical transistors and ion pumps.[49–51] While these concepts were explored in the 1980s and 1990s,[52–54] this interest has spurred the design of new materials targeted toward redox switching and importantly, significant computational efforts that have led to new understanding of these systems.[55]

As the understanding of the structure-property relationships in these materials has grown over the years, their applications have typically leveraged the combination of

polymer properties (processability, phase separation, mechanical strength and toughness) with electronic properties (charge transport, exciton formation, optical absorbance). The richness of possible new chemistries accessible as π-conjugated polymers could be functionalized inspired a truly remarkable breadth of work in conjugated polymer sensors.[29] Various design motifs have been exploited for the recognition of gases, ions, enzymes, proteins, oligonucleotides, etc. which have particular relevance to the field of printed electronics discussed in Section 1.1 above.

Yet, many concepts in conducting polymers remain to be fully explored. New chemistries are always at the forefront with many opportunities for the incorporation of heavy metals into the backbone for truly unique electronic structures.[35] Despite its long history in the conducting polymer literature, doping studies are still uncovering new concepts for understanding electronic and ionic transport in these materials, especially recently in the area of thermoelectrics. A better understanding of the connection between physical properties and molecular/micro-structure, future syntheses are sure to continue to push the field forward to higher power conversion efficiencies, thermoelectric figure of merit (ZT) values, electron/hole mobilities, and sensitivity to analytes.

1.2.1 Development of PEDOT

Out of the thousands of conjugated polymer structures synthesized to date, PEDOT stands out as uniquely successful in terms of its reach throughout academic research and its commercial relevance as an anti-static coating (PEDOT:PSS). PEDOT was first synthesized at Bayer in the 1980s, and the first commercially available PEDOT:PSS, known as Baytron-P was developed in order to render the material solution-processible.[56]

Compared to poly(aniline) (PANI) which was well known to offer improved performance in terms of cost, the possibility of generating highly carcinogenic benzidine degradation in PANI ultimately limited its commercial production.

As an aqueous dispersion, PEDOT:PSS can achieve high conductivities (10^3 S cm^{-1}), and as thin films is highly transmissive (80-90%). Its stability in ambient conditions has played a large factor in its success over other conducting polymers as a conductor. Commercially-available PEDOT:PSS is used ubiquitously in organic solar cells as a hole-transport layer,[57] as an electrode material for flexible and stretchable devices,[58] and as an active layer in electrochromic devices[59] and depletion-mode organic electrochemical transistors.[50] This success has driven large-scale production of the material where kilogram quantities are easily available – a remarkable quantity for a conducting polymer.

The EDOT monomer can be obtained in 5 steps from thiodiglycolic acid and is now easily produced at kg scales for the production of conductive PEDOT materials. Compared

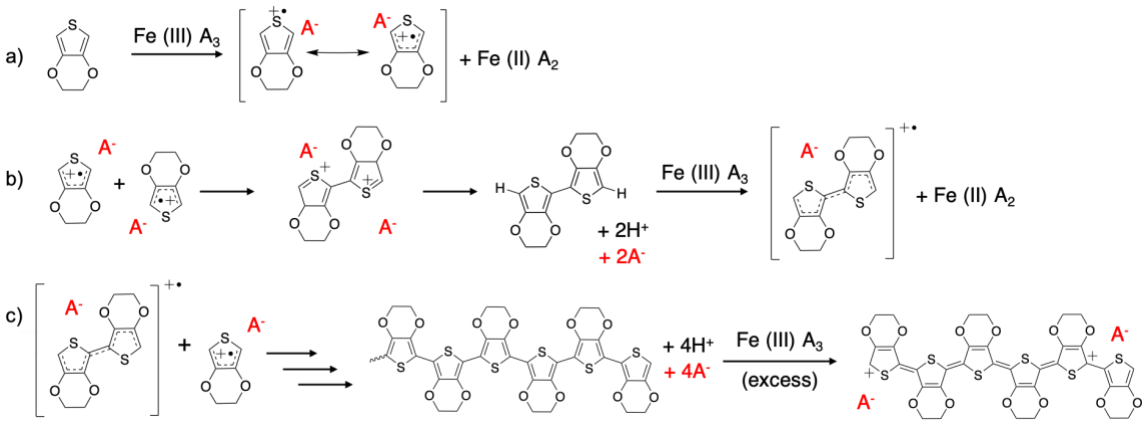

Figure 1-1. A route to obtain PEDOT by oxidative polymerization using iron (III) salt as the oxidant with anions shown as A^-. (a) The rate-limiting step of monomer oxidation followed by coupling and regeneration of a radical cation (b) with final termination and oxidation of the polymer by excess oxidant.

to unsubstituted thiophenes, the 3,4-dioxy substitution in EDOT eliminates unwanted coupling at these positions that can lead to defects during the polymerization. Substitution in EDOT eliminates unwanted coupling at these positions that can lead to defects in the polymerization. Additionally, the electron donation into the thiophene ring by the oxygens at the 3,4 positions makes EDOT easily oxidized to form PEDOT. Through the oxidative polymerization mechanism depicted in Figure 1-1, PEDOT is deposited in its oxidized, conductive form with the charge-balancing anions from the polymerization medium incorporated into the film. Despite estimates that PEDOT materials are typically composed of 5-15-mer oligomers, PEDOT can easily reach conductivities surpassing 1000 S cm^{-1}.[60,61]

Ever since the high thermal stability of PEDOT in its oxidized state was demonstrated in the late 1980s, investigations into novel synthesis, structures, and transport properties have continued to this day. Oxidative polymerizations performed using vapor-phase EDOT and iron (III) oxidants set several records for thin-film conductivity in work led by Peter Murphy and co-workers in the early 2000s.[62–64] Olle Inganäs and coworkers have studied PEDOT materials extensively, including PEDOT-tosylate, showing the propensity for tosylate anions to intercalate between PEDOT chains, leading to highly ordered, and conductive materials. Further vapor-phase work showed the incorporation of the block copolymer, PEG-PPG-PEG (Pluronic p127, 5800 kDa) in the oxidant layer ($Fe(Tos)_3$) consistently produced films exceeded 3000 S cm^{-1}. It has been hypothesized that the p127 copolymer templates the growing PEDOT chains and inhibits crystallization of the oxidant salt under vacuum leading to higher crystallinities in the solid film.[63,65–67] Additionally, the ability of the anion to fully dissociate from the Fe^{3+} has shown improvements in the thin-film conductivity values obtained.[68]

Oxidative chemical vapor deposition of EDOT using $FeCl_3$ has been employed more recently with the ability to control microstructure through the deposition temperature.[69] This work showed an intriguing transition from predominantly "edge-on" orientations of PEDOT crystallites at 190˚C to predominantly "face-on" orientations at 300˚C with enhanced π-π stacking and in-plane conductivities (σ = 6000 S cm^{-1}) following a HBr post treatment (Figure 1-2a).[69]

In addition to these vapor-phase techniques, *in situ* polymerization of EDOT in solution has also been demonstrated as a route toward highly conducting thin films.[70] These polymerizations presumably proceed through the same oxidative mechanism shown in Figure 1-1. Conductivities of 3500 S cm^{-1} were reported with the inclusion of NMP as a cosolvent (and likely a rate retarder) which were subsequently improved with an anion exchange in sulfuric acid to 5400 S cm^{-1}. Physical inspection of these films often shows 5-10 nanometer crystallites via electron microscopy and metallic-like transport phenomena near room temperature (Figure 1-2b) suggesting the film is composed of conducting

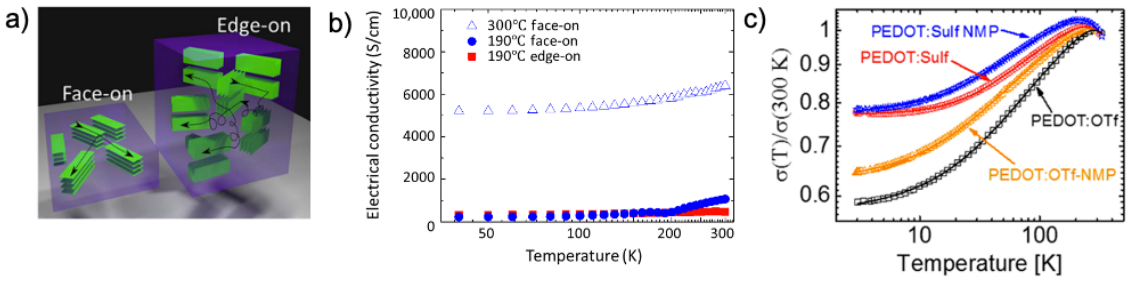

Figure 1-2 (a) Schematic showing face-on versus edge-on orientation of PEDOT crystallites and (b) corresponding temperature-dependent conductivity of PEDOT prepared by oxidative chemical vapor deposition at various deposition temperatures. Reproduced with permission from ref 69 © 2018 AAAS. (b) Temperature-dependent conductivity of PEDOT prepared by *in situ* polymerization with various additives and anions. Reprinted with permission from ref 70 © 2016 American Chemical Society.

crystalline islands with intrinsically high conductivities, interconnected by amorphous PEDOT. Lower energy barriers to transport between the crystalline islands leads to a decreased temperature dependence on conductivity (Figure 1-2c) and an overall higher conductivity (> 5000 S cm^{-1}). The current record holder for PEDOT conductivity remains single-crystal PEDOT prepared from nanoscale-confined oxidant layers giving over 8000 S cm^{-1},[71] approaching the quasi-metal intrinsic conductivities (10^4 S cm^{-1}) estimated for highly ordered regions from thin film studies.[70]

While PEDOT is an insoluble and infusible material, solution-processible PEDOT dispersions were generated by performing the oxidative polymerization EDOT in the presence of the polyanion PSS, allowing the material to be dispersed as an aqueous suspension.[72] The commercial grade material known to give the highest conductivity is composed of gel-like particles with a bimodal size distribution of 30 nm and 480 nm as measured by DLS (Clevios PH1000).[73] These gel-like particles are thought to contain crystalline PEDOT$^+$ cores enveloped by excess PSS$^-$ in order to render the particles stable in suspension. Therefore, several phases exist in thin PEDOT:PSS films as depicted in Figure 1-3a. Many acidic post-treatment methods have been developed to render PH1000 films highly conductive through the removal of the excess PSSH and reorganization of the PEDOT microstructure. In this material, enhanced interchain coupling is paramount for improving electrical conductivity of thin films. The addition of DMSO as a cosolvent has been shown to improve π-π stacking, and thus interchain coupling whereas the immersion in ethylene glycol (EG) after film deposition was determined to improve inter-grain transport rather than to facilitate reorganization in the polymer chains.[74] In recent reports, conductivities over 3000 S cm^{-1} have been common, with a few reports of conductivities

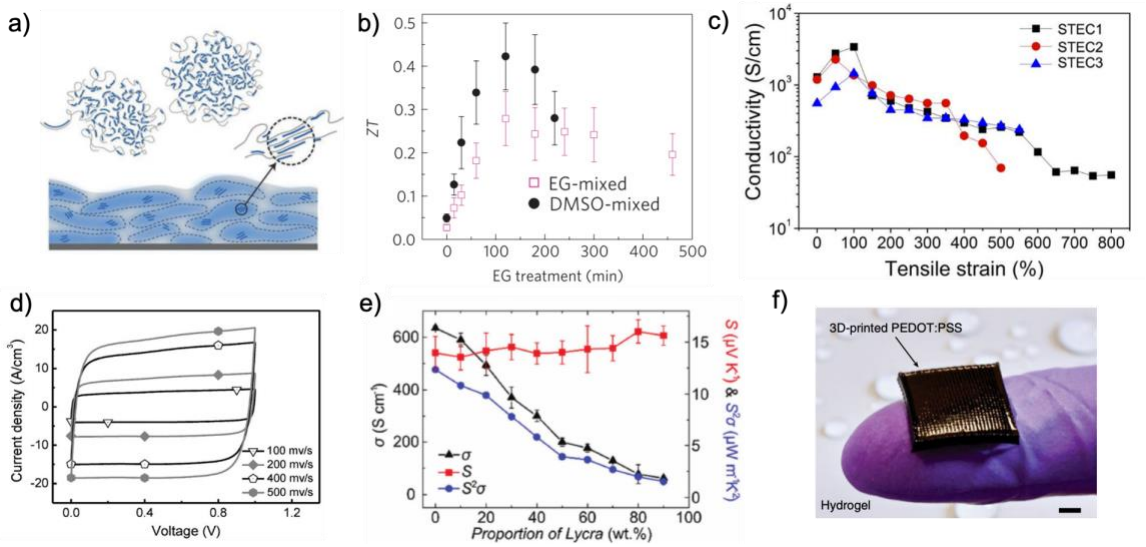

Figure 1-3 (a) Schematic of a PEDOT:PSS film composed of crystallites (blue lines) dispersed in a matrix of PEDOT-rich phases (darker blue) and PSS-rich phases (light blue). Reproduced from permission with permission from ref. [75] **© 2016 Springer Nature. (b) Thermoelectric figure of merit (ZT) for PEDOT:PSS films showing record performance upon mixing with DMSO. Reproduced with permission from ref.** [76] **© 2013 Springer Nature. (c) Conductivity vs. strain of stretchable PEDOT:PSS upon the incorporation of ionic liquid "stretchability and electrical conductivity" (STEC) enhancers. (d). Reproduced with permission from ref 58, © 2018 AAAS. (d) PEDOT:PSS treated with sulfuric acid used as supercapacitor electrodes in devices with sub-second charging/discharging. Reproduced with permission from ref.** [77] **© 2016 John Wiley & Sons. (e) PEDOT:PSS/poly(urethane) composites and their corresponding thermoelectric performance metrics. Reproduced with permission from ref.** [78] **© 2018 John Wiley & Sons. (f) a 3D printed PEDOT:PSS hydrogel. Reproduced from ref.** [79] **with permission © 2020 Springer Nature.**

exceeding 4,000 S cm^{-1} after post treatments.[58,80,81] These studies have been geared not only toward developing PEDOT:PSS as a high-performance transparent conductor, but have been found to achieve some of the highest thermoelectric power factors for organic materials (Figure 1-3b).[76] The addition of ionic liquid additives has recently been demonstrated as a means to achieve a high conductivity (>1000 S cm^{-1}) even at high strains (> 100 %, Figure 1-3c), making this an exciting material for conformable, wearable electronics.[58] As a widely accessible material, the mixed ionic-electronic conduction of

PEDOT:PSS has also received extensive scientific attention as a high-performance supercapacitor electrode where sub-second cycling was seen for free-standing μm-thick films after treatment with H_2SO_4 (Figure 1-3d).[77] PEDOT:PSS has also been studied in blends with commodity polymers such as polyurethane where it could find use as a thermoelectric textile generator (Figure 1-3e).[78] Much of the recent work on organic electrochemical transistors for transducing biological signals has incorporated PEDOT:PSS as an active material.[51] Recent studies have also pursued novel processing methods to form conductive 3-dimensional structures for conductive hydrogels (Figure 1-3f).[79]

As the utility of PEDOT:PSS became apparent as early as the 1990s, synthetic effort directed toward developing PEDOT derivatives to achieve soluble materials without the incorporation of PSS. This approach allowed for polymer systems that could be more thoroughly characterized (molecular weight, NMR, etc) prior to their deposition as thin films. Kumar and Reynolds first reported a fully soluble PEDOT by substituting a C_{14}-alkyl chain onto the ethylene bridge as shown in Figure 1-4a.[82] Over the years, new monomers with alternative heteroatoms and varying bridge lengths (up to butylene-

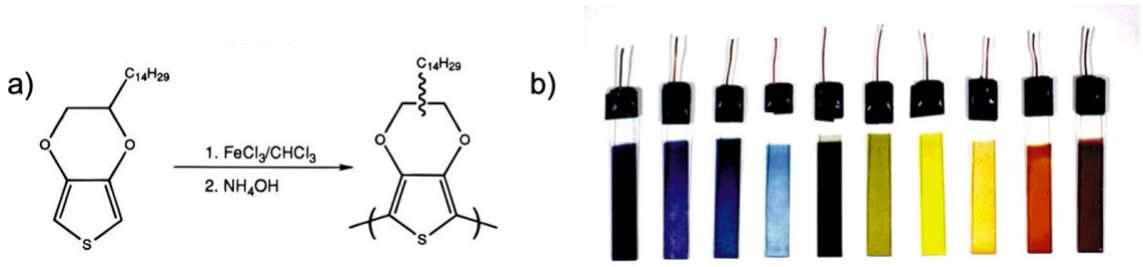

Figure 1-4 (a) A soluble PEDOT-C_{14} (reproduced with permission from ref. 82 © 1996 American Chemical Society). (b) Attainable colors in conducting polymers based on dioxythiophenes and their copolymers. Reproduced with permission from ref. 72 © 2000 John Wiley & Sons.

dioxythiophene) were prepared electrochemically and studied in terms of their redox and optical properties. These materials have led to a broad set of polymers and copolymers with chromophores whose absorbance spans the visible spectrum (Figure 1-4b). In a review article published by Groenendaal, et al., it was stated that "To date, little has been done to exploit the synthesis of true A-B copolymers based on EDT. This promises to be an area of extensive research in the future".[72] This has come to fruition since the article was published in 2000.[26,83]

In particular, propylenedioxythiophene (ProDOT) has been a key building block for electrochromic materials (see section 1.2.3 below), as side chains can be easily appended to the 2 position of the propylene bridge, affording solubility without impacting regioregularity. The slight distortion of the propylene bridge is hypothesized to reduce inter-chain interactions which reduces the visible absorbance of these materials in their oxidized states, leading to high contrast electrochromic materials.[84] These materials are inherently distorted compared to their unsubstituted counterparts, thus forming disordered films that can be switched rapidly between redox states despite lower electrical conductivities (10^{-3}-10^{-1} S cm^{-1}). Dioxypyrroles (DOPs) are an interesting class of extremely electron-rich systems with poly(3,4-ethylene dioxypyrrole) (EDOP) being the most electron-rich conducting polymer known.[85] As these copolymers incorporating DOPs can be so easily oxidized, they offer a route toward the elusive stable, short-wavelength electrochromics (yellow-to-clear) though their electron-richness makes their incorporation by direct(hetero) arylation polymerization extremely difficult.

1.2.2 Properties of π -conjugated polymers

The previous sections have detailed many advances in the field of printed electronics and conjugated polymers with a particular emphasis on PEDOT-based conductive materials. In this section, fundamentals of the electronic structure will be presented which underpin the characteristic optical absorbance profiles and transport properties in π-conjugated polymers. It should be noted that the polymer structure spanning length scales from the atomic configuration (sub-angstrom) to the 10s-100s of nanometers will affect the electronic environment, and thus the resulting optoelectronic and transport properties of these materials.[86–88] Understanding these structure-property relationships over these length scales is the essence of much of the work in conjugated polymer science, with the goal of rationally designing new materials to provide a desired property.

The electronic structure arising in discreet molecules is described by molecular orbital theory where n-atomic orbitals covalently bound gives rise to n-molecular orbitals which are half-occupied, half-unoccupied. Of principle concern are the energy levels corresponding to the highest occupied molecular orbital (HOMO) and the lowest unoccupied molecular orbital (LUMO) as electronic transitions between these two states (π-π* transitions for conjugated molecules) are often what determine optical transitions for neutral molecules. When applying molecular orbital theory to a chain of alternating single

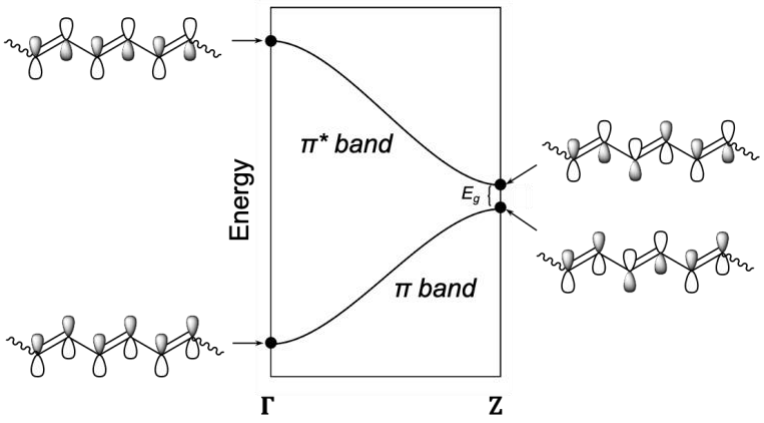

Figure 1-5 Hypothetical band structure of a semi-infinite chain of polyacetylene.

and double bonds, this theory predicts a continuum of energy levels where the HOMO level and the LUMO approach the same energy. If we consider the periodicity of a poly(acetylene) chain, Bloch's theorem allows us to draw the band structure (in inverse space) shown in Figure 1-5 where the highest-energy in the π-band (alternating bonding across the double bonds) approaches that of the lowest-energy in the π*-band (alternating antibonding across the double bonds) at Z. In the idealized chain, the energy states would be half filled with no energy gap between the occupied and unoccupied state, making poly(acetylene) a metal. In reality however, energetic relaxation along the backbone of an "infinite" chain, known as a Peierls distortion, separates these two levels and gives rise to an energy gap (Eg). For an in-depth discussion on the buildup of energy bands in this hypothetical infinite chain, the reader is referred to two excellent resources.[37,89]

It is here where the terminology from molecular orbital theory and semiconductor physics becomes intertwined. While conjugated polymers behave like semiconductors in many instances, their optical absorption resembles that of discreet molecules. The

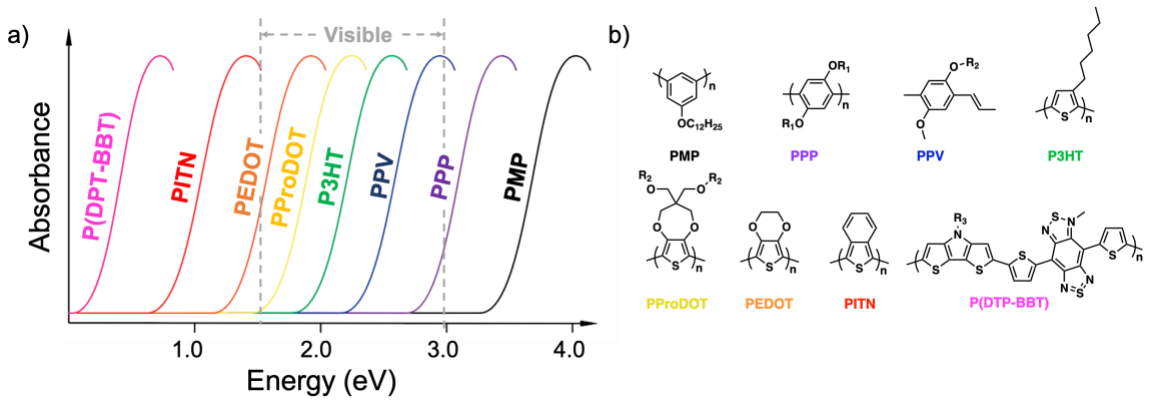

Figure 1-6 Optical absorbance of various conducting polymers in their neutral state.

electronic structure of the conjugated polymer is largely responsible for the observed absorbance spectrum of the material in its neutral state where the extent over which the polymer can delocalize its π-electrons determines its optical band gap (onset of absorption) as shown in Figure 1-6.[90] Smaller dihedral angles between the monomer rings leads to extended conjugation, and a lower-energy gap (longer wavelength absorption). A classic example of bandgap control is the polymer poly(isothianaphene) which adopts a quinoidal structure giving it a low optical gap close to 1 eV.[91] In addition to the backbone structure, interchain interactions are also well-known to influence the optical absorbance in conjugated polymers. This has been well studied both experimentally and with the development of theory describing H- and J-aggregates in P3HT.[92]

One of the key features of π-conjugated polymers is their ability to be doped using redox reactions to oxidize or reduce the polymer. Doping studies of poly(acetylene) laid the foundation for generating high-conductivity materials. Iodine-doped poly(acetylene) that had been aligned through extension of the solid represents the highest conductivity seen in organic materials (10^4-10^5 S cm^{-1}).[93]

The doping process, and generation of charge carriers is depicted in Figure 1-7a-c for a section of a P(ProDOT) chain. Doping can be performed electrochemically through the application of an oxidizing potential. Figure 1-7d shows a cyclic voltammogram where a notable oxidation onset of a P(ProDOT) derivative at ~0.2 V vs. Ag/Ag^+ bleaches the neutral absorbance (magenta-to-clear) and is followed by a broad- capacitive-like current response. Through this removal of an electron (p-type doping), a radical cation charge carrier is generated in the polymer backbone leading to a locally planarized structure where the thiophene ring adopts a quinoidal conformation as shown by the red portion of the chain in Figure 1-7b. An emergence of optical absorbance at 900 nm has been typically associated with the creation of an inter-gap state upon doping (Figure 1-7e, red curve) that becomes half-filled with spin ½ polarons. This picture has been recently revised according to DFT calculations depicting the polaron as an empty inter-gap energy level.[94,95] Spin signals detected by electron paramagnetic resonance once attributed to a polarons in the inter-gap state likely arise from electrons in the occupied orbitals (or valence "band") as shown in Figure 1-7f for PEDOT at low oxidation levels. Further removal of electrons results in a nearly full depletion of the neutral state absorbance at 550 nm and a growth of absorbance at wavelengths greater than 1000 nm. This absorbance is associated with the dication state depicted in Figure 1-7c and has been a topic of debate in the literature whether the term "bipolaron" or "polaron-pairs" is more suitable. Recent DFT calculations on PEDOT explain the shift to a broadly absorbing material in the near IR results arise from the generation of many polaron and bipolaron transitions (P1, B1) from the occupied energy levels, distinguished by their ground-state spin.[94] The proportion of available

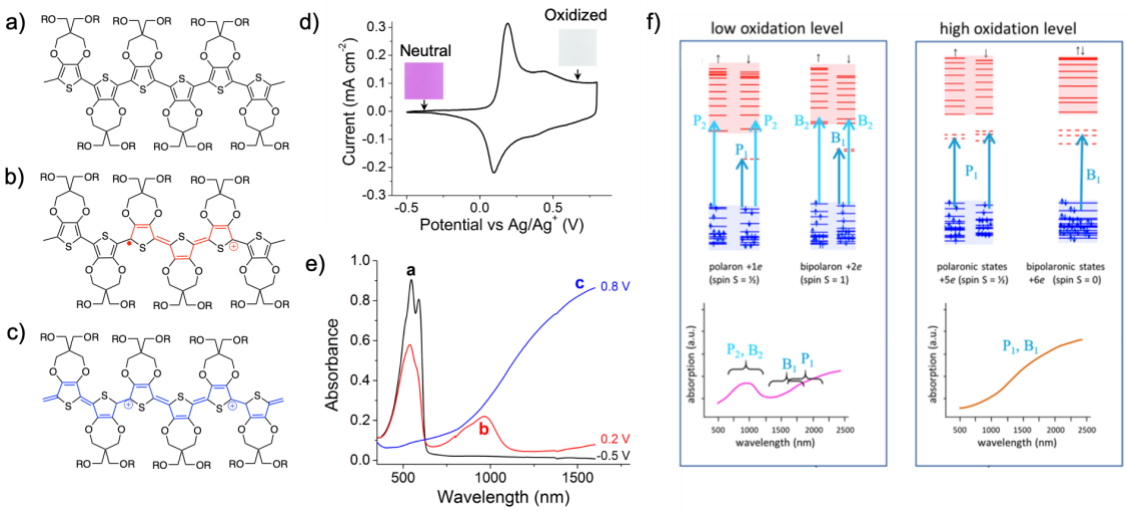

Figure 1-7 Generation of charge carriers in P(ProDOT-(OEtHx)$_2$) showing the neutral state (a), the radical cation state (b) and the dication state (c). (d) Cyclic voltammogram of P(ProDOT-(OEtHx)$_2$) performed on a glassy carbon working electrode in 0.5 M TBAPF$_6$ / PC (Ag/Ag$^+$ reference). Inset shows the color of the polymer in its neutral and oxidized state. (e) Optical absorbance of neutral, radical cation, and dication states of the polymer material. (f) DFT-calculations for optical transition of PEDOT for low oxidation levels in the material (radical cations, P1,B1, P2 and B2) and for high oxidation levels (P1, B1). Reproduced with permission from ref. 94 © 2019 American Chemical Society.

transitions shift toward bipolaron-dominated transitions at high degrees of oxidation (Figure 1-7f).

Electrochemically, the shift from a neutral, insulating polymer to a conductive material acting as an extension of the electrode has been well studied experimentally and theoretically. The Aoki phase propagation model, depicted in Figure 1-8a, shows a non-uniform transition to an oxidized state (black) propagating from the electrode surface.[96] Charge-transfer across the oxidized/neutral interface, governed by Butler-Volmer kinetics, limits the oxidation rate and gives rise to the characteristic current response observed upon the application of a oxidizing potential. The initial increase in current is attributed to the

growing conducting zone, which then decays exponentially once the conductive front has reached the surface of the film.[97]

Once electrochemically oxidized, the now conducting form of the polymer can be probed by *in situ* conductivity methods developed by Mark Wrighton and colleagues.[98] In this method, the polymer film is held at a set potential while small I-V sweeps are performed to measure the film's resistance. Results from a family of dioxythiophenes prepared in the Reynolds group show that the polymers indeed become conductive above a certain electrochemical potential with the onset of conductivity tracking the oxidation onset for each material.[99,100] As the mixed conduction of conjugated polymers has attracted interest from researchers in the bioelectronics world, newer methods have been developed to extract the ion mobility in these materials, building off of the moving-front experiments performed in the 2000s.[101] Results from a one-dimensional moving front configuration

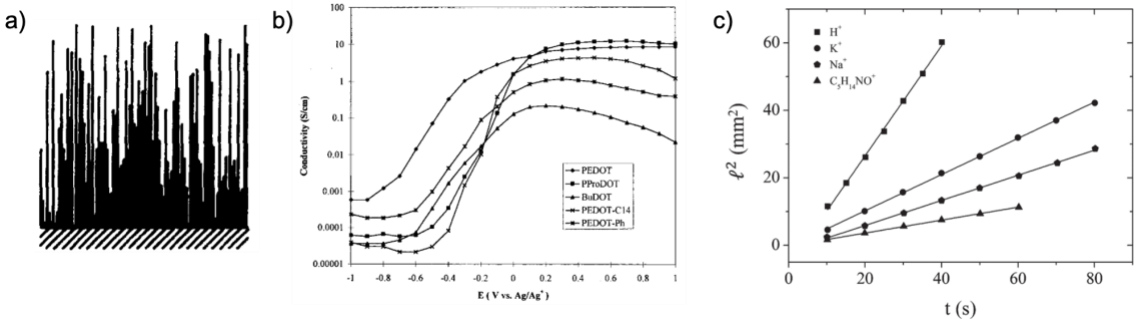

Figure 1-8 (a) Schematic of a conductive front from a metal electrode (bottom) represented by black lines upon electrochemical oxidation of a conducting polymer. Reproduced with permission from ref [96] © 1990 Elsevier BV. (b) *In situ* conductivity of several poly(3,4-dioxythiophenes). Reproduced with permission from ref. [99] © 1998 American Chemical Society. (c) Drift length versus time for various cations upon de-doping of PEDOT:PSS in a one-dimensional ionic mobility measurement. Reproduced with permission from ref. [102] © 2013 John Wiley & Sons.

developed by Stavrinidou, et al. are shown in Figure 1-8c for the de-doping of PEDOT:PSS (the reverse of the process described by Aoki).[102]

Like the optical properties, electrochemical switching in conducting polymers is determined by both the repeat-unit structure as well as the thin-film microstructure. However, most materials studied for their redox activity do not exhibit significant long-range or crystalline order.[83,103] The redox properties of thin films of conjugated polymers are further complicated by need to understand the polymer/electrode interface, and the roles of solvent and ion transport in the films. In general, the incorporation of unsubstituted, electron-rich repeat units such as ProDOT, EDOT, and dioxypyrrole lead to lower oxidation potentials resulting both from their electron density as well as steric relaxation.[83,104] Fundamental questions regarding the nature of the capacitive current seen after the initial oxidation remain ripe for future experimental work.[103,105]

1.2.3 Introduction to electrochromism

Electrochromism is the process of a color change driven by an electrochemical potential. As materials that can be reversibly cycled between a colored neutral state and a transparent oxidized state as shown in the previous section, π-conjugated polymers are ideal candidates for color-changing electrochromic devices. While several other classes of materials are known to exhibit electrochromism (WO_3, V_2O_4, viologens, metallopolymers, $Fe(CN)_6^{3+/4+}$), the color vibrancy achieved by fine tuning the repeat-unit structure really distinguishes conjugated polymers. Figure 1-9a shows a variety of repeat unit structures employed to access a broad color gamut in their neutral state.[106,107] These materials all

bleach to a highly colorless oxidized (dication) state enabling high contrasts, defined as the transmittance change of the π-π* transition or the maximum absorbance wavelength.

Electrochromic devices fall into two main categories, transmissive (window-type) and reflective. A standard architecture of a transmissive device architecture is shown in Figure 1-9b. In this case a solid electrochromic polymer (ECP) film is deposited onto one transparent electrode (P(ProDOT-$(OEtHx)_2$) and a minimally color changing polymer (poly(3,4-propylenedioxypyrrole-C_{18})) is deposited on the other. The purpose of this minimally color-changing material is to equalize the charge capacity of each electrode to enable switching between the fully-oxidized and fully-reduced state of the color-changing

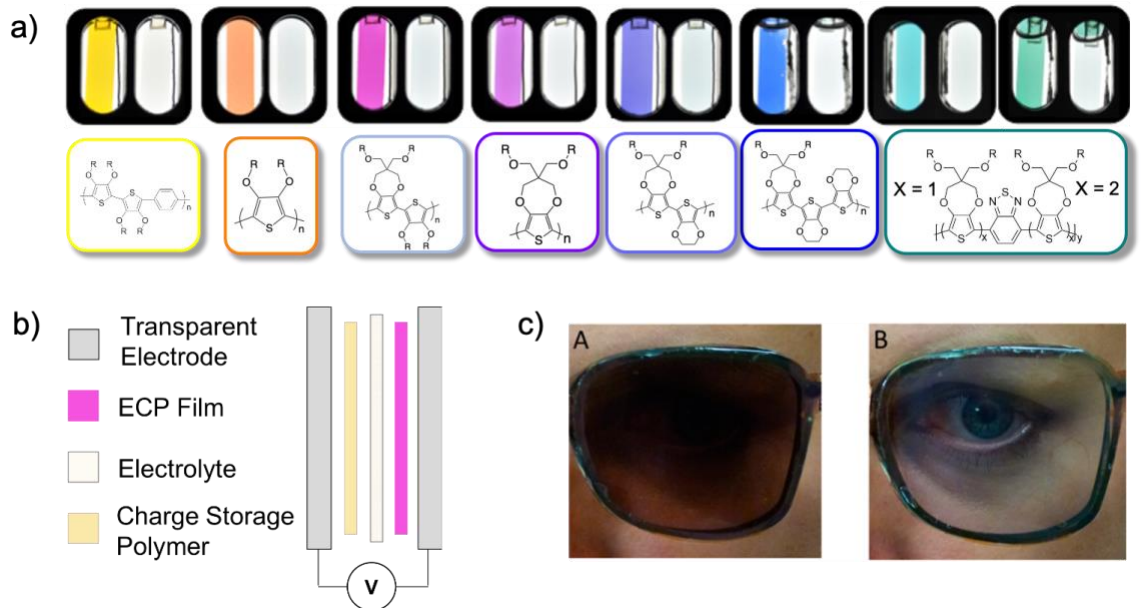

Figure 1-9 (a) Overview of electrochromic polymers developed in the Reynolds group showing their repeat-unit structure and their corresponding neutral (colored) and oxidized (clear) states. (b) Schematic showing an electrochromic device architecture composed of two transparent electrodes and 3 inner layers (window type device). (c) Example of electrochromic brown-to-clear eyewear achieved through solution blending of soluble conjugated polymers. Reproduced with permission from ref. 108 © 2015 American Chemical Society.

active material. The minimally color-changing polymer absorbs in the UV region in its neutral state, and the near-IR in its oxidized state, thus minimizing its impact on the colored and clear states of the device. Prior to device construction, the minimally color changing polymer is set in its oxidized state to establish a voltage in the device that can be reversed to drive the color change of the ECP. The two transparent electrodes are then sandwiched together around an electrolyte layer (typically tetrabutylammonium hexafluorophosphate ($TBAPF_6$) dissolved in propylene carbonate with poly(methyl methacrylate)).

Electrochromic devices (ECDs) are evaluated based on a number of performance metrics including their optical contrast (Δ%T), voltage requirements (V), switching times (for coloration and bleaching), coloration efficiency ($cm^2\ C^{-1}$), and bi-stability (how long the device will maintain each state without power). ECDs composed of conducting polymers (particularly dioxythiophenes) constructed with proper charge balance between both electrodes can typically achieve contrasts of 40-50% and can be driven by less than 1 V. These materials are efficient in terms of charge required upon switching (~300-500 $cm^2\ C^{-1}$).[109] The bi-stability of both the colored and clear states in conjugated polymers can be largely dictated by electrolyte, but is a clear distinction from ECDs based on viologens which need a constant power supply to maintain their colored state.[110]

Redox stability and photostability are two practical concerns for ECDs. Applying low voltages (< 1 V) and short pulse times (~1 s), conducting polymers can easily withstand 10^4 oxidation/reduction cycles making them suitable for low-cost displays that don't need to last for years of continuous cycling. Photodegradation of the active materials is a more pressing challenge for these materials. While stable in ambient conditions for several days, electrochromic polymers are easily degraded by prolonged exposure to both oxygen and

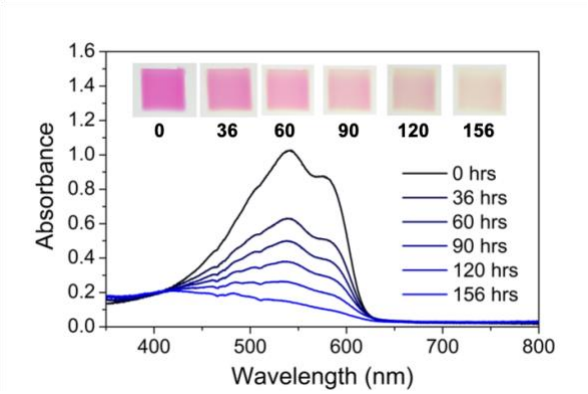

Figure 1-10 Photo-chemical degradation of a P(ProDOT-(OEtHx)$_2$) thin film exposed to ambient atmosphere and indoor laboratory lighting over the course of 1 week.

light.[111,112] Even indoor lighting conditions can cause P(ProDOT-(OEtHx)$_2$ to degrade if it is left unencapsulated as shown in Figure 1-10.

Fortunately, this degradation process can be dramatically delayed by encapsulating the material in an oxygen-free atmosphere. Extensive photodegradation studies on P3HT have been performed suggesting degradation originates from hydrogen abstraction in the side chain.[113,114] However, there is less understanding of structure-property relationships governing the photostability of ProDOT materials, as side chains are appended further from the backbone and they are more disordered than P3HT. Furthermore, if these materials are to be deployed as active layers in printed electronics, their stability upon encapsulation under ambient conditions with moderate-performance barriers must be determined as discussed in Chapter 5.

With the basics of conjugated polymers and electrochromic devices described above, the next section will provide a discussion of the structure and properties of cellulose derived from wood. A discussion of top-down modifications to wood-based materials is presented, followed by bottom-up approaches utilizing nanocellulose particles.

1.3 Structure and Properties of Cellulose: Advances in Control Over Nanostructure

Cellulose is truly a ubiquitous polymer found in nearly every kingdom of life (including plats, protists, bacteria, algae, and even animals). As the most abundant polymer on Earth, cellulose is produced naturally at roughly 10^{11}-10^{12} tons per year. It is the principle structural material that gives plant cell walls their mechanical strength. The repeat-unit structure, consisting of β-linked D-glucose units leads to strong inter- and intra-chain hydrogen bonding, and highly crystalline structures in nature. This section will detail the unique hierarchical structure wood which has recently been exploited for a variety of engineered functional materials. A broad overview of some applications will be discussed to demonstrate the variety of accessible structures used for enhanced thermal, electrical, fluidic/ ionic, or optical transmission in materials derived from wood.

1.3.1 Hierarchical structure of wood

Trees represent some of the most extreme forms of life on earth and exhibit truly remarkable diversity. They encompass the largest and oldest organisms known as well as the tallest and fastest-growing plants. The Pando clonal aspen colony in Utah is widely regarded as both the largest living organism weighing 6 million kg and as one of the longest living (estimates range 12,000-200,000 years). Bristlecone pines are often cited as the oldest living non-clonal organism, some of which have been dated to over 5,000 years old. Bamboo of "certain generas" claimed Guinness World Record for the fastest growing plant, reaching rates of over 90 cm or 35 inches per day. There is even evidence that trees the forest can support each other's growth through the exchange of sugars and are able communicate distress signals through a common mycelium connecting root systems.[115,116]

Identified by French chemist Anselme Payen in 1838, the molecular formula was determined to be $C_6H_{12}O_5$ yet the repeat-unit structure was unknown until studies by future Nobel laureate Hermann Staudinger in 1920. The β 1-4 acetal linkage between the two glucose units (rotated 180˚ relative to each other) gives rise to a ribbon like polymer structure of relatively planar configuration of each glucopyranose ring due to the hydrogen bond donation by the C3 and C6 hydroxyls (Figure 1-11a).[117] The intra-chain hydrogen bonding between C2 and C5 hydroxyl groups serves to stabilize the glycosidic bond, making the chain stiff. Hydrogen bonding between chains results in the highly crystalline nature of cellulose and its insolubility in water. The lamellar ordering of cellulose chains is shown in Figure 1-11b where the inter and intra-chain hydrogen bonds are depicted by dotted lines. The cellulose I crystal structure showing a cross-sectional view of the cellulose chains stacking is shown in Figure 1-11c. Light-scattering studies have estimated degrees of polymerization of cellulose in wood from 5,000 – 9,000 typically and up to 15,000. Note for further reading into the natural biosynthesis of cellulose by cellulose synthase in plants, the reader is directed to a recent review.[118]

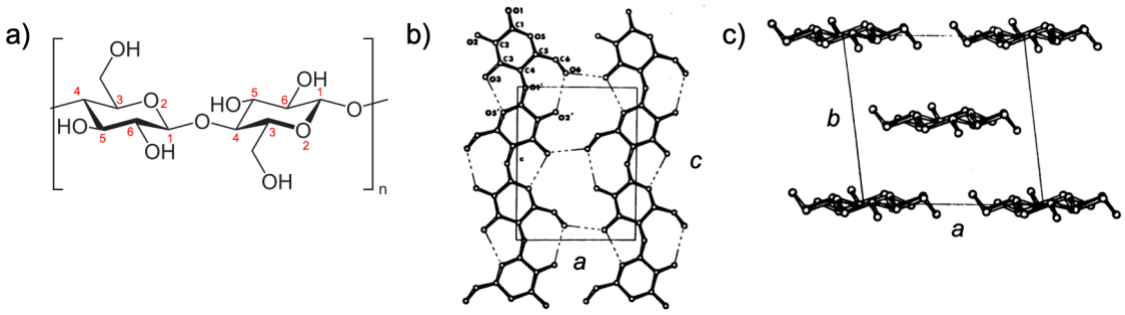

Figure 1-11 Structure of native cellulose showing the molecular repeat unit (a) and the axial (a) and planar (b) projection of the Cellulose I crystal structure reproduced with permission from ref. 117, © 1974 American Chemical Society.

Beyond this crystalline structure, cellulose assembles into a complex, hierarchical structure in wood spanning the length scales shown in Figure 1-12a from the cellular structure (~500 μm) down to the cell wall structure (~20 μm) to the elementary nanofibril (~5 nm).[119] Figure 1-12a depicts bulk wood, composed of a porous microstructure of cellulose fibers bound in a lignin and hemicellulose matrix. The individual cell is depicted showing the lumen, the secondary, and primary cell wall which is composed of bundles of crystalline cellulose fibers (shown by the elementary fibril and cellulose crystal structure). The cross section of the microfibril bundle is shown in Figure 1-12b depicting the core of elementary fibrils encased in hemicellulose and lignin. The lateral cross section shows the presence of both crystalline and amorphous regions in the microfibril. The main molecular constituents present in the cell wall, cellulose, hemicellulose, and lignin (shows as precursors to the lignin polymer) are also depicted.

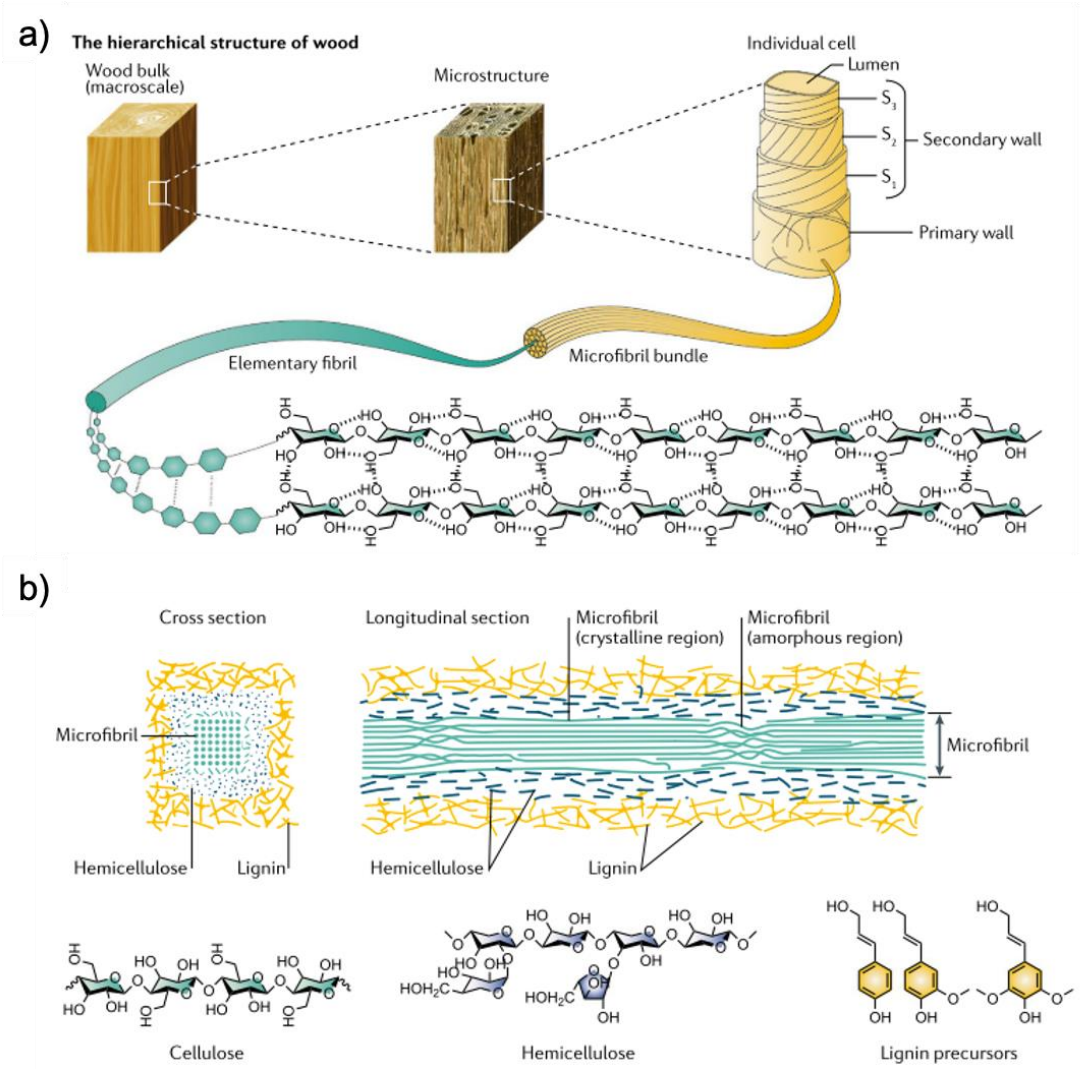

Figure 1-12 (a) Hierarchical structure of wood shown from the scale of a tree's cross-section down to individual cellulose chains. Cross-section of cellulose showing the three major chemical components, cellulose (40-50%), hemicellulose (25-35%), and lignin precursors (18-35%). Reproduced with permission from reference 119 © 2020 Springer Nature.

1.3.2 Functional materials based on wood and nanocellulose

A new class of engineered wood materials has emerged over the past four years leveraging the development of delignification procedures that retain the natural structure of the cellulose scaffold.[120] Multifunctional modifications have rendered the wood

conductive via carbonization and used as a non-tortuous electrode in asymmetric pseudocapacitors.[121] More recently, the *in situ* polymerization of poly(pyrrole) was demonstrated for a solar-steam generating device[122] and for electromagnetic interference shielding[123] to avoid the detrimental effects of carbonization on the mechanical properties of the wood skeleton. Additionally, poly(aniline) has been synthesized *in situ* in wood veneers as another potential conductor embedded in wood.[124] Other functional materials have also been incorporated into wood including organic dyes for lasing and quantum dots for optically active wood. [125,126] Light emission in both of these cases exhibited high degrees of anisotropy from the wood template. Novel anisotropic composites have also shown unique properties as strong and tough hydrogels mimicking the mechanical properties of muscles.[127] Recently, highly porous wood aerogels have been fabricated by the partial dissolution of the cellulose in the cell wall to achieve high specific surface areas (247 m^2 g^{-1}) and facile incorporation of nanoparticles and PEDOT:PSS.[128]

These processes access the hierarchical structure of natural cellulose from the top down offering advantages in terms of the energy required for processing. In addition, bottom-up approaches utilizing nanocellulose particles have also been well studied over the past 10-15 years providing access to unique 3D structures. Cellulose nanocrystals and nanofibrils (CNCs and CNFs) are the basic building blocks that have generated significant research interest from multidisciplinary teams interested in the high elastic modulus and strength, the great potential for multi-functionality, the assembly of cellulose nanocrystals in water forming a chiral-nematic liquid crystalline phase, etc.[129] These nanocrystalline particles, present in biomass, are most-often isolated by chemically breaking down

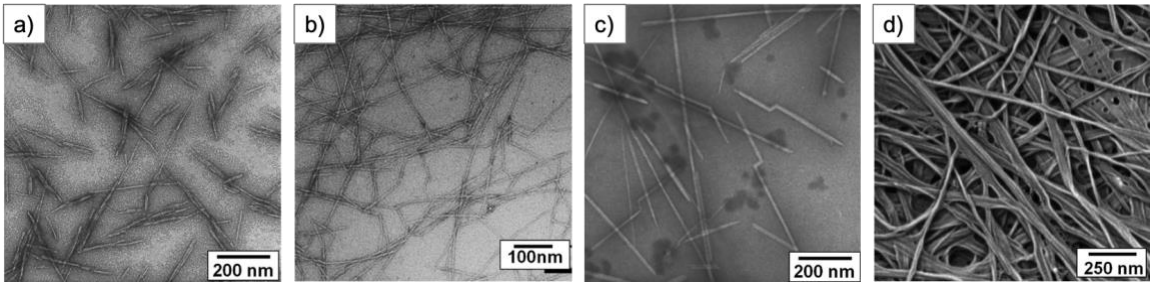

Figure 1-13. (a) Wood CNCs observed by TEM. (b) TEMPO-oxidized CNF. Reproduced with permission from ref. [130] © 2007 American Chemical Society. (c) Tunicate CNCs. (d) Bacterial nanocellulose. Reproduced with permission from ref [131] © 2007 American Chemical Society. (a) and (c) adapted from ref. [129] with permission from the Royal Society of Chemistry © 2011.

surrounding amorphous tissue. Cellulose nanocrystals (CNCs) from biomass are typically generated through sulfuric acid hydrolysis of woody biomass. The sulfuric acid hydrolysis reacts with amorphous cellulose and hemicellulose present in cellulose fibers but does not penetrate the crystalline regions, instead yielding nanoparticles with sulfate half ester surface functionality. CNCs derived from trees have rectangular 5 x 5 nm cross sections and are 200-400 nm in length Figure 1-13a). Cellulose nanofibrils maintain a much higher aspect ratio reaching lengths that exceed 1 μm (Figure 1-13b). One typical method of extracting CNFs is through a TEMPO-mediated surface oxidation with bleach, performed at a pH of 10. Beyond woody biomass, nanocellulose can also be found in tunicates (Figure 1-13c and from bacteria Figure 1-13d).

In aqueous suspension, CNCs assemble into a chiral nematic phases above 4 weight% concentrations with a pitch that reflects visible light, leading to iridescent films when cast from solution. A variety of interesting optically active materials have been developed taking advantage of these properties including elastomers that change color based on how much they are strained, or responsive photonic materials.[132] Shear aligned CNCs, deposited from concentrated suspensions, have been used for barrier coatings with improved barrier

properties and thermal transport over their isotropic counterparts.[133] CNFs have been studied rather extensively as an alternative to plastic for barrier films (more on this in Chapter 5) and as a composite showing fire-resistant properties.[134,135] Furthermore, the area of 3D hydrogels and aerogels contains rich varieties in the structures present owing to the many easily accessible surface chemistries of nanocellulose.[136]

As atomistic and continuum-based modeling efforts continue to advance alongside ever-higher-resolution characterization techniques, understanding of structure-processing-property relationships in nanocellulose materials promises to continue to advance the field.[137] With all of the advantageous properties listed above and the increased production of both CNC and CNF in recent years, nanocellulose promises to be a commercial reality for a variety of functional applications in the near future.

1.4 Advances in conjugated polymer/cellulose composites

The synthetic tunability and low-energy processing frequently touted by the organic electronic community makes conjugated polymers an attractive class of materials for providing electronic functionality to cellulose-based materials. This section will outline the developments in conjugated polymer/ cellulose composites over the years that have utilized cellulose in two main formats: (1) as low cost substrates (i.e. paper) and (2) as an additive to make high-surface-area electrodes.

1.4.1 Paper as a low-cost substrate for conjugated polymer electronics and electrochromic devices

As mentioned in section 1.1, paper has been investigated broadly as a substrate for low-cost printed electronics over the years. Since PEDOT:PSS is a high-performance conductor that is commercially available, a large portion of the work has centered on incorporating PEDOT-based materials onto paper. Figure 1-14a summarizes one of the device demonstrations including a microcontroller patterned by wax printing channels that were later filled with PEDOT:PSS.[11] The device works as a heater that is triggered by the presence of salt water in the fluid reservoir. This is an exciting developing for using paper and PEDOT:PSS in an analogous fashion to printed circuit boards already widely available for hobbyists. Figure 1-14b shows the fabrication process for PEDOT-based electrodes synthesized through *in situ* polymerization directly onto paper.[138] By repeating the *in situ* polymerization, a high mass loading of PEDOT could be deposited while the cycling rate of the device was preserved from the porosity of the paper. PEDOT:PSS has also been printed onto paper substrates as shown in Figure 1-14c where a series of resistors were

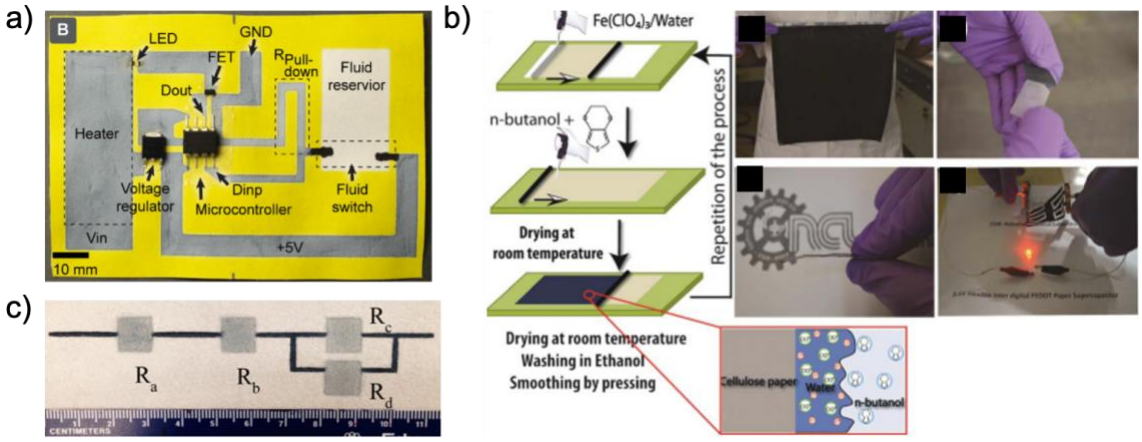

Figure 1-14. Paper-based devices incorporating PEDOT. (a) Paper-based printed circuit board demonstration of a microcontroller-based heater patterned by wax printing. Reproduced with permission from ref. 11 © 2016 John Wiley & Sons. (b) *In situ* polymerized PEDOT on paper for supercapacitors. Reproduced from ref. 138 © 2015 with permission by the Royal Society of Chemistry. (c) Patterned PEDOT:PSS resistors deposited by screen printing onto paper. Reproduced with permission from ref. 139 © 2016 American Chemical Society.

patterned via screen printing connected by low-resistance PEDOT:PSS "wires" of low resistivity.[139]

1.4.2 Nanocellulose as a high-surface-area matrix

Conducting polymer / cellulose composites have also been an active area of research aimed at generating high-surface-area electrochemical electrodes for charge storage devices.[140] Much of the work combining cellulose and conducting polymers has come from the supercapacitor literature to study composite electrodes. By utilizing the mechanical properties and the inherently high surface areas accessible with micro-fibrillated cellulose and nanocellulose, electrodes with higher mass loadings could be created without sacrificing the fast-redox kinetics seen for thin conducting polymer films. The earlier work included oxidative polymerizations of poly(pyrrole) in the presence of

nanocellulose which was then filtered to make the composite electrode.[141] Figure 1-15a shows a similar approach, but with the oxidative polymerization of EDOT using $FeCl_3$ and bacterial nanocellulose as the binder. Supercapacitors based on PEDOT:PSS and CNF were then studied by Malti, et al. where the addition of DMSO and glycerol enabled the fabrication of high-toughness composite electrodes (Figure 1-15b).[142] At the time, there was a hypothesis that the CNF was templating the ordering of PEDOT:PSS on its surface which was later explored in depth in comparison to similarly charged carboxymethyl

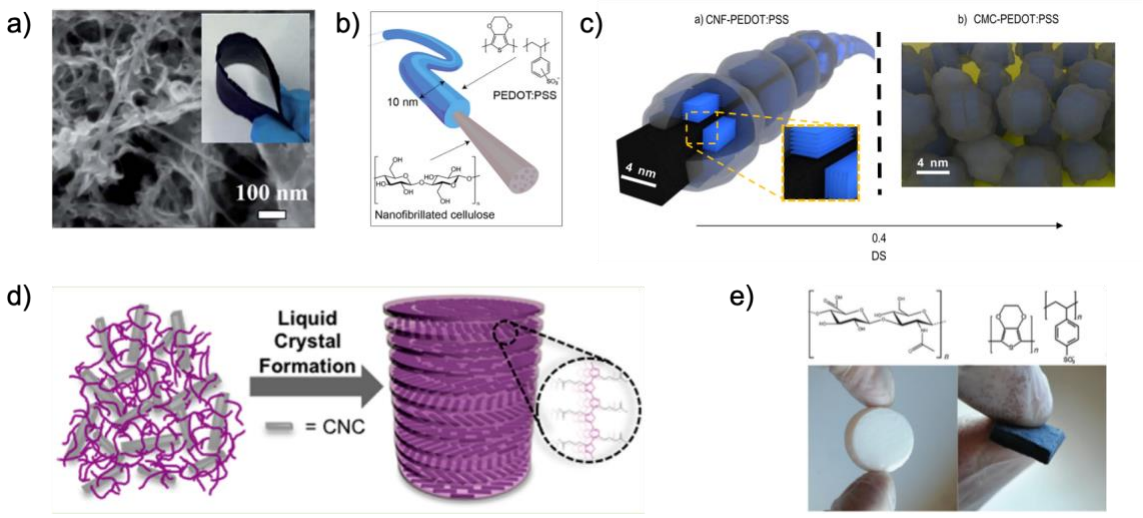

Figure 1-15. Nanocellulose composites with conducting polymers for redox applications (a) Composite electrodes composed of PEDOT and bacterial nanocellulose for supercapacitor electrodes. Reproduced from ref. [143] © 2016 with permission by the Royal Society of Chemistry. (b) CNF-PEDOT:PSS composites prepared as mixed conductors for strong and tough supercapacitor electrodes. Reproduced from ref. [142] (open access) © 2015 John Wiley & Sons. (c) Organization of PEDOT:PSS onto CNF compared to carboxymethyl cellulose. Reproduced with permission from ref. [144] © 2019 American Chemical Society. (d) Templated water-soluble polythiophene derivative by the chiral nematic phase of CNCs in solution. Reproduced from ref. [145] with permission © 2017 American Chemical Society. (e) Layer-by-layer deposition of PEDOT:PSS onto CNF aerogel. Reproduced with permission from ref. [146] with permission © 2013 John Wiley & Sons.

cellulose where higher crystallinities and conductivities were seen for the CNF-based (Figure 1-15c).[144] Nanocellulose has also be incorporated as a templating agent for PEDOT:PSS, where after its removal with concentrated sulfuric acid, highly anisotropic PEDOT crystallites remained.[147] The terahertz complex conductivity of PEDOT:PSS has also been shown to be dependent on the blending ratio with CNCs where higher CNC content was shown to result in more highly localized charge carriers in PEDOT.[148] Recently, news of a pilot-scale plant fabricating these PEDOT:PSS/CNF composites for charge storage electrodes was announced as a collaboration between RISE and the Laboratory of Organic Electronics at Linköping University.

With the research excitement surrounding organic bioelectronics largely driven by the success of PEDOT:PSS, several attempts have been made to replace the polyanion, PSS, with biomolecules such as dextran sulfate, guar gum, and other polysaccharides.[149] Despite lower conductivities compared to PEDOT:PSS, this is a promising approach toward investigating both bioderived materials and new systems for templating the oxidative polymerization of EDOT. In fact, templating conducting polymers with liquid crystals have been explored previously using PEDOT[150] and more recently for poly[3-(potassium-4- butanoate) thiophene-2,5-diyl] (PPBT) with cellulose nanocrystals (Figure 1-15d).[145] Utilizing the anisotropic structure of cellulose to template conducting polymers remains a rather unexplored topic with the potential of new composite materials with interesting optical and transport properties.

Finally, as high-surface-area, 3D structures are easily accessible with nanocellulose, they have served as an attractive candidate for the formation composite electrodes for charge storage. Figure 1-15e shows a CNF aerogel that was modified with a variety of

functional materials including PEDOT:PSS (shown) as well as P3HT and carbon nanotubes. Intricate structures have been achieved using this approach were a layer-by-layer assembly of a supercapacitor was demonstrated by Nyström, et al.[151] From these examples, it's clear there has been a significant desire to combine the properties of nanocellulose with conducting polymers for electrochemical devices.[140] Lessons learned over the years of research regarding how to improve capacitance and ion mobility in these nonporous materials should prove useful as these remain important concepts in the areas of electrochemical transistors, ion pumps, solar steam generators, and even redox-active thermoelectric devices. With the growing interest in top-down approaches for generating high-surface area structures, wood-based materials promise to continue to play a role in the engineering of new functional materials.[128]

1.5 Dissertation Summary

This dissertation explores the use of cellulosic materials in electrochromic devices to demonstrate their utility as substrates and oxygen barrier films. By studying solution-processed and acid-treated PEDOT:PSS as an electrochemical electrode on these substrates, we show its general utility for redox active devices through its broad conductive potential window, stability, and transparency.

For redox-active devices such as electrochromic displays, a transparent electrode with redox stability is essential. Despite the abundance of methods reported in the literature to improve the conductivity of PEDOT:PSS above 1000 S cm^{-1}, relatively little has been reported on the redox properties of PEDOT:PSS after the addition of cosolvents or acidic post-treatments. One previous report noted a substantial shift (up to 500 mV) in oxidation onset to lower potentials of several types of PEDOT:PSS treated with dimethyl sulfoxide (DMSO) accompanied by an increase in capacitance.[152] Another study reported an expansion in the conductive potential window of PEDOT:PSS by lowering the conductive onset by 100 mV after treatment with 1 M *p*TSA/DMSO.[153] Further understanding of the changes that take place during these acidic post treatments could lead to the use of PEDOT:PSS as an electrochemical electrode for easily oxidized materials for electrochromics and charge storage. Chapters 3 and 4 highlight the ability to process PEDOT:PSS onto cellulose-based substrates and support stable switching for electrochromic devices.

Another major challenge for electrochromic devices is photochemical degradation of the active materials upon exposure to sunlight and oxygen. While previous studies have

shown the ability to dramatically extend the lifetime of chromophores in electrochromic polymers through encapsulation in ambient atmosphere,[111,154] there remain many unanswered questions regarding photodegradation in these materials. For instance, how does the repeat-unit structure influence the photodegradation of these materials? How do moderate oxygen barriers impact the photostability? How does the oxidation state of the polymer influence its degradation? And what can the degraded polymer films tell us about the photo-chemical mechanism driving the loss in optical density? Chapter 5 aims to shed light on the influence of moderate oxygen barriers composed of renewable materials on the photodegradation of lateral devices.

Finally, Chapter 6 contains a perspective on the field of electrochromics with an emphasis on developing a better understanding of photostability. Some of the material challenges that paper-based electronics face are discussed to give insight into the field at large. Next, opportunities for wood-conducting polymer composites are presented including some fundamental questions regarding *in situ* syntheses and characterization of the three-dimensional structures. Future studies in this area will hopefully lead to the successful bridging of the controlled redox properties of π-conjugated polymers and the advantageous mechanical properties of cellulose through the use of top-down fabrication methods.

CHAPTER 2. EXPERIMENTAL METHODS

This chapter will cover the experimental methods used throughout this dissertation. This first section on processing will detail PEDOT:PSS post-treatments for high conductivity, processing of electrochromic films and devices, and encapsulation with multilayer barrier films composed of cellulose and chitin. Characterization methods used to quantify molecular structure and physical properties are presented in section 2.2 including optical absorption, conductivity, and redox properties.

2.1 Processing Techniques

2.1.1 Processing highly conducting PEDOT:PSS with acidic post-treatments

As described in Chapter 1, the need for a solution-processible conductor is essential for enabling cellulose-based electrochromic devices. In the following studies of PEDOT:PSS, thin films were prepared by blade coating, drop casting, and inkjet printing. The suspension used for blade coating was prepared by first filtering Clevios PH1000 through a 1 µm syringe filter, adding 0.1 wt% Triton-X100 (a nonionic surfactant), then mixing thoroughly by placing on a VWR stir plate for 60 minutes at 400 rpm. The substrates used for blade coating included glass slides and transparent wood prepared by Dr. Yuanyuan Li at KTH.[120,155] To ensure the glass slides were clean, four sonication steps were performed using sodium dodecyl sulfate (SDS) in deionized water, deionized water, acetone, and isopropanol as cleaning solvents, each for five minutes of sonication. After drying with argon, the slides were then further cleaned through a 15-minute exposure in a Novascan PSD Pro series UV-Ozone chamber (185 + 254 nm). In order to avoid solvent

damage to the poly(methyl methacrylate) matrix of the transparent wood composite, the surface was rinsed with SDS/deionized water followed by pure deionized water and dried with argon. With the suspension and substrates ready, blade coating was then performed using a Zehntner ZAA 2300 automatic blade coater with a tunable blade height (Zehntner ZUA 2000, 0-3000 µm height, 10 µm intervals) and adjustable speed (1-99 mm s^{-1}). The thickness of blade-coated films was adjusted primarily through the blade speed where all films were coated in the Landau-Levitch regime (faster coating speeds increase film thickness).[156,157] The thin films prepared in Chapter 3 used a 400 µm gap height, 8 mm s^{-1} coating speed, and 5 µL cm^{-2} of suspension volume. After coating, PEDOT:PSS thin films were then dried at 50˚C using a VWR Symphony vacuum oven equipped with a solvent trap cooled with dry-ice/isopropanol.

For the electrochemical measurements detailed in Section 2.3.3 below, PEDOT:PSS suspensions (+1 wt% Triton X-100) were drop-cast onto polished glassy carbon button electrodes (BASi, 0.07 mm^2), then dried in the vacuum over at 50˚C.

The inkjet printing of PEDOT:PSS discussed in Chapter 4 was performed using a Microfab Jetlab II printer located in the organic cleanroom as part of the Institute of Electronics and Nanotechnology (Marcus Building). The printer was equipped with a 50-µm-diameter piezoelectric nozzle and a temperature-controlled stage. PEDOT:PSS ink was prepared by diluting Clevios PH1000 to 0.65 wt% (1/2 of the initial solids concentration) followed by the addition of 0.05 wt% Triton-X100. To achieve stable jetting of the PEDOT:PSS ink, a square-wave voltage was applied, with the following parameters. Rise time 1: 4 µs, dwell time: 27 µs, fall time 4 µs, echo time 48 µs, rise time 2: 4 µs, dwell voltage: 22 V, echo voltage -22 V. Adjustments to the dwell time and the dwell/echo

voltage were the principle adjustments made in order to obtain single droplets of ca. 65 µm in diameter (~150 pL) with velocities between 1 and 3 m s^{-1} as measured by a horizontal camera. Once stable jetting was achieved, printing was then performed at 60˚C onto paper samples prepared on a pilot paper machine by Michael Bilodeau at the Forest Products Research Institute at the University of Maine. Two calendared-paper samples were used as substrates: standard office paper and a CNF-coated office paper (4.4 g m^{-2} CNF). Thickness control of the printed films was achieved through adjustments of the droplet spacing in the x and y directions as well as through subsequent overprints. These films were then dried under vacuum at 50˚C.

The acidic post-treatment was performed by drop-casting 1 M *p*TSA/EG onto the dried PEDOT:PSS coatings at room temperature. After 10 minutes, the 1 M *p*TSA/EG solution was rinsed off of the PEDOT:PSS with deionized water three times to ensure complete removal. These films were dried again at 50˚C at ambient pressure before characterizing the optical, electrical, and electrochemical properties (Section 2.3).

The mechanism of the conductivity enhancement arising from both polar solvent additives and acidic post-treatments has been detailed extensively in the literature through insight gained from x-ray scattering experiments and x-ray photoelectron spectroscopy.[75,158–160] These studies have shown that strong acids are capable of protonating the PSS^-, leading to its removal from the thin film. Upon PSSH removal, PEDOT crystallites grow and are hypothesized to adopt a fibril-like microstructure, resulting in the observed 10^3-fold improvement in electrical conductivity. A similar coarsening of the PEDOT crystallite structure is seen with the inclusion of polar co-solvents such as ethylene glycol, where increases in ethylene glycol mass fractions resulted

in higher crystallinity and higher purity in the PEDOT-rich domains of the thin film.[75] This transformation of PEDOT:PSS microstructure is the most plausible mechanism responsible for the conductivity improvement of treated PEDOT:PSS electrodes in this dissertation (1 M *p*ara-toluene sulfonic acid (*p*TSA) / ethylene glycol (EG)). For overviews of x-ray scattering techniques applied to conducting polymers, the interested reader is directed to two comprehensive review articles.[161,162]

2.1.2 Electrochromic device processing

Poly(3,4-propylenedioxythiophene-(ethyl hexyloxy)$_2$), or P(ProDOT) was used as the primary electrochromic active material throughout this dissertation (transparent wood ECDs, paper-based ECDs, and in the encapsulated ECDs). This material was synthesized at BASF using direct (hetero)arylation polymerization in their scale-up efforts. The molecular weight of this polymer was characterized using a THF GPC to determine Mn = 15 kDa and Đ = 1.5. In assembling window-type electrochromic devices, poly(3,4-propylenedioxypyrrole-N-C$_{18}$) (P(ProDOP)) was used as the counter electrode material. P(ProDOP) was synthetized using dehalogenative polycondensation (95.6 kDa, Đ =1.8 by THF GPC, polystyrene standards) as previously reported.[163]

Other polymers used in Chapter 4 were incorporated to demonstrate the effectiveness of the inkjet-printed electrodes for a broad color gamut. These polymers were ECP-Cyan (Mn = 55 kDa; Đ = 1.2, vs polystyrene in THF) and ECP-Yellow (Mn = 226 kDa; Đ = 1.9, vs polystyrene in THF), both synthesized by direct (hetero)arylation polymerization. The random copolymer, ECP-Black (Mn = 21 kDa; Đ = 4.6, vs polystyrene in $CHCl_3$) was synthesized using Stille polymerization.[164]

Electrochromic films were deposited via airbrush spray coating from 5 mg mL^{-1} solutions in toluene using an Iwata Eclipse spray gun and inert carrier gas at 15-20 psi. The optical density of the films was monitored to control the film thickness using an Ocean Optics USB 2000+ spectrophotometer to observe the peak absorbance of the electrochromic film. In order to maximize the contrast between the oxidized and neutral state of the electrochromic polymer, films were sprayed to an absorbance of 0.95 ± 0.05 (versus the substrate + electrode as a blank).[165] The P(ProDOP) counter electrode films were spray cast to 0.40 ± 0.05 for the equivalent charge density as ECP-Magenta films.[109] These spray cast films were then be incorporated as the working electrode in a three-electrode electrochemical cell, or assembled into an electrochromic device.

Window-type electrochromic devices were assembled by sandwiching two electrodes together and filling with a gel electrolyte composed of 0.5 M tetrabutylammonium hexafluorophosphate ($TBAPF_6$) dissolved in propylene carbonate (PC) and 6 wt% polymethylmethacrylate (Mw = 996 kDa) dissolved to increase the viscosity. The working electrode was composed of the substrate, electrode, and spray-coated electrochromic polymer film. The counter electrode was composed of the substrate, electrode, and the spray-coated P(ProDOP) and was set into its oxidized state prior to device assembly.[109] VHB tape was applied to the working electrode in two concentric rectangles - one to define the active area of the device and the other to contain the spill-over of electrolyte during the device assembly. Once sandwiched together and sealed, the electrochromic device was characterized by the techniques detailed in materials characterization section (2.2).

To fabricate lateral electrochromic devices onto paper, inkjet-printed PEDOT:PSS was deposited to form relatively two 5 x 5 mm color-neutral films with droplet spacings of 70 µm in the x-direction and 40 µm in y-direction. Thick PEDOT:PSS contacts were printed with three passes of droplet spacings of 0.1 mm in the x-direction and 0.07 mm in the y-direction. Thick PEDOT:PSS contacts were deposited by printing two layers with a 0.07 mm x-spacing and a 0.04 y-spacing.

Encapsulated lateral devices on glass substrates were fabricated for photostability studies in Chapter 5. PEDOT:PSS electrodes were deposited on clean glass substrates via blade coating the PEDOT:PSS ink followed by drying on a hot plate at 120˚C for 5 minutes. The electrochromic polymer, P(ProDOT) was spray cast from a 5 mg mL^{-1} toluene solution to an optical density of 0.9 ± 0.05. Then, 80 µL of the iongel solution was deposited onto ECP active layer covering an additional 3 mm in excess around the perimeter of the lateral electrodes. The electrolyte was dried under vacuum at 50˚C for at least 3 hours. Finally, the ECDs were encapsulated with each barrier film and sealed around the edges with 4 mm strips of polyisobutylene (ADCO) edge sealant at 120˚C for 1 minute making sure to eliminate air bubbles and gaps between the edge of the electrolyte and the ADCO edge sealant. During lamination, pressures of roughly 5 psi were used and air bubbles were eliminated from the device. Fast-drying silver paint was applied to the exposed PEDOT:PSS for electrode contacts.

2.1.3 Processing renewable barrier films

The renewable barrier films studied in Chapter 5 were composed of biomass-derived nanoparticles spray-coated onto commercially-available cellulose acetate substrates (Goodfellow) by Yue Ji in Professor Carson Meredith's laboratory.

Chitin nanofibers were extracted using a three-step process using 5 wt% NaOH at 140˚C for 6 hours, followed by 7 wt% HCl for 6 hours, and finally with 35 wt% NaOH, again at 140˚C for 100 minutes. The suspension was passed through a high-pressure homogenizer to obtain the disintegrated nanoparticles, dispersed in pH 3 acetic acid. The average length and width of the particles was 169 nm and 4.5 nm, respectively as measured by atomic force microscopy (AFM) of >100 particles on deposited onto cleaned silicon wafers. AFM measurements were performed on a Bruker Dimension Icon instrument in tapping mode with MPP-TAP150 probes exhibiting resonant frequencies of 120-180 kHz and spring constants of 5 N m^{-1}. Due to tip-broadening effects and the small cross-section of the particles, the height was used for the "width" measurements. ImageJ was used for manual particle counting to generate the size distributions shown in the Chapter 5 supporting information.

The multilayer barrier films were prepared by airbrush spray coating from a ChNF suspension (0.5 wt%) onto a heated substrate (60˚C), at a mass loading of roughly 0.7 mg cm^{-2}. Next, a 0.5 wt% suspension of CNCs (sulfuric acid hydrolyzed at the Forest Products Lab) was spray coated on top of the ChNF coating at an equal mass loading to create the bilayer film (roughly 10 μm in thickness). Previous results showed that spray coating alternating layers of Chitin (with positively charged protonated amines) and negatively

charged CNCs (surface sulfate groups) coalesce into barrier films that are less hazy and perform better as oxygen barriers compared to the equivalent thickness of monolayer coatings of each particle.[166] This result suggests there is an electrostatic attraction between CNCs and ChNFs, leading to more dense particle packing in the spray-coated layers. After spray coating, the barrier films were let dry under ambient conditions for 4 days prior to their use in electrochromic device encapsulation.

2.1.4 Photostability Measurements

Encapsulated lateral ECDs were exposed to 24-hour cycles of irradiation under 1 sun using an Atlas XLS+ Suntest solar simulator equipped with a xenon arc lamp and a daylight filter. The irradiance was controlled at 55 mW cm^{-2} between 300-400 nm by a broadband photo detector per ISO 9370. During the irradiation, the black standard temperature was maintained between 45 and 55˚C while the chamber air temperature was roughly 35˚C. 24-hour irradiation experiments produced energy doses of 4740 ± 10 kJ m^{-2}. The devices were set initially to +1.0 V where the left electrode was bleached and the right electrode was colored. During irradiation, the devices were not driven by a voltage during irradiation, rather they were let to relax to an intermediate state. The relative humidity was expected to fluctuate between ambient laboratory levels (30 – 60 %) during the irradiation cycle. After each irradiation cycle (24 h) 20 potential square wave break-in cycles were performed and spectra, photographs, and videos of switching were recorded (see section 2.3 below).

2.2 Materials Characterization

Of key importance in materials development, particularly of polymers, is the molecular characterization. It is critical to be certain of the chemical composition (elemental analysis), chemical structure (NMR), and molecular weight (GPC, MALDI) so as to be sure the materials carried through further experiments are understood and pure. While a necessary step in performing polymer materials research (especially from a group as synthetically oriented as the Reynolds group), these techniques will not be covered in depth here. The reader is directed to the dissertations of Dr. James Ponder, Dr. Dylan Christiansen, and Dr. Ben Reeves for synthetic procedures and molecular characterizations of electrochromic materials, particularly ProDOT-based materials. For a detailed discussion on synthetic methods, Dr. Rylan Wolfe's dissertation is an excellent resource.

2.2.1 X-ray Photoelectron Spectroscopy

X-ray Photoelectron spectroscopy (XPS) is an analytical technique for determining the chemical species present, and their surrounding chemical environment (called chemical states) on the surface of solid materials. Although X-rays penetrate the full sample thickness, it is only the electrons in the top 3-10 nm of the sample that are recorded, making this is a surface-sensitive technique. In order to record the core-level electrons ejected from the sample, an ultra-high vacuum is necessary (10^{-8} mbar), thus precluding volatile compounds from being analyzed with this method. The reader is directed to the following useful resources for more detailed descriptions of XPS (casaxps.com and xpssimplified.com) and an exhaustive list of characteristic binding energies.[167]

XPS measurements were performed using a Thermo K-alpha instrument located in the materials characterization facility (MCF) as part of the institute for electronics and nanotechnology. XPS was used to analyze the photo-degraded P(ProDOT) as discussed in Chapter 5. To prepare films for the XPS measurement, the encapsulated electrochromic devices were disassembled by removing the barrier film and the iongel electrolyte. The films were then soaked in acetone followed by 3 rinsing steps to remove any residual salt. The films were then left to dry under ambient conditions for 24 hours before performing XPS characterization.

A typical XPS instrument contains a metal anode (Aluminum in the case of the Thermo K-alpha) that is bombarded with an electron beam to generate x-rays which are then monocromated to 1486.6 eV. These X-rays were then directed toward the sample where they will eject the core-level electrons (C(1s), S(2p), O(1s)) for the degraded P(ProDOT)). The X-ray spot size can be adjusted for small samples, but for the P(ProDOT) samples studied in Chapter 5, a 400 μm elliptical spot was used to obtain the highest signal to noise ratio. The ejected electrons then pass through a series of lenses and are separated by energy in a hemispherical detector. The degree to which the electrons are slowed by the lenses, called the pass energy influences the resolution of the measurement (lower pass energy = higher resolution). The kinetic energy at which core-level electrons are ejected is characteristic of the atom as well as the binding environment (e.g. C(1s) electrons from alkyl carbons have higher kinetic energies than those from oxidized carbon functional groups such as ethers). For all measurements of P(ProDOT), an argon ion gun is used to neutralize insulating samples as they are bombarded with X-rays.

Typically, spectra are reported in terms of intensity versus binding energy, which is the difference between the x-ray energy and the kinetic energy (1486.6 – KE). Two types of spectra were recorded for photodegraded P(ProDOT): survey spectra spanning the range of binding energies 0-1486 eV and elemental spectra which scan 10-20 eV around a characteristic binding energy. An example survey spectrum is shown in Figure 2-1a where several elemental peaks appear. The survey spectrum gives an overview of the sample allowing for a qualitative observation of the elements present. Energy resolution for the survey spectrum were 1 eV as determined by the electron "pass energy" of 200 eV. Example high resolution scans for the C(1s) (Figure 2-1b) and the S(2p) (Figure 2-1c) of P(ProDOT) thin films show how multiple peaks can be deconvoluted to obtain chemical state information. These high-resolution scans were performed with a 40-eV pass energy giving 0.1 eV of binding energy resolution in the spectra. Additionally, the integrated areas, normalized to the relative sensitivity factor (tabulated for all elements in CasaXPS) can be compared to calculate the relative abundance of certain elements, thus giving information such as anions per ring for doped polymers.

For the photostability studies of lateral devices encapsulated by multilayer barrier films, high-resolution spectra were recorded for C(1s), O(1s), S(2p), N(1s), and F(1s), the spectra were processed in CasaXPS. The background signal, arising from both extrinsic losses (electron-phonon coupling, inelastic scattering) as well as intrinsic events (e.g. electron-electron interaction) was fit using the Shirley background type. Next, an energy calibration was performed by setting the principle C(1s) peak associated with alkyl C-C

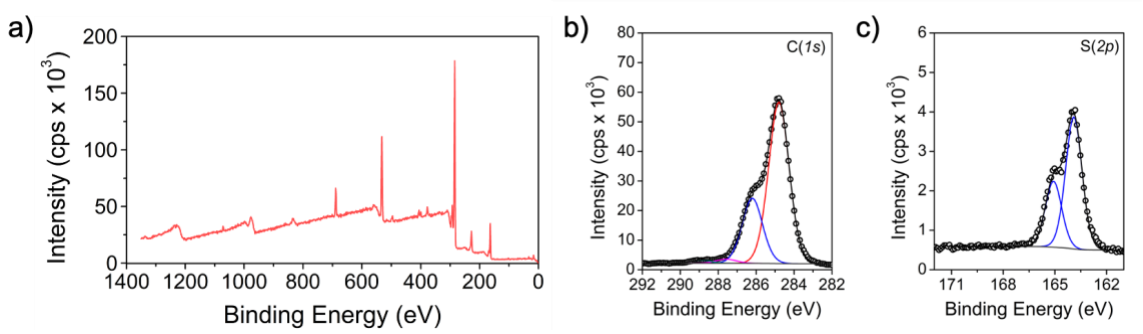

Figure 2-1 (a) A typical survey spectra of P(ProDOT) (b) high-resolution C(1s) spectra taken of a P(ProDOT) thin film prior to photo-degradation experiments.

bonds to 284.8 eV. This allowed for sample-to-sample binding energies to be comparable as each measurement may experience different levels of charging, shifting in binding energy slightly. Deconvolution was performed by adding peaks whose envelope most closely matched the experimental spectra. A composite Gaussian, Lorentzian line shape was used 30-60% gaussian composition (e.g. GL(30) is 30% Lorentzian, 70% Gaussian). All peaks attributed to the same atoms (C(1s), S(2p), etc.) were constrained to the same full-width at half maximum. Peaks arising from the p-, d- or f-shells such as the S(2p) spectra exhibit a doublet for each chemical species present due to the spin-orbit splitting of the ejected electrons that occurs for electron shells with the angular momentum quantum number, $l > 0$. As this peak splitting is a constant, it was fixed to 1.16 eV for the S(2p) spectra and the peak areas were constrained such that the higher-energy peak had half of the area as the peak appearing at lower binding energies. With these peaks fitted, the relative areas of the chemical species present were determined using the following formula.

$$Atomic\ ratio = \frac{Arel}{KE^{0.6}(RSF)} \tag{2.1}$$

Where A_{rel} is the integrated area of each peak, KE is the kinetic energy, and RSF is the relative sensitivity factor of the element provided by CasaXPS or xpssimplified.com.

2.2.2 Optical Properties Characterization

2.2.2.1 Absorbance

UV-Vis-NIR spectroscopy (~1-3 eV) is a key probe of the electronic structure of conjugated polymers in their neutral and charged states. Absorbance spectra of conjugated polymer thin films were performed using either a Varian Cary 5000 UV-Vis spectrophotometer or an Ocean Optics USB 2000+ fiber optic spectrophotometer. The Cary 5000 spectrophotometer enables broader spectral measurements into the near IR (up to 3500 nm wavelengths) with higher sensitivity. Therefore, all measurements aimed at recording charge-carrier absorbance were performed on the Cary 5000. The Cary 5000 is equipped with solid-film sample holder, a cuvette holder for running spectroelectrochemistry, a temperature-controlled cuvette holder, and an integrating sphere attachment (discussed in section 2.2.1.2).

In the characterization of electrochromic polymer films, spectroelectrochemical experiments were performed to observe the evolution of absorbance of the polymer film as is becomes electrochemically oxidized. For this measurement, three-electrode electrochemical cells were assembled containing the ECP-coated working electrode, a platinum flag counter electrode (~1 cm^2), a Ag/Ag^+ reference electrode calibrated versus

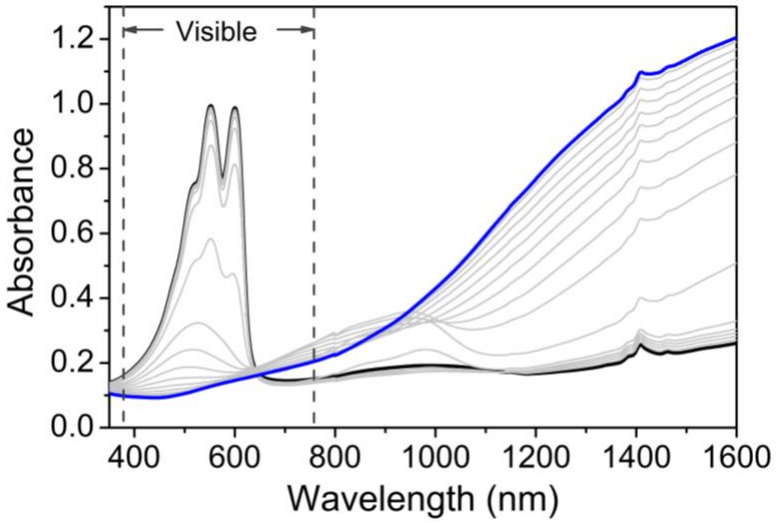

Figure 2-2. Spectroelectrochemical series for a P(ProDOT) thin film on a PEDOT:PSS/glass electrode in 0.5 M $TBAPF_6$. Spectra were recorded at 50 mV increments between -0.3 V and 0.8 V vs. Ag/Ag^+.

ferrocene (see cell assembly details in section 2.2.4.1), and 0.5 M $TBAPF_6$ / PC electrolyte. A reference cell containing the electrode and electrolyte in an identical cuvette was used for the instrument baseline and for the reference beam during measurement. These reference cells were used for the baseline measurement in the scan software. In the spectroelectrochemistry measurement, the electrochromic film was first broken in by performing five cyclic voltammograms (more on this in section 2.2.4) and then set in its neutral state by applying -0.3 V vs Ag/Ag^+ for 30 seconds using a EG&G Princeton Applied Research potentiostat/galvanostat under CorrWare software control. The neutral state absorbance was then recorded by the spectrophotometer. The electrochemical potential was increased 50 or 100 mV increments and held for 30-60 seconds at each potential to establish equilibrium prior to recording the absorption spectrum.

Figure 2-2 shows an example spectroelectrochemical series for a P(ProDOT) thin film on a PEDOT:PSS/glass electrode. The π-π* transition is shown for the neutral

P(ProDOT) held at -0.3 V vs Ag/Ag^+ (black trace). The wavelength of maximum absorbance (λ_{max}) appears at 550 nm and is tracked as the polymer becomes oxidized to calculate the electrochromic contrast (change in % Transmittance of λ_{max} between the fully neutral and oxidized polymer). The secondary peak at 600 nm arises due to vibronic coupling of the chromophore ($\lambda_{max} - \lambda_{vibronic} \sim 100$ meV) which is corresponds to commonly-seen intra-ring vibrational energy.[92] As the polymer becomes oxidized, the neutral-state absorbance bleaches with a minor blue-shift to 510 nm. This shift indicates some heterogeneity in the film were more easily-oxidized domains will bleach first. At 0.2 V vs. Ag/Ag^+, radical cation charge-carriers appear at 970 nm, and the longer-wavelength (> 1200 nm) absorbance attributed to dication species begins to grow in.[94] At 0.8 V (blue trace) the neutral state absorption is fully bleached, leaving only the broad absorbance from cation and dication charge carriers in the film. Differences in the charge-carrier absorbance wavelengths between polymers can be used to assess a polymer's ability to delocalize electrons in its charged state, rationalizing differences in charge-transport properties. Spectroelectrochemistry measurements were also performed on electrochromic devices, primarily to extract contrast and colorimetric data (See section 2.2.2.3).

Electrochromic switching kinetics were also probed using the Cary 5000 UV-Vis. Using the CaryWinUV kinetics software and the same electrochemical setup and reference cells as the spectroelectrochemistry experiments. Potential square waves of varying lengths were applied to the film while the absorption at λ_{max} was recorded every 30 ms. The pulse lengths varied from 60 seconds to 1 second in order to observe the switching time for both coloration and bleaching of the film. These switching times were reported as the time required to reach 95% of the maximum contrast upon bleaching and coloration (t_b and t_c).

A switching time constant was calculated from the kinetics data by plotting the contrast (Δ%T @ 550 nm) versus pulse length and fitting to the following exponential equation.[168]

$$\Delta\%T = \Delta\%T_{max}(1 - \exp(-t/\tau)) \quad (2.2)$$

Where Δ%T is the contrast at given pulse time *t*, and $\Delta\%T_{max}$ is the maximum contrast of the material.

UV-Vis absorbance was also used to track the photodegradation of P(ProDOT) in encapsulated electrochromic devices (Chapter 5). Observation of how these absorbance features evolved upon extended sunlight irradiation provided information on the rate of loss of the chromophore in comparing barrier films. Other changes in the neutral-state absorbance such as shifts in λ_{max} and relative absorbance of the π-π* transition to the near infrared absorbance were used in conjunction with the XPS results to compare the differences in degradation seen for the left versus right electrodes.

2.2.2.2 Haze and reflectance in highly scattering materials

While cellulose and chitin do not contain light absorbing chromophores these materials interact with light as scatterers both in suspension and in disordered films. Light scattering takes place at any interface between two materials of different refractive indices. Haze measurements were performed for transparent wood samples (Chapter 3) as well as for the multilayer barrier films discussed in Chapter 5. Haze was measured using the integrating sphere (Diffuse Reflectance Accessory 2500) attachment for the Cary 5000. This attachment includes a 150 mm integrating sphere coated with a PTFE-based reference material, Spectralon, to provide uniform, diffuse reflection from 250-2500 nm. This

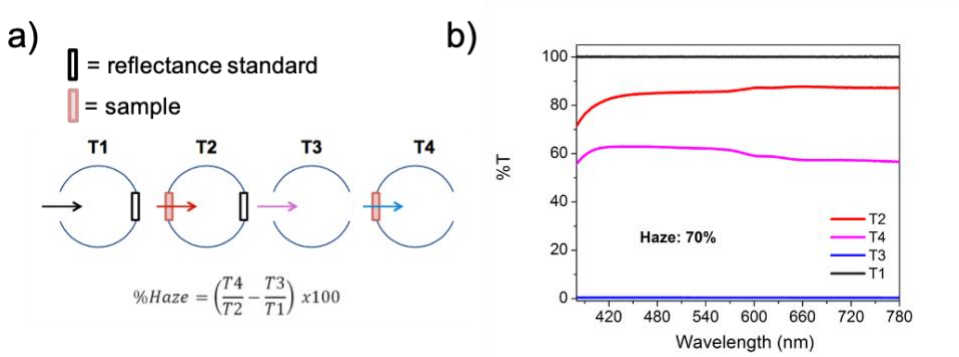

Figure 2-3 (a) Sample configurations used to calculate haze. (b) Example spectra from a sample with 70% haze for each configuration.

integrating sphere is equipped with a sample holder for the transmission port at the entrance of the sphere and a reflection port at the back. A reference beam also enters the integrating sphere and is reflected off of a Labsphere diffuse white reflectance standard (USRS-99-020) oriented perpendicular to the sample beam. The incident light beam passes through the transmission port at an 8˚ angle relative to normal incidence (di:8˚ geometry) and reflects off of a diffuse reflectance standard at the back of the sphere. Ultimately, a minority of the incident light is collected by the detector at the base of the sphere, thus scan rates of 600 nm min^{-1} were used as opposed to the 1800-2000 nm min^{-1} possible for standard absorption/transmission measurements in the Cary 5000 in order to improve the signal to noise of the spectra.

Four sample configurations were used to measure haze as depicted in Figure 2-3a.[169] T1 and T3 were instrument corrections were T1 represents the baseline, 100% T scenario and T3 was close 0%T as the light beam completely exited the integrating sphere. The two configurations with the sample in place (T2 and T4) allowed for the collection of the total transmitted light (T2) and the diffusely transmitted light (T3) as shown in the example spectra in Figure 2-3b. Haze is then calculated using the following expression.

$$Haze\ (\%) = \left(\frac{T4}{T2} - \frac{T3}{T1}\right) x100 \quad (2.2)$$

Reflectance measurements of paper and inkjet-printed PEDOT:PSS electrodes onto paper were performed using the ocean optics spectrophotometer equipped with a 30 mm integrating sphere (ISP 30-6-R) and the same diffuse reflectance standards used for the haze measurements (Labsphere USRS-99-020). The relatively low reflectance signal generated using this setup required integration times of roughly 20 seconds for collecting spectra, thus precluding its use for kinetics studies of the lateral ECDs.

2.2.2.3 Basics of Colorimetry

Colorimetric analysis was used to quantify the color of printed PEDOT:PSS electrodes in addition to the color change of electrochromic devices discussed in this dissertation. All colorimetric analyses were performed in the CIE 1964 ($L^*a^*b^*$) color coordinate system, which is used extensively in the electrochromic literature for quantifying color. Colorimetric data was computed in Matlab from transmittance or reflectance spectra as well as from photographs using a known D50 light source. D50 light has a known spectral power density (stored in the lab_calc.m file on the Reynolds Group Fileserver) which is used to calculate the tristimulus values (X, Y, and Z) needed for computing the L^*, a^*, b^* color coordinates reported. The interested reader is directed to the 2004 *Commission Internationale de l'Eclairage (CIE)* technical report where the relationships between spectra, color-matching functions, tristimulus values, and L^*, a^*, b^* coordinates are detailed.[170] Finally, in order to calculate the color difference (ΔE^*) between

two objects with known $L^*a^*b^*$, the Euclidian distance is between color coordinates is computed as follows:

$$\Delta E^* = \sqrt{\Delta L^{*2} + \Delta a^{*2} + \Delta b^{*2}} \tag{2.4}$$

All photographs were captured using a Nikon N95 DSLR camera with the following exposure settings. The shutter speed was 1/80th of a second from transmissive samples and 1/50th of a second for reflecting samples. The ISO sensitivity was kept at 200 and the f-stop was 5.6 for all photographs.

2.2.2.4 Video-Frame Analysis for Kinetics Quantification

Colorimetric analysis of the reflective paper-based electrochromic devices was performed using image analysis in Matlab (Chapter 4). Photographs were taken in the light booth (D50 lighting) with the top lamp illuminated and the backlight off. To analyze photos and videos, a Matlab script was written to open the first video frame and allow the user to select the analysis area by clicking on two opposite corners of the square electrode with their cursor. The selected area was then divided into 5 subsections (1-5 mm) to observe the color change as the electrochromic moving front crossed the pixel from the center to the contact. The time vector was generated by multiplying the number of frames times the camera frame rate (24 fps). RGB data was collected from each video frame for each subsection and stored into a x-by-y-by-3-by-time element matrix. This RGB data was then averaged over the subsection and converted to $L^*a^*b^*$ coordinates using the built-in *rgb2lab* function (using D50 as the white point). Subsequently, the two $L^*a^*b^*$ coordinates were

converted to ΔE^* versus time was using equation 2.4. The switching times for each subsection was calculated based on the time required to reach ΔE^*_{max} – 2.3, or the point at which the color change becomes indistinguishable to the human eye.[170]

2.2.3 Electrical Properties

2.2.3.1 Solid-state dc conductivity

The DC resistance of PEDOT:PSS thin films was measured and the conductivity using the Van Der Pauw method.[171] The Van der Pauw method is another common four-probe technique for thin film samples where the electrodes make contact the edges of a film of arbitrary shape in Figure 2-4. For this method, small contacts of 1-2 mm diameter were applied to the corners of the PEDOT:PSS thin films through the use of fast-drying silver paint (Ted Pella). This ensured that the distance between electrodes was large compared to the contact diameter (~10x as errors scale with d/L).[172] For the measurement, four resistance measurements were made by applying a current across one edge of the sample, while measuring the voltage across the opposite edge ($R_{12,34} = V_{34} / I_{12}$) using spring-loaded gold pins and a Kiethley 2410 SourceMeter. Averages of the resistances measured across parallel edges were made, giving two resistance values ($R_{vertical}$, $R_{horizontal}$).

$$R_{vertical} = \frac{R_{12,34}+R_{34,12}}{2} \tag{2.5}$$

$$R_{horizontal} = \frac{R_{23,14}+R_{14,23}}{2} \tag{2.6}$$

$$\sigma = \frac{1}{t}\frac{1}{R_S} \tag{2.8}$$

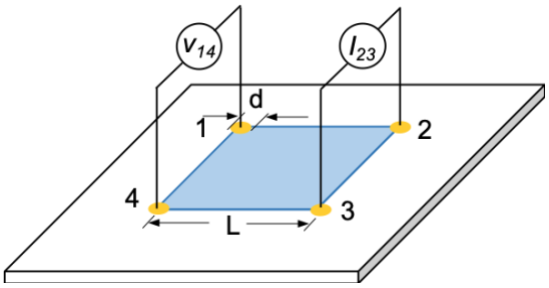

Figure 2-4 A schematic of a resistance measurement using the van der Pauw geometry with four contacts of diameter *d* deposited at the outside edge of and *L x L* PEDOT:PSS film (1-4).

These two resistance values are then plugged into the Van der Pauw formula that can be solved for the sheet resistance (R_s).

$$e^{-\frac{\pi R_{vertical}}{R_S}} + e^{-\frac{\pi R_{horizontal}}{R_S}} = 1 \qquad (2.7)$$

With the sheet resistance known, the sample thickness was measured using a Dektak stylus profilometer. PEDOT:PSS films were roughly 80-150 nm in thickness. The sample conductivity (σ) was then calculated using equation 2.8 below and reported with the units S cm^{-1}.

In order to assess the performance of transparent conductors a figure of merit (FoM) was defined by Haacke, et al. as the ration between the dc conductivity, σ_{DC}, and optical conductivity, σ_{opt}, at 550 nm which can be written as follows.[173]

$$FoM = \frac{\sigma_{DC}}{\sigma_{opt}} = \frac{188.5}{R_S\left(T(\lambda)^{-1/2}-1\right)} \qquad (2.9)$$

Where $T(\lambda)$ is the dc conductivity of the electrode and R_S is the sheet resistance. For reference, commercially available ITO has a FoM of 35, and PEDOT:PSS-coated TW had

a FoM of 14. Some of the highest-performance transparent conductors in the literature exceed FoM values of 100.[174]

2.2.4 Electrochemical analyses

As an analytical method, electrochemistry offers precise control over the energy associated with a chemical process (potential) as well as a high degree of sensitivity for detecting small amounts of redox-active species. Electrochemical experiments were performed both for the characterization of PEDOT:PSS electrodes and of electrochromic polymers and devices. Extensive literature exists on the electrochemical characterization of conjugated polymers in several instructive book chapters[52,97,175] and review articles[176] Additionally, a tutorial on cyclic voltammetry published in *J. Chem. Ed.* serves as a practical guide for those utilizing this method.[177]

2.2.4.1 Cell setup

Apart from the *in situ* conductivity method (1.3.3.2), all of the electrochemical methods described below were performed in three-electrode cells. The working electrode was composed of thin polymer films deposited by drop casting from solution onto polished glassy carbon electrodes or spray-cast electrochromic polymers onto transparent electrodes. The Ag/Ag^+ reference electrode used for all organic-electrolyte measurements was composed of a silver wire immersed in 0.5 M $TBAPF_6$ / acetonitrile with the addition of 10 mM $AgNO_3$ capped at the bottom with a porous glass frit to allow for electrolyte exchange. Reference electrodes were calibrated versus the ferrocene/ferrocenium redox couple (50-100 mV, typically). For aqueous electrolytes, commercially available Ag/AgCl electrodes are used where the concentration of the KCl inner solution dictates the reference

potential (3 M KCl = 0.21 V vs. normal hydrogen electrode). Platinum flags were used as the counter electrode to provide sufficient charge compensation. For thin film measurements on glassy-carbon electrodes, the cell was degassed with Argon (5-10 minutes bubbling through solution) prior to measurement.

2.2.4.2 Cyclic Voltammetry

While cyclic voltammetry (CV) can provide quantitative interpretations of electrochemical kinetics, it is most-often used as a qualitative probe of the redox behavior conducting polymer films, showing the presence of redox couples and capacitive-like current responses as the polymer is cycled between its neutral and fully oxidized state. Kinetic information cycling can be assessed by observing the peak current (i_p) dependence on the CV scan rate. If i_p scales linearly with scan rate, there is no diffusion limitation on the redox kinetics whereas if i_p scales with the square root of the scan rate, the reaction is deemed diffusion limited as can be the case for 1 µm-thick conducting polymer films studied for supercapapcitors.[178] The interested reader is directed to Chapter 2 of *Electroactive Polymer Electrochemistry* for further quantitative analyses possible with CV.[97]

2.2.4.3 Electrochemical Impedance Spectroscopy

Electrochemical Impedance Spectroscopy (EIS) is a subclass dielectric spectroscopy, using small amplitude excitation waves to distinguish between electrochemical processes occurring at various rate constants. This technique has been applied to a wide-range of redox-active conjugated polymers in the literature.[179,180] EIS experiments were performed on thin PEDOT:PSS films drop-cast onto glassy carbon

button electrodes to determine the difference in charge transport properties resulting from the mild acid post treatment. For these experiments, a 5 mV excitation wave was applied to the electrode, generated the elliptical current response known as a Lissajous plot. PEDOT:PSS films were measured at frequencies from 10^5 Hz down to 0.01 Hz at DC offsets from -0.8 V vs. Ag/Ag^+ to 0.8 V vs. Ag/Ag^+. The total impedance $|Z|$ is calculated as the change in voltage over the change in current, which can be decomposed into its real (Z') and imaginary (Z'') contributions as described below.

$$Z' = |Z| \cos \phi \tag{2.10}$$

$$Z'' = |Z| \sin \phi \tag{2.11}$$

Where ϕ is the phase angle. As the EIS experiment is performed from high to low frequencies, the Bode plot shown in Figure 2-5a is filled in from right to left. The Bode plot includes $|Z|$ (log scale) and ϕ versus frequency for 1M *p*TSA/EG-treated PEDOT:PSS at 0 V vs. Ag/Ag^+. In this case, the film behaves as a pure resistor, acting as an extension of the glassy carbon electrode above frequencies of 10 Hz where electronic conduction is detected. At lower frequencies, where ionic motion is detected, the film behaves as a capacitor with an increase in impedance and a phase angle close to -90˚. The imaginary impedance can also be plotted versus the real impedance as shown in Figure 2-5b, called a Nyquist plot. In this experiment, the low frequency points appear toward the top right corner and track toward the origin as the frequency is increased. Interpretation of the impedance data is performed through fitting with an equivalent circuit meant to contain elements that reflect physical processes occurring in the film. Figure 2-5c shows the equivalent circuit used to fit the PEDOT:PSS EIS data.

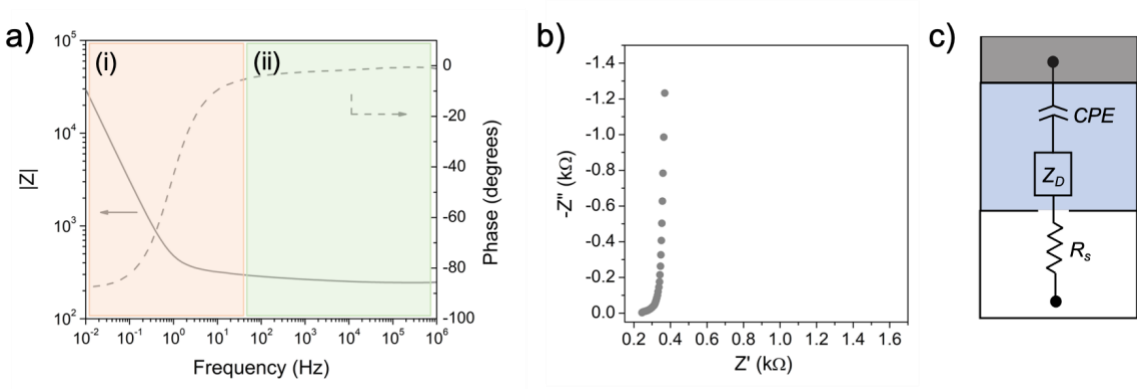

Figure 2-5 Example data collected from an EIS measurement on acid treated PEDOT:PSS. (a) a Bode plot showing the total impedance and phase angle (dotted) versus frequency. The color-coded frequency zones are marked based on the dominant transport mechanism occurring at that time scale including ionic transport (i) and electronic transport (ii). (b) The complex Nyquist plot showing the imaginary vs. real portions of the impedance. (c) A plausible equivalent circuit used for fitting the EIS spectra for acid-treated PEDOT:PSS films showing solution (R_S) and charge-transfer resistance (R_{CT}) and a Warburg diffusion element (Z_D).

First a solution resistance is included to capture the electrolyte resistance. The impedance of a resistor is frequency independent.

$$Z = R \tag{2.12}$$

Next a 'finite-length' Warburg diffusion element (Z_D) is included to represent the ionic diffusion and migration through the PEDOT:PSS film. This element contains parameter for the time-constant for mass transfer (τ_D) and a capacitive element (C_D). The impedance of the diffusion element is given by the following equation.

$$Z_D = \left(\frac{\tau_D}{C_D}\right)\frac{\coth(j\omega\tau_D)^{\alpha}}{(j\omega\tau_D)^{\alpha}} \tag{2.13}$$

Z_D is a frequency dependent impedance defined in terms of the diffusional time constant (τ_D) and the diffusional pseudocapacitance of the film (C_D): where $j = \sqrt{-1}$, ω is the angular frequency in radians sec^{-1} equal to $2\pi f$, and α is an exponent where a value of 0.5

represents ideal diffusion described by Fick's second law.[181] Finally a constant phase element is included to capture the double-layer charging preset at the polymer-electrolyte interface or the electrolyte-electrode interface. The impedance of the constant-phase element is defined below.

$$CPE = (1/j\omega C_d)^p \tag{2.14}$$

where C_d is the bulk electronic capacitance and p = 1 (ideal) for all potentials between -0.6 an 0.4 V where charging effects are absent. Several factors can cause the electrode to deviate from ideal capacitive behavior including surface roughness and non-linear current distributions, thus there is not a consensus on the physical meaning of the fitting parameter, α.

This equivalent circuit was generated using Zview software and then used to fit the experimental data using a non-linear least square fitting algorithm. The goodness-of-fit parameter, χ^2, was minimized for each impedance spectra and can be found tabulated in the supporting information for Chapter 3. Overall, impedance is a powerful technique for studying redox-active conjugated polymers where many future opportunities exist in this area of understanding ionic transport and capacitance in these systems through further EIS analysis, model validation through thickness-dependence studies, tweaking of equivalent circuit elements, and connecting microstructure to the relevant transport properties.

2.2.4.4 In situ Conductance

To probe the conductivity of conjugated polymers as a function of their oxidation level, steady-state *in situ* conductivity methods have been developed. Early reports of

derivatized microelectrodes with poly(N-methyl pyrrole) and poly(3-methyl thiophene) were the first conjugated polymers studied by this method as electrochemical transistors.[98,182] Over the years, several geometries (and experiments) have been explored for *in situ* conductance measurements including disk electrodes, sandwich electrodes, and interdigitated microelectrodes.[97,98] For the purposes of this dissertation, only the interdigitated microelectrode was used for the analysis of PEDOT:PSS films after the acidic post treatment.

In this measurement, one working electrode holds the polymer in equilibrium at the desired potential while the second working electrode sweeps above and below the steady state potential by ±5-10 mV to generate an *I-V* curve. The sweep rate kept at 0.5 mV s^{-1} to avoid current contributions from ion transport. From the *I-V* curve, the conductivity can be measured from the polymer's neutral state (-1.2 V vs. Ag/Ag^+ for the PEDOT:PSS film in Figure 2-6a) in incremental steps as it becomes oxidized and conducting (0.8 V vs. Ag/Ag^+). While conceptually the same as the ON/OFF operation of organic electrochemical transistors, there is a key distinction. These *in situ* conductivity methods use a 5-10 mV difference in potential between the two working electrodes whereas the source-drain bias in OECTs is 100s of mV. Therefore, the doping level near the source electrode could in principle be much different than the doping level by the drain electrode. Another factor is the significant area of polymer/electrode overlap area relative to the channel length for interdigitated microelectrodes compared to microfabricated OECTs

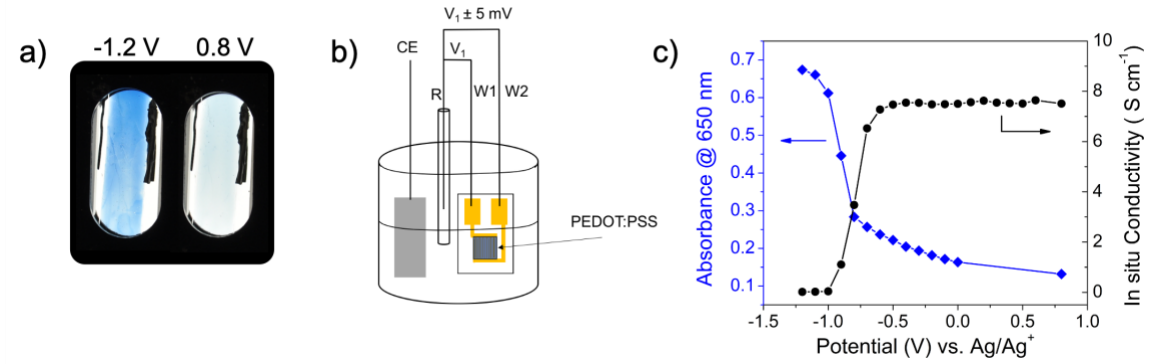

Figure 2-6 (a) Photographs showing 1M *p*TSA/EG treated PEDOT:PSS films blade coated on glass and assembled into an electrochemical cell held at -1.2 V and 0.8 V vs. Ag/Ag$^+$. (b) Schematic representation of the 4-electrode cell for in-situ conductivity measurements showing the two working electrodes (W1 and W2) , the counter electrode (CE), and the Ag/Ag$^+$ reference electrode. (c) Potential dependent absorbance and *in situ* conductivity for 1 M *p*TSA/EG treated PEDOT:PSS films on glass.

with a single source, drain, and gate. Therefore, contact resistance can play a major role limiting the current measured for these *in situ* conductivity methods, thus meriting the quantification of the contact resistance prior to performing a series of studies.

For the characterization of PEDOT:PSS by *in situ* conductivity, thin films were deposited onto interdigitated microelectrodes (50 fingers, 5 µm spacing) via drop casting 0.5 µL of solution. The solid film dried in uniform circle whose diameter did not exceed the width of the microelectrode fingers. Untreated and 1 M *p*TSA/EG-treated PEDOT:PSS films were measured by assembling the microelectrode pair as the two working electrodes of a four-electrode cell as shown in Figure 2-6b (Reference (R) = Ag/Ag$^+$ as described in section 1.3.3.1, and a Pt flag counter electrode (CE)). The film resistance was calculated from the slope of the *in situ I-V* curves measured at potentials from 0.8 V down to -1.2 V vs. Ag/Ag$^+$ (100 mV increments). After the measurement, the thickness was estimated using profilometry of the film on top of the interdigitated electrodes. The evolution of the

conductivity vs. potential is shown in Figure 2-6c with the π-π* absorbance (650 nm) overlaid. Correlating *in situ* conductance trends with the bleaching of the neutral state absorption and the generation of charge carriers can give more detailed information about the doping process and the nature of the charge carriers being generated electrochemically.[103]

While the PEDOT:PSS shows a flat conductivity in its oxidized state, it is common for poly(3,4-dioxythiophenes) to exhibit decreased conductivity with increasing potential.[183,184] This behavior has been highlighted as evidence of a interchain charge-hopping process being the primary conduction mechanism in these materials. As the density charge carriers builds up in the film, the hopping process becomes limited, and the mobility decreases dramatically. Like EIS, *in situ* conductivity promises to continue to be a powerful technique as we move forward studying how structural manipulations of conjugated polymers affect their absorption and transport properties.

CHAPTER 3. ELECTROCHROMIC DEVICES CONSTRUCTED ON TRANSPARENT WOOD SUBSTRATES

Adapted from:

Lang, A. W.; Li, Y.; De Keersmaecker, M.; Shen, D. E.; Österholm, A. M.; Berglund, L.; Reynolds, J. R. "Transparent Wood Smart Windows: Polymer Electrochromic Devices Based on Poly(3,4-Ethylenedioxythiophene):Poly(Styrene Sulfonate) Electrodes". *ChemSusChem* **2018**, 11 (5), 854–863.

3.1.1 Development of Transparent Wood Composites

As a hierarchical structural material, wood has played a dominant role in the building industry for hundreds of years. Recent research efforts toward the modification of wood to further improve its mechanical properties have yielded densified materials competitive with aerospace-grade polymer composites in terms of specific strength and modulus.[185] Furthermore, as cellulose does not intrinsically absorb light, mild chemical used to remove lignin chromophore, yet retain the cellular structure have generated widespread excitement for transparent wood composites (TW) as a replacement for glass.[120,186–189] To date, a variety of strategies have been adopted to generate TW. In 2016, Lars Berglund and coworkers demonstrated TW through an immersion into sodium chlorite solution to bleach the wood and remove lignin followed by vacuum infiltration of poly(methyl methacrylate).[120] Separately, Liangbing Hu and coworkers fabricated TW through a slightly different NaOH and Na_2SO_3 lignin-removal process followed by

infiltration with a clear epoxy.[190] The hierarchical wood skeleton in these composites gives rise to a high degree of anisotropy depending on the wood-fiber orientation, both in the mechanical and optical properties of the composites. These initial demonstrations have inspired a number of research efforts to develop new materials with novel optical properties arising from the unique hierarchical and anisotropic structure of wood. Additionally, fundamental studies of light propagation in transparent wood have been undertaken to understand how light is transmitted and polarized by the oriented crystalline cellulose structures in the cell walls.[191] The first generation of transparent wood composites were highly transmissive, yet exhibited high haze (~60%). Through acetylation of cellulose fibers, less hazy wood was generated where sample thicknesses up to 1 cm were demonstrated.[186] Additionally, Liangbing Hu and coworkers recently demonstrated a rotary cutting technique to achieve haze as low as 15% in balsa wood-poly(vinyl alcohol) composite.[188] The principle advantages of transparent wood over glass include its low thermal conductivity (5x lower) and high toughness (30x higher) compared to glass. Rough calculations using midrise apartments as a standard showed that the average energy savings of installing a double-pane TW window in new and old buildings was 28 and 32 MJ m^{-2} respectively per year (roughly 1 kWh m^{-2} $year^{-1}$).[188] This technology represents a promising route toward improving the energy efficiency of buildings using renewable materials.

3.1.2 Towards Electrochromic Devices on Transparent Wood

Consistent with these efforts of expanding the use of wood-based materials toward energy efficiency in the building sector is the idea of modulating transmitted light through electrochromic "smart windows" that can control incident irradiation into a building.[192] As mentioned in Chapter 1, electrochromic polymers (ECPs) offer several advantages in the construction of electrochromic devices (ECDs). Synthetic control of the polymer backbone provides fine control of the neutral state color, enabling even color-neutral materials to be synthesized. Additionally, colors of subtly varying hues, as well as blacks and browns, have been accessed through blending of primary and secondary colors.[108,193–196] Long electrochemical cycle lifetimes of 10^5 cycles, as well as stability to prolonged light exposure with proper encapsulation, have also been demonstrated.[26,111] The bi-stability of ECP-based electrochromic devices in both the colorless and colored state is another attractive feature of using these materials when energy efficiency is a primary goal.

In order to realize transparent wood ECDs, a transparent conductor that is redox stable with sufficient conductivity is needed. Among the material candidates mentioned in Chapter 1 for transparent conductors, PEDOT:PSS offers many benefits. It is a commercially available, low-cost ($5/gram of solid), solution-processible conductor that can be rendered highly conducting (>1000 S cm^{-1}) with a range of co-solvents and post-treatments.[58,81,153,158,197,198] One post treatment in particular has been studied for rendering PEDOT:PSS electrodes suitable for fast-switching electrochromic devices. Anil Kumar and coworkers developed a 1 M *p*TSA/DMSO post-treatment capable of improving thin-film conductivity above 1400 S cm^{-1} and lowering the de-doping potential from -0.57 V to -0.72 V vs. Ag/Ag^+.[153] Magenta-to-colorless electrochromic devices were demonstrated

with fast-switching kinetics (2 second switching speed for 40% contrast between colored and colorless states). In terms of electrical charge required to switch, these devices were fairly efficient (420 cm^{-2} C^{-1}) yet lagged the efficiency of similar devices constructed on the standard transparent conductor, ITO (600 cm^{-2} C).

This chapter details a simple process for generating highly conducting PEDOT:PSS electrodes using benign solvents compatible with TW substrates. The TW substrates derived from birch wood and PMMA as a matrix polymer. A post treatment with 1M *p*TSA dissolved in ethylene glycol (EG) at room temperature enhanced the conductivity to 1200 S cm^{-1} – high enough for color-neutral electrodes, sufficiently low in sheet resistance to switch electrochromic polymers between their colored and colorless states. This post-treatment was chosen as other acids (> 3 M HNO_3, glacial acetic acid) were found to partially dissolve the PMMA matrix and destroy the transparent wood. The low driving voltage (0.8 V) as well as the high haze allow for an exceptionally colorless bleached state of the device (L^* = 75, a^* = -0.8, b^* = -0.2). The facile processing of both the electrode and active materials combined with the low energy requirement (coloration efficiency of 590 cm^2 C^{-1}) and optical memory make these TW ECDs attractive options for energy-saving smart windows and roofs.

3.1.3 Properties of Transparent Wood Substrates

Transparent wood composites were prepared as previously reported.[120] Birch wood was delignified by immersion into a solution of sodium hypochlorite buffered to pH 4.6. The delignified wood was infiltrated with pre-polymerized methyl methacrylate and 2,2'azobis(2-methylpropionitrile) (AIBN) initiator followed by a baking step at 70˚C to

form the PMMA matrix. The mechanical properties of TW were evaluated with three-point flexural bending tests and microstructural analysis was performed to understand the structural properties of the composite. Figure 3-1a presents the typical stress-strain curves of TW and glass from 3-point bending test showing the increased strength and dramatically improved toughness compared to glass. The stress-strain curve for glass demonstrates its brittle nature after small strains (0.20 ± 0.02 %) whereas the transparent wood exhibits yielding behavior followed by fracture at 2.9 ± 0.2 % strain.

The stress at break of 140 ± 10 MPa for TW is higher than the original birch wood (98 ± 7 MPa), neat PMMA (72 ± 6 MPa) and glass (116 ± 13 MPa). The excellent mechanical performance of the TW is mainly due to the reinforcing wood skeleton in the composite.[120] Meanwhile, the wood-PMMA bond integrity appears favorable for load transfer between the fibers and the matrix in the composites. The scanning electron micrograph in Figure 3-1b shows the fracture surface of the TW where the PMMA matrix has fully infiltrated into the hollow wood cell and strong interfacial bonds between the cell wall and PMMA are evident by the rough fracture surface. Lower magnification SEM

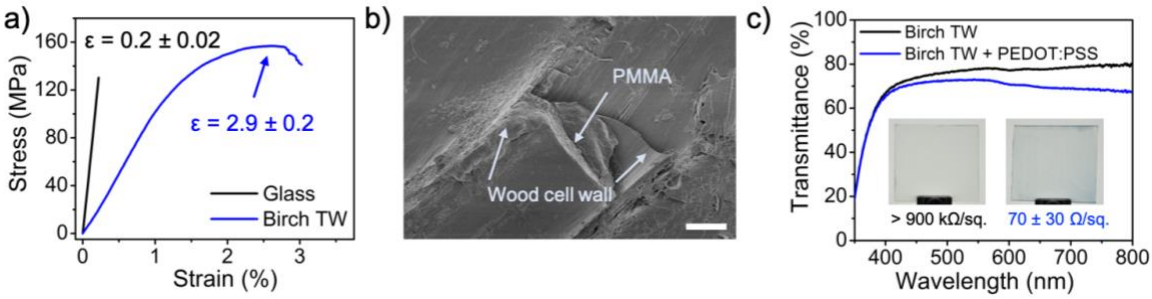

Figure 3-1. Transparent Wood from Birch. a) Stress–strain curves comparing glass and TW composite with the failure strain labeled. b) SEM image of the TW fracture surface, scale bar 5 mm. c) Visible transmittance of birch TW with and without the PEDOT:PSS coating. Inset images show the uncoated (left) and coated (right) substrates with their corresponding sheet resistances.

images of the fracture surface are shown in the supplementary figures at the end of this chapter (Figure S3-1). Macroscale surface roughness around the fibers is further indication of efficient load transfer between the fibers and the matrix. The stiff and strong cellulosic skeleton leads to the improved mechanical performance compared to neat PMMA. The high failure strain of the TW corresponds to a work of fracture of 3.2 MJ m-3. This is 30 times higher than the work of fracture for glass samples, 10.2 J m-3, which have fracture strains of 0.20 ± 0.02 %. This highlights the benefit of using the tough TW over glass where brittle fracture and shattering are a safety concern. In terms of optical properties, the TW samples used in this study provide a transmittance of 80 % at a wavelength of 550 nm with high haze (70 %) (Figure 3-1c). The transmittance is uniform across the visible spectrum, which results in a colorless substrate. The high haze of TW is a unique feature compared to glass. This haze enables the TW to offer indoor privacy while its high transmittance continues to offer diffuse lighting.

In addition, TW has lower thermal conductivity (0.23 W $m^{-1}K^{-1}$) compared with glass (1.0 W $m^{-1}K^{-1}$), which can serve to further insulate buildings. The TW properties highlighted here demonstrate several advantages over glass for generating energy saving smart windows/roofs when high transparency is not required.

3.1.4 Electrochemical Properties of PEDOT:PSS

Prior to fabricating ECDs, the redox properties of PEDOT:PSS were evaluated to determine its suitability as an electrode material for ECP-Magenta and the minimally color changing charge storage polymer (MCCP) (Figure S3). To support the complete redox

switching of these polymers, PEDOT:PSS must maintain a high conductivity over a potential window from -0.5 to 0.8 V vs. Ag/Ag^+.

Despite its broad electroactive window, the conducting $PEDOT^+$ can be de-doped to its neutral, insulating form at sufficiently low electrochemical potentials. To probe the de-doping of PEDOT:PSS, cyclic voltammetry experiments were performed along with 4-electrode *in situ* conductance measured as a function of potential from 0.8 V to -1.2 V vs. Ag/Ag^+. The effect of the acidic post treatment on the onset of de-doping can be seen in the cyclic voltammograms shown in Figure 3-2a. New redox peaks emerge at -0.78 and -0.92 V vs. Ag/Ag^+ suggesting the formation well-ordered PEDOT domains with a lower onset of oxidation.[103,152,153] The corresponding conductivity values were calculated from the conductance using the film cross sectional area and footprint dimensions (Figure 3-2b). This ordering extends the polymer's effective conjugation length and reduces the oxidation potential for a portion of the *p*TSA/EG treated material.

In situ conductivity measurements were performed in order to assess the window over which the PEDOT:PSS electrodes maintain their conductivity. The conductivity values were calculated from the conductance data using the film cross sectional area and footprint dimensions (Figure 3-2b). A sharp decrease in conductivity is observed at -0.7 V and -0.6 V for *p*TSA/EG treated and untreated films, respectively. At -1.0 V, the acid treated PEDOT:PSS is rendered insulating whereas this transition occurs at -0.8 V for the untreated films. The difference in this onset of de-doping is consistent with the new redox peaks observed in the cyclic voltammograms and with previously reported post-treatments of PEDOT:PSS.[152,153] As many of the reported cathodically coloring ECPs switch to their colored state at potentials above -0.7 V vs. Ag/Ag^+ and switch to their colorless states

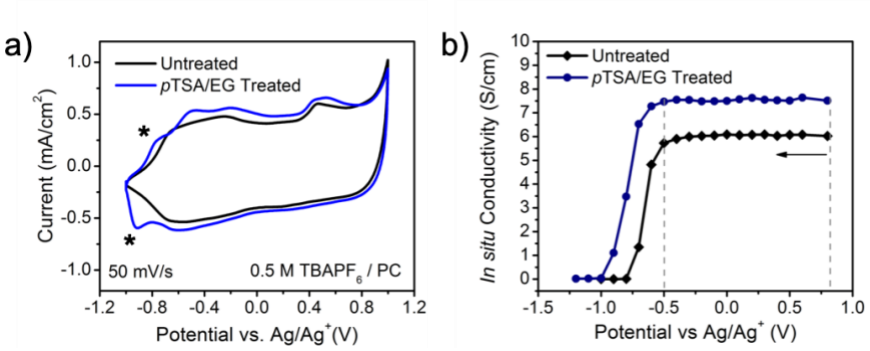

Figure 3-2. (a) Cyclic voltammogram of acid-treated and untreated PEDOT:PSS (1.6 µm thickness) on glassy carbon electrodes in 0.5 M $TBAPF_6$ / propylene carbonate at 50 mV/s. Peaks denoted with the asterisk correspond to a new redox couple apparent after the *p*TSA/EG treatment. a) In situ conductivity of treated and untreated PEDOT:PSS from 0.8 to -1.2 V vs. Ag/Ag+ in 0.5m tetrabutylammonium hexafluorophosphate /propylene carbonate ($TBAPF_6$/PC) electrolyte.

below 0.8 V vs. Ag/Ag^+, these results demonstrate that PEDOT:PSS is suitable for use as a TCE for these polymer-based ECDs.

Electrochemical Impedance Spectroscopy (EIS) was used to further elucidate the physical changes occurring in the PEDOT:PSS layer over the potential window from -0.5 V to 0.8 V, and how these changes affect the kinetics related to the various redox processes occurring during ECP switching. The equivalent circuit used for fitting the EIS data is shown in Figure 3-3a. The Nyquist plot in Figure 3-3b shows the EIS spectra for *p*TSA/EG treated PEDOT:PSS compared to untreated PEDOT:PSS measured at a DC potential of 0.0 V vs. Ag/Ag^+. Comparing the data qualitatively, the maximum impedance of the untreated films (f = 0.1 Hz) is higher than that of the *p*TSA/EG treated films where $|Z| = 700\ \Omega\ cm^2$ compared to $|Z| = 340\ \Omega\ cm^2$ for the *p*TSA/EG treated films. This increased impedance for the untreated films is due to the lower electronic conductivity of the film compared to the *p*TSA/EG treated PEDOT:PSS. The impedance measurements at high frequencies probe

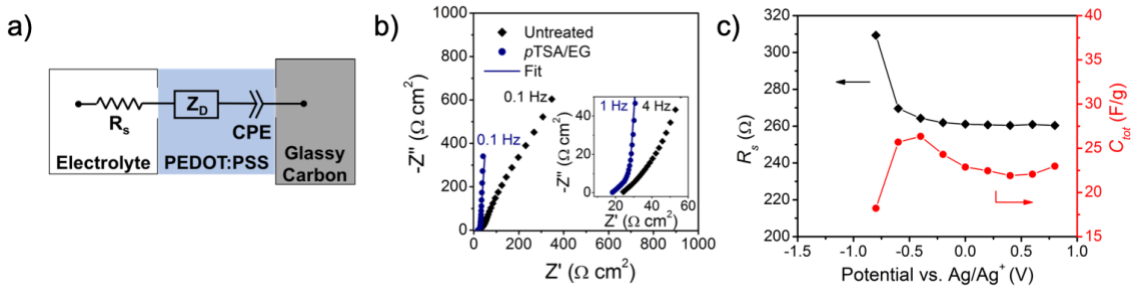

Figure 3-3. (a) Equivalent circuit used for fitting impedance spectra for the *p*TSA/EG-treated PEDOT:PSS polymer films. b) Nyquist plot comparing EIS spectra for treated and untreated PEDOT:PSS from 100 kHz to 0.1 Hz. Inset shows high-frequency data points (100 kHz to 1Hz) for treated and untreated PEDOT:PSS. c) Equivalent circuit used to fit the EIS data for treated PEDOT:PSS films. d) Fitted values for solution resistance and total capacitance versus potential for pTSA/EG-treated PEDOT:PSS.

the ion diffusion in the film, which gives a sloped line at 45˚ in the Nyquist plot (Figure 3-3b, inset). This behavior persists in the untreated films even at low frequencies indicating the presence of a slow diffusion process not seen for the *p*TSA/EG treated films. At low frequencies, the imaginary impedance increases with little change in the real impedance (vertical line) for the *p*TSA/EG treated PEDOT:PSS indicating a purely capacitive response in the film. Both the reduction in total impedance and the emergence of this capacitive behavior in the *p*TSA/EG treated PEDOT:PSS relative to the untreated material highlights that the improved charge transport and electroactivity of the *p*TSA/EG treated PEDOT:PSS persists when immersed in electrolyte. In accordance with the *in situ* conductivity results, the onset of de-doping of the untreated PEDOT:PSS is apparent in the EIS spectra at -0.8 V where a charge transfer semicircle appears in the high frequency region and the maximum impedance increases to $|Z| = 1200\ \Omega\ cm^2$ (Figure S3-2a). The pTSA/EG treated PEDOT:PSS shows only minimal change in the EIS spectra at this potential (Figure S3-2b). This result gives further evidence that the untreated film has

become insulating at -0.8 V, whereas the *p*TSA/EG treated film remains highly electroactive. By fitting the EIS data for the *p*TSA/EG treated PEDOT:PSS with the equivalent circuit shown in Figure 3-3, the electrolyte resistance, diffusional time constant, and capacitance were extracted over the potential range from 0.8 to -0.8 V.[199] The R_s resistor element in the circuit takes into account the electrolyte resistance of the cell and can be impacted by a change in the resistance of the PEDOT:PSS electrode. The second element, a 'finite length' Warburg diffusion element (Z_D), accounts for the ion diffusion through the PEDOT:PSS film. This element in the equivalent circuit reproduces both the diffusion-limited behavior at high frequencies and the pseudocapacitive response at low frequencies seen in Figure 3-3b. Previous reports have shown that PEDOT:PSS can form dense films with tortuous ion diffusion pathways resulting in hindered "subdiffusion".[181] Ions in these films will diffuse more slowly than predicted by Fick's second law. This behavior was taken into account when fitting the EIS spectra for acid treated PEDOT:PSS where a minor adjustment setting $\alpha = 0.48$ was found to improve the fits dramatically to obtain goodness-of-fit value (χ^2) of 7.6 $\times 10^{-4}$. The constant phase element (CPE) is proportional to the PEDOT:PSS pseudocapacitance. All EIS spectra for *p*TSA/EG treated and untreated films are shown in Figure S3-2. The fit parameters are listed in Table S3-1. Examining the fitted parameters for the acid treated PEDOT:PSS, changes in resistance, diffusional time constant, and capacitance were monitored over 0.8 to -0.8 V. Figure 3-3c shows the evolution of R_s and total capacitance ($C_{tot} = (1/C_D + 1/C_d)^{-1}$) as a function of potential. The R_s values remain relatively constant at 260 Ω between 0.8 V and -0.6 V, consistent with the *in situ* conductance results. Similarly, the capacitance shows a slight increase from 22 F g^{-1} at 0.8 V to 27 F g^{-1} at -0.4 V coupled with an increase in the ion

diffusion time constant from 0.086 to 0.15 s over the same potential range. This trend suggests that decreasing potentials cause morphological compaction of the PEDOT:PSS film, hindering ion transport.[200] Changes in the *in situ* conductance are not seen over this same potential range as ion diffusion cannot be perceived at low scan rates below 0.5 mV s^{-1}. At -0.8 V, R_s increases to 310 Ω and the total capacitance drops from an average of 27 F g^{-1} to 18 F g^{-1}. These changes indicate that the PEDOT:PSS film is transitioning to an insulating state. These results from both the *in situ* conductance and the EIS measurements highlight that the PEDOT:PSS will remain charged and highly conductive over the potential window between -0.6 to 0.8 V vs. Ag/Ag^+ after treatment with *p*TSA/EG though minor changes in ion transport and film compaction occur in this potential window.

3.1.5 PEDOT:PSS Electrodes supporting ECP Switching

Next, ECP-Magenta films were evaluated with CV in order to compare their electrochemical response on *p*TSA/EG treated PEDOT:PSS/glassy carbon and on plain glassy carbon electrodes. Figure 3-4a shows the CV for an ECP-Magenta film where a similar current density profile is seen for both electrodes, highlighting the ability to use PEDOT:PSS as an electrode capable of oxidizing ECP-Magenta. The anodic peak is shifted by 50 mV on the PEDOT:PSS electrodes compared to glassy carbon electrodes while the cathodic peak remains at 0.10 V . The slight shift of the anodic peak indicates that there is a higher resistance to oxidize (bleach) the ECP on the PEDOT:PSS electrodes. An increase in current density over the entire potential range in Figure 3-4a is attributed to the pseudocapacitance of the PEDOT:PSS. This current contribution of the PEDOT:PSS can be determined by subtracting the ECP-Magenta/glassy carbon current from that of the ECP-Magenta/PEDOT:PSS/glassy carbon electrode (Figure 3-4b). This subtracted current

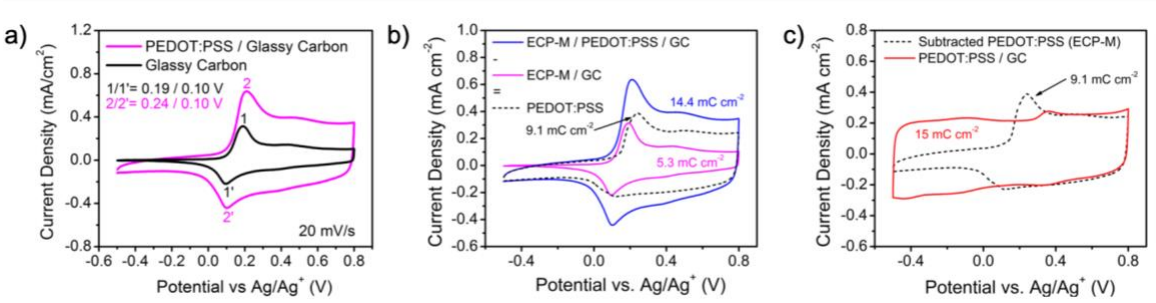

Figure 3-4. (a) CVs of ECP-Magenta on glassy carbon and on PEDOT:PSS/glassy carbon working electrodes at 20 mV s^{-1} in 0.5 M $TBAPF_6$/PC. The anodic and cathodic redox peaks for ECP-Magenta are labeled 1/1' for the glassy carbon electrode and 2/2' for the PEDOT:PSS/glassy carbon electrode. (b) Cyclic voltammograms showing the redox response of ECP-Magenta on glassy carbon and PEDOT:PSS / glassy carbon electrodes at 20 mV s^{-1} (0.5 M $TBAPF_6$ / PC) . The dotted line corresponds to the current arising from the redox active PEDOT:PSS electrode. (c) Cyclic voltammograms of the subtracted current from the PEDOT:PSS / glassy carbon electrode and a PEDOT:PSS film on glassy carbon at 20 mV s^{-1}.

density matches the current density of PEDOT:PSS from 0.3 to 0.8 V where ECP-Magenta is oxidized, but is lower than the PEDOT:PSS current from -0.5 to 0.0 V where the ECP-Magenta film is charge neutral (Figure 3-4c). The decrease in current seen at potentials less than 0 V indicates that while neutral, ECP-Magenta blocks ion transport into the PEDOT:PSS electrode and therefore only a portion of the film is electrochemically accessed.

3.1.6 Transparent Wood Electrodes

To construct transparent electrodes using TW substrates, PEDOT:PSS was blade coated to achieve a thicknesses of roughly 140 nm and then treated with 1M *p*TSA/EG at 40 ˚C. Above this thickness, the PEDOT:PSS will contribute a substantial blue tint to the electrochromic device and compromise the electrode transmittance and the optical contrast that can be achieved. This specific treatment method was chosen to avoid damage to the

substrate while still providing a three-order-of-magnitude increase in conductivity compared to untreated PEDOT:PSS from 1 S cm^{-1} to 1200 S cm^{-1}.

As a control experiment, treated PEDOT:PSS films were prepared on glass and achieved conductivities of 1200 ± 100 S cm^{-1} (58 ± 5 Ω sq^{-1}) which shows an improvement over ethylene glycol treatments (980 ± 60 S cm^{-1}) or 1M *p*TSA/H_2O (400 ± 100 S cm^{-1}). The improvement in conductivity using the *p*TSA/EG treatment is due to the combined effect of larger crystallite size and removal of PSSH.[159,197] The thickness of the PEDOT:PSS films is difficult to accurately measure on the TW substrates due to the relatively high surface roughness of 670 ± 70 nm perpendicular to the wood fibers and 90 ± 10 nm parallel to the fibers. We expect that the similar sheet resistance for similar transmittance between the TW and glass indicates that the DC conductivities are comparable between the two substrates as well.

Figure 3-1c shows the UV-Vis spectra comparing the transmittance of bare TW and PEDOT:PSS/TW electrode. The TW electrodes provide 70 % transmittance at 550 nm with a 70 Ω sq^{-1} surface resistance (FoM = 14). See Equation 2.9 for the FoM calculation. Ignoring the substrate, a FoM of 50 is achieved with the 1M *p*TSA/EG treatment which is on par with the commercial standard for ITO (FoM = 35). The color contribution from the PEDOT:PSS can be quantified using CIE Lab color coordinates where: L^*, a^*, and b^* are defined to quantify the lightness (L^*) and the hue/saturation of an object from green to red (a^*) and from blue to yellow (b^*). The color difference between two samples is given by equation (3-1), defined as the Euclidian distance between each color coordinate.

$$\Delta E^* = \sqrt{(\Delta L^*)^2 + (\Delta a^*)^2 + (\Delta b^*)^2} \quad (3\text{-}1)$$

At a color difference $\Delta E^* < 2.4$, two samples become indistinguishable to the human eye. Therefore, maintaining a color difference less than 2.4 relative to standard white ($L^* = 100$, $a^* = 0$, $b^* = 0$) would be a perfectly color neutral electrode and would not impact the ECP contrast. The color difference between the PEDOT:PSS/TW electrodes ($L^* = 87$, $a^* = -1.2$, $b^* = 1.2$) and bare TW ($L^* = 90$, $a^* = -1.8$, $b^* = 2.7$) is only 3.8, highlighting the color neutrality of the PEDOT:PSS coating.

Having established PEDOT:PSS's ability to support redox switching of ECP-Magenta when deposited on a small area glassy carbon electrode (0.07 cm^2), we proceeded to investigate the feasibility of using PEDOT:PSS as the sole conducting electrode on TW (2 cm^2). Figure S3-3a shows the CVs of ECP-Magenta on PEDOT:PSS/TW (70 ± 30 Ω sq^{-1}) and on an ITO/glass electrode with equivalent sheet resistance (70 Ω sq^{-1}). The anodic oxidation peaks from ECP-Magenta are found at the same potential on both the ITO and PEDOT:PSS/TW electrodes, whereas the reduction peak is shifted cathodically (-60 mV) on the PEDOT:PSS/TW. This similarity in redox peaks between electrodes highlights that the PEDOT:PSS supports sufficient lateral electron transport to oxidize/reduce the larger area ECP-Magenta at reasonable time scales. The higher current recorded on the PEDOT:PSS/TW electrodes is again due to a contribution from PEDOT:PSS's pseudocapacitance as previously observed in Figure 3-4. The charge stored in the ECP-Magenta working electrode is 1.7 mC cm^{-2} for ITO and 3.3 mC cm^{-2} for PEDOT:PSS/TW. This enhancement in capacity for the PEDOT:PSS/TW electrode is even larger than that

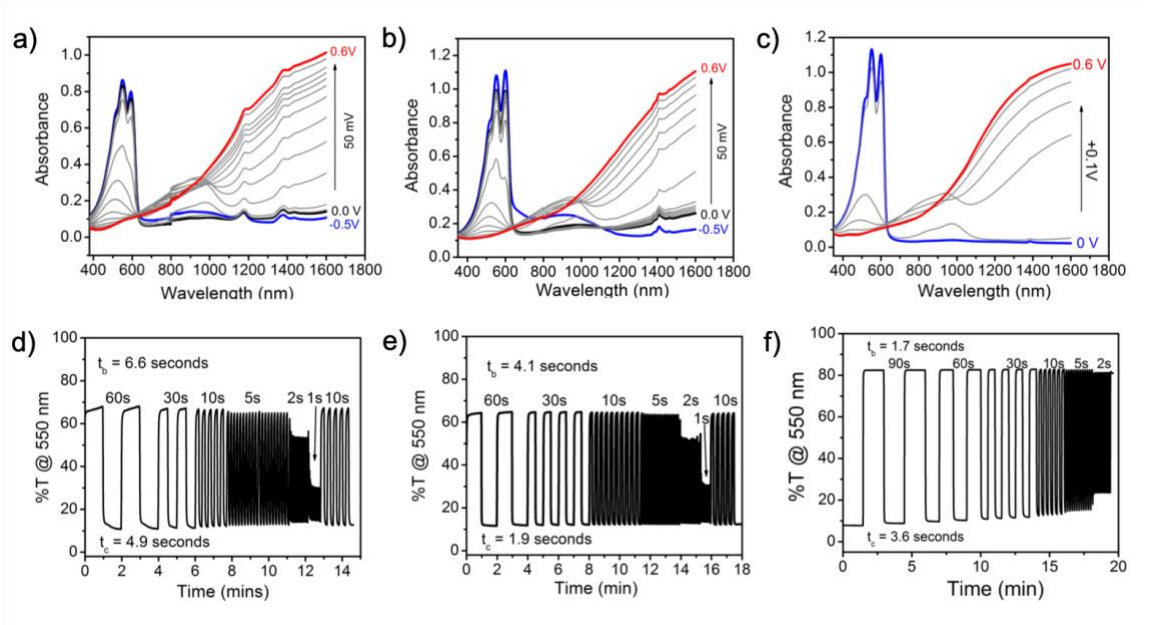

Figure 3-5. (a) Stepwise spectral change upon the electrochemical oxidation of ECP-Magenta films on PEDOT:PSS/TW electrodes (a), PEDOT:PSS/glass electrodes (b), and ITO/glass electrodes (70 Ω sq^{-1}) (c) from -0.5 to 0.6 V. d) Film switching kinetics for potential square-wave pulse times ranging from 60 to 1s for PEDOT:PSS electrodes on TW (d) and glass (e). Switching kinetics from 90 seconds to 2 second pulses of ECP-M films deposited on ITO/glass electrodes (f). t_b and t_c to reach 95%of full contrast are labelled. (c) Inset photographs show the ECP-Magenta film in its neutral (-0.5 V) and oxidized (0.6 V) state.

for a PEDOT:PSS/glass electrode (2.8 mC cm^{-2}, Figure S3-3b) due to the slightly larger surface area from the roughness on the TW substrate.

Examining the spectral change upon oxidation of ECP-Magenta on PEDOT:PSS/TW shown in Figure 3-5a below, a strong visible absorption from the neutral polymer is observed at potentials below 0 V. At higher potentials, the polymer is oxidized to form radical cation species at 0.1 V, which are converted to broadly absorbing dication charge carriers at 0.6 V vs. Ag/Ag^+. For comparison, the ECP-Magenta films on PEDOT:PSS/glass have a similar contrast of 66 Δ%T (Figure 3-5b).This spectral change upon electrochemical oxidation is similar to the behavior seen on ITO electrodes (Figure

3-5c) with matching contrasts of 68 Δ%T. These transitions to radical cation and dication charge carrier bands occur at the same potentials for PEDOT:PSS/TW compared to ITO and PEDOT:PSS/glass electrodes. Despite the fact that PEDOT:PSS exhibits its own electrochromism in this potential range, the use of thin PEDOT:PSS films makes this change nearly imperceptible. The absorbance change between -0.5 V and 0.8 V is 0.06 (9 %T) as shown in Figure S3-4.

The switching kinetics of ECP-Magenta were evaluated by applying potential square wave pulses between -0.5 and 0.6 V for a range of durations from 60 seconds down to 1 second (Figure 3-5d). Switching times are quantified by calculating the time required to reach 95 % of the full contrast upon both bleaching and coloring. The ECP-Magenta film on PEDOT:PSS/TW electrodes bleaches in 6.6 seconds and recolors in 4.9 seconds. This switching speed is slightly slower than the switching speed on PEDOT:PSS/glass (t_b = 4.1 s, t_c = 1.9 s; Figure 3-5e) and on ITO glass (t_b = 1.7 s, t_c = 3.7 s; Figure 3-5f). For both glass and TW substrates, the PEDOT:PSS electrodes support faster coloration than bleaching. whereas the trend is opposite on ITO. This behavior can be explained considering the EIS results presented in Figure 3-3b and Table S3-1. Unlike ITO, which is electrochemically inactive in the potential window required to switch the ECP, PEDOT:PSS exhibits small changes in capacitance and diffusional resistance. As the ECP-Magenta is being bleached, electrons removed from the film are injected into the PEDOT:PSS electrode. The injection of electrons temporarily reduces a portion of the $PEDOT^+$ resulting in both the compaction of the film and hindered charge transport through the electrode as shown by the EIS results. In the opposite process where the ECP is re-

colored, electrons are transferred from the PEDOT:PSS electrode into the ECP film, and the highly conducting, fast ion diffusion properties of the PEDOT:PSS are maintained.

3.1.7 Transparent Wood ECDs

Electrochromic devices (4 x 2.5 cm) were assembled by sandwiching gel electrolyte in between two PEDOT:PSS/TW electrodes, one coated with ECP-Magenta as the working electrode, the other coated with MCCP as the counter electrode. MCCP was used for the counter electrode of the device as a charge storage layer that remains colorless in both its neutral and oxidized states. When constructing polymer-based ECDs, one of the electrodes is usually oxidized prior to ECD assembly, setting the opposite charged state to achieve full device contrast.[109] For the ECDs based on PEDOT:PSS/TW electrodes however, no pre-oxidation was required, highlighting an advantage of using PEDOT:PSS as an electrode material. This phenomenon is likely a combined result of the partial oxidation of MCCP to a radical cation species seen after spray coating on the PEDOT:PSS (Figure S3-5) as well as the charge storage capacity of the PEDOT:PSS able to compensate the charge and discharge of the electrochromic polymer. TW ECDs provided a vibrant magenta-to-colorless switch (ΔE^* = 43.4) between -0.5 V to 0.8 V. The spectra showing the transition from the magenta state at -0.5 V to the transmissive state at 0.8 V is shown in Figure 3-6a. The device contrast is 38 Δ%T at 550 nm compared to 46 Δ%T for devices constructed with PEDOT:PSS/glass electrodes (Figure 3-6d). The higher contrast of the glass-based devices is attributed to the higher transmittance of the glass substrates, allowing for a more

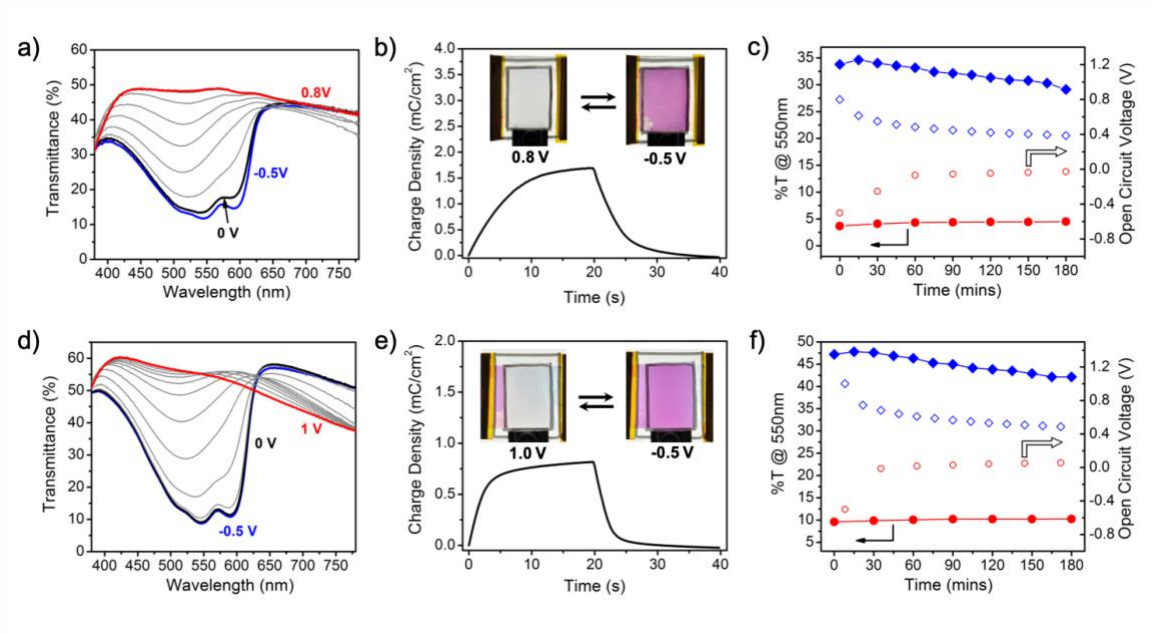

Figure 3-6. (a) Stepwise spectral change of the magenta-to-clear TW ECD upon oxidation from -0.5 to 0.8 V. (b) Charge density versus time for 20 s potential square-wave pulses for the TW ECD. Inset photographs show the device in its colorless (0.8 V) and colored (-0.5 V) states. (c) Optical memory for a 3 cm2 TW ECD constructed under an inert atmosphere showing the evolution of transmittance (filled points) and V_{OC} (open points) in both the colored and bleached state. (d) Stepwise spectral change of Magenta ECD constructed using PEDOT:PSS/glass electrodes upon oxidation from -0.5 V to 1.0 V. (e) Device charge density versus time for 20 second potential square-wave pulses. Inset photographs show device in its bleached (1.0 V) and colored (-0.5 V) states. (f) Optical memory for 3 cm^2 glass ECD constructed under inert atmosphere showing the evolution of transmittance (filled points) and open circuit voltage (open points) in both the colored and bleached state.

transmissive state. At 0.8 V, the TW ECD exhibits an even transmittance of 48 % from 420 - 600 nm with a minor drop to 42 % from 650 - 780 nm. This constant transmittance over visible wavelengths makes the TW ECD exceptionally color neutral at 0.8 V (L^* = 75, a^* = -0.8, b^* = -0.2). Glass-based ECDs required a higher driving voltage of 1 V to reach the transmissive state. At this higher voltage, counter electrode becomes reduced and therefore contributes more of a blue hue to the device (L^* = 75, a^* = -2.6, b^* = -4.5). This color is evident from the spectra shown in Figure 3-6d where the transmittance at 1 V increases from 37 % at 780 nm to 60 % at 420 nm. We determined the charge required to switch the

device by cycling the TW ECD between its extreme states at 0.8 V and -0.5 V as shown in Figure 3-6b. As 0.8 V is applied to the device for 20 seconds, 1.7 mC cm^{-2} (0.47 µAh cm^{-2}, 590 cm^2 C^{-1}) is accumulated during oxidation of the ECP-Magenta working electrode and the device reaches its colorless form (inset image). Application of -0.5 V reduces the ECP-Magenta working electrode and results in the recoloring of the device. This small charge required for device switching means that a standard 1500 mAh smartphone battery could power this 10 cm^2 ECD for 300,000 cycles. The low energy requirement of 3 mWh m^{-2} and a maximum power of 2 W m^{-2} further highlight the energy efficiency of these TW devices. The glass-based ECDs are even more energy efficient where a charge of 0.8 mC cm^{-2} (0.2 mAh m^{-2}, 1250 cm^2 C^{-1}) is required for switching due to the lower amount of PEDOT:PSS on the smooth glass substrates (Figure 3-6e).

Polymer-based ECDs also exhibit optical memory where the bleached and colored states can be maintained without power consumption. This effect is due to the ability of conducting polymers to stabilize charge carriers in their oxidized, colorless state and their sufficiently high oxidation potentials that stabilize colored state in air. To evaluate optical memory, TW ECDs were constructed under inert atmosphere and sealed to limit the amount of oxygen present in the electrolyte. The optical memory was tested by setting the device in its fully bleached or colored state and then removing the power input and measuring the change in transmittance as well as the open circuit voltage over a three-hour time period. Figure 3-6c shows the evolution of the transmittance at 550 nm with time for both optical states. The transmittance decreases from 35% to 29% for the bleached state and increases from 3.7% to 4.5% for the colored state over a three-hour period. In comparison, the glass based ECD shows a comparable optical memory for both the

bleached state (47% - 42%) and the colored state (9.6% -10.2%) as shown in Figure 3-6f. The open data points in Figure 3-6c show the change in open circuit voltage (V_{OC}) over the three-hour experiment. For both the bleached and colored state, the V_{OC} relaxes rapidly to 0.5 and -0.1 V after 60 minutes but then changes only minimally over the final two hours. The final V_{OC} for the device was 0.39 V for the bleached state and -0.03 V for the colored state. This stability in the V_{OC} allows the TW ECD to be reset to either the fully bleached or fully colored state with a minimal amount of charge. Re-bleaching the device requires 0.08 mC cm^{-2} (0.02 mAh m^{-2}) and re-coloring the device requires 0.2 mC cm-2 (0.05 mAh m^{-2}). A similar trend is seen for the glass-based ECDs (Figure 3-6f) where the V_{OC} drops from 1 V to 0.49 V in the bleached state and from -0.5 to 0.06 V in the colored state after three hours. In agreement with the charge-to-switch values above, the glass-based device requires slightly less charge to reset the bleached state (0.05 mC cm^{-2}) and the colored state (0.03 mC cm^{-2}).

Ultimately, the color change in the device over the three-hour open-circuit hold is minimal for both the TW ECD and the glass based ECD as shown in Figure S3-6. After 30 minutes, ΔE^* = 2.3 for the TW device and ΔE^* = 5.3 for the glass-based device. This difference is due to the initial color that is bluer for the glass-based device as discussed above. After 3 hours, ΔE^* = 7.8 for the TW device and ΔE^* = 9.5 for the glass-based device (Figure S3-6a). This highlights that, while there is a perceptible color change after 3 hours, they are able to maintain a fairly colorless state without power consumption over this time period. Photos of the devices before and after the three-hour hold are shown in Figure S3-6c and Figure S3-6d. The colored state has a better optical memory where very minimal color-change is observed in the device (ΔE^* = 4.9 for TW and ΔE^* = 1.7 for glass) (Figure

S3-6e,f). To maintain the device in its colored or colorless state, refresh pulses could be applied to the device every 3 hours for 21 hours (7 pulses), which would consume the same energy as 1 full switch between states. This optical memory further demonstrates the energy efficiency of these devices for smart window/roofing applications.

3.1.8 Conclusions

Electrochromic devices were successfully demonstrated on TW substrates. TW shows great potential to replace glass for smart windows due to its high strength (140 MPa), excellent work of fracture (3.2 MJ m^{-3}, 30 times higher than glass), low thermal conductivity (0.23 W m^{-1} K^{-1}), and diffuse transmittance (80 %T and haze of 70%). PEDOT:PSS treated with 1M *p*TSA/EG demonstrated a conductivity of 1200 S cm^{-1} as well as a retention of this high conductivity and electroactivity over the potential window of interest: -0.6 V to 0.8 V vs. Ag/Ag^{+}. Treated PEDOT:PSS is therefore a suitable electrode material for a vast range of cathodically coloring electrochromic polymers. ECP-Magenta exhibits a nearly identical redox response on PEDOT:PSS/TW as on ITO (-0.5 to 0.8 V). Magenta-to-clear TW electrochromic devices demonstrated a contrast of 38 Δ%T (ΔE^{*} = 43.2) and a highly color neutral bleached state (L^{*} = 75, a^{*} = -0.8, b^{*} = -0.2) without the need for chemical or electrochemical pre-oxidation. The low driving voltage, optical memory, as well as the small charge required to switch the device between in its colored and bleached states (1.7 mC cm^{-2}, 0.02 µAh m^{-2}) highlight the possibility of using these devices for energy-saving, smart windows. Further advances in water-processable electrochromic polymers will both expand the potential colors for TW ECDs as well as allow for more environmentally benign device fabrication. Additionally, a better understanding of ECP photodegradation will enable these materials to enter applications

requiring longer lifetimes from the active materials. As a highly anisotropic substrate, delignified wood scaffolds present some exciting opportunities for templating conducting polymer microstructure as is discussed in Chapter 6.

3.1.9 Supporting Information

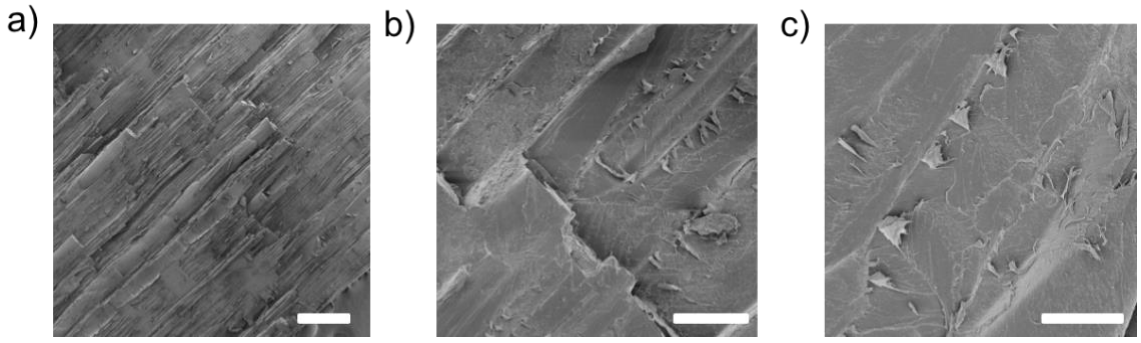

Figure S3-1. Scanning electron micrographs of the fracture surface of birch transparent wood at various magnifications. Scale bar is (a) 500 µm, (b) 20 µm, and (c) 15 µm.

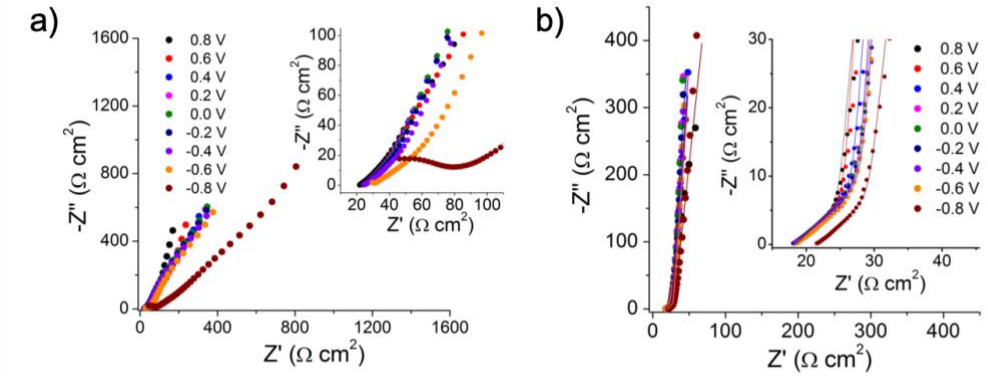

Figure S3-2. Nyquist plot of untreated PEDOT:PSS from 0.8 to -0.8V. (b) Nyquist plot of *p*TSA/EG treated PEDOT:PSS on glassy carbon current collectors (thickness = 0.8 µm) at potentials from 0.8 V to –0.8 V vs. Ag/Ag^+.

Table S3-1. EIS Fitted values for *p*TSA/EG Treated PEDOT:PSS electrodes. Film thickness is roughly 590 nm.

Potential (V)	R_s (Ohm)	C_D (mF)	τ (s)	$\propto$	C_d (mF)	*p*	C_{tot} (mF)
0.8	260	0.32	0.086	0.48	3.7	0.85	0.29
0.6	261	0.32	0.095	0.48	3.0	0.95	0.29
0.4	260	0.32	0.110	0.48	2.9	1	0.29
0.2	261	0.34	0.130	0.48	2.1	1	0.29
0	261	0.34	0.130	0.48	2.5	1	0.30
-0.2	262	0.35	0.140	0.48	3.1	1	0.31
-0.4	264	0.39	0.150	0.48	3.0*	1	0.35
-0.6	270	0.38	0.140	0.48	3.0*	1	0.34
-0.8	310	0.28	0.087	0.47	1.5	0.95	0.24

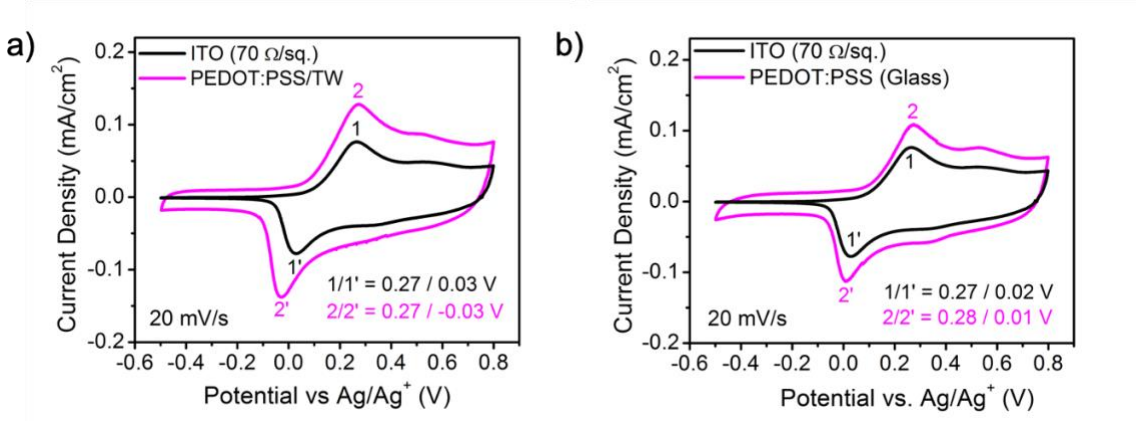

Figure S3-3. (a) Cyclic voltammograms of ECP-Magenta films on PEDOT:PSS/TW and ITO/glass electrodes measured at 20 mV s^{-1}. (b) Cyclic voltammograms of ECP-Magenta films on PEDOT:PSS/glass and ITO/glass electrodes measured at 20 mVs^{-1}.

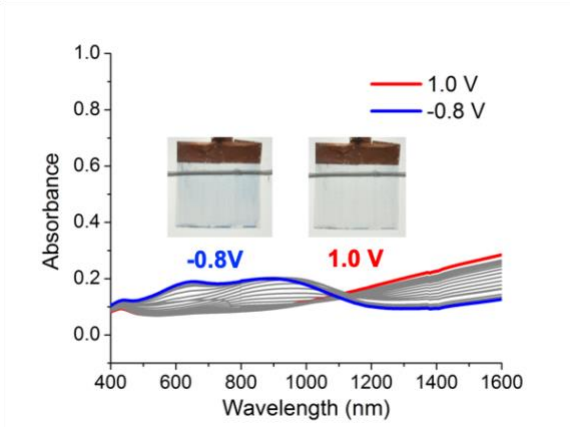

Figure S3-4. Absorbance change with potential of the transparent wood electrode showing contribution of PEDOT:PSS electrochromism over a wide potential range of -0.8 V to 1.0 V (0.1 V increments). Inset photos show PEDOT:PSS coated transparent wood electrodes held at the extreme potentials.

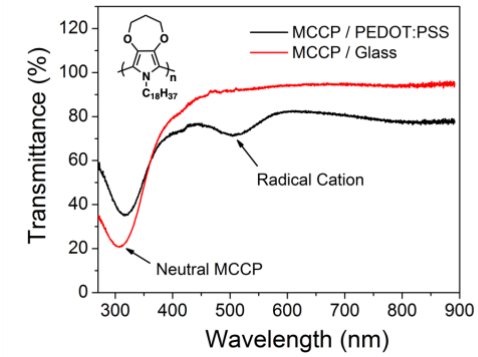

Figure S3-5. UV-Vis spectra of dried MCCP sprayed on glass vs. dried MCCP sprayed on *p*TSA/EG treated PEDOT:PSS in the absence of electrolyte the neutral and radical cation peaks for the polymer are labeled.

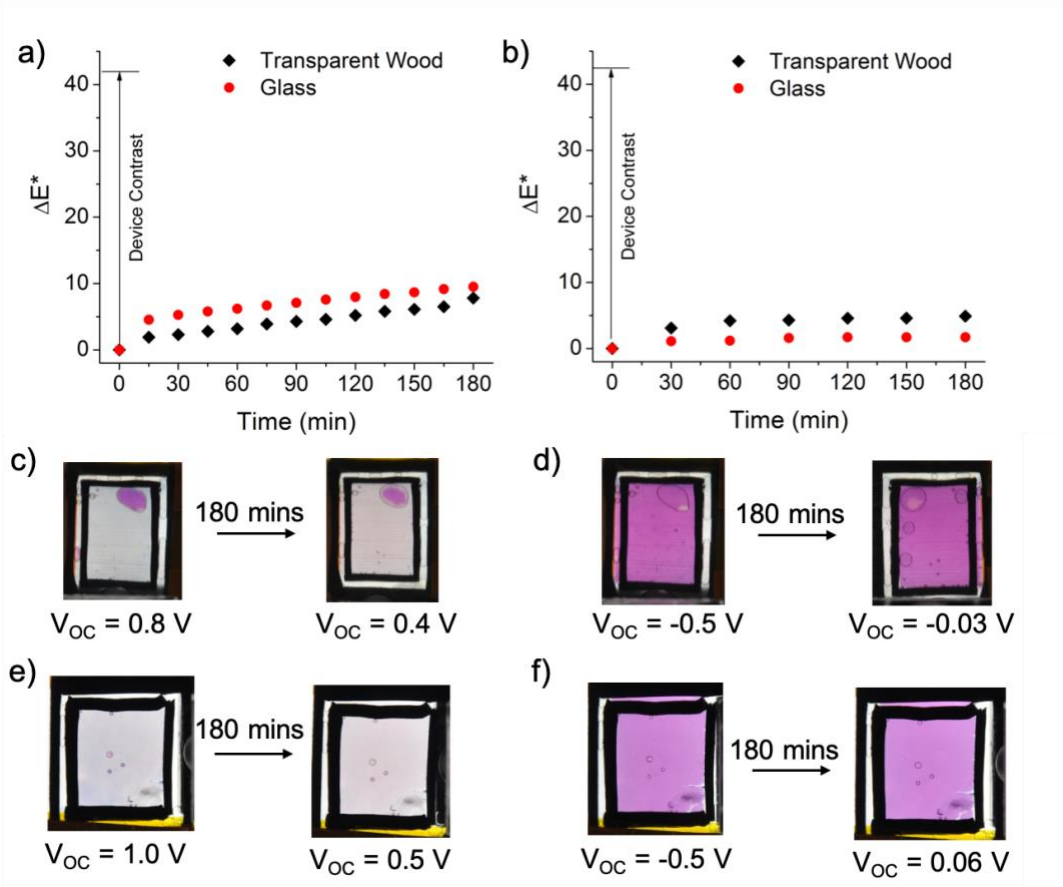

Figure S3-6. Color change versus time for a TW-ECD and a glass-based ECD set in the colorless state (a) and colored state (b) and held at open circuit for 3 hours. Photographs of TW-ECD in its bleached state (c) and colored state (d) before and after the 3-hour hold at open circuit. Photographs of glass-based ECD in its bleached state (e) and colored state (f) before and after the 3-hour hold at open circuit. Corresponding open circuit voltages are labeled for each image.

CHAPTER 4. PAPER-BASED ELECTROCHROMIC DEVICES

Adapted from:

Lang, A. W.; Österholm, A. M.; Reynolds, J. R. Paper-Based Electrochromic Devices Enabled by Nanocellulose-Coated Substrates. *Adv. Funct. Mater.* **2019**, *29* (39), 1–11.

4.1.1 Background and Motivation

The development of lightweight, disposable, and transient displays promises to enable a variety of technologies including dynamic signage, rewritable paper, smart packaging, and biomedical sensors.[9,13,14,28] These next-generation displays will provide enhanced functionality over standard labeling/signage without compromising the ability to safely dispose of the devices. Advances in materials development for printed displays, and their supporting circuitry, have provided an extensive library of solution processable conductors, semiconductors, and light-emitting/color-changing active materials that have enabled the fabrication of fully printed devices. In addition, engineered polymeric substrates with ink-compatible surface energy, thermal stability, and barrier properties have been critical for the success of printed electronics.[16,201,202] Since the substrate on which these electronics are printed represents the majority of the device mass, the ability to replace glass or plastic with renewable and biodegradable materials is a step toward realizing truly disposable displays.

As a substrate, paper offers advantages over commonly used plastics such as poly(ethylene terephthalate) (PET) or poly(ethylene naphthalate) (PEN) as it is renewable, biodegradable, and already mass produced. The porous nature of paper, and its ability to wick solvents, has been utilized extensively in the field of microfluidic paper-based analytical devices (μPADs). μPADs have enabled advanced colorimetric sensing of various biomolecules allowing for rapid and inexpensive disease diagnosis.[9] Recently, electronic functionality and electrochromic readouts have been incorporated into these devices to further enhance their versatility.[11,203] However, while the rough and porous nature of cellulose paper is ideal for promoting capillary uptake and transport of analytes, deployment of many optoelectronic materials onto paper is challenging as these materials typically require thin-film architectures (10s to 100s of nm) with minimal defects to promote the best charge transport. To address these shortcomings, significant research and development efforts have introduced specialty paper with a surface roughness reduced to tens of nanometers.[17] Additionally, the incorporation of a barrier layer retains functional inks on the surface of the paper enabling the formation of smooth, thin films and the fabrication of a number of paper-based electronics such as printed transistors and solution-processed light-emitting electrochemical cells.[11,16,204–207]

Optoelectronic applications requiring transparent substrates with increased thermal stability (up to 150˚C) have prompted the development of cellulose nanofibril (CNF) paper.[18,208] Over the past 10 years, many electronic devices have been prepared on nanocellulose paper including solar cells,[209] transistors,[210] light-emitting devices,[21] memory devices,[211] touch screens,[212] and even several blue-to-colorless electrochromic devices.[213] The performance of these devices based on CNF have approached what is seen

using smooth, nonporous commodity polymer substrates. ECDs are particularly interesting for dynamic signage and smart packaging as they offer color change with high optical contrast (40-60 Δ%T) at low operating voltages (1-2 V).[214,215] To date, paper-based ECDs have been successfully demonstrated for a variety of electrochromic materials ranging from inorganic oxides,[216,217] viologens,[218,219] redox-active molecules,[203] and conducting polymers.[59,213,220–222] However, the accessible color space remains dominated by blue-to-colorless devices.

One challenge for achieving high color contrasts in paper-based ECDs is the fabrication of a color-neutral electrode with sufficient conductivity and redox stability. Recently, conductive paper with exceptionally low surface resistances (tens of $m\Omega\ sq^{-1}$) has been demonstrated through the deposition of metal nanoparticles.[223,224] However, these approaches render the paper metallic in appearance and are therefore not suitable for colored-to-colorless ECDs. Carbon-nanotube conductors have also been explored as transparent electrodes, showing high performance for filtered membranes on cellulose, but typically suffer from resistances greater than $10^3\ \Omega\ sq^{-1}$ for solution-coated films (%T > 70%).[225,226] Silver nanowire and silver microgrid electrodes have been well-studied as highly performing transparent electrodes for ECDs composed of metal-oxide active materials that are electrochemically active below the oxidation potential of silver.[217,227–229] For polymer-based devices, silver grid electrodes coated with the conducting polymer suspension, poly(3,4-ethylenedioxythiophene):poly(styrene sulfonate) (PEDOT:PSS) were demonstrated in roll-to-roll coated ECDs.[230] The authors incorporated PEDOT:PSS coatings in order to obtain more homogenous color changes and protect silver from rapid electrochemical degradation. However, since silver is electrochemically active in the same

potential range as the majority of colored-to-clear cathodically coloring dioxythiophene ECPs, it makes sense to eliminate it as an electrode material and utilize solely PEDOT:PSS. In addition to being redox-stable, PEDOT:PSS can be rendered highly conductive using a variety of acidic post treatments.[153,155,231] As it can be easily formulated into printable, aqueous inks, PEDOT:PSS is an outstanding candidate for transparent electrodes applied to paper ECDs.

To date, PEDOT:PSS has been explored extensively as an electrochromic active material on paper substrates.[59,213,221,232,233] one of the highest performing paper ECDs in terms of the color contrast was demonstrated by Berggren and coworkers. By depositing a magenta-to-colorless ECP, onto printed PEDOT:PSS, a high color contrast of $\Delta E^{*} = 54$ was achieved for a segmented display.[221] More recently, Crispin and coworkers have demonstrated free-standing electrochromic paper based on a blend of CNF and PEDOT:PSS with a contrast up to $\Delta E^{*} = 31.2$ achieved by blending TiO2 particles into the active material to enhance scattering.[213] However, relying on the PEDOT:PSS color change for electrochromic contrast not only limits the accessible color palette, but typically requires higher driving voltages during operation.

In this work, we present fully solution-processed paper-ECDs incorporating color-neutral, printed PEDOT:PSS electrodes. In contrast to previous work investigating the electrochromism of PEDOT:PSS, we demonstrate how thin PEDOT:PSS layers can be used as a color-neutral electrode in order to achieve multicolored electrochromism on paper. The use of a thin CNF-coating (4.4 g m^{-2}, 2-3 µm thickness) provides a smoother

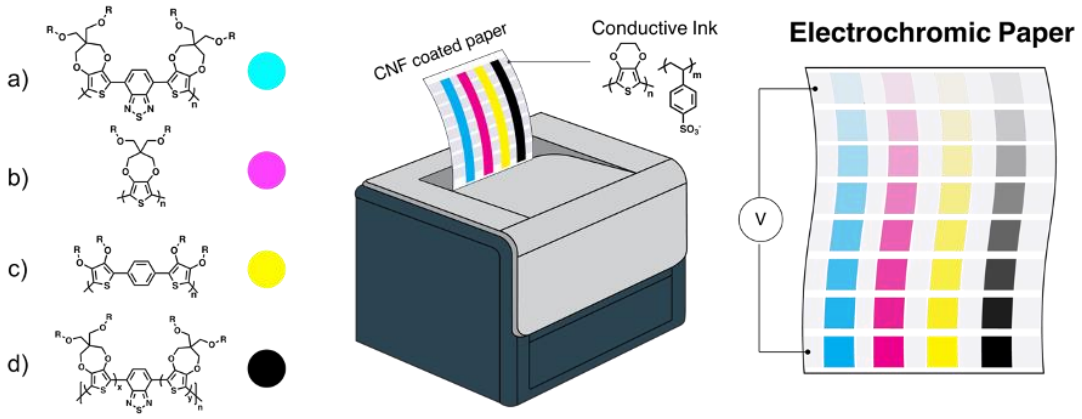

Figure 4-1 Schematic showing printing of colored-to-clear electrochromic paper incorporating CNF-coated paper substrates and PEDOT:PSS electrodes as well as the repeat-unit structures of ECP-Cyan (a), ECP-Magenta (b), ECP-Yellow (c), and ECP-Black (d).

surface with reduced porosity for printing continuous, thin films of PEDOT:PSS. For sufficient conductivity, a mild-acid post treatment of the printed PEDOT:PSS provided color-neutral, redox-stable electrodes, with a sheet resistance of 460 Ω sq^{-1}, which is sufficient to support redox-switching of colored-to-colorless 3,4-propylenedioxythiophene-based electrochromic polymers (ECPs). . Note that although specialty papers like photo paper provide even smoother surfaces with higher specular reflectance, this post treatment was found to render the paper yellow and thus not suitable for continued investigation in this work. ECPs with the three primary colors (Cyan, Magenta, and Yellow shown in Figure 4-1) were effectively switched on these paper-based electrodes with color contrasts of ΔE_C^* = 17, ΔE_M^* = 37, and ΔE_Y^* = 42, respectively. In addition to the three primary colors, black-to-colorless ECDs were also fabricated demonstrating a color contrast of ΔE_K^* = 29, stable switching for 9,000 cycles, and stable operation under flexed conditions. This work provides an effective method for fabricating

disposable electrochromic devices on paper in full color as highlighted in the schematic in Figure 4-1.

4.1.2 Tuning inkjet-printing parameters

To preserve the color contrast of the electrochromic material, paper ECDs require the electrode material to have sufficiently low surface resistance to effectively switch the electrochromic pixels without compromising color neutrality. PEDOT:PSS films that are too thick contribute a blue color, whereas films that are too thin are too resistive. As inkjet printing can provide fine control over printed thickness by tuning droplet spacing and number of overprint layers, a range of electrode thicknesses were prepared and their reflectance (at 550 nm) and sheet resistance after an acidic post-treatment were measured.

To prepare printed PEDOT:PSS films, Clevios PH1000 (Heraeus) PEDOT:PSS was diluted to 0.65 wt% solids with Millipore ultrapure water followed by the addition of 0.1 wt% of Triton-X100. Solid *p*TSA (Alfa Aesar, 98%) was dissolved at 1 M concentration in ethylene glycol (EG, Millipore Sigma, 99.8%) and used to enhance the conductivity of PEDOT:PSS traces after printing. Inkjet printing of the PEDOT:PSS ink was performed using a MicroFab Jetlab II inkjet printer equipped with a 50 µm diameter piezoelectric nozzle and a temperature controlled stage. Jetting parameters were adjusted to obtain droplets of ca. 65 µm (~150 pL) as measured by a horizontal camera. Droplet spacings (dx and dy) and number of overprints were tuned to obtain a range of thicknesses of PEDOT:PSS films on glass, paper, and CNF-coated paper substrates. The printed electrodes were dried in a vacuum oven at 50 ˚C for 1 hour then treated with 1 M *p*TSA/EG

solution for 5 minutes at room temperature to enhance their conductivity.[155] The printed electrodes were then rinsed with water and dried under ambient conditions.

In order to evaluate printed PEDOT:PSS electrodes on various substrates, the resistance and reflectance of these films were evaluated to determine printing parameters that would offer the optimum balance of low resistance and color neutrality. Reflectance measurements were carried out using an integrating sphere attachment to the Ocean Optics Spectrophotometer (di: 8˚ geometry, ca. 25 s integration time, diffuse white reflectance standard) and sheet resistance was measured using the Van der Pauw geometry.

Figure 4-2 summarizes the impact of the substrate on the performance of printed electrodes, PEDOT:PSS films of various thicknesses were prepared on glass, CNF-coated paper, and standard cellulose paper. Target values for the paper electrode reflectance (%R) was 50% or greater to ensure the bleached state of the ECD would remain colorless. Additionally, sheet resistances below 500 Ω sq^{-1} were desired, highlighted by the green

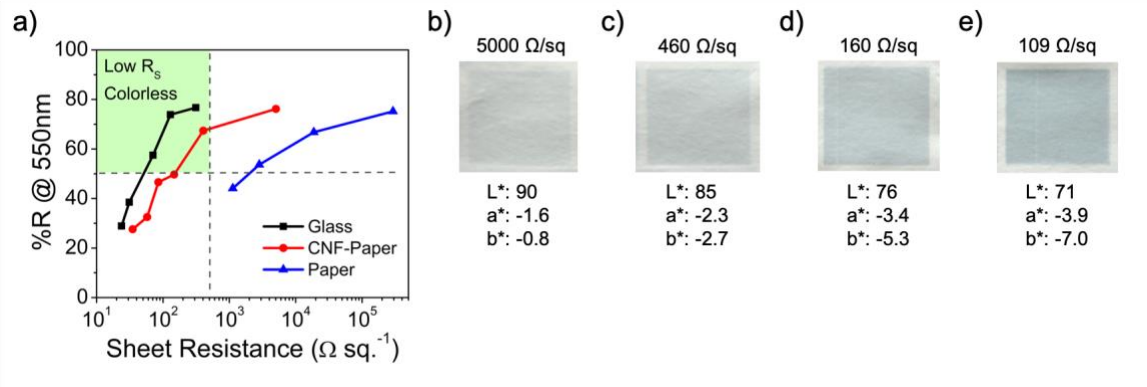

Figure 4-2. Optimization of printed electrodes showing (a) reflectance as a function of sheet resistance for printed electrodes on glass, CNF coated paper, and office paper. Photographs of PEDOT:PSS electrodes on CNF coated paper with sheet resistances of (b) 5000 Ω sq^{-1}, (c) 460 Ω sq^{-1}, (d) 160 Ω sq^{-1}, and (e) 109 Ω sq^{-1}. CIELAB color coordinates are labeled below each image.

square in upper right-hand corner of

Figure 4-2a. At this surface resistance and a typical ECD peak load current of 0.5 mA cm^{-2}, a 1x1 cm pixel is expected to have an iR drop up to 0.25 V which would avoid the need for high driving voltage to switch the center of the pixel. Since this iR drop scales linearly with the lateral pixel dimension, a doubling of the pixel size would require lower sheet resistances in order to maintain ECD operation in a voltage window that produces the color change but does not over-oxidize the polymer.

Figure 4-2a demonstrates the benefit of having a CNF coating on the paper where a 1000x decrease in resistance was seen for treated-PEDOT:PSS films printed on coated paper relative to standard office paper. Being an aqueous ink, the PEDOT:PSS readily soaks into the fibers of the office paper resulting in a poorly conductive film with sheet resistances exceeding 1000 Ω sq^{-1} even for dark films at 40 %R. With the addition of a CNF coating, the surface roughness of the paper decreases from 15 µm to 1.4 µm, as highlighted by the SEM images in Figure S4-1. In addition to a decreased roughness, the CNF coating reduces the paper porosity, therefore retaining the ink on the surface during drying allowing for the formation of a continuous, conductive film. This was verified via time-resolved contact angle measurements (Figure S4-2) where the CNF coated paper substrates demonstrated reduced absorption time for water droplets as shown by the evolution of both angle and height versus time. The two thickest PEDOT:PSS films on each substrate were prepared using 2 and 3 overprints, which drove the reflectance below 40%. These overprinted electrodes on CNF-paper approach the sheet resistance measured on glass suggesting that additional printed layers dry on top of already-formed PEDOT:PSS and electrode resistance becomes substrate independent.

The color of the printed electrodes was quantified using CIELAB color coordinates calculated from the reflectance spectra shown in Figure S4-3. The L^* component represents the lightness of a color, where 100 is diffuse white and 0 is black, the a^* is the red/green component and the b^* quantifies the yellow-blue component. To maximize color neutrality, the paper electrodes should have high L^* values and low a^*, b^* values. For reference, the color coordinates for the white CNF-coated paper were L^*: 99, a^*: -0.4, b^*: -0.2. Figure 4-2b-e show photographs of the PEDOT:PSS electrodes on CNF-coated paper with their corresponding color coordinates and sheet resistance. As expected, the most color neutral films are the most resistive highlighting the trade-off between optical and electrical properties.

In selecting printed PEDOT:PSS electrodes for paper ECDs, it is critical that the electrode coloration does not impact the contrast of the ECP. As ECPs reach their bleached state, there typically remains a small absorbance (0.1 optical density) across the visible. Since paper substrates are diffusely reflecting, this residual absorption can be amplified in comparison to equivalent film thicknesses on ITO/glass substrates measured in transmission.[213] In order to achieve the highest electrochromic contrast, the PEDOT:PSS/CNF-paper electrode shown in Figure 2c (460 Ω sq^{-1}) was chosen for further evaluating the performance of electrochromic polymers and devices. This electrode, referred to hereafter as CNF-460, provides a sheet resistance of 460 Ω sq^{-1} and L^*: 85, a^*: -2.3, b^*: -2.7 after the acid post treatment. Compared to the electrode with 5000 Ω sq^{-1}, this electrode is only slightly more colored and provides an order of magnitude lower sheet resistance enabling these electrodes to support electrochromic switching at low potentials (< 1 V) for reasonably sized electrodes (cm^2 range).

4.1.3 Switching of ECP-Cyan, Magenta, and Yellow

Since PEDOT:PSS is redox-active, and an electrochromic material itself, it is important that the potential window used for switching an ECP film is limited to potentials where PEDOT:PSS will remain conductive. As shown in Chapter 3, PEDOT:PSS treated with 1 M *p*TSA/EG retains its conductance from between 0.8 and -0.6 V as shown by *in situ* conductivity and impedance analysis. A decrease in conductivity is shown beginning at -0.7 V accompanied by an increase in absorbance indicating that the formation of the neutral PEDOT chromophore. To ensure that the ECP switching is not compromised by electrochemically induced charges in the PEDOT:PSS electrode, it is important that these electrodes not be operated at electrochemical potentials below -0.7 V vs Ag/Ag^{+}.

Because the three subtractive primary colors, ECP-Cyan, ECP-Magenta, and ECP-Yellow (Figure 4-1), are all 3,4-propylenedioxythiophene-based materials, they are sufficiently electron-rich to have a relatively low oxidation potential (< 1 V vs. Ag/Ag^{+}). At the same time, they are less electron-rich and more sterically strained than PEDOT so that they are easier to electrochemically reduce to ensure that they can be switched to their fully colored state without reducing the electrode. This was confirmed by spray coating the three primary ECPs on printed CNF-460 electrodes and switching them between their neutral/colored (0 V) and oxidized/colorless (0.8 V) states.

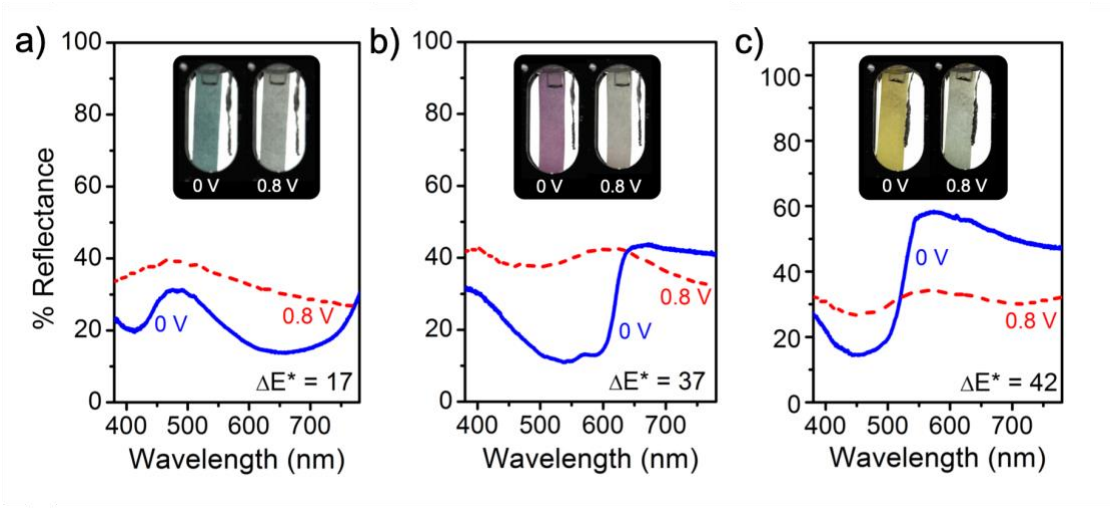

Figure 4-3. Reflectance spectra in the neutral (0 V) and oxidized (0.8 V) states for a) ECP-Cyan, b) ECP-Magenta, and c) ECP-Yellow films in a three- electrode cell with a Ag/Ag+ reference electrode and a Pt flag counter electrode immersed in 0.5 m TBAPF6/PC. Photographs of the ECP coated CNF-460 are shown as inserts and color contrast between each state is labeled.

All of the ECPs reach their fully colored state at 0 V vs. Ag/Ag^+, far above the potential at which PEDOT:PSS will become electrochemically reduced, as shown by the reflectance spectra in Figure 4-3. The three ECPs reached their fully oxidized state at 0.8 V vs. Ag/Ag^+ on the paper electrodes. These potentials are comparable to what is observed for the same films on ITO/glass (Figure S4-4), indicating that the PEDOT:PSS is sufficiently conductive to act as an effective electrode material. The ability to repeatedly switch the primary colored ECPs between their colored and colorless states opens up the opportunity to use these PEDOT:PSS/paper electrodes for multicolored ECDs where a wide color gamut can be accessed through e.g. solution blending.[194,195] Because the paper substrate absorbs some of the propylene carbonate electrolyte, the reflectance of the films in their colorless states is 10-20 % lower than for the same ECP films on reflective ITO/glass/PTFE electrodes (Figure S4-4).

Despite the darkening of the electrode, the color change (ΔE^*), between the colored and colorless states is the more important film metric as these materials are envisioned for color-changing displays. The calculated ΔE^* values highlight that these ECP films reach nearly the same color change on the CNF-460 electrodes as the ECP-films deposited on ITO/glass electrodes although the vibrancy is somewhat reduced due to the lower overall reflectance across the visible spectrum of the paper electrodes. The higher reflectance is evident at wavelengths where the ECPs do not exhibit strong absorption (550 nm for ECP-Cyan, >700 nm for ECP-Magenta, and >600 nm for ECP-Yellow). In each of these regions, the films on PEDOT:PSS/ paper/ exhibit ~10% lower reflectance than ITO/glass samples. ECP-Cyan reached ΔE^* = 17 and ECP-Magenta a ΔE^* = 37 on both electrodes, whereas ECP-Yellow reached a ΔE^* = 42 on CNF-460 and 43 on ITO/glass/PTFE. Quantifying the color coordinates from the reflectance spectra for ECP films in their colored states on both substrates affords a direct comparison of color purity and color change relative to the color coordinates of the oxidized states. As shown in Table S4-1 through Table S4-3, the a^* and b^* values are similar for films deposited on ITO/glass and CNF-460 paper electrodes whereas the L^* coordinate is lower for the CNF-460 paper electrodes due to the 10-20% lower reflectance across the visible spectrum.

In their oxidized states, the ECP films are all fairly color neutral with a^* and $b^* < 5$ with the exception of ECP-Yellow, which has a residual blue color on paper (b^* = 8.1) as well as a lower overall lightness (L^* = 64). It should be noted that this is an inherent property of the polymer as ECP-Yellow deposited on ITO/glass/PTFE (where the back PTFE coating is added to provide a white background behind the glass) also has a lower L^* and higher positive b^* than ECP-Cyan and ECP-Magenta in the bleached state.

While these reflectance measurements show the same absorption peaks as seen for thin ECP films measured in absorbance, some important distinctions should be made. First is the fact that light that is reflected off of two interfaces is collected (ECP-Air, ECP-Paper) is collected by the integrating sphere, rather than measuring only the transmitted beam. The reflectance peaks are broader compared to absorbance peaks and there is a non-logarithmic dependence between film thickness and %R (in contrast to %T). In-depth study of ECP reflectance was outside of the scope of this work, yet remains an important topic where more fundamental understanding is needed, especially for films in their oxidized states.

For comparison with standard printer ink, cyan, magenta, yellow, and black color swatches were printed on office paper and reflectance spectra recorded (Figure S4-5). From these spectra, the color differences relative to the white paper used as a reference (used as $L^* = 100$, $a^* = 0$, $b^* = 0$) were calculated to give an ideal ΔE^* for each of these primary colors. As shown in Figure S4-5, $\Delta E_C^* = 45$, $\Delta E_M^* = 61$, $\Delta E_Y^* = 79$, and $\Delta E_K^* = 55$. While these ΔE^* values are higher than the ECP-coated electrodes, these values were derived from dry paper that has not been darkened by the uptake of electrolyte and therefore the color change of ECPs on paper can be enhanced by fabricating ECDs with a solid electrolyte, as will be shown below.

4.1.4 Solid, Lateral ECDs Incorporating ECP-Magenta and ECP-Black

The fabrication process for constructing lateral paper-based ECDs is outlined in the schematic in Figure 4-4. These devices incorporate a solid ion gel electrolyte that allows all device components to be applied using high-throughput printing and coating methods. First, two 460 Ω sq^{-1} PEDOT:PSS (5 x 5 mm) pixels are inkjet-printed on the CNF-paper,

and thicker PEDOT:PSS lines (2 x 5 mm, 106 Ω sq^{-1}) are printed as connectors to ensure a low contact resistance when connected to a power source (Step 2 in Figure 4-4). Magenta-to-colorless ECD pixels were fabricated by spray casting ECP-Magenta (18 %R at 550 nm) from toluene. The ion gel electrolyte was blade coated over the ECD pixels and dried at 50 ˚C for 30 minutes in ambient atmosphere. Black-to-colorless ECDs were prepared in an identical fashion by spray-casting ECP-Black (20% R at 550 nm) from toluene. The charge balance in the device, which ensures that the device switches rapidly with maximum contrast at a low operating voltage, was controlled by ensuring that the amount of ECP coated on both PEDOT:PSS pixels was identical. This lateral geometry reduces the number of material layers in the device leading to enhanced color contrasts. While these devices employ the simplest possible geometry, more complex features could be easily envisioned where appropriate charge balancing could be controlled by printing equivalent areas for each electrode.

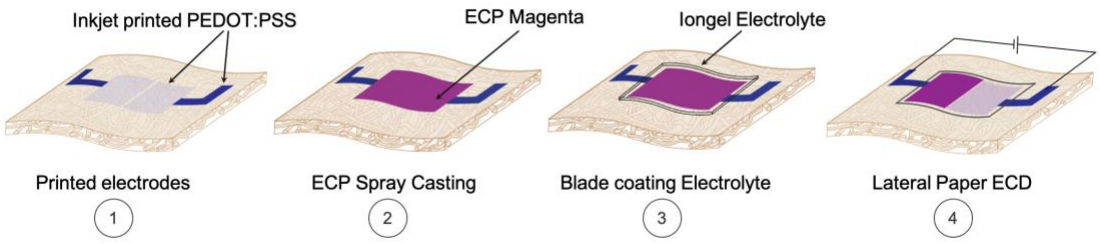

Figure 4-4. Fabrication process for lateral paper-ECDs showing inkjet-printed PEDOT:PSS electrodes, deposition of ECPs, and [EMI][TFSI]/P(VDF-HFP) ion gel electrolyte layer. Devices are operated by applying a 0.8 V bias across the two lateral pixels.

The electrochromic pixels on the lateral paper-based ECDs can be switched on and off relative to one another using a low operating voltage of +/- 0.8 V. If we consider, for example, the left pixel of the device to be the working electrode, a device voltage of 0.8 V would result in the left pixel changing from a colored to a clear state (charge passed at t_{30sec}: 0.82 mC cm^{-2}) and the opposite electrode switching from a clear to a colored state (Figure 4-5a and b). Conversely, if the bias is reversed to -0.8 V the left pixel will recolor while the right pixel bleaches. Similarly, after a full switch, black-to-colorless paper-ECDs (Figure 4-5e and f) pass 1.3 mC cm^{-2} at t_{20sec}. For reference, a typical rechargeable AAA battery provides 3600 C of charge meaning paper ECDs the size of office paper (8.5 x 11

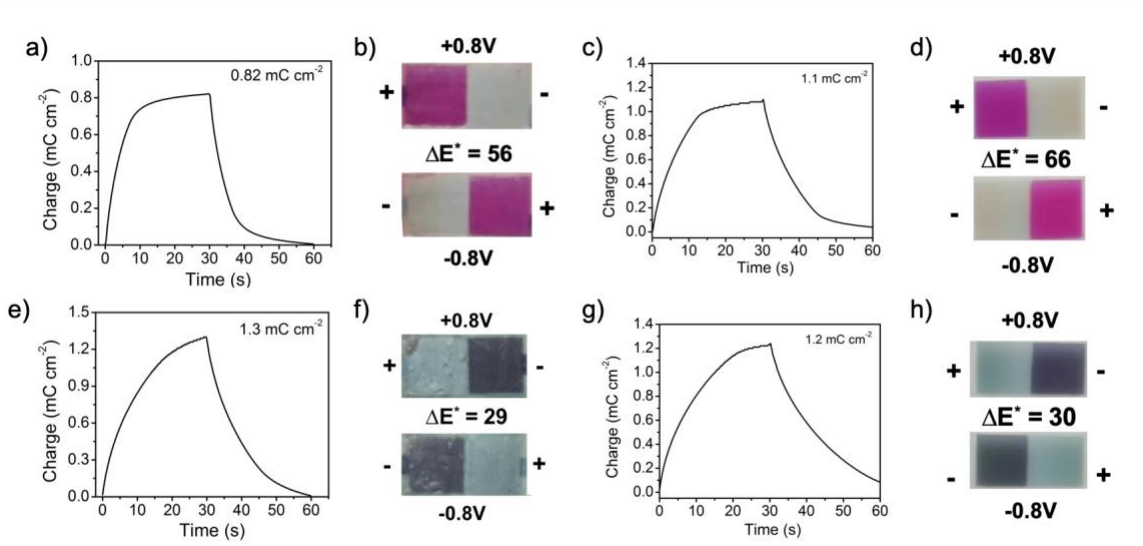

Figure 4-5. Lateral ECDs. (a) Charge density as a function of time for a magenta-to-colorless paper-ECD. b) Photographs of magenta-to- colorless paper-ECD with the left pixel/working electrode charged (0.8 V and discharged (−0.8 V). (c) Charge density versus time for a magenta-to-colorless ITO/glass-ECD. (d) Photographs of magenta-to-colorless ITO/glass-ECD with the left pixel/working electrode charged (0.8 V and discharged (-0.8V). (e) Charge density versus time curve for a black- to-colorless paper-ECD with the same switching voltage. (f) Photographs of black-to-colorless paper-ECD in each charged state. (g) Charge density versus time curve for a black-to colorless ITO/glass-ECD. (h) Photographs of black-to-colorless ITO/glass-ECD in each charged state.

in) could be switched 4500 times with a single charge. The low voltage requirements are a significant advantage over the current state-of-the-art paper-based ECDs that use the electrochromism from PEDOT:PSS alone.[59,213,220] These ECDs require between 1.5 to 3 V in order to fully reduce the PEDOT as a result of the low onset of oxidation and presence of excess immobilized PSS^- counter ions.

Using an RGB converter and the photographs taken under D50 controlled lighting conditions; we can calculate the average color contrast of the device in its colored and colorless states. The $L^*a^*b^*$ coordinates for the magenta pixels in their colored state are (37.1, 44.4, -17.1) that then bleach to (65.1, -0.5, 2.9) in the colorless state (Table S4-4), resulting in a color contrast of $\Delta E^* = 56$. This contrast is approaching the ΔE^* for standard printing ink ($\Delta E^* = 61$, Figure S4-5a). Additionally, in comparison to other reported paper-ECDs, a remarkably colorless oxidized state ($a^* = -0.5$, $b^* = 2.9$) is achieved with this paper ECD due to a combination of the high contrast of the polymer, and the thin, colorless PEDOT:PSS electrode ($L^* = 85$, $a^* = -2.3$, $b^* = -2.7$). Lateral magenta-to-colorless ECDs were also constructed on ITO/glass with a sheet resistance of 10 Ω. sq^{-1} (referred to here as ITO-10, Figure 4-5c,d) and similar performance is observed in terms of the charge density per switch (1.3 mC cm^{-2}). The color contrast of the ITO device was $\Delta E^* = 66$, even higher than on paper, and exceeded the color difference for the magenta printer ink referenced to white paper ($\Delta E^* = 61$).

The black-to-colorless paper ECD exhibits $L^*a^*\ b^*$ coordinates of (32.6, 1.0, -7.7) and (60.9, -6.9, -4.9) in the colored and colorless states, respectively. As shown in Figure 4-5f, the color contrast of the black ECD is $\Delta E^* = 29$, i.e. lower than that of the magenta-

to-colorless devices due to the inherently lower contrast stemming from residual green-gray color in the oxidized state of ECP-Black (a^* = -8, b^* = 6).[164] As with the magenta-to-colorless devices, lateral devices constructed with ECP-Black on ITO-10 electrodes performed similarly to those on paper requiring slightly diminished charge to switch (0.8 mC cm^{-2}) and a similar contrast of ΔE^* = 30 (Figure 4-5g and h).

4.1.5 Switching Kinetics of Lateral ECDs

One consequence of the lateral device architecture is a slower switching time (~15-25 seconds for 5 x 5 mm devices) compared to similarly sized absorption-transmission (window-type) ECDs with a vertical architecture (3 cm^2, ~5 sec).[231] As the voltage bias is reversed from -0.8 to +0.8 V, an electrochromic moving front is seen starting at the center of the device and moving to the outer edge of each pixel toward the current collector. As the moving front crosses the pixel, the charge extracted from the ECP film (and PEDOT:PSS electrode) increases until the pixel is completely bleached. The charge density then plateaus indicating that the redox switch is complete and additional charge buildup likely stems from capacitive charging (Figure 4-5a,c, e and g). From these charge density curves, it is apparent that both the magenta-to-colorless and black-to-colorless ECDs require 15-20 seconds to fully switch.

In order to further explore the switching kinetics of these lateral devices, colorimetric data were extracted from video files recording the electrochromic switching using MATLAB. From this data, both time- and spatially-resolved color changes could be quantified as shown in Figure 4-6 and Figure S4-6. Video frames of a magenta-to-colorless paper-ECD are shown in Figure 4-6a following a switch in voltage bias from -0.8 V to

+0.8V for the left-hand pixel. The middle of the device undergoes nearly the full color change in six seconds. The moving front then crosses the pixel toward the contact slowly reaching the bleached state between 12 and 18 seconds. To visualize the difference in the time required to switch for the middle portion of the device compared to the entire pixel area (5 x 5 mm), five-pixel subsections were analyzed in MATLAB starting from a subsection containing the first 1 mm lateral distance, then subsections including additional 1 mm distances, through the full 5 mm pixel. The evolution of color change (ΔE^*) as a

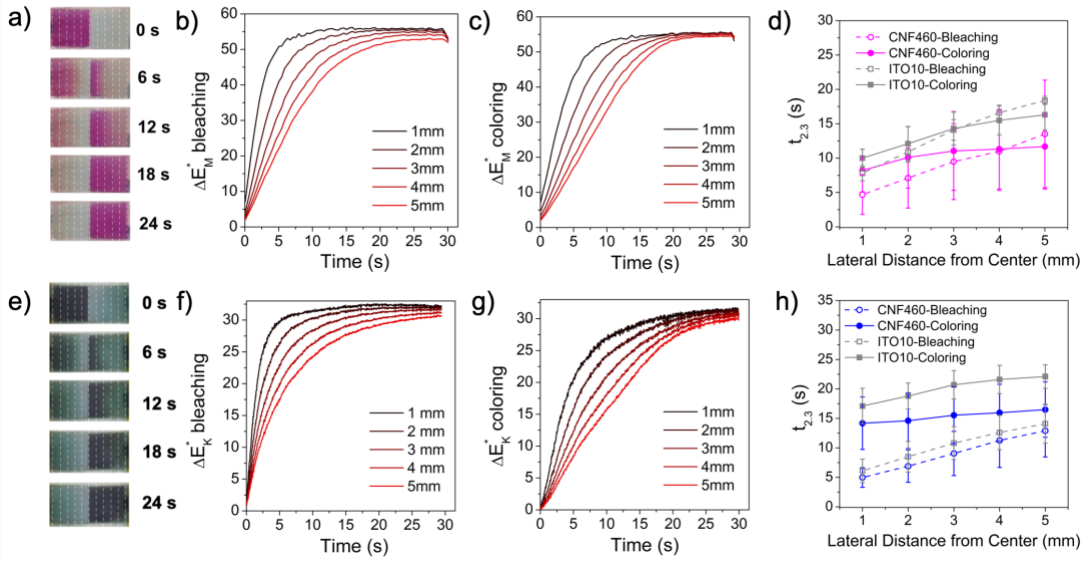

Figure 4-6. Switching kinetics of paper ECDs. a) Photographs of magenta-to-colorless paper ECD at 6 s time intervals after the application of +0.8 V to the left pixel. White dotted lines mark every millimeter from the center as a guide to the eye. Color change upon b) bleaching and c) coloring as a function of time for pixel subsection area increasing from 1 to 5 mm from the center of the device. d) Switching time ($t_{2.3}$) required to reach a ΔE^* of 2.3 less than ΔE^*_{max} for magenta-to-clear paper devices (460 Ω sq−1 electrodes) compared to ITO/glass devices (10 Ω sq−1 electrodes). e) Photographs of black-to- colorless paper ECD at 6 s intervals upon application of +0.8 V to the left electrode. Color contrast as a function of time for black-to-colorless devices during f) bleaching and g) coloring for a range of areas beginning with the first 1 × 5 mm section near the middle and expanding to the full 5 × 5 mm pixel. h) Switching time ($t_{2.3}$) for black-to-colorless ECDs constructed on paper electrodes and ITO/glass electrodes for both bleaching and coloring.

function of time is shown in Figure 4-6b and c referenced to an initial colored state or bleached state, respectively. From these ΔE^* curves, the time required to reach the colorless (or colored state) can be determined by finding the time required to reach a ΔE^* of 2.3 less than ΔE^*_{max} for the pixel, i.e. a color change that is indistinguishable to the human eye. This switching time, labeled $t_{2.3}$, can be calculated for both the coloration and bleaching for each subsection of the lateral ECD. As expected, the switching times for the first 1 mm subsection are the fastest (8 seconds for bleaching and 5 seconds for coloring) and as the subsection grows in size, the switching time is increased to 12 second coloration and 13 second bleaching for the entire pixel.[234] For both the paper and ITO ECDs, there is a slight difference between the bleaching and coloring of the pixel indicated by differing slopes in the $t_{2.3}$ as a function of time data. As the pixel bleaches, there is a uniform moving front of bleaching from the center to the contact (constant increase in $t_{2.3}$ with lateral distance) whereas the coloration occurs more uniformly over the pixel area 3 to 5 mm from the center (nearly constant $t_{2.3}$ with lateral distance). This trend highlights that ionic transport plays a critical role in the switching kinetics of these lateral devices. We expect that, upon bleaching, ions move freely from the center to the electrochromic front, through the oxidized and swollen ECP. Upon coloring, the ions likely have a more tortuous path through the neutral, compacted ECP film and thus vertical transport from the ion gel above the film may contribute to the more uniform coloration 3-5 mm from the center of the device.

Lateral devices on ITO-10 were constructed in an identical fashion to those on the CNF-460 paper electrodes in order to evaluate the impact of the electrode resistance on the switching speed of the device. Magenta-to-colorless devices built on ITO-10 electrodes

exhibit the same behavior as the paper-based analogs where an electrochromic moving front crosses the pixel from the center, outward toward the contacts (Figure S4-6a-c). In fact, the speed of the moving front, and consequently the switching speed of these ITO-based lateral devices, is comparable to the paper ECDs (Figure 4-6d). The first 1 mm subsection of the ITO-10 devices required 10 seconds to color and 7 seconds to bleach, and the entire pixel required 16 and 18 seconds, respectively. The similar switching speeds measured for both ITO-10 and CNF-460 devices is an important observation that demonstrates that the limiting factor governing switching speed for this device geometry is the ion gel electrolyte and not the sheet resistance of the electrode.

The kinetics of black-to-colorless ECDs constructed on lateral CNF-460 electrodes were also evaluated and showed similar behavior as the magenta-to-colorless devices, as shown in Figure 4-6e-h. A moving front for the coloration and the bleaching of the device moves from the center outward to the contacts though the bleaching and coloration occur at different rates during the beginning of the switch. The first 1 mm subsection of devices constructed on CNF-460 electrodes requires 5 seconds to bleach and 14 seconds to recolor. As the pixel subsection area is expanded, the time required for bleaching increases to 13 seconds where the coloration time increases only slightly to 16 seconds. This uniform coloring of the entire pixel is shown in Figure 6h where a steady increase in the bleaching time is accompanied by only a small change of coloration time between the 1 mm subsection and the 5 mm pixel area, similar to what was seen for the magenta-to-colorless devices. This behavior is a characteristic of the ECP as the same trend is observed on both CNF-460 and ITO-10 electrodes (Figure S4-6d-f).

To probe the electrolyte effect on the switching speed, magenta-to-colorless lateral devices constructed on ITO-10 were immersed in 5, 50, and 500 mM [EMI][TFSI]/propylene carbonate and the switching performance was compared to what was observed using the solid ion gel electrolyte (Figure 4-7). Both bleaching and coloration occur much more rapidly for these liquid electrolyte devices where a moving front crossing the pixel is just barely noticeable for the 5 mM concentration. As the concentration of ionic liquid in propylene carbonate is increased, the conductivity increases from 0.2 to 5.0 mS cm^{-1}, which results in a decrease in switching time for the pixel from 0.6 to 0.3 seconds for

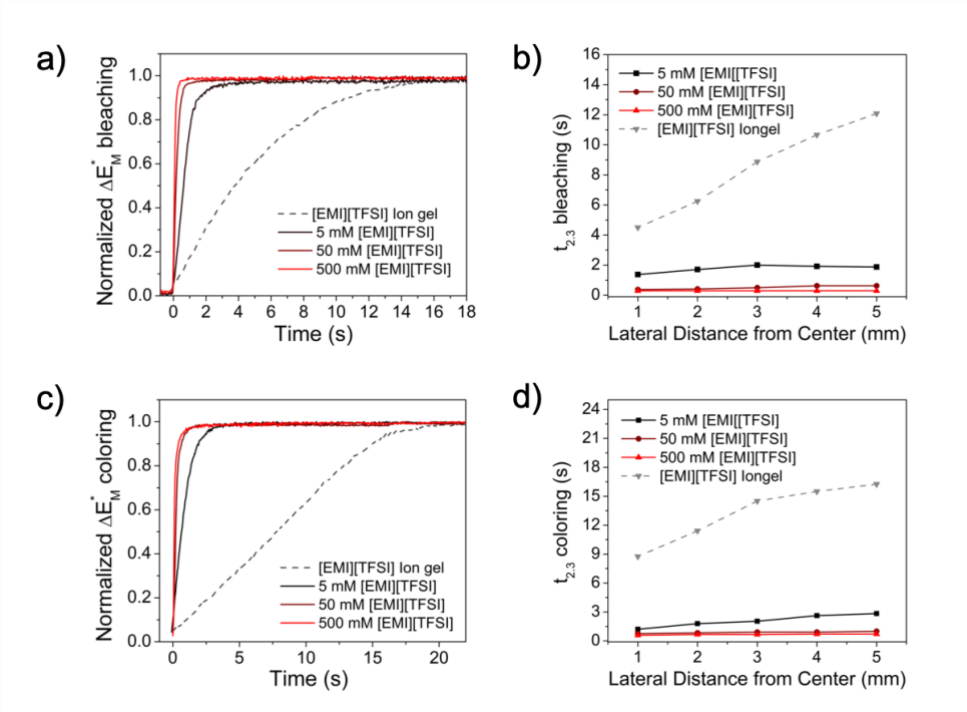

Figure 4-7. (a) Bleaching kinetics of lateral magenta-to-clear ITO/glass devices constructed with the [EMI][TFSI] ion gel electrolyte, and 5, 50, and 500 mM concentrations of [EMI][TFSI] in propylene carbonate. (b) Switching times for lateral sections 1-5 mm from the center of the device for each electrolyte upon bleaching of the ECD pixel. (c) Coloration kinetics of lateral device for the four electrolytes measured and corresponding switching times for five lateral pixel sections (d).

bleaching and 1.0 to 0.7 seconds for coloration (Figure 4-7b, d). Even the 5 mM [EMI][TFSI] electrolyte supports rapid electrochromic switching in roughly 1/10th of the time required for the ion gel despite the two having comparable conductivity (0.2 mS cm^{-1} for 5 mM [EMI][TFSI] and 0.1-1 mS cm^{-1} for the ion gel).[235]

In addition, PEDOT:PSS electrodes with a 480 Ω sq^{-1} sheet resistance (PEDOT-480) were prepared on glass as a more direct comparison to the CNF-460 electrodes. While these devices switched more slowly than ITO-10 devices, they still showed switching times of around 2 seconds for both bleaching and coloration (Figure 4-8) with 500 mM [EMI][TFSI] – nearly a factor of 10 faster than when using the ion gel. Figure 4-8c shows the switching times for the same 1-5 mm pixel subsections discussed above where there is no clear increase in switching time moving from the center of the device outward, indicating a uniform switch of the entire pixel. The absence of a moving front seen when using high-resistance PEDOT-480 is distinct from what was observed for the various

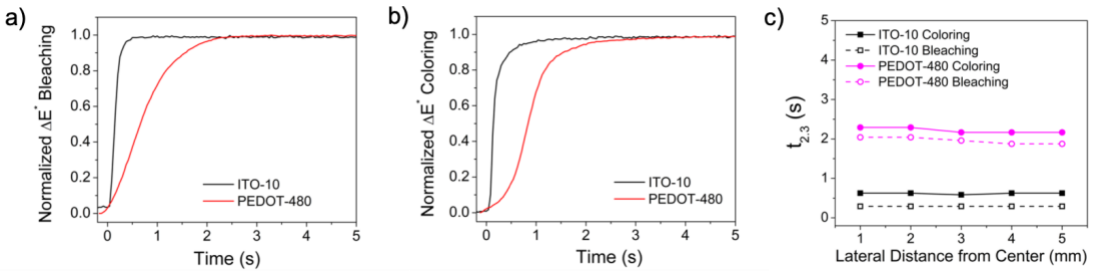

Figure 4-8. (a) Bleaching kinetics of lateral magenta-to-clear ECDs constructed on ITO-10/glass and PEDOT-480/glass in 500 mM [EMI][TFSI]/PC electrolyte with a driving voltage of 0.8V. (b) Coloring kinetics for magenta-to-clear ECDs constructed on ITO-10 and PEDOT-480 electrodes. (c) Switching time for devices for bleaching (dashed lines) and coloration (solid lines) for magenta-to-clear devices in liquid electrolyte.

devices incorporating the ion gel highlighting the impact of sheet resistance on switching kinetics. When high conductivity electrolytes are used, switching speed can become limited by high surface resistance electrodes, as in the case of these PEDOT-480 films. In this case, the color change appears as a slow fading in/out of the electrochromic film. For the electrolyte-limited switching kinetics seen for devices incorporating the ion gel electrolyte, the color change appears as an electrochromic moving front crossing the pixel. These kinetics results further highlight that improved ion mobility in the ECP is key for improving the switching speed of these lateral devices. Carefully chosen combinations of ECP and electrolytes focused on enhancing swelling and therefore liquid-like ion transport in the film could be explored in the future further optimization of switching kinetics.

4.1.6 Device Stability, Flexibility, and Combustion.

Another important device metric is redox and switching stability. If a device is switched 100 times per day, roughly 10^4 cycles would enable a device to be used for 10 weeks. In order to test the viability of these electrodes for multiple color switches, repeated cycling of a black-to-colorless paper ECD was performed with 20 second square-wave pulses at both +/- 0.8V under an ambient environment. There is only minimal decay in the charge density required to switch the pixels from 1.75 mC cm^{-2} to 1.44 mC cm^{-2} after 9,000 cycles (Figure 4-9). The inset photographs show that the color contrast is maintained at $\Delta E^* = 25$ at the 9,000th cycle, demonstrating practical stability of both the PEDOT:PSS electrodes and ion gel electrolyte under ambient cycling.

As these paper ECDs are composed entirely of polymeric components with thin active layers (100-300 nm), they can retain their operation while being flexed. Figure 7b shows

the evolution of charge density in one of the pixels at decreasing bending radii where only a slight drop in charge density from 0.52 mC cm^{-2} to 0.46 mC cm^{-2} is seen as the device is bent to a 1 mm radius. A photograph of the device bent to a 1 mm radius is shown in the figure inset illustrating the degree of bending these devices can withstand before without compromising the switching performance. Photographs of an operating device bent to a 2.5 mm radius are shown in Figure 7c to highlight the retention of the electrochromic function during bending where the contrast in the center of the device is maintained at ΔE^* = 28 at 1 mm bending radius. The PEDOT:PSS/paper and the ECP/PEDOT:PSS interfaces are both robust with strong adhesion between the different layers as no delamination is observed even at bending radii < 1 mm. However, the observed failure point during the bending tests was delamination of the ion gel electrolyte from the ECP film.

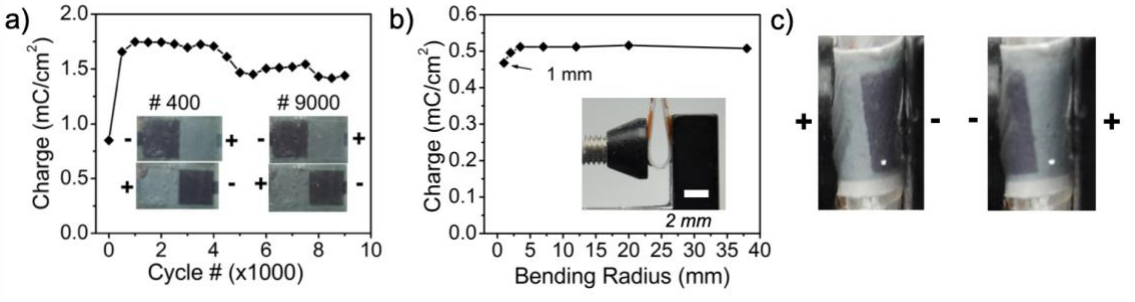

Figure 4-9. (a) Charge density as a function of switching cycle for a black-to-colorless ECD for 9000 switching cycles. Inset photographs show the device during the 400th cycle and the 9000th cycle. (b) Charge density as a function of bending radius for the black-to-colorless electrochromic device. (c) Photographs show the device bent to a 1 mm bending radius in a cross-sectional view, 2 mm scale bar and face on when biased at ±0.8 V.

Another major advantage to using paper as a substrate material with ECPs, conducting polymer electrodes and organic electrolytes is the ability to combust the materials at the end of the ECD's lifetime to avoid buildup of electronic waste. With this in mind, a pixel of the lateral ECD was combusted in a thermogravimetric analyzer in order to observe the residual mass of the ECD after burning. Figure 4-10 shows the percent mass lost as the temperature is increased to above 600˚C in air. The CNF-coated paper substrate comprises 50% of the device mass with roughly 30% coming from the PVDF-based electrolyte. Ultimately, 3% of the initial device mass is left as ash at 600˚C indicating that these devices could be disposed and incinerated with minimal waste. Admittedly, the combustion of fluorinated electrolyte polymers creates an environmental concern as HF can be produced as a byproduct. Therefore, efforts toward developing aqueous compatible ECPs is important for enabling the use of more benign polymers for the electrolyte gel such as poly(vinyl alcohol) and cellulose derivatives.[26,236,237]

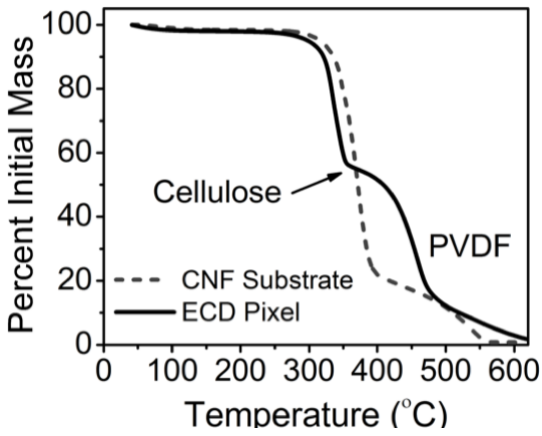

Figure 4-10. Combustion of ECD pixel in air showing mass loss versus temperature. Decomposition of cellulose and the P(VDF-HFP) copolymer from the iongel are labelled.

4.1.7 Conclusions

In this work we demonstrate the ability to inkjet print color-neutral, low-resistance electrodes on paper from PEDOT:PSS ink, followed by a mild acid treatment. By utilizing cellulose nanofiber-coated paper substrates, the sheet resistance of the paper electrodes was reduced by three orders of magnitude, enabling their use for switching three ECPs (cyan, magenta, yellow) between their neutral and oxidized states at low voltages (0.8 V). Lateral devices constructed with a semi-solid ion gel electrolyte showed high-contrast and stable switching for both magenta-to-clear ($\Delta E^* = 56$) and black-to-clear ($\Delta E^* = 29$ 9,000 cycles) active layers. The switching kinetics of these ECDs were evaluated using colorimetric image analysis in MATLAB which provided higher temporal and spatial resolution than what was possible with a spectrophotometer. This analysis provided insight into the device kinetics where the ion gel electrolyte was the limiting factor governing switching speed.

With these results in mind, we consider paper-based organic displays as a promising route for enabling disposable diagnostic tools and low-cost electronics. Organic conductors and semiconductors are promising material candidates for enabling displays that can be solution processed at low temperatures to provide mechanically compliant active layers. As these thin active layers typically represent a minor portion of the device mass, end-of-life disposal via combustion or recycling becomes an option when compatible substrates are selected. In this work, the active materials make up less than 0.5% of the device mass – roughly 0.012 mg cm^{-2} and 0.045 mg cm^{-2} for the PEDOT:PSS electrodes and ECP film respectively – compared to the paper substrate and electrolyte (8.5 mg cm^{-2} and 8 mg cm^{-2}, respectively). The small mass loading highlights than only small amounts of the relatively costly active materials can be used for large device footprints (1 mg for 17 cm^2),

but that environmental impact can be largely controlled through the substrate and electrolyte components.

This work therefore represents a path toward high-throughput fabrication of readouts for disposable electronics, however, some challenges still exist. While the contrast of these paper-based devices is on par with other paper ECDs reported in the literature, the vibrancy of the color change suffers from the diffuse reflective nature of the paper. Additionally, since the switching speed of the device is highly dependent on the electrolyte, solid-state devices would likely be limited to switching speeds greater than 10 seconds (5 x 5 mm devices) as solid electrolytes typically suffer from much lower conductivities than their liquid or gel counterparts. Therefore, in order to further improve upon the performance of these devices, engineering of the substrate to enhance specular reflection as well as the incorporation of higher conductivity gel electrolytes is needed. In particular, incorporating biopolymer-based electrolytes and green encapsulation materials are an ideal route toward realizing truly environmentally benign devices.

An additional practical consideration for ECDs in general is the need for encapsulation to exclude oxygen transmission into the device. Photodegradation studies of ECPs show that practical device lifetimes can be achieved with the application of barrier films or by constructing devices under inert conditions.[111,238] Additionally, the highly hydrophilic nature of paper warrants the use of hydrophobic barrier films to protect devices from rapidly disintegrating when exposed to high humidity environments or water. These device considerations will be important challenges to address as disposable displays continue to be developed. Along with the various low-cost electronic devices currently

investigated, we expect that paper-based displays are poised to play an important role in enabling new device applications working towards limiting environmental impact.

4.1.8 Supporting Information

4.1.8.1 Instrumentation

The electrochemical measurements were made using a EG&G PAR 273 potentiostat/galvanostat controlled by CorrWare software. *In situ* conductivity measurements and PEDOT:PSS spectroelectrochemistry measurements were made using a Pine bipotentiostat controlled by aftermath software. Spectra taken during stepwise reduction of the oxidized PEDOT in PEDOT:PSS films on glass were measured using an Ocean Optics USB2000+ UV-Vis spectrophotometer. Scanning electron micrographs were recorded with a Hitachi SU8320 field emission SEM with a 1 kV accelerating voltage. Surface roughness measurements were made with a Bruker DektakXT profilometer. Thermogravimetric analysis of ECDs was performed using a Perkin Elmer Pyris 1 Thermogravimetric Analyzer. Water contact angle measurements were performed using a Rame Hart 300 Goniometer where the droplet height and contact angle were recorded at 0.1 s intervals. Reflective photographs of ECP films on ITO/glass/poly(tetrafluoroethylene) (PTFE) electrodes were taken using a Nikon D90 Digital SLR camera under diffuse D50 lighting.

4.1.8.2 Inkjet Printing Parameters

Jetting parameters were adjusted to obtain droplets of ca. 65 µm (~150 pL) as measured by a horizontal camera. In order to achieve stable jetting, a bipolar voltage wave was applied to the piezoelectric nozzle with a dwell and echo voltage of +22 and -22 V, respectively. Typical rise and fall times between the dwell and echo waves were 5 µs. The

dwell and echo times were 25 µs and 48 µs, respectively. During printing, the jet was kept 5 mm above the sample and the stage was held at 55˚C.

4.1.8.3 [EMI][TFSI] Synthesis

The [EMI][TFSI] ionic liquid was synthesized according to a literature procedure.[239] First, impurities from the 1-ethyl-3-methylimidazolium chloride (EMICl, Sigma Aldrich, 98%) were removed by dissolving 20.07g of EMICl with 5.4 g of decolorizing carbon in approximately 100 mL of deionized water. The solution was refluxed at 90˚C in a 250 mL round bottom flask overnight and then rinsed with water over a Celite 545 pad. This process was repeated twice in order to remove all residual yellow color. Next, 47.19 g of lithium bis(trifluoromethylsulfonylimide) (LiTFSI, Acros Organics, 99%) was dissolved in 50 mL of deionized water and added to the EMICl solution. This mixture was stirred at room temperature overnight until two layers had formed. The [EMI][TFSI] was extracted with dichloromethane (DCM) using a separatory funnel. Finally, the DCM was removed under vacuum and the remaining ionic liquid was dried overnight in a vacuum oven at 60˚C.

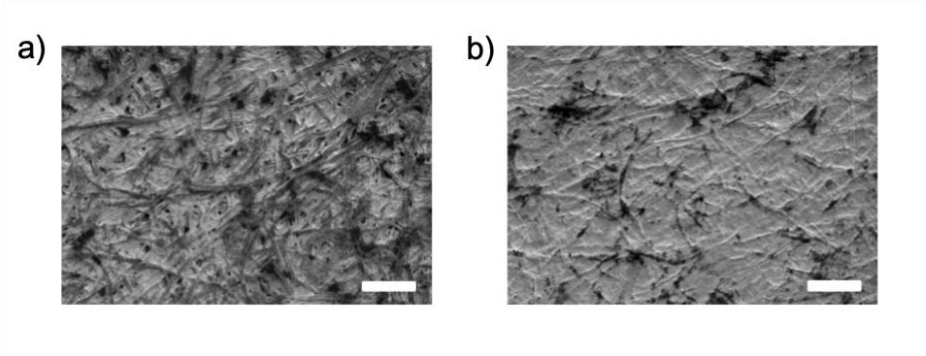

Figure S4-1. SEM micrographs of office paper surface and CNF-coated paper surface. Scale bar is 500 µm.

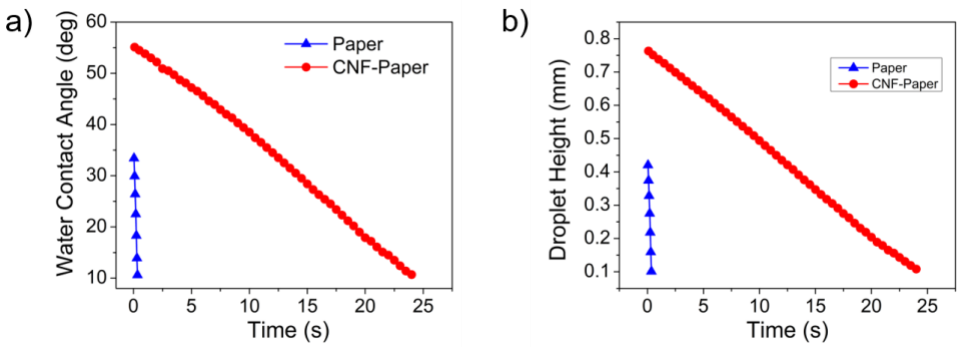

Figure S4-2. Absorption of water into paper and CNF-paper substrates measured by a contact angle goniometer. Water contact angle (a) and droplet height (b) were monitored versus time for each substrate.

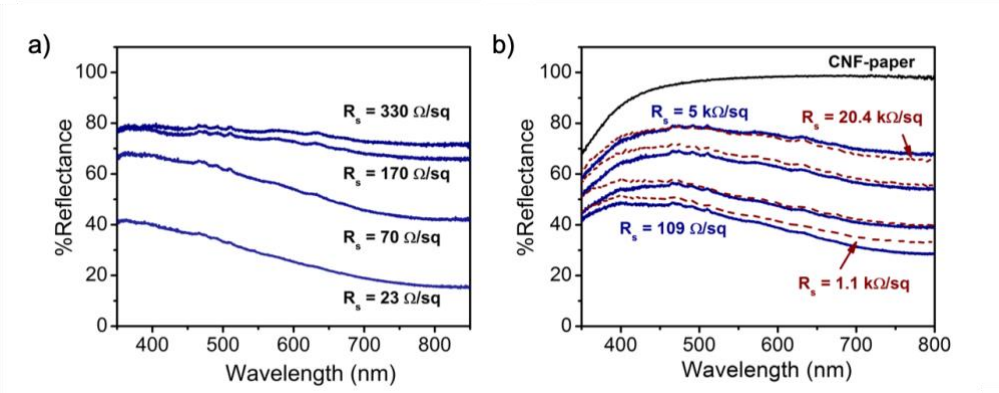

Figure S4-3. Percent reflectance for PEDOT:PSS films printed on glass slides (a) and paper substrates (b) at various thicknesses. Blue labels refer to the sheet resistance for CNF coated paper (blue, solid lines) whereas red labels refer to the sheet resistance for films printed on office paper (red/brown dashed line).

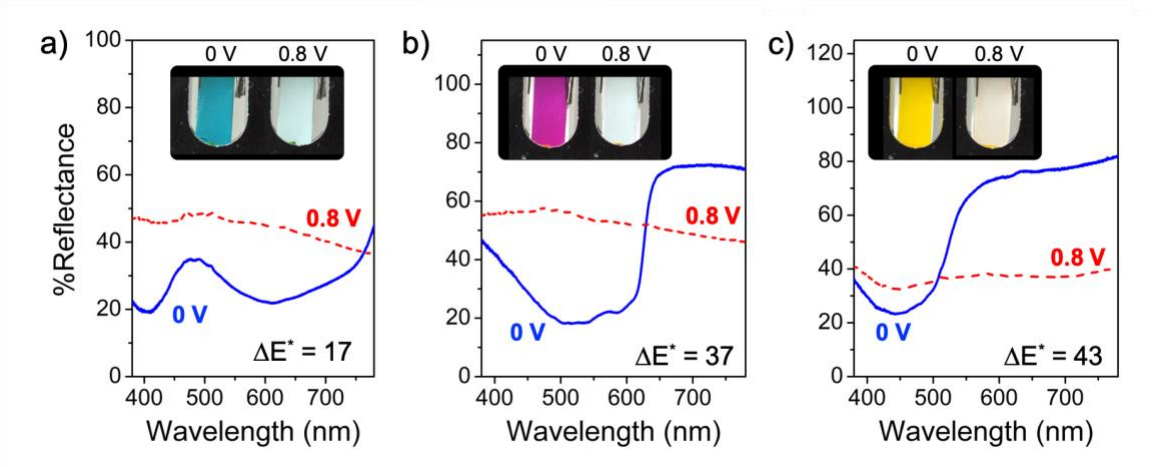

Figure S4-4. Reflectance spectra in the neutral (0 V) and oxidized (0.8 V) states for ECP-Cyan (a), ECP-Magenta (b), and ECP-Yellow (c) films on ITO/glass/PTFE electrodes in a three-electrode cell with a Ag/Ag^+ reference electrode and a Pt flag counter electrode immersed in 0.5 M $TBAPF_6$/PC. Photographs of the ECP coated ITO/glass/PTFE electrodes taken using a D50 lamp positioned above the film to provide diffuse reflectance to the camera.

Table S4-1. CIELAB color coordinates calculated from the reflectance spectra of ECP-Cyan films on PEDOT:PSS/paper and ITO/glass/PTFE.

	Colored (0 V)			Colorless (0.8 V)		
	*L**	*a**	*b**	*L**	*a**	*b**
PEDOT:PSS/Paper	45.9	28.1	-10.7	69.6	2.4	2.4
ITO/glass/PTFE	55.9	27.8	-6.0	78.2	-1.6	-3.0

Table S4-2. CIELAB color coordinates calculated from the reflectance spectra of ECP-Magenta films on PEDOT:PSS/paper and ITO/glass/PTFE.

	Colored (0 V)			Colorless (0.8 V)		
	*L**	*a**	*b**	*L**	*a**	*b**
PEDOT:PSS/Paper	53.7	-14.4	-9.7	65.9	-4.7	-4.0
ITO/glass/PTFE	58.2	-8.0	-5.9	73.6	-2.3	-1.0

Table S4-3. CIELAB color coordinates calculated from the reflectance spectra of ECP-Yellow films on PEDOT:PSS/paper and ITO/glass/PTFE.

	Colored (0 V)			Colorless (0.8 V)		
	*L**	*a**	*b**	*L**	*a**	*b**
PEDOT:PSS/Paper	75.5	3.4	49	64.1	-1.6	8.1
ITO/glass/PTFE	83.2	6.9	43.6	67.4	-0.4	4.8

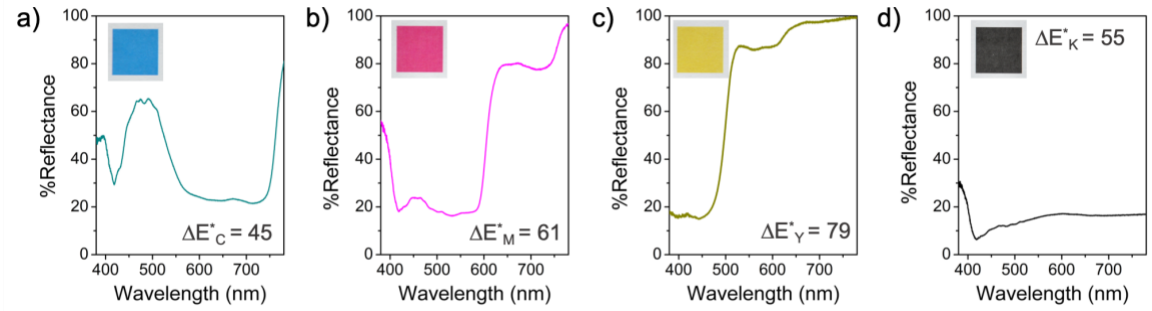

Figure S4-5. Reflectance spectra of standard Cyan (a), Magenta (b), Yellow (c), and Black (d) printer ink using office paper as a white reflectance standard. ΔE^* values calculated versus white paper (L^*: 100, a^*: 0, b^*: 0) as a reference value for ECP color contrasts.

Table S4-4. Comparison of CIE $L^*a^*b^*$ color coordinates for paper-based ECDs reported here and elsewhere in the literature.

Active Material	*Applied Voltage (V)*	*L**	*a**	*b**	*Reference*
ECP-Magenta	+0.8 V	65.1	-0.5	2.9	This Work
	-0.8 V	37.1	44.4	-17.1	
ECP-Black	+0.8 V	60.9	-6.9	-4.9	This Work
	-0.8 V	32.6	1.0	-7.7	
ProDOT-Hx2 /PEDOT:PSS	+1.5V	60	-5	10	(4)
	-1.5 V	29	16	-32	
PEDOT:PSS	1 V	58.16	-4.05	-7.55	(5)
	-1 V	28.83	-0.22	-26.68	

Table S4-5. CIELAB color coordinates for lateral devices constructed on ITO/glass electrodes for the colorless (0.8 V) and the clear (-0.8 V) states.

Active Material	*Applied Voltage (V)*	*L**	*a**	*b**	*ΔE**
ECP-Magenta (ITO/glass)	+0.8 V	66	0.8	5.5	66
	-0.8 V	37.4	54.5	-20.6	
ECP-Black (ITO/glass)	+0.8 V	60.4	-8.4	-3.8	30
	-0.8 V	32.7	1.3	-10	

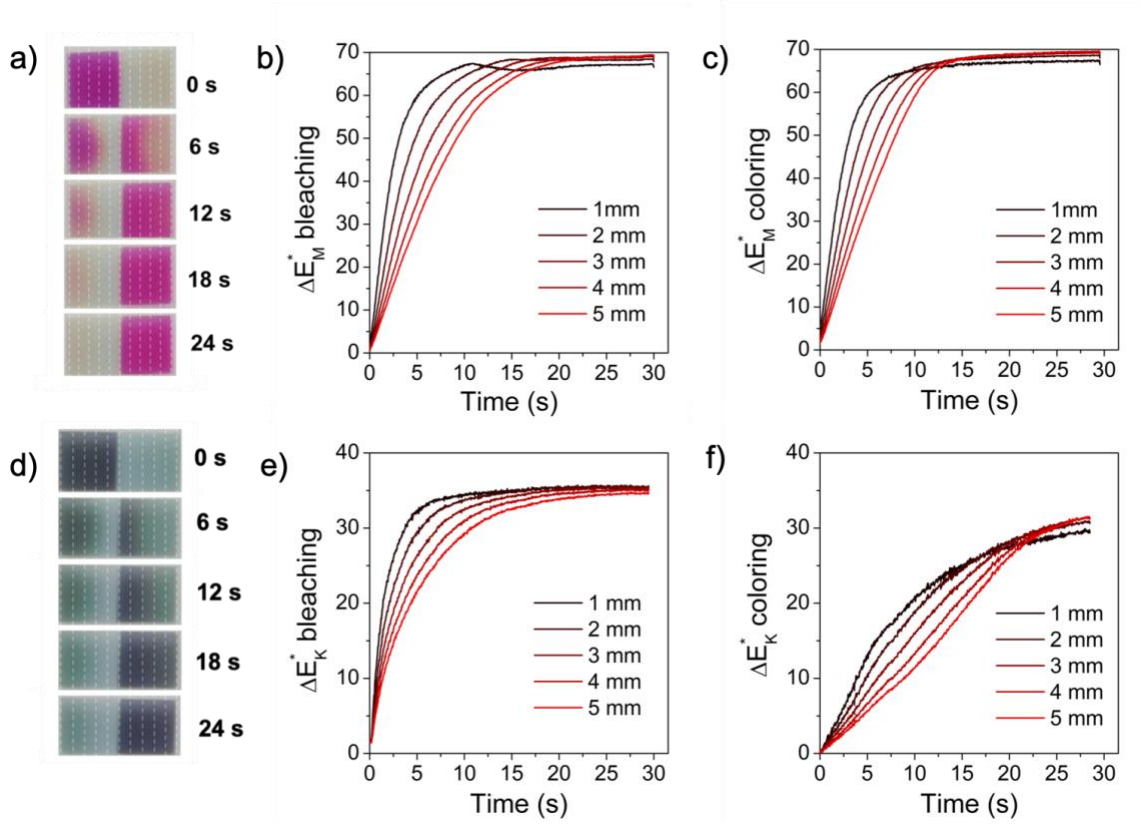

Figure S4-6. Switching kinetics of lateral ITO/glass ECDs. (a) Photographs of a magenta-to-colorless lateral ECD at six-second time intervals after the application of +0.8 V to the left pixel. Color contrast upon bleaching (b) and coloring (c) as a function of time for 5 pixel sections of growing thickness from the center (1-5 mm). (d) Photographs of a black-to-colorless lateral ECD at six-second time intervals. Color contrast upon bleaching (e) and coloring (f) of the device for 5-pixel sections of growing thickness from the center (1-5 mm).

CHAPTER 5. RENEWABLE BARRIER FILMS FOR ENHANCED PHOTOSTABILITY OF ELECTROCHROMIC DEVICES

5.1.1 Background and Motivation

Each year, roughly 150 million tons of flexible plastic packaging are produced for a range of consumer goods from food to pharmaceuticals to electronics.[240] The vast majority of these plastic packages are composed of polyethylene, polypropylene, and poly(ethylene terephthalate), each derived from petroleum. These materials offer many benefits in terms of their cost, processability, and gas-barrier properties, yet remain persistent in the environment, posing a major environmental challenge. While recycling offers and ideal solution to this challenge, the rise of single-use packaging and commoditized cost of these materials has rendered recycling efforts largely a failure as it's estimated that only 9% of petroleum-based plastics have ever been recycled.[240] In recent studies, it's become clear that the plastic pollution problem is one of utmost importance for continued research into new chemistry, materials science and chemical engineering to mitigate waste and plastic permanence.[241–243] To address this challenge, we must find renewable material substitutes that provide equivalent strength, durability, and gas barrier properties with much lower environmental impact over the course of their life cycle. Furthermore, these new materials must be highly scalable and cost-competitive the commoditized petroleum products.

To fulfill these sustainability criteria, materials derived from biomass become an obvious choice, especially those abundant in natural supply that can be processed with

sustainable and energy-efficient processingsu.[244] Cellulose is the most abundant polymer on the planet, present in a multitude of organisms from plants to fungi to tunicates, and is already processed industrially at massive volumes (100s of Mt).[129] Cellulose nanocrystals and nanofibrils can be readily extracted from biomass and represent a promising alternative to petroleum-derived barrier plastics due to their high levels of crystallinity.[133,166,245]

Chitin has also generated recognition as a promising biomass-derived alternative to petroleum products for packaging.[166,246–250] Chitin offers the advantage of being widely available as a waste product from the crustacean industry (roughly 8 tones per year)[251,252] and is present in micro-organisms such as fungi.[253] Highly crystalline chitin nanofibers (ChNFs) can be extracted from crab, shrimp, or lobster shells via deproteination with base and demineralization with acid, generating dispersible nanoparticles after size reduction via high-pressure homogenization.[166,246] Due to the renewable origin, aqueous processability, and opposite surface charges of ChNFs (cationic) and CNCs (anionic), multilayer barrier films composed of these materials form dense gas barrier layers that offer a more sustainable alternative to conventionally used barrier plastics such as PET. Previous work showed that multilayer barrier films composed of alternating charged CNC and ChNF layers coated on poly(l-lactic acid) had OTR values near that of PET of similar thickness.[166]

Beyond the sustainability considerations for manufacturing new barrier films, the opportunity for reducing waste produced by package's contents (such as food) through active or interactive packaging approaches represents another strategy in the sustainability of food consumption with the goal of reducing food waste.[254] Active packaging efforts have focused on incorporating UV-absorbers and eluting antioxidants into packaging

materials in order to improve the shelf life of perishable goods.[255] Many of the approaches for active packaging have focused on developing materials from bio-based feedstocks to generate monomers or additives that improve the gas barrier or antimicrobial properties of the barrier films.[256,257] For instance, a bio-based ionic liquid, choline salicylate was found to exhibit antimicrobial properties in preserving apple slices.[255]

In terms of interactive packaging, commercially-available materials have also begun to incorporate color-changing elements that can indicate the level of volatile amines associated with microbial growth to notify the user of imminent spoilage.[258] Additionally, printed electronics capable have been developed in order to enable a smartphone user to determine the degree of degradation of a packages contents.[259] A major challenge for the practical use of electrochromic conjugated polymers is their relatively short photo-oxidative stability (~1 week) when exposed to both light and oxygen.[111,114,154] Previous work has shown that the use of high-performance, oxygen barriers can delay the progression of photo-oxidative damage in conjugated polymers.[111,154] However, these studies typically utilize multi-layer barriers composed of petroleum-based polymers and/or inorganic oxides. Furthermore, these devices were encapsulated under inert atmosphere. Currently, there is little understanding of electrochromic polymers' sensitivity to photo-oxidation when encapsulated with moderate oxygen barriers (oxygen transmission rates of 10-50 $cm^3\ m^{-2}\ day^{-1}$), more compatible with existing roll-to-roll manufacturing methods in ambient environments.

Photostability studies on poly(3-hexylthiophene) have been carried out rigorously and extensively, resulting in a reasonably complete picture of key features that dictate the polymer's stability. Singlet oxygen and water, often cited as a reactants leading to

photodegradation were found not to play a major role, though high humidity sped up photodegradation.[114] Structurally, the allylic carbon of the hexyl side chain forms resonance-stabilized radicals that lead to loss of optical density.[112,260] Oxygen diffusion into crystallites is poor, thus leading to improved stabilities of more crystalline systems and regioregular systems.[261] While these lessons are instructive when considering electrochromic polymers, it is unknown how generalizable they are to electrochromic polymers based on P(ProDOT) derivatives.

In this chapter, lateral electrochromic devices encapsulated under ambient conditions were studied using with three barrier films offering a range of oxygen transmission rates (7 – 30 cm^2 m^{-2} day^{-1}). Multilayer barrier films derived from biomass (cellulose and chitin), processed in mild acetic acid (pH = 3) were compared to single-layer poly(ethylene terephthalate) (PET) and multilayer Al_2O_3/PET, a commercially available flexible transparent barrier manufactured by 3M (FTB). These devices were then irradiated under a xenon light source mimicked daylight (AM 1.5) and monitored as they photodegraded. The results from irradiation studies demonstrated that the incorporation of a moderate oxygen barrier results in a 10x improvement in contrast retention over the unencapsulated devices. The lateral device geometry used here allowed for the measurement of the poly(3,4-propylenedioxythiophene-(ethyl hexyloxy)$_2$) (PProDOT) active material in both its oxidized (colorless) and neutral (colored) form. Distinct rates of degradation were able to be discerned with the oxidized polymer degrading more quickly than the neutral ECP. The buildup of photo-oxidized species was observed by XPS, where differences in carbonyl formation and loss of sulfur in the PProDOT were found to correlate with the loss in optical density. This result, combined with the slowing of

switching kinetics, loss of solubility, and trapped charge carrier absorbance in the near infrared region, suggests both electrolyte reactivity and crosslinking as a major driver for loss of electrochromic performance as has been observed by photo-degradation studies in other conjugated polymers.[262]

5.1.2 Properties of barrier films: bioderived versus petroleum-based barriers

Bioderived multilayer barrier films were prepared by spray-coating the particle suspensions onto cellulose acetate substrates and were first evaluated in terms of the optical, mechanical, and barrier properties in order to make a comparison to PET and FTB films. Table 5-1 summarizes the physical properties of each barrier film subsequently used for encapsulation. While each materials' transmissivity differs, the barrier sample transmittance integrated over the visible spectrum (380-780 nm) matches for all three barrier films, thus providing similar light transmission into the device as shown in Figure 5-1. The main differences in transmittance between barrier samples are the short wavelength absorbance of the CA-ChNF/CNC and its higher haze compared to the PET, and FTB samples. As the FTB barrier is composed of PET and Al_2O_3, the transmittance oscillates in the visible region due to the refractive index differences between the layers.

Table 5-1. Summary of properties of barrier films studied for encapsulating ECDs.

	3M FTB	PET	CA-ChNF/CNC
Thickness (μm)	49 ± 3	103 ± 3	80 ± 1
Transmittance (*%, 380-780 nm*)	91.7 ± 0.2	88 ± 2	90 ± 2
Haze (*%, 380-780 nm*)	0.48 ± 0.08	1.3 ± 0.1	3.8 ± 0.8
Ultimate Tensile Strength (*MPa*)	82 ± 6	59 ± 2	27.7 ± 0.3
Breaking Strain (*%*)	62 ± 6	95 ± 7	35 ± 7
Oxygen Transmission Rate ($cm^3\ m^{-2}\ day^{-1}$)	< 1	8.5 ± 0.3	29.2 ± 0.3

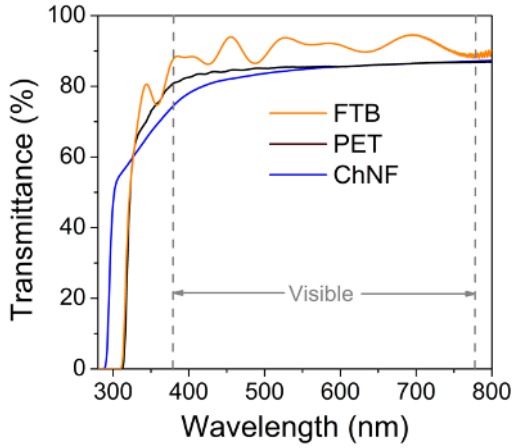

Figure 5-1. Transmittance spectra of the barrier film samples used for encapsulating lateral ECDs with the visible spectrum, 380-780 nm, marked.

Both the FTB and PET barrier begin to absorb strongly at 320 nm where the transmittance drops to < 0.01% due to the terephthalate core of the polymer. The CA-ChNF/CNC material drops in transmission beginning at 450 nm but remains greater than 50% transmissive until it begins to absorb strongly at 290 nm most likely from the carbonyl groups. Barrier films irradiated for 240 hours with the xenon lamp (AM 1.5 G, 100 mW cm^{-2}) were also characterized for their transmittance and haze which showed slight changes relative to the unirradiated samples, but no yellowing was observed as would be expected for major UV-induced degradation in the polymer films (Figure S5-2).

The mechanical properties of the film assessed by puncture testing (HT-Mech, developed in the Meredith group) demonstrate that the CA-ChNF/CNC is a weaker, more brittle material compared to the PET and FTB as both the ultimate tensile strength and yield strain are 2-3x lower. The oxygen transmission rate measured at 50% RH shows that the PET and CA-ChNF/CNC barriers offer similar oxygen permeabilities (~10 cm^3 m^{-2} day^{-1}) while FTB barrier which had an undetectable oxygen transmission rate (<1 cm^3 m^{-2} day^{-1}).

5.1.3 Contrast retention of encapsulated lateral ECDs

Next, these barrier films were utilized to encapsulate lateral electrochromic devices composed of blade-coated PEDOT:PSS electrodes, spray-cast P(ProDOT) and a drop-cast iongel electrolyte as shown in Figure 5-2a. Each electrode of the lateral device was 5 x 5 mm, defined by the removal of excess spray-cast P(ProDOT) with toluene. ADCO Helioseal edge sealant was applied around the perimeter of the barrier film to define the exposed area of the device of roughly 10 x 15 mm. Therefore, oxygen transmission from the barrier films was expected to be < 0.6 x 10^{-4} cm^3 day^{-1} for the FTB-encapsulated devises, 5 x 10^{-4} cm^3 day^{-1} for PET devices, and 14 x 10^{-4} cm^3 day^{-1} for CA-ChNF/CNC-encapsulated devices initially assuming a perfect edge seal by the ADCO barrier. This rate increased by 50% after 10 days of irradiation as highlighted by the OTR and OP values recorded in Table S5-3.

Note to the reader that silicone and epoxy edge sealants were also explored for encapsulating these devices but were found to be ineffective for limiting oxygen transmission. The curing of the epoxy also bleached the encapsulated ECP film, but this oxidation was reversible.

Prior to irradiation, spectra were taken of each device electrode in both the -1.0 V state (Figure 5-2b) and the +1.0 V state (Figure 5-2c). Optical changes in both pixels were then measured as a function of irradiation time in 24-hour increments under AM 1.5G light by returning the devices to each of these charged states.

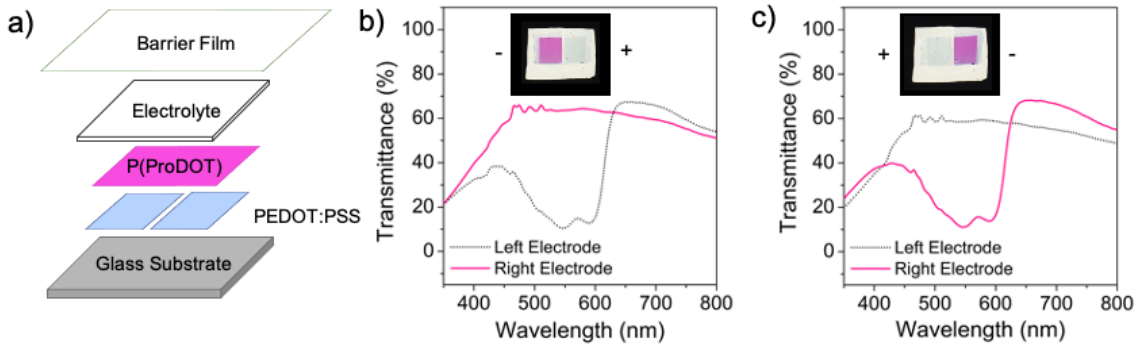

Figure 5-2 (a) Schematic showing lateral device construction with each layer deposited sequentially and a pre-formed barrier film used for encapsulation. (b) Spectra and photograph (inset) of an example lateral device in the -1 V charged state (left electrode neutral, right electrode oxidized). (c) Spectra and photograph (inset) of an example lateral device in the +1 V charged state (left electrode oxidized, right electrode neutral).

After encapsulation, the lateral ECDs were exposed to 1 sun of irradiation in 24-hour increments for a total of 240 hours. Under these accelerated aging conditions, the degradation of the ECDs was examined in terms of change in optical contrast and in the switching times. At each time interval, spectra, photographs, and videos were recorded. Photographs of a representative device encapsulated by each barrier film are shown in Figure 5-3 for both the -1.0 V state (Figure 5-3a-c) and the +1.0 V state (Figure 5-3d-f). For convention, the device electrode that is bleached in the +1.0 V state (set to this state prior to irradiation) is hereby referred to as the "left" electrode. The device electrode that is colored in the +1.0 V state is referred to as the "right" electrode based on the orientation of all photographs and videos recorded. Upon photoirradiation, both the left and right electrodes lost optical density over time (Figure 5-3), yet they differed in terms of the magnitude of the loss of absorbance along with the evolution of transmittance in the 600 – 800 nm portion of the spectrum (Figure S5-5). From Figure 5-3, it is evident that the left electrode (irradiated in its bleached state) photobleached to a greater extent and changed in

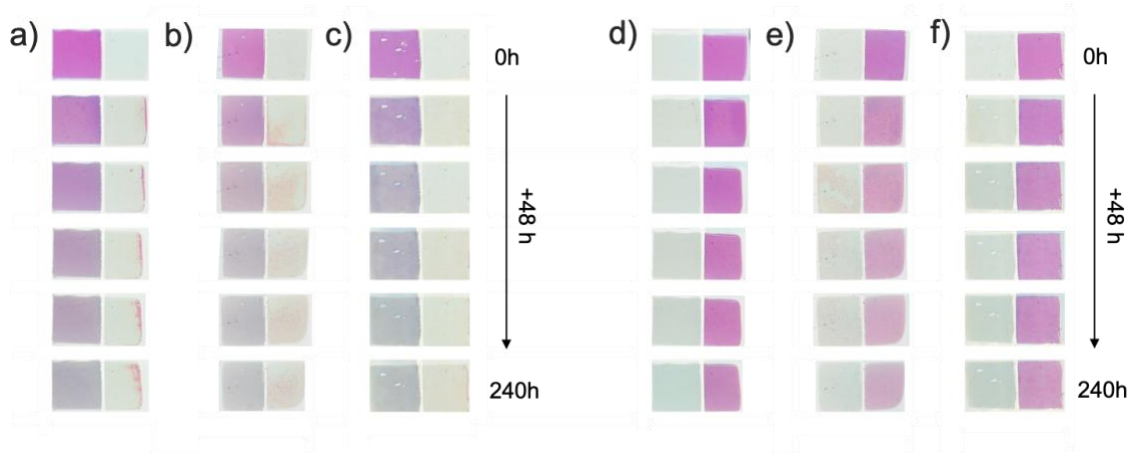

Figure 5-3. Photographs of lateral devices shown in each state (left electrode neutral and oxidized) encapsulated by PET (a, d), CA-ChNF/CNC (b,e), and 3M FTB (c,f). Each column shows the evolution of the device in 48-hour irradiation intervals from 0 to 240 hours.

color to a more purple/gray hue in as little as 96 hours of exposure. Spectrally, the transmittance of the left electrode broadened to a uniform, featureless trace compared to the right electrode where there was little change in the transmittance from 600-800 nm (Figure S5-5). Both electrodes also lost transmittance in their oxidized states at all visible wavelengths, causing the bleached state to appear darker seen in Figure 5-3d-f and Figure S5-6, and contributing to the loss of electrochromic contrast of the devices.

The right electrode maintained a higher optical density, despite what appears to be degradation around the edges from oxygen permeation at the ADCO/barrier film interface. There is a slight blue shift in the absorbance peak for the P(ProDOT) in its neutral state for the right electrode for devices encapsulated by each of the barrier films (FTB: 5 nm, PET: 6 nm, and CA-ChNF/CNC: 5 nm). The contrast of the right electrode was similarly impacted by a loss in optical density of the neutral state (Figure S5-5d-f) as well as a lower transmittance in the oxidized state due to incomplete bleaching of the right electrode as can be seen in the photographs in Figure 2 as well as the spectra in Figure S5-6d-f.

The evolution of contrast was determined from the spectra of each electrode in its colored and bleached states at 24 h increments up to the full 240 h irradiation. The contrast was expressed both in terms of the change in transmittance at 550 nm (Figure S5-7) as well as the colorimetric contrast (ΔE^*), or the Euclidean distance between $L^*a^*b^*$ color coordinates in each state (Equation 3.1 below).

$$\Delta E^*_{12} = \sqrt{(L^*_2 - L^*_1)^2 + (a^*_2 - a^*_1)^2 + (b^*_2 - b^*_1)^2} \tag{3.1}$$

The evolution of this colorimetric contrast over time is shown in Figure 5-4 where the left electrode (a) and right electrode (b) are compared for each device type. As all of these devices were fabricated under identical conditions, in ambient atmosphere, this result highlights the importance of limiting the oxygen diffusion to the ECP for preserving its function. The change in contrast over time shown in Figure 5-4a and Figure 5-4b illustrates that the left electrode degrades much more quickly than the right electrode.

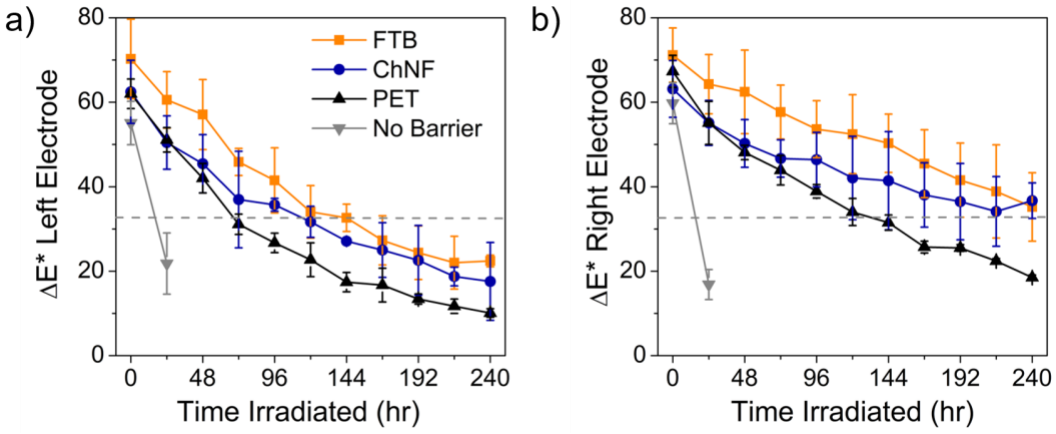

Figure 5-4. Evolution of the color change (ΔE^*) of encapsulated lateral ECDs showing the decay in contrast of the left electrode (a) and right electrode (b).

Taking the point where each curve passes the dotted line (50% contrast loss) gives the device lifetime for each barrier film. These lifetimes are 95, 160, and 170 hours for the left electrode of the PET, PABP (ChNF-typical), and FTB barrier films respectively, while the right electrode exhibits lifetimes of 140, 200, and 240 hours. Each of these lifetimes represents a dramatic improvement over the unencapsulated devices which lose 50% of their contrast in 16 hours.

For further insight into the mechanism driving the loss of contrast, UV-Vis spectroscopy was also performed on disassembled and rinsed devices that had undergone the 240 hours of irradiation as shown in Figure S5-8. Spectra of the degraded devices after 240 hours shows a substantial long-wavelength absorbance peak for the left electrode at 820-860 nm which gave the electrode its greyish-hue. This broad absorbance grew in intensity for the left electrode of each encapsulated device (Figure S5-5a-c), suggesting that the irradiation in the oxidized state trapped a portion of the P(ProDOT) in a charged state. After just 48 hours of irradiation, the neutral state could not be fully be recovered when the device was then driven at -1.0 V. Notably, there is no major absorbance seen at wavelengths greater than 1600 nm as shown for the pristine device (Figure S5-8a). Both these near-infrared peaks and the peak related to the neutral state absorption of this partially oxidized P(ProDOT) film show a blue-shift compared to the pristine device (80-100 nm for the near-IR peak and 20 nm for the neutral peak). Blue-shifting absorbance peaks are characteristic of a decrease in effective conjugation length in the material and have been shown for irradiation studies of conjugated polymers in solution with substantial chain fragmentation assessed by high-resolution matrix-assisted laser desorption/ionization (MALDI) experiments.[263] The right-electrode absorbance shows a similar trend in terms of

the blue shift of the neutral state absorption (10 – 20 nm) and also shows a peak in the near-infrared at longer wavelengths (860-960 nm), likely due to a partially de-doped underlying PEDOT:PSS electrode. This near-infrared peak also shows a blue shift in comparison to the pristine device, again highlighting a decrease in conjugation length for the P(ProDOT) resulting from the irradiation experiment. In addition to the shifts of the absorbance peaks, the P(ProDOT) from irradiated devices was rendered insoluble in toluene as shown in Figure 9 where the pristine sample dissolved immediately, and the irradiated samples were not changed after a 10-minute soak.

5.1.4 Kinetics evolution of encapsulated lateral ECDs

In addition to the decrease in contrast, the switching speed of the devices was also impacted by irradiation. For each device, four switching times were recorded at 48h irradiation intervals: bleaching and coloring of both the left and right electrodes (Lb, Lc, Rb, Rc) respectively. Figure 5-5 shows the evolution of these switching times during the irradiation for a representative device encapsulated by each barrier film. The uniformity of

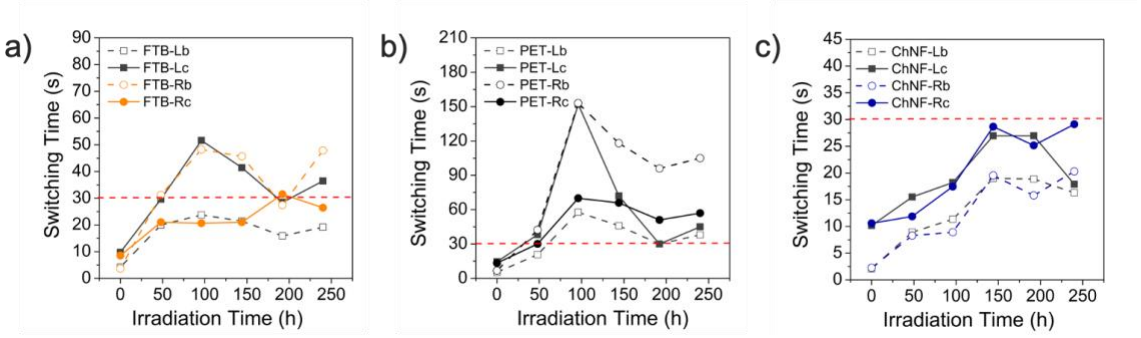

Figure 5-5. Evolution of the switching times of lateral devices for both the bleaching and coloring of each electrode of devices encapsulated by PET (a), CA-ChNF/CNC (b), and FTB (c) barrier films. The red dotted line at 30 seconds is included as a guide to the eye.

the switch is also highlighted by the video snapshots for each representative device switching from both the +1.0V to the -1.0 V states (Figure S5-9-Figure S5-14).

The FTB-encapsulated device (Figure 5-5a) and the PET-encapsulated device (Figure 5-5b) both show an increase in switching time that peaks between 96 and 144 h of irradiation, followed by a decrease in the switching time to 240 h. This response is likely a result of the decreasing total contrast of the device where a smaller total ΔE^* was achieved with each switch. Notably for the FTB- and PET- encapsulated devices, the bleaching of the right electrode (and coloring of the left electrode) were evolved in the same fashion over the course of the irradiation time corresponding to driving the device to its -1.0 V state, or opposite state from the +1.0 V irradiation state. The + 1.0 V switching times show a more monotonic increase from the initial 7-10 second switch to 20-40 sec after 240 hours of irradiation giving further evidence of a difference in degradation mechanism between the left and right electrodes.

The evolution of the switching times in the CA-ChNF/CNC-encapsulated devices is distinct from the PET-based barrier films. For this device, the switching times increase slightly from 7 to 30 seconds over the course of the irradiation experiment. The coloration remains consistently slower than the bleaching until the 240-hour point. There is not an asymmetric evolution in switching times corresponding to applying -1.0V or +1.0V as was seen for the FTB and PET barrier films. The overall slowing of the switching speeds suggest that the electrolyte may be photodegrading, but the differences observed in the individual electrodes further point to differences in degradation between the right and left electrodes of these devices.

The progression of the color change across the left and right electrodes also differed over the course of the irradiation. Figure S5-9-Figure S5-14 show snapshots of the switch upon application of both +1.0 V and -1.0 V for devices encapsulated by each barrier film. Initially, there is a moving front for both coloration and bleaching for both the right and left electrodes. As the devices degrade, the left electrode loses this moving front character and exhibits a slow fading in and out across the entire electrode. This switching performance has been observed previously for lateral electrochromic devices where the electrode resistance became limiting for the switching speed rather than ionic conductivity of the electrolyte.[264] For the FTB- and CA-ChNF/CNC-encapsulated devices, the moving front character of the switch was maintained even at 240 hours of irradiation. The PET-encapsulated device showed much slower switching combined with an incomplete bleaching of the electrode thus obscuring any visible moving-front.

Taking into account the spectral changes, differences in switching speed, and the insolubility of the ECP active layers in toluene after the irradiation experiment suggests that the left-electrode P(ProDOT) films are being at least partially locked into a charged state where ionic mobility in the film is not dramatically hindered. Distinctly, the right electrodes are likely becoming crosslinked in their neutral state making bleaching difficult by hindering ionic mobility. Overall, the PET-encapsulated devices exhibited the largest degradation in both the contrast and switching speed whereas the FTB- and CA-ChNF/CNC-encapsulated devices showed comparable performance over the irradiation experiment.

5.1.5 Chemical analysis of P(ProDOT) active layer

In order to understand these differences in performance for the barrier films, the buildup of oxidized species was assessed by X-ray photoelectron spectroscopy. This experiment was performed to assess differences in the XPS peak ratios give insight into the chemical products formed during the course of the 240-hour irradiation. Two elemental peak fractions from XPS are shown in Figure 5-6: carbonyl / carbon, and SO_x (sulfone + sulfoxide)/ sulfur. The buildup of carbonyl species is often associated with photochemical breakdown of the alkyl side chains, whereas sulfone and sulfoxide species arise from photo-oxidation of the thiophene sulfur. The buildup of carbonyl functional groups follows the trend in loss of optical density with the PET-encapsulated device showing the highest fraction, followed by the CA-ChNF/CNC-, then FTB-encapsulated devices. Interestingly, sulfone and sulfoxide buildup, a major photo-oxidative product seen in both poly(3-hexylthiophene),[113] PEDOT,[265] and P(ProDOT),[111] in previous studies, does not trend with loss of electrochromic performance and differs between the left electrode and the right.

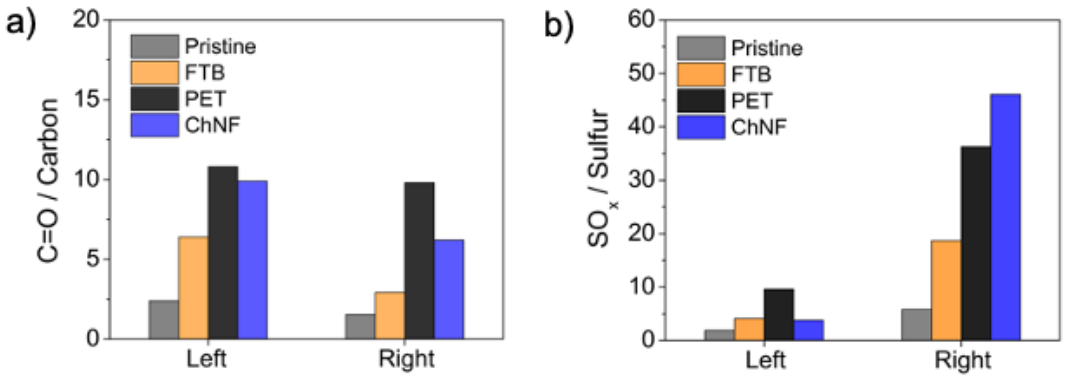

Figure 5-6. (a) Carbonyl / carbon atomic ratio for the P(ProDOT) active layer of a pristine device, and a device encapsulated by each barrier after 240 h of irradiation. (b) Sulfone + sulfoxide (SO_x) / sulfur ratio for the devices shown in part a.

There are several plausible degradation pathways of the ECP in these devices with the possibility of several happening simultaneously. While oxygen is often considered a major reactant for photochemical breakdown, there are additional proposed mechanisms that occur under an inert atmosphere.[112,114,266–269] Based on these XPS data, decomposition of the organic electrolyte is a potential driver of photochemical bleaching, especially for the left electrode of the device where minimal evidence of photo-oxidation is present. The right electrode shows typical photo-oxidation products (sulfone/sulfoxide) in higher quantities, suggesting that oxygen could be a key driver of degradation for this portion of the active layer.

For the pristine device, the N(1s) signal was deconvoluted in order to determine the excess of anions in the left electrode (oxidized). However, in the irradiated devices, analysis of the N(1s) and F(1s) signals showed relative abundance of each to be far different from what is expected given the [EMI][TFSI] chemical formula (Figure S5-15 - Figure S5-18) thus indicating degradation of the organic electrolyte occurred as a result of the irradiation experiment.

5.1.6 Discussion

Through these photo-degradation experiments, it is clear that by limiting oxygen flux to the active layer even for devices processed in ambient conditions, the photostability can be successfully improved by one order of magnitude. However, the oxygen transmission rate of the barrier film was not found to be the determining factor governing photo-degradation, thus suggesting both a lower sensitivity to oxygen than previously assumed, as well as the influence competing photochemical degradation mechanisms.

Furthermore, the samples containing the most chemical oxidation by XPS were not the most optically degraded thus suggesting that light-induced reactions with atmospheric oxygen were not the dominant driver of performance loss.

Rather than the barrier film performance determining the degradation rate, the more dramatic difference was seen between individual device electrodes. The lateral device geometry employed in this study demonstrated that despite absorbing less visible light, P(ProDOT) in its oxidized state degrades more quickly than the neutral form, in contrast to some previous studies on PEDOT.[270] It is hypothesized that the charged state of the device with a large quantity of counterions incorporated is more reactive to crosslinking and/or chain scission. The differences in switching speed, and the insolubility of the ECP active layers in toluene after the irradiation experiment suggests that the left-electrode P(ProDOT) films are being at least partially locked into a charged state where ionic mobility in the film is not dramatically hindered. Distinctly, the right electrodes are likely becoming crosslinked in their neutral state making bleaching difficult and hindering ionic mobility.

Overall, photostability is a complex process passing through many possible mechanisms likely dependent upon oxygen, the chromophore, and the irradiation conditions (temperature, wavelength, etc.). Questions remain regarding the oxygen sensitivity of ECPs, where quantitative analysis of experiments with known oxygen concentrations would aid the future design of ECDs where a threshold of barrier film performance could be established. While this study examined only one electrolyte with some evidence of the organic ions sensitizing photodegradation, alternative compositions

could dramatically influence degradation rates, thus a better understanding of the interplay between electrolyte and ECP are needed.

5.1.7 Conclusions and Future Work

This work set out to determine the influence of bioderived barrier films on the photodegradative stability of electrochromic devices in comparison to petroleum-derived alternatives. These degradation results show not only that bioderived barrier films are a promising technology for ECDs (and thus a variety of printed organic electronics) but also that designing future conjugated polymers for optoelectronics to avoid side-chain crosslinking would render them both more photostable (and useful in devices) as well as more easily degradable at the end of their lifetime.

When considering the environmental impact of electrochromic devices, processing these materials from aqueous solvents and the incorporation of cellulose substrates has been previously proven effective through side-chain modification.[26,27,219,221,233] The ability to encapsulate electrochromic devices with barrier films under ambient conditions represents another step toward sustainable electrochromics for next-generation packaging. In the future, combining these barrier films with substrates and electrolytes derived from biomass would increase the mass fraction of bio-derived materials in ECDs above 0.99. Furthermore, designing future devices with a more complete perspective on the materials life cycle – taking into account energy inputs, green-house gas emissions, energy use during their lifetime, and finally their disposal is a necessary next step toward sustainable expansion of this technology for a broad variety of smart packaging and environmental monitoring applications, particularly in indoor settings.

5.1.8 Supporting Information

5.1.8.1 ChNF Extraction, Purification, and Size Characterization.

ChNF particles were extracted from crab shells (Neptune's Harvest, USA). A mass of 50 grams of crab shells was first deproteinated with 1500 mL of 5 wt% sodium hydroxide solution, refluxing for 6 h. Then, they were demineralized with 1500 mL of 7 wt% hydrochloric acid solution, stirring for 6 h. The pre-purified chitin was then deacetylated with 25-mL/gram-pre-purified-chitin of 35 wt% sodium hydroxide solution, refluxing for 100 min. After each step, the solid was washed with tap water until the pH of the supernatant was 7, rinsed with DI water, and dried in oven at 60 °C overnight. The dried solid was ground into powder (<600 μm) with a DS77-R8 grinder (Mr. Coffee). The powder was dispersed in deionized water to prepare a 0.5 wt% chitin suspension, acidified to pH = 3 with acetic acid, and then homogenized into ChNF suspension. The homogenization process was carried out with a Mini DeBEE Homogenizer (BEE International, USA). It involved two sequences: 20 passes at 19000 psi with a 0.008" nozzle, and 10 more passes at 29800 psi with a 0.005" nozzle. The spray coater consists of a 1.52 mm spray nozzle (Central Pneumatic, GA) connected to a liquid reservoir containing a 0.5 wt % ChNF or 0.5 wt % CNC suspension. A nitrogen gas cylinder was connected to the spray coater to supply carrier gas at 35 psi.[166]

Suspensions were diluted to 0.001 wt% (in pH HOAc for ChNF and DI water for CNCs) then deposited onto clean silicon wafers for particle size measurements. Particle sizes were quantified using a Bruker Dimension Icon atomic force microscope in tapping

mode using cantilever tips with resonant frequencies between 150-180 kHz and a spring constant of 5 N m^{-1}.

Table S5-1. ChNF suspension properties

Properties of ChNF suspension	Concentration	0.5 wt%
	Degree of acetylation	94.9±2.6 %
	Size of fibers	180 ± 80 nm (length) 14 ± 3 nm (x-section)
	Viscosity	1000 cp @ 0.1 s^{-1}& 25 cp @ 1000s^{-1}
	Contact Angle Measurements (°)	40~60

Table S5-2. CNC suspension properties.

Properties of CNC suspension	Concentration	0.5 wt%
	Sulfate content	0.86 wt% *
	Size of crystal	90 ± 40 nm (length) 8 ± 2 nm (x-section)
	Viscosity	1000 cp @ 0.1 s^{-1}& 20 cp @ 1000s^{-1}

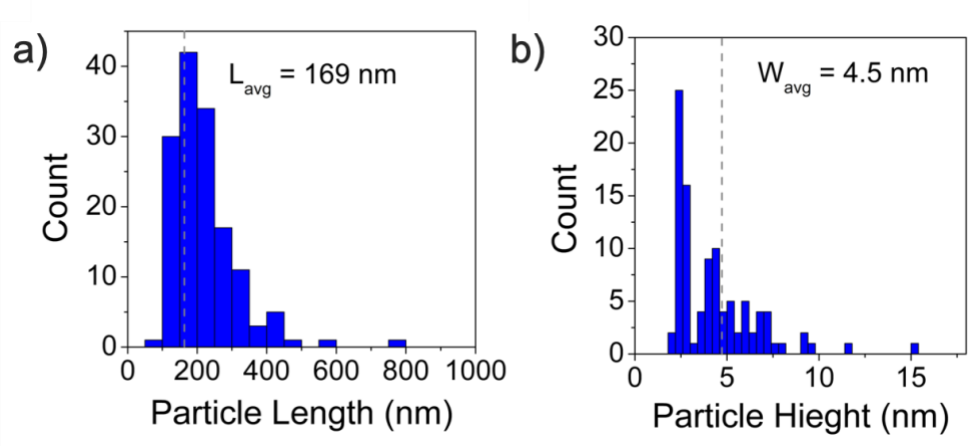

Figure S5-1. Particle size distributions from ChNF suspensions (a) and CNC suspensions (b).

5.1.8.2 Additional Barrier Film Data

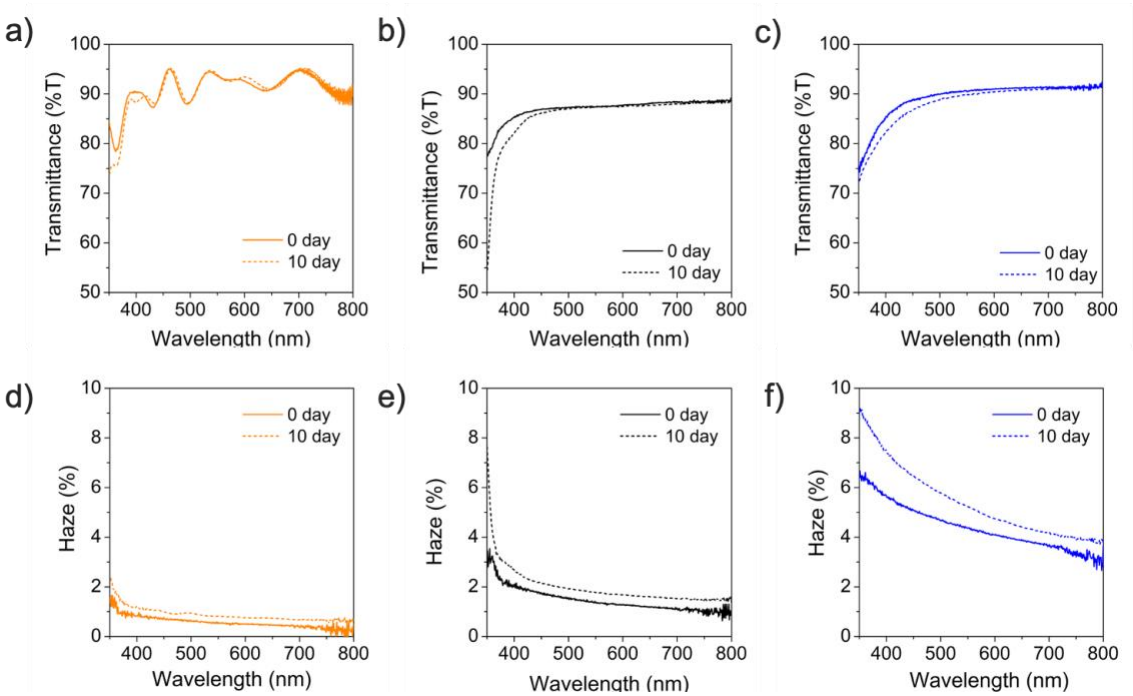

Figure S5-2. Transmittance of the FTB (a, d), PET (b,e) and CA-ChNF/CNC (c,f) over the visible spectrum for pristine films and after 10 days of irradiation.

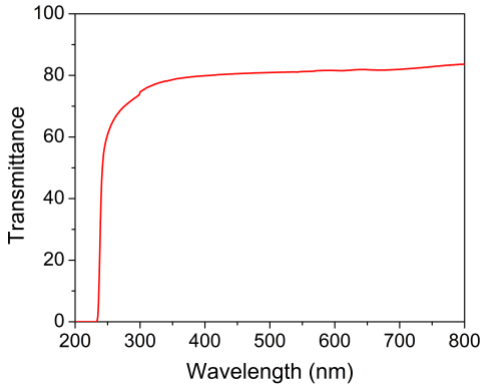

Figure S5-3. Transmittance of [EMI][TFSI] / P(VDF-HFP) iongel electrolyte.

Table S5-3. Barrier film properties after 10 days of irradiation under 1 sun (55˚C BST). Pressure of pure oxygen (101 kPa) used for permeability calculation.

	3M FTB	PET	CA-ChNF/CNC
Oxygen Transmission Rate ($cm^3\ m^{-2}\ day^{-1}$)	6.8 ± 0.08	10.6 ± 0.1	30.3 ± 0.5
Oxygen Permeability (cm^3-$\mu m\ m^{-2}\ day^{-1}\ kPa^{-1}$)	3.50 ± 0.04	10.5 ± 0.1	24.0 ± 0.4

5.1.8.3 Lateral Device Spectra

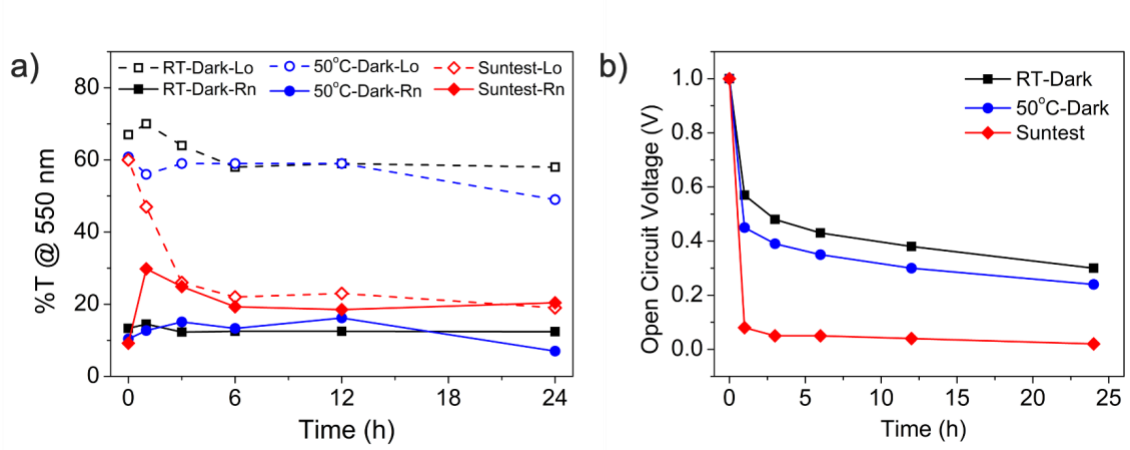

Figure S5-4. Lateral device bistability under three conditions: In the dark at room temperature (RT-Dark), in the dark at 50˚C (50˚C Dark), and in the Suntest chamber at 1 sun (BST 55˚C) for 24 hours after setting the device in the +1 V state. (a) Transmittance of the device left electrode beginning in its oxidized state (dotted line, Lo) and right electrode beginning in its neutral state (solid line, Rn). (b) Open-circuit voltage versus time over 24 hours.

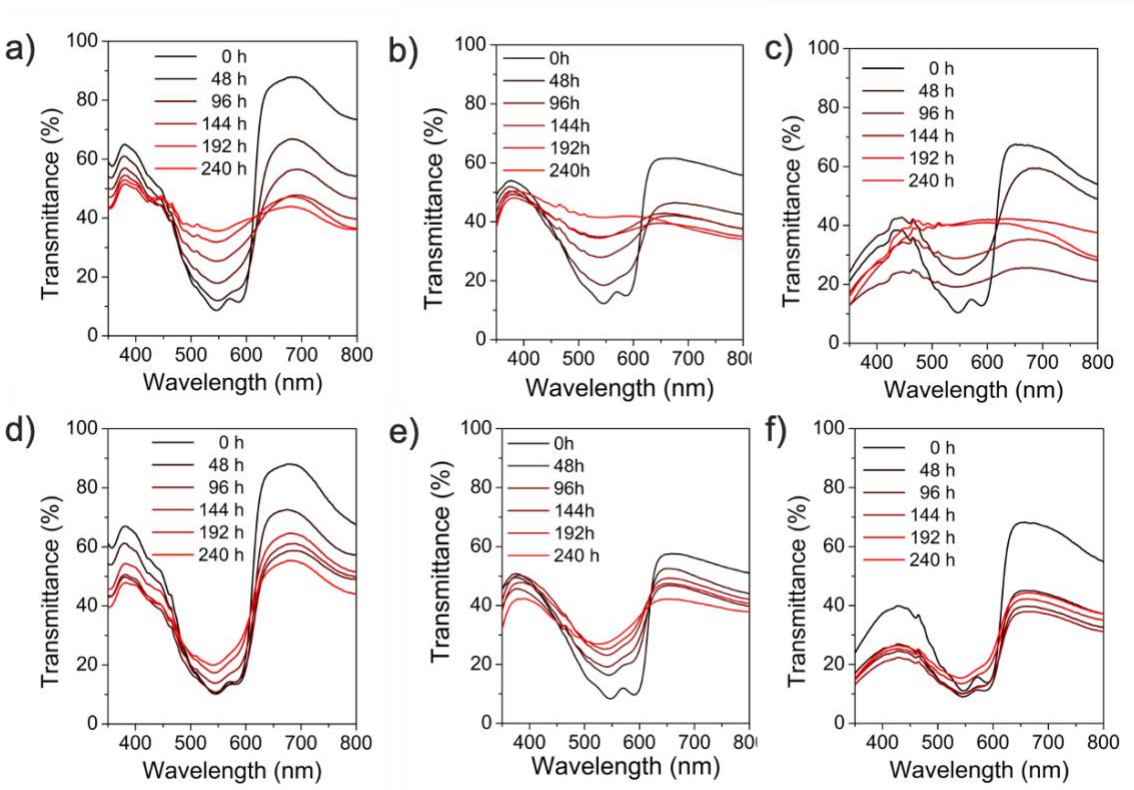

Figure S5-5. Evolution of the neutral (colored) spectra of lateral devices encapsulated by PET (left electrode (a), right electrode (d)), CA-ChNF/CNC (left electrode (b), right electrode (e)), and 3M FTB (left electrode (c), right electrode (f)) from 0 to 240 h of irradiation under 1 sun.

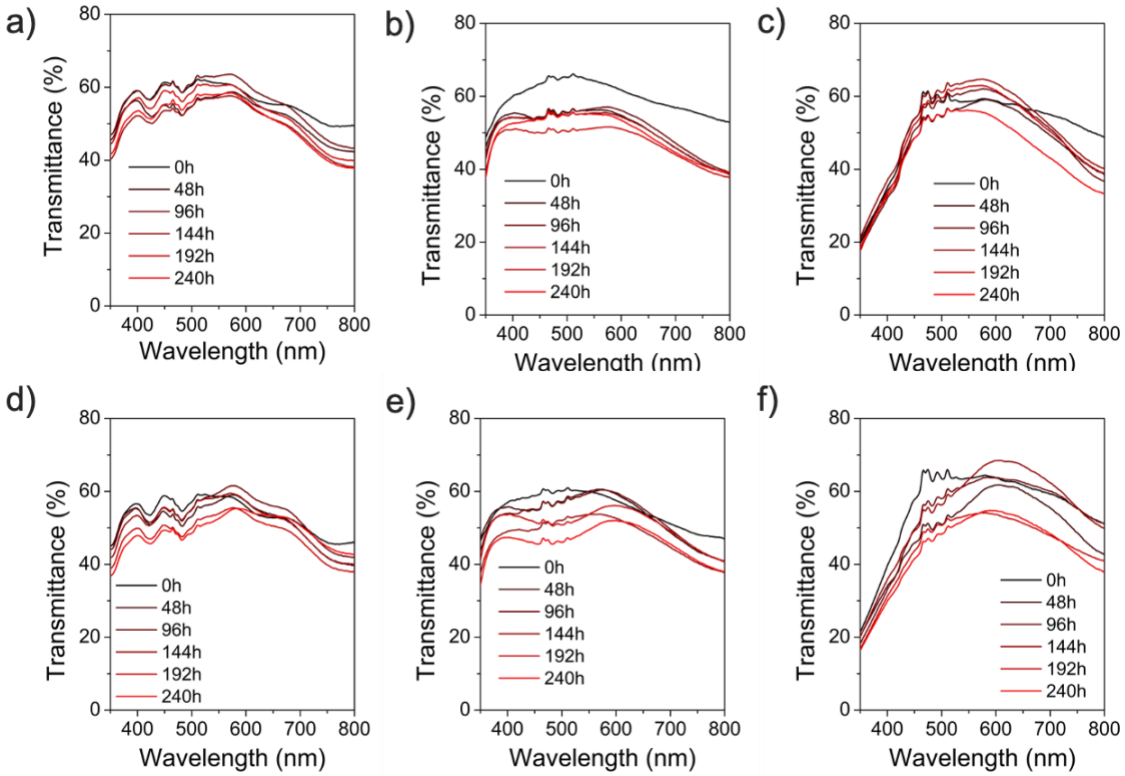

Figure S5-6. Evolution of the oxidized (colorless) spectra of lateral devices encapsulated by FTB (left electrode (a), right electrode (d)), PET (left electrode (b), right electrode (e)), and CA-ChNF/CNC (left electrode (c), right electrode (f)), from 0 to 240 h of irradiation under 1 sun

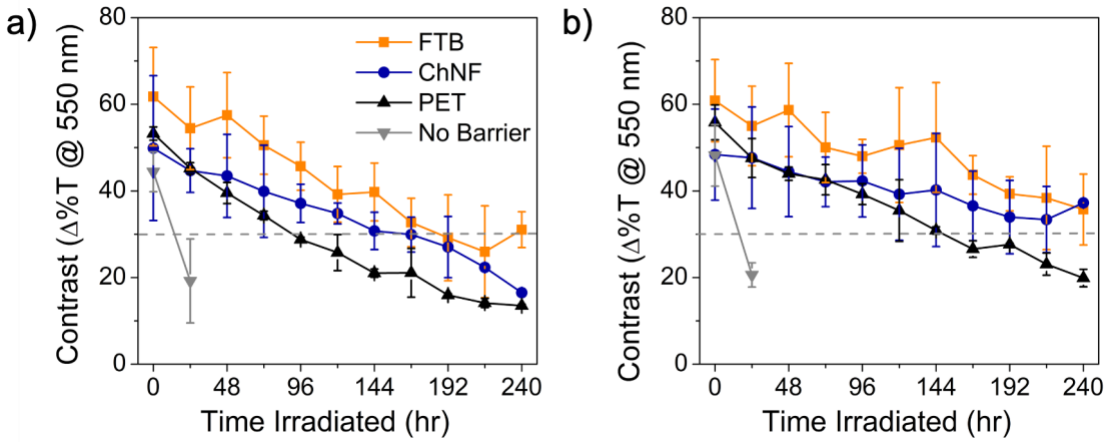

Figure S5-7. Evolution of the contrast ($\Delta\%T_{550}$) of encapsulated lateral ECDs showing the decay in contrast of the left electrode (a) and right electrode (b) for unencapsulated devices and those encapsulated by the three different barrier films.

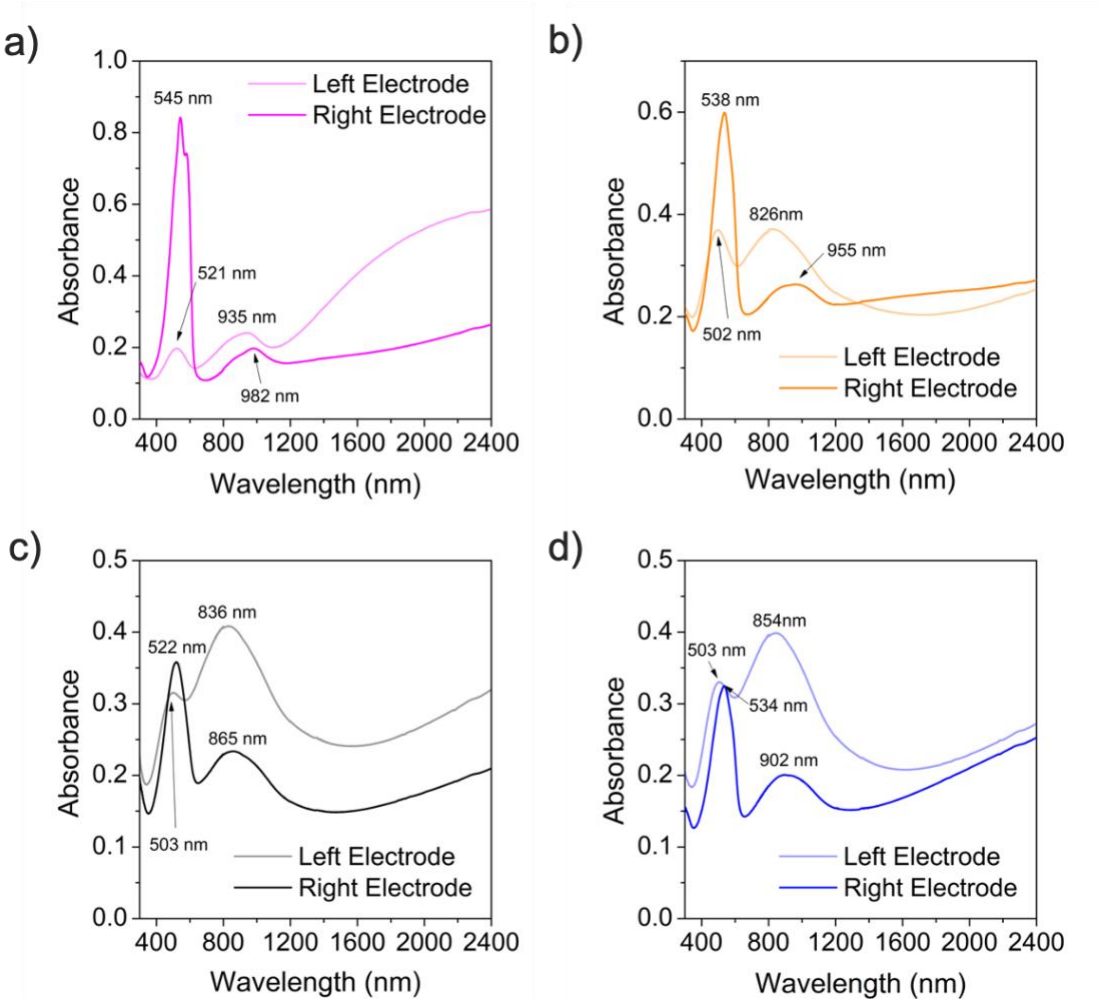

Figure S5-8. Spectra recorded for the left electrode and right electrode of lateral devices prior to XPS measurements for an unirradiated, pristine device (a), and devices irradiated for 240 hours encapsulated by FTB (b), PET (c), and (CA-ChNF/CNC) (d) barrier films.

5.1.8.4 Lateral Device Kinetics Snapshots

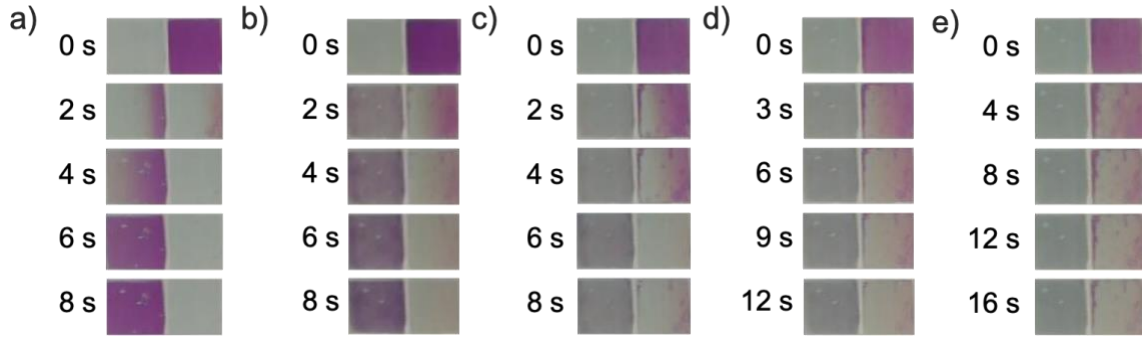

Figure S5-9. Snapshots of a FTB-encapsulated device switching from the +1.0 V state to the -1.0 V state at 0 (a), 48 h, (b), 96h (c), 144h (d), 240 (e).

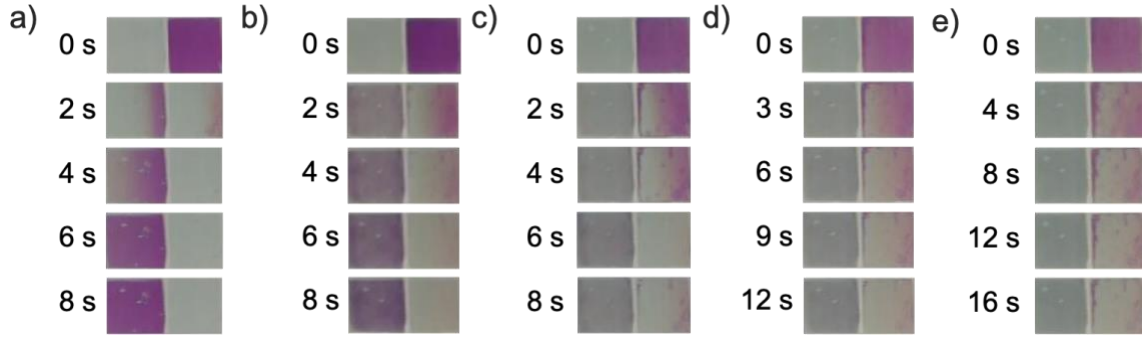

Figure S5-10. Snapshots of a FTB-encapsulated device switching from the -1.0 V state to the +1.0 V state at 0 (a), 48 h, (b), 96h (c), 144h (d), 240 (e).

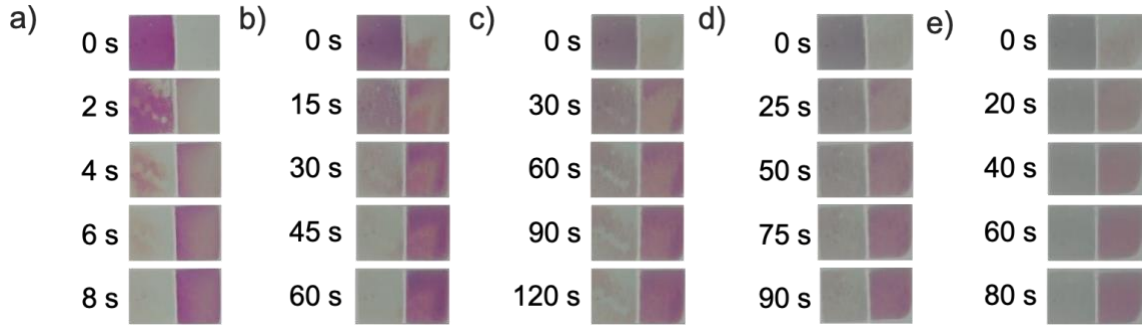

Figure S5-11. Snapshots of a PET-encapsulated device switching from the +1.0 V state to the -1.0 V state at 0 (a), 48 h, (b), 96h (c), 144h (d), 240 (e).

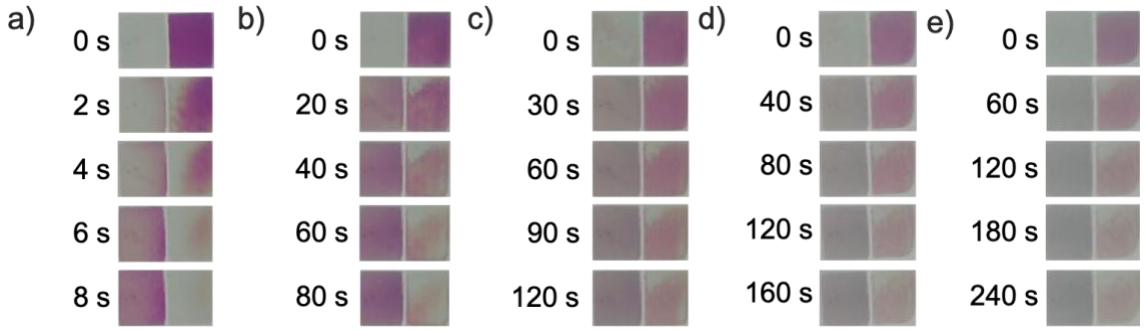

Figure S5-12. Snapshots of and PET-encapsulated device switching from the -1.0 V state to the +1.0 V state at 0 (a), 48 h, (b), 96h (c), 144h (d), 240 (e).

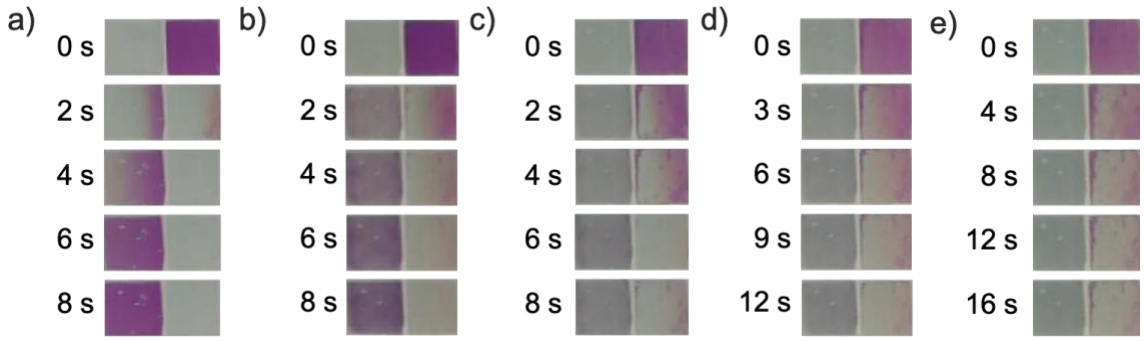

Figure S5-13 Snapshots of a CA-ChNF/CNC-encapsulated device switching from the +1.0 V state to the -1.0 V state at 0 (a), 48 h, (b), 96h (c), 144h (d), 240 (e).

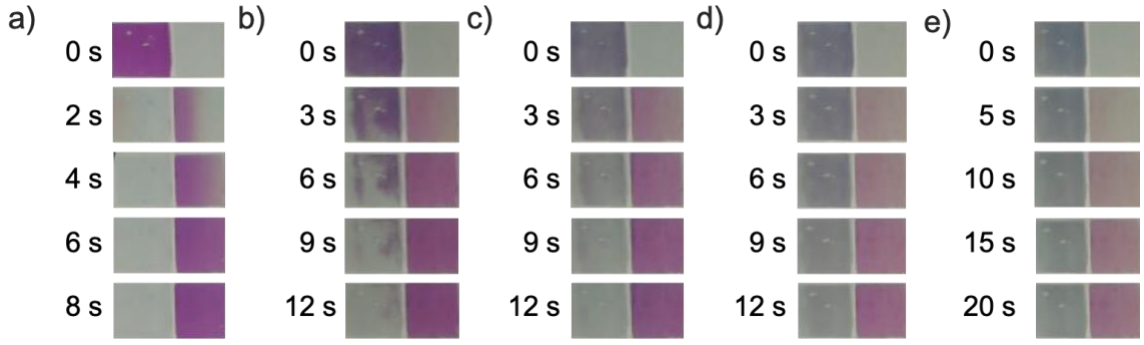

Figure S5-14. Snapshots of and CA-ChNF/CNC -encapsulated device switching from the -1.0 V state to the +1.0 V state at 0 (a), 48 h, (b), 96h (c), 144h (d), 240 (e).

5.1.8.5 XPS Peak Fitting and Analysis

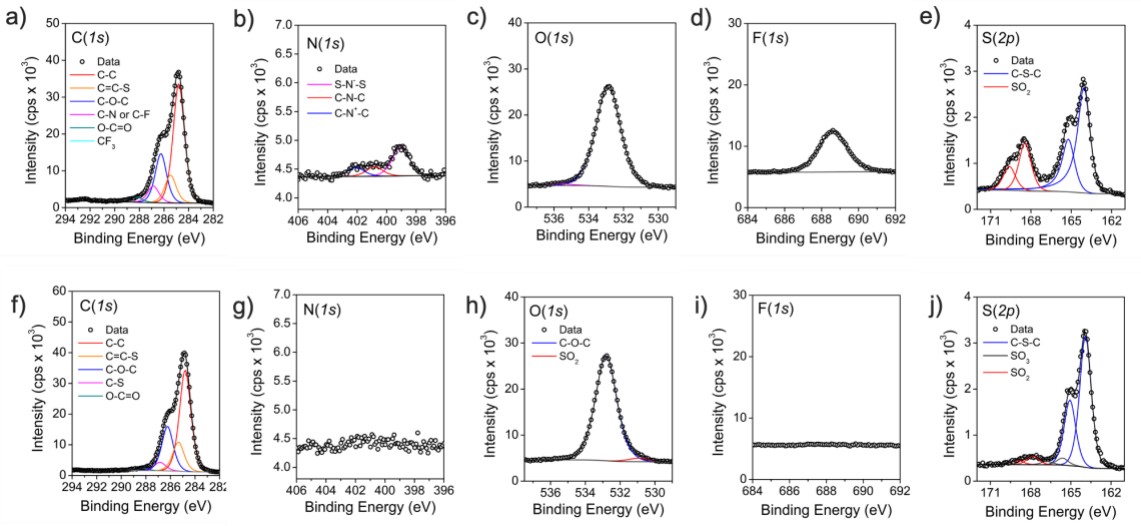

Figure S5-15. XPS raw data of the pristine device showing the peak deconvolution for the left electrode (a) C(*1s*), (b), N(*1s*), (c) O(*1s*), (d) F(*1s*), (e) S(*2p*) and for the right electrode (a) C(*1s*), (b), N(*1s*), (c) O(*1s*), (d) F(*1s*), (e) S(*2p*).

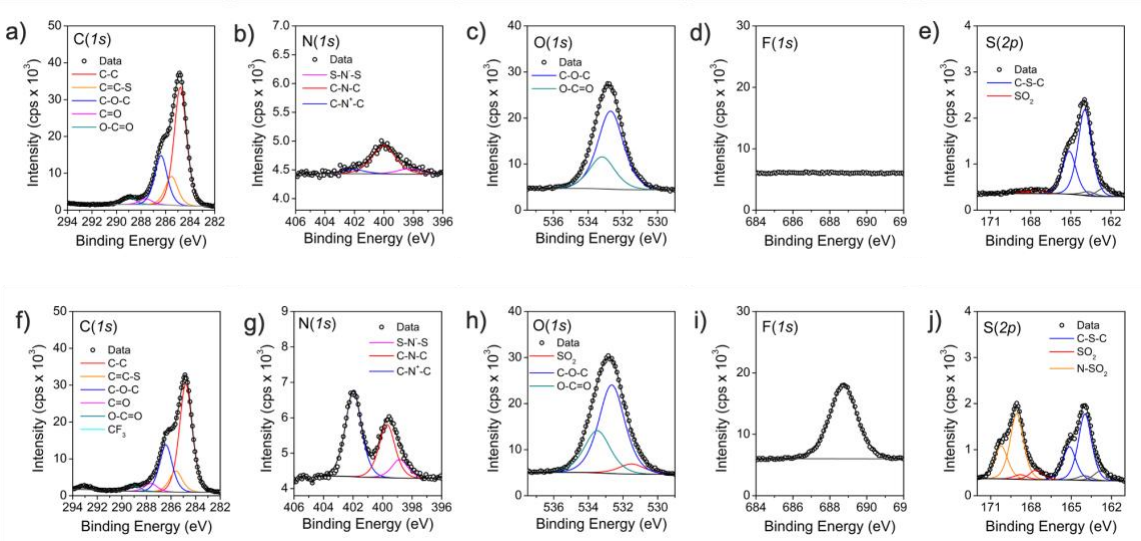

Figure S5-16. XPS raw data of a FTB-encapsulated device after 240 hr of irradiation showing the peak deconvolution for the left electrode (a) C(*1s*), (b), N(*1s*), (c) O(*1s*), (d) F(*1s*), (e) S(*2p*) and for the right electrode (a) C(*1s*), (b), N(*1s*), (c) O(*1s*), (d) F(*1s*), (e) S(*2p*).

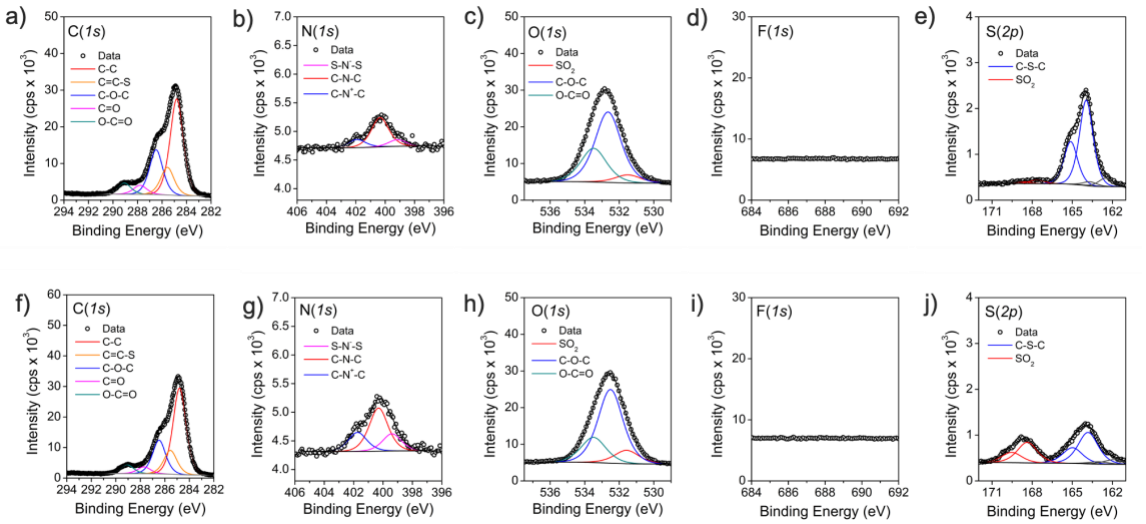

Figure S5-17. XPS raw data of a PET-encapsulated device after 240 hr of irradiation showing the peak deconvolution for the left electrode (a) C(*1s*), (b), N(*1s*), (c) O(*1s*), (d) F(*1s*), (e) S(*2p*) and for the right electrode (a) C(*1s*), (b), N(*1s*), (c) O(*1s*), (d) F(*1s*), (e) S(*2p*).

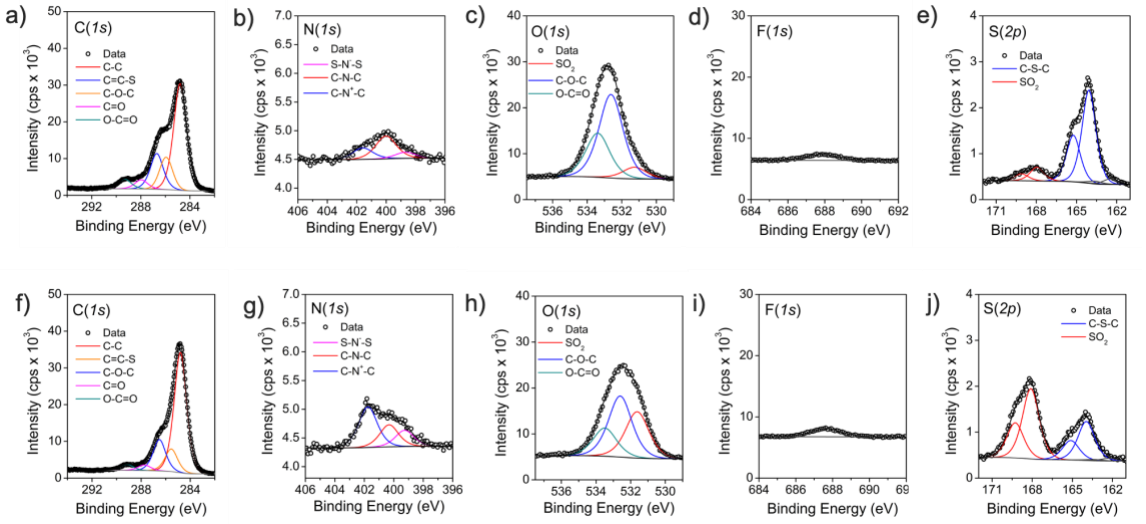

Figure S5-18. XPS raw data of a CA-ChNF/CNC-encapsulated device after 240 hr of irradiation showing the peak deconvolution for the left electrode (a) C(*1s*), (b), N(*1s*), (c) O(*1s*), (d) F(*1s*), (e) S(*2p*) and for the right electrode (a) C(*1s*), (b), N(*1s*), (c) O(*1s*), (d) F(*1s*), (e) S(*2p*).

CHAPTER 6. CONCLUSIONS, FUTURE RESEARCH QUESTIONS, AND PERSPECTIVE

The development of new materials, techniques, and theory have driven tremendous growth in the field of π- conjugated polymers. Each of these advances have been co-dependent, all advancing the understanding of structure-processing-property relationships. For instance, new synthetic methods promise to give further control over accessible repeat units and molecular weight.[35] Tools for characterizing physical processes *in situ* have begun to give insight into the influence of microstructure on charge transport.[161] And ever-improving density functional theory methods have refined our understanding of charged states, optical transitions, and energetic disorder.[272,273] In terms of computation, the rising field of materials informatics is sure to play a role in aiding the design of new materials that reliably exhibit the desired properties.

This chapter will summarize some of the key insights gained form the research described in Chapters 3 through 5 in section 6.1 culminating in a brief discussion on the path forward for photostability studies. A more general perspective on paper electronics will be given in section 6.2. In terms of promising avenues for new materials, the three-dimensional structures accessible with from wood will be discussed as a potential platform for studying electronic, ionic, and thermal transport in cellulose-conjugated polymer hybrids in section 6.3. Finally, a perspective on need for new tools for probing the relevant length, time, and energy scales of conducting polymer-based materials will be given in to conclude this dissertation.

6.1.1 Summary of cellulose-based ECDs and future work in photostability

This work in this dissertation has centered around incorporating PEDOT:PSS as a sufficiently conductive and color-neutral electrode for enabling cellulose-based electrochromic devices. Chapter 3 investigated transparent wood as a substrate showing the PEDOT:PSS could be easily applied to a relatively non-polar and rough surface (compared to glass) and still serve as an effective electrode material. The high haze of the transparent wood substrate improved the colorless state of the device compared to glass where a blue-hue from the partially reduced PEDOT:PSS in the counter electrode was transmitted. In Chapter 4, a nanocellulose-coated paper was shown to support PEDOT:PSS electrodes patterned by inkjet printing capable of switching cyan-to-clear, magenta-to-clear, yellow-to-clear, and black-to-clear electrochromic films. Despite the relatively high surface resistance of 460 Ω sq^{-1}, effective switching was demonstrated for lateral ECDs where the electrolyte conductivity was found to be the limiting factor in switching speed. Chapter 5 explored the impact of oxygen barrier films used to encapsulate lateral ECDs showing that a 10x improvement in device lifetime was achieved with the use of a bioderived multilayer barrier film. Insights from XPS showed that the left electrode set in its oxidized state during irradiation progressed through non-oxidative photochemical degradation whereas the right electrode set in its neutral state during irradiation showed signs of oxidative damage.

As Chapter 5 involved a device-level characterization of P(ProDOT) photodegradation, the principle question remains – why do we see a difference in photostability among electrochromic polymers? This question becomes even more

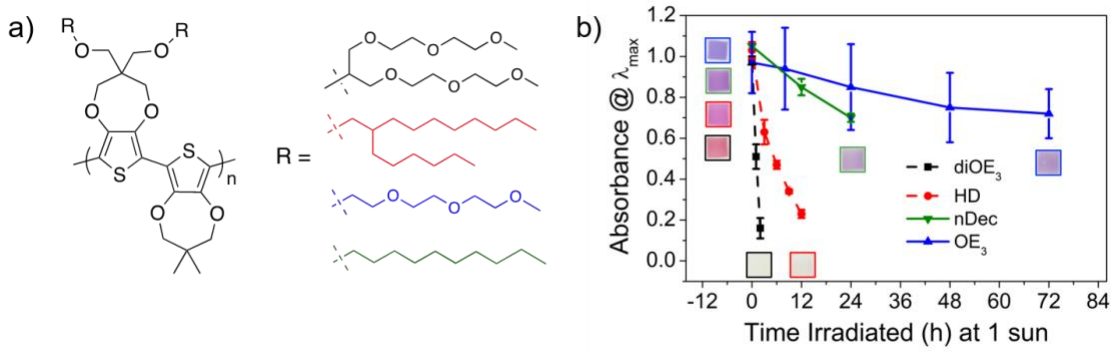

Figure 6-1 (a) poly(ProDOT(X)-*alt*-ProDOT(Me$_2$) repeat-unit structure showing a family of materials with four different sidechain structures (X). (b) Absorbance of thin films of each polymer versus irradiation time in air under 1 sun.

intriguing given recent work comparing a family of ProDOT-based copolymers shown in Figure 6-1a. These polymers share the same backbone structure, and ProDOT(Me$_2$) comonomer. They differ in their side-chain structures and exhibit remarkably different photostabilities. Figure 6-1b shows the evolution of absorbance versus irradiation time in air, at 1 sun (Xe lamp, daylight filter, 55 mW cm^{-2} between 300-400nm). The polymers with linear side chains degrade more slowly, maintaining greater than 50% of their initial optical density past 24 and 72 hours for the *n*-decyloxy and (oligoether)$_3$ side chains, respectively. The branched counterparts quickly lose optical density where the polymer with hexyl decyloxy side chain decays to 50% its initial absorbance in 6 hours and the branched di-(oligoether)$_3$ side chains decay an equivalent amount after 1 hour.

Future chemical analyses including XPS, Raman spectroscopy, NMR, and MALDI will hopefully shed light on the degradation products being formed in these materials upon sunlight exposure. Given the evidence in the literature of conformational changes associated with photodegradation, analyses of the thermal properties of these polymers

could shed light on the relative free volume in each film which to see how this property correlates with photostability.

From previous reports, a number of photo-degradation mechanisms have been proposed for conjugated polymers. Studies of the photodegradation of P3HT and other poly(3-alkylthiophenes) showed the emergence of carbonyl-functional groups likely arising from hydrogen-abstraction from the α-methylene carbon in the side chain.[113,274,275] Kinetics studies of the degradation under controlled pressure, humidity, and oxygen concentrations suggested a radical chain reaction mechanism responsible for the buildup of oxidized species in the side chains.[114] Thiophene ring attack by oxygen was also observed for P3HT in an XPS study where photo-oxidation produced sulfides then sulfones then sulfite esters in the thiophene sulfur (ambient environment, mercury lamp irradiation, glass filter for light below 295 nm).[251] Polymer-morphology influences on photostability have also been investigated in depth both for P3HT[261] and for for polymers designed for OPV applications including polymers containing benzo[1,2-*b*;3,3-*b*]dithiophene (BTD) units such as PTB7 and its derivatives.[268,276–278] In these studies, polymer films with enhanced microstructural retained optical density to a greater extent than did the less-ordered films, suggesting aggregation or packing of the backbones somewhat limits photodegradation. Interestingly, polymer molecular weight was not found to play a major role in dictating photostability despite chain scission be a dominant mechanism for loss of absorbance in solution irradiation studies.[261,263] Two popular electron acceptor molecules were also studied as they degraded under high-intensity laser light (457 and 633 nm at 10^6 W m^{-2}) where a conformational twist was hypothesized to precede photodegradation.[266]

Dioxythiophene-based polymers have also been studied for their photochemical degradation where similar degradation products have been observed. The emergence of carbonyl and sulfone functional groups in PEDOT-PF_6 were observed by XPS after irradiation by UV light (320-400, 7 mW cm^{-2}).[265] Irradiation of P(ProDOT) using a Xe-lamp with a daylight filter showed rapid emergence carbonyl and sulfone chemical species in the presence of oxygen.[111] Other electrochromic polymers have also been studied during irradiation with 1 sun where two distinct chain-scission mechanisms (terminal, and random) were used to rationalize differences between materials' photostabilities.[154]

Based on these previous studies it is clear that radical hydrogen abstraction and oxidation of the thiophene rings could play a major role in the photodegradation P(ProDOT) derivatives. However, in the absence of uniformity of sample preparation and irradiation conditions, general design rules for photostable materials remains lacking. Therefore, as future photostability experiments are carried out on materials such as the P(ProDOT(X)-*alt*-ProDOT($Me)_2$) series, a clear understanding, control, and reporting of the irradiation environment will be important for developing fundamental insight into the photochemical degradation processes.

6.1.2 Future development of cellulose-based electronics

With the many demonstrations of paper-based electronics, it's clear that these lab-scale devices are primed to enable a number of new applications especially in sensing, smart labels, disposable diagnostics, and environmental monitoring.[16,207,279–281] Beyond improved understanding of photodegradation in π-conjugated active materials, two main

hurdles remain for these devices: the stability of cellulosic materials in wet/humid environments and cost.

Moisture tolerance of cellulose-based materials has been an ongoing challenge as cellulose fibers are prone to swelling when in contact with water or humid air. This is particularly challenging for electronic components which are often brittle and deposited as thin films with 10s of μm of resolution. While less sensitive to dimensional changes compared to ceramics, PEDOT:PSS is prone to delamination and redispersion if not treated with a crosslinking agent like (3-glycidyloxypropyl)trimethoxysilane (GOPS) or divinyl sulfone (DVS).[282,283] For printed displays, electrochromic devices show a relatively low sensitivity to moisture, especially compared to organic light emitting diodes which require ultra-barrier films (WVTR < 10^{-4} g m^{-2} day^{-1}).[284] As the redox-active P(ProDOTs) are highly disordered, they can easily be fabricated on flexible, rough substrates as shown in Chapter 4.

When it comes to barrier films based on biopolymers, the barrier properties are known to be highly moisture sensitive with their properties deteriorating rapidly even at modest humidity levels. Several strategies exist for improving the moisture tolerance of cellulose nanofiber-based barrier films. Physical crosslinking with multivalent metal cations has been shown to maintain the oxygen barrier properties below 0.1 mL μm m^{-2} kPa^{-1} day^{-1} for oven-dried TEMPO-oxidized CNF crosslinked with Ca^{2+} (from $CaCl_2$).[285] Rigorous drying conditions have proven similarly effective where drying at 145˚C (with the inclusion of $NaBH_4$ to prevent coloration) resulted in oxygen permeabilities of 0.5 mL μm m^{-2} kPa^{-1} day^{-1} measured at 50% relative humidity.[134] Additionally, crosslinking can provide wet strength to CNF-based materials through the inclusion of chitosan.[286] Other

approaches involve using alkyl-silane treatments, where water-resistant paper was demonstrated after exposure to fluoroalkane trichlorosilane gas. However, though these strategies impair the ability to recycle the material.[201]

New approaches to achieve moisture tolerance with all-bioderived materials would be a major achievement for sustainable packaging. Mars-Wrigley has pledged to use 100% reusable, recyclable, or compostable packaging by 2025, while reducing virgin plastic use by 25%. As noted in Chapter 5, achieving competitive properties in bioderived materials, especially when it comes to toughness and moisture resistances is not trivial. However, as the problem of plastic waste has become apparent, significant steps toward improving bioderived and biodegradable packaging materials are sure to follow. These materials can be directly translatable to printed electronics where further improvements in optical clarity, temperature resistance, and barrier properties would enable better performance and stability.

One of the primary considerations for paper-based electronics is cost. As a commodity substrate, it makes little sense to utilize electronic active materials that cost $1000s/gram as paper-based electronics are typically assumed to carry an equivalently commodity-level cost. PEDOT:PSS, while produced at large scales and deposited as thin layers costs roughly \$5 g^{-1} (or \$1 m^{-2} for a 150 nm thick film). Further cost reductions could be achieved with poly(aniline) conductors given sufficient conductivities.[287] Electrochromic polymers are currently more costly, but it's reasonable to expect with scaled up syntheses, the same order of magnitude as PEDOT:PSS is achievable (~10 \$ g^{-1} , \$6 m^{-2} for a 300 nm thick film). This leaves the electrolyte and the barrier film. Barrier films composed of cellulose acetate, CNCs, and ChNFs as presented in Chapter 5 are

dominated in cost by the nanoparticles which require energy-intensive methods and some costly reagents to extract. However, these materials are likely to continue to decrease considering scaling up industrial production of CNCs already underway (CA: \$0.50 m^{-2}, CNC: \$10 m^{-2}). In the lateral devices shown in Chapters 4 and 5, the iongel electrolyte incorporates an expensive ionic liquid (due to the TFSI anion, ~\$5 g^{-1}) with PVDF-HFP (\$0.60 g^{-1}), leading this to be the most expensive device component by far (\$1,000 m^{-2}). Therefore, less expensive electrolytes could easily drive the materials cost of electrochromic displays down to the \$10s / m^{-2}, competitive for disposable electronic devices.

In terms of future active materials, the growing interest in the electronic properties of naturally occurring H-bonded semiconductors offers an interesting path forward. Indigo, epindolidione, and quinacridones are well-known pigments with promising photo-stability of electronic properties even while being immersed in aqueous environments. These naturally-derived semiconductors fulfil sustainability criteria for renewable materials synthesis and are known to biodegrade under proper conditions.[271] Therefore, these natural semiconductors offer a renewable option at extremely low cost for moderately-performing transistors.[288,289] Along with more development in the understanding of the redox-properties and conductivity in these materials, developing derivatives of these materials that can be solution-processed would be a major achievement on the path toward sustainable electronics. Paper-based devices are attractive additions to a growing number of "frugal science" projects in academic research labs such as the paper centrifuge,[290] \$0.98 hearing aids,[291] and \$1 microscopes.[292] It will be exciting to see the developments with this theme of ultra-low-cost devices and the impact this field can make.

6.1.3 Utilizing wood for 3D structures

Beyond the use of cellulosic materials for substrates and barrier films, the natural three-dimensional structure of wood offers a unique platform upon which to engineer new electroactive materials with conjugated polymers. Exploiting natural wood offers a scalable method of nanostructure control from the top-down.[293]

The combination of oriented pores and crystalline cellulose along the growth direction of the wood has been shown to provide anisotropic optical, mechanical, thermal, and ion transport properties in these materials. The deposition of conducting polymers within wood has been dominated by either vapor-phase polymerization techniques, which suffer from poor control over the polymer structure and long reaction times.[122,123] Recently some of the first *in vivo* polymerizations of conducting polymers have been demonstrated highlighting a growing interest in combing these materials with biology. Eleni Stavrinidou and coworkers have successfully polymerized an bis[3,4-ethylenedioxythiophene]-3-thiophene butyric acid trimer *in vivo* inside the plant xylem.[294] This work built off of their earlier *in situ* polymerizations of EDOT inside plants by eliminating the $FeCl_3$ oxidant deemed harmful to the plant tissue. Subsequent experiments *in vitro* confirmed the enzymatic catalysis of the polymerization where peroxide serves as the oxidizing agent.[295] This kind of *in vivo* polymerization of conducting polymers has also expanded to neuron cells which were genetically modified to produce H_2O_2 for the oxidative polymerize aniline in the cell's plasma membrane.[296] This ability to deposit conducting polymers inside living tissue sparks some fundamental questions from a materials science perspective. For instance, how does the interface influence the resulting polymer microstructure and

properties? And how might we measure the polymerization and resulting polymer structures?

Considering the *in situ* polymerization inside wood scaffolds, there is a wealth of possible pairs of monomers and surface functional groups that could be exploited to facilitate the self-assembly of conducting polymers in the wood cell wall. As a diffusion-controlled process, there was little templating effect seen in preliminary experiments polymerizing EDOT and various ProDOTs onto shear-aligned nanocellulose, thus confining the diffusion of oxidant and monomer in the wood cell lumen (or even smaller pores) could prove to yield some interesting materials and insight into how one might better control these *in situ* polymerizations. Targeting monomers that adopt highly coplanar geometries, or monomers could participate in hydrogen bonding with the cellulose structure would be interesting options for exploring structure-property relationships. As ionic transport in conducting polymer materials has seen a resurgence of research interest (especially related to oligo-ether-functionalized materials),[297–299] the anisotropic pore structure of natural wood could provide a unique scaffold for non-tortuous ion diffusion.[121] As one of nature's best fluid transporters, these kinds of cellular structures are promising for the study of future mixed transport materials that could easily reach length scales of meters. These larger structures would be ideal for tough and strong membranes for charge storage or capacitive desalination devices.[300,301]

With the anisotropic alignment of the cellulose crystal structure, impressive thermal conductivities have been shown for films of CNCs.[302] Wood, therefore, is poised to be a highly anisotropic thermal conductor making its composites with conducting polymers interesting for thermal transport studies. Similarly, the anisotropic crystal structure of the

wood cell wall has inspired fundamental studies of light propagation.[191] These studies may open the door for novel optical materials that could be modulated by conjugated polymer coatings deposited on the cell wall where tunable absorbance, but also refractive index can be easily achieved.[303]

One major challenge in answering the questions above is the characterization of polymer structure at the nanoscale with sufficient spatial resolution for determining how these structures assemble in the wood cell wall. While x-ray scattering methods offer high resolution for probing nanoscale order of crystalline domains, this technique falls short as the crystallinity of cellulose would likely obscure anything attributable to the order of the conjugated polymer. Neutron-based methods proved an interesting opportunity to examine polymer structure but will not give much spatial resolution of the nanostructures. Confocal methods are seldom used for conducting polymer-based materials but could provide the right platform for studying wood-conducting polymer materials in three dimensions.[304] One could imaging utilizing fluorescence from the conjugated polymer, or derivatization of monomer units with fluorescent molecules to provide detailed structural information of these materials, shedding light on how self-assembly *in situ* takes place. The growing adoption of *in situ* measurement techniques has proven effective for establishing a better understanding of thin film solidification after blade coating and for visualizing phase changes upon electrochemical cycling.[157,305,306] Recently, an *in-operando* technique for the probing phase changes in poly[2,5-bis(thiophenyl)-1,4-bis(2-(2-(2-methoxyethoxy)ethoxy)- ethoxy)benzene] (PB2T-TEG) during electrochemical cycling.[298] Further work in methods development promises to be a key step for better understanding

the interrelations of molecular structure, processing, and material microstructure, thus leading to more rational materials design moving forward.

REFERENCES

(1) Waldrop, M. M. More than Moore. *Nature* **2016**, *530*, 145–147.

(2) Chang, J. S.; Facchetti, A. F.; Reuss, R. A Circuits and Systems Perspective of Organic/Printed Electronics: Review, Challenges, and Contemporary and Emerging Design Approaches. *IEEE J. Emerg. Sel. Top. Circuits Syst.* **2017**, *7* (1), 7–26.

(3) Forrest, S. R. Electronic Appliances on Plastic. *Nature* **2004**, *428* (6986), 911–918.

(4) Andersson Ersman, P.; Lassnig, R.; Strandberg, J.; Tu, D.; Keshmiri, V.; Forchheimer, R.; Fabiano, S.; Gustafsson, G.; Berggren, M. All-Printed Large-Scale Integrated Circuits Based on Organic Electrochemical Transistors. *Nat. Commun.* **2019**, *10* (1), 1–9.

(5) Hanson, A. N. 4681, 1903.

(6) Gilleo, K. The Circuit Centennial. *ET-Trends*. 2003, pp 1–16.

(7) Cai, G.; Wang, J.; Lee, P. S. Next-Generation Multifunctional Electrochromic Devices. *Acc. Chem. Res.* **2016**, *49* (8), 1469–1476.

(8) Gao, W.; Emaminejad, S.; Nyein, H. Y. Y.; Challa, S.; Chen, K.; Peck, A.; Fahad, H. M.; Ota, H.; Shiraki, H.; Kiriya, D.; et al. Fully Integrated Wearable Sensor Arrays for Multiplexed in Situ Perspiration Analysis. *Nature* **2016**, *529* (7587), 509–514.

(9) Martinez, A. W.; Phillips, S. T.; Whitesides, G. M. Diagnostics for the Developing World Microfluidic.Pdf. **2010**, *82* (1), 3–10.

(10) Güder, F.; Ainla, A.; Redston, J.; Mosadegh, B.; Glavan, A.; Martin, T. J.; Whitesides, G. M. Paper-Based Electrical Respiration Sensor. *Angew. Chemie - Int. Ed.* **2016**, *55* (19), 5727–5732.

(11) Hamedi, M. M.; Ainla, A.; Güder, F.; Christodouleas, D. C.; Fernández-Abedul, M. T.; Whitesides, G. M. Integrating Electronics and Microfluidics on Paper. *Adv. Mater.* **2016**, *28* (25), 5054–5063.

(12) Pardee, K.; Green, A. A.; Ferrante, T.; Cameron, D. E.; Daleykeyser, A.; Yin, P.; Collins, J. J. Paper-Based Synthetic Gene Networks. *Cell* **2014**, *159* (4), 940–954.

(13) Irimia-Vladu, M. "Green" Electronics: Biodegradable and Biocompatible Materials and Devices for Sustainable Future. *Chem. Soc. Rev.* **2014**, *43* (2), 588–610.

(14) Irimia-Vladu, M.; Głowacki, E. D.; Voss, G.; Bauer, S.; Sariciftci, N. S. Green and Biodegradable Electronics. *Mater. Today* **2012**, *15* (7–8), 340–346.

(15) Zimmerman, J. B.; Anastas, P. T.; Erythropel, H. C.; Leitner, W. Designing for a Green Chemistry Future. *Science (80-.).* **2020**, *367* (6476), 397–400.

(16) Tobjörk, D.; Österbacka, R. Paper Electronics. *Adv. Mater.* **2011**, *23* (17), 1935–1961.

(17) Määttänen, A.; Ihalainen, P.; Bollström, R.; Toivakka, M.; Peltonen, J. Wetting and Print Quality Study of an Inkjet-Printed Poly(3-Hexylthiophene) on Pigment Coated Papers. *Colloids Surfaces A Physicochem. Eng. Asp.* **2010**, *367* (1–3), 76–84.

(18) Zhu, H.; Luo, W.; Ciesielski, P. N.; Fang, Z.; Zhu, J. Y.; Henriksson, G.; Himmel, M. E.; Hu, L. Wood-Derived Materials for Green Electronics, Biological Devices, and Energy Applications. *Chem. Rev.* **2016**, *116* (16), 9305–9374.

(19) Fang, Z.; Zhu, H.; Bao, W.; Preston, C.; Liu, Z.; Dai, J.; Li, Y.; Hu, L. Highly Transparent Paper with Tunable Haze for Green Electronics. *Energy Environ. Sci.* **2014**, *7* (10), 3313–3319.

(20) Preston, C.; Fang, Z.; Murray, J.; Zhu, H.; Dai, J.; Munday, J. N.; Hu, L. Silver Nanowire Transparent Conducting Paper-Based Electrode with High Optical Haze. *J. Mater. Chem. C* **2014**, *2* (7), 1248–1254.

(21) Zhu, H.; Xiao, Z.; Liu, D.; Li, Y.; Weadock, N. J.; Fang, Z.; Huang, J.; Hu, L. Biodegradable Transparent Substrates for Flexible Organic-Light-Emitting Diodes. *Energy Environ. Sci.* **2013**, *6* (7), 2105–2111.

(22) Ryan, J. D.; Mengistie, D. A.; Gabrielsson, R.; Lund, A.; Müller, C. Machine-Washable PEDOT:PSS Dyed Silk Yarns for Electronic Textiles. *ACS Appl. Mater. Interfaces* **2017**, *9* (10), 9045–9050.

(23) Romero, I. S.; Schurr, M. L.; Lally, J. V.; Kotlik, M. Z.; Murphy, A. R. Enhancing the Interface in Silk-Polypyrrole Composites through Chemical Modification of Silk Fibroin. *ACS Appl. Mater. Interfaces* **2013**, *5* (3), 553–564.

(24) Patil, A. O.; Ikenoue, Y.; Wudl, F.; Heeger, A. J. Water-Soluble Conducting Polymers. *J. Am. Chem. Soc.* **1987**, *109* (6), 1858–1859.

(25) Beaujuge, P. M.; Amb, C. M.; Reynolds, J. R. A Side-Chain Defunctionalization Approach Yields a Polymer Electrochrome Spray-Processable from Water. *Adv. Mater.* **2010**, *22* (47), 5383–5387.

(26) Ponder, J. F.; Österholm, A. M.; Reynolds, J. R. Conjugated Polyelectrolytes as Water Processable Precursors to Aqueous Compatible Redox Active Polymers for Diverse Applications: Electrochromism, Charge Storage, and Biocompatible Organic Electronics. *Chem. Mater.* **2017**, *29* (10), 4385–4392.

(27) Schmatz, B.; Lang, A. W.; Reynolds, J. R. Fully Printed Organic Electrochemical Transistors from Green Solvents. *Adv. Funct. Mater.* **2019**, *29* (44), 1–7.

(28) Feig, V. R.; Tran, H.; Bao, Z. Biodegradable Polymeric Materials in Degradable Electronic Devices. *ACS Cent. Sci.* **2018**, *4* (3), 337–348.

(29) Tyler McQuade, D.; Pullen, A. E.; Swager, T. M. Conjugated Polymer-Based Chemical Sensors. *Chem. Rev.* **2000**, *100* (7), 2537–2574.

(30) Rasmussen, S. C. The Early History of Polyaniline: Discovery and Origins. *An Int. J. Hist. Chem. Subst.* **2017**, *1* (12), 99–109.

(31) Jr., V. V. W.; Labes, M. M.; Perstein, J. H. Polysulfur Nitride - a One-Dimensional Chain with a Metallic Ground State. *Phys. Rev. Lett.* **1973**, *31*, 29–32.

(32) Shirakawa, H. Nobel Lecture: The Discovery of Polyacetylene Film - The Dawning of an Era of Conducting Polymers. *Rev. Mod. Phys.* **2001**, *73* (3), 713–718.

(33) Heeger, A. J. Nobel Lecture: Semiconducting and Metallic Polymers: The Fourth Generation of Polymeric Materials. *Rev. Mod. Phys.* **2001**, *73* (3), 681–700.

(34) MacDiarmid, A. G. "synthetic Metals": A Novel Role for Organic Polymers. *Curr. Appl. Phys.* **2001**, *1* (4–5), 269–279.

(35) Swager, T. M. 50th Anniversary Perspective: Conducting/Semiconducting Conjugated Polymers. A Personal Perspective on the Past and the Future. *Macromolecules* **2017**, *50* (13), 4867–4886.

(36) Bredas, J. L.; Street, G. B. Polarons, Bipolarons, and Solitons in Conducting Polymers. *Acc. Chem. Res.* **1985**, *18* (10), 309–315.

(37) Hoffman, R. How Chemistry and Physics Meet in the Solid State. *Angew. Chemie* **1987**, *26*, 846–878.

(38) Su, W. P.; Schrieffer, J. R.; Heeger, A. J. Solitons in Polyacetylene. *Phys. Rev. Lett.* **1979**, *42* (25), 1698–1701.

(39) Pyo, M.; Reynolds, J. R. Electrochemically Stimulated Adenosine 5′-Triphosphate (ATP) Release through Redox Switching of Conducting Polypyrrole Films and Bilayers. *Chem. Mater.* **1996**, *8* (1), 128–133.

(40) Pyo, M.; Reynolds, J. R. Potential Dependent Dual Ion Transport of Conducting Polymer: Redox Polymer Bilayers. *J. Phys. Chem.* **1995**, *99* (20), 8249–8254.

(41) Rogers, J. A.; Dodabalapur, A.; Bao, Z.; Katz, H. Low-Voltage 0.1 Mm Organic Transistors and Complementary Inverter Circuits Fabricated with a Low-Cost Form of near-Field Photolithography. *Appl. Phys. Lett.* **1999**, *75*, 1010–1012.

(42) Lamport, Z. A.; Haneef, H. F.; Anand, S.; Waldrip, M.; Jurchescu, O. D. Tutorial: Organic Field-Effect Transistors: Materials, Structure and Operation. *J. Appl. Phys.* **2018**, *124* (7).

(43) Quinn, J. T. E.; Zhu, J.; Li, X.; Wang, J.; Li, Y. Recent Progress in the Development of N-Type Organic Semiconductors for Organic Field Effect Transistors. *J. Mater. Chem. C* **2017**, *5* (34), 8654–8681.

(44) J. H. Burroughes, D. D. C. B.; Brown, A. R.; Marks, R. N.; Mackay, K.; Friend, R. H.; Burns, P. L.; Holms, A. B. Light-Emitting Diodes Based on Conjugated Polymers. *Nature*. 1990, pp 539–541.

(45) Adachi, C.; Baldo, M. A.; Thompson, M. E.; Forrest, S. R. Nearly 100% Internal Phosphorescence Efficiency in an Organic Light Emitting Device. *J. Appl. Phys.* **2001**, *90* (10), 5048–5051.

(46) Baldo, M. A.; O'Brian, D. F.; Shoustikov, A.; Sibley, S.; Thompson, M. E.; Forrest, S. R. Highly Efficient Phosphorescent Emission from Organic Electroluminescent Devices. *Nature* **1998**, *395* (September), 151.

(47) Cui, Y.; Yao, H.; Zhang, J.; Xian, K.; Zhang, T.; Hong, L.; Wang, Y.; Xu, Y.; Ma, K.; An, C.; et al. Single-Junction Organic Photovoltaic Cells with Approaching 18% Efficiency. *Adv. Mater.* **2020**, *1908205*, 1–7.

(48) Mainville, M.; Leclerc, M. Recent Progress on Indoor Organic Photovoltaics: From Molecular Design to Production Scale. *ACS Energy Lett.* **2020**, *5* (4), 1186–1197.

(49) Rivnay, J.; Owens, R. M.; Malliaras, G. G. The Rise of Organic Bioelectronics. *Chem. Mater.* **2014**, *26* (1), 679–685.

(50) Zeglio, E.; Inganäs, O. Active Materials for Organic Electrochemical Transistors. *Adv. Mater.* **2018**, *30* (44), 1–18.

(51) Rivnay, J.; Inal, S.; Salleo, A.; Owens, R. M.; Berggren, M.; Malliaras, G. G. Organic Electrochemical Transistors. *Nat. Rev. Mater.* **2018**, *3*.

(52) *Handbook of Conducting Polymers, 4th Edition - 2 Volume Set*, 4th ed.; Reynolds, J. R., Thompson, B. C., Skotheim, T., Eds.; CRC Press: Boca Raton, FL, 2019.

(53) Simon, D. T.; Gabrielsson, E. O.; Tybrandt, K.; Berggren, M. Organic Bioelectronics: Bridging the Signaling Gap between Biology and Technology. *Chem. Rev.* **2016**, *116* (21), 13009–13041.

(54) Malliaras, G. G. Organic Bioelectronics: A New Era for Organic Electronics. *Biochim. Biophys. Acta - Gen. Subj.* **2013**, *1830* (9), 4286–4287.

(55) Modarresi, M.; Mehandzhiyski, A.; Fahlman, M.; Tybrandt, K.; Zozoulenko, I. Microscopic Understanding of the Granular Structure and the Swelling of PEDOT : PSS. **2020**.

(56) Jonas, F.; Gerhard, H.; Schmidtberg, W.; Jürgen, H.; Dietrich, M. Neue Polythiophene, Verfahren Zu Ihrer Herstellung Und Ihre Verwendung. 339340,

1988.

(57) Hau, S. K.; Yip, H. L.; Jen, A. K. Y. A Review on the Development of the Inverted Polymer Solar Cell Architecture. *Polym. Rev.* **2010**, *50* (4), 474–510.

(58) Wang, Y.; Zhu, C.; Pfattner, R.; Yan, H.; Jin, L.; Chen, S.; Molina-Lopez, F.; Lissel, F.; Liu, J.; Rabiah, N. I.; et al. A Highly Stretchable, Transparent, and Conductive Polymer. *Sci. Adv.* **2017**, *3* (3), 1–11.

(59) Kawahara, J.; Andersson Ersman, P.; Nilsson, D.; Katoh, K.; Nakata, Y.; Sandberg, M.; Nilsson, M.; Gustafsson, G.; Berggren, M. Flexible Active Matrix Addressed Displays Manufactured by Printing and Coating Techniques. *J. Polym. Sci. Part B Polym. Phys.* **2013**, *51* (4), 265–271.

(60) Elschner, A.; Kirchmeyer, S.; Lövenich, W.; Merker, U.; Reuter, K. *PEDOT: Principles and Applications of an Intrinsically Conductive Polymer*; CRC Press: Boca Raton, FL, 2011.

(61) Petsagkourakis, I.; Kim, N.; Tybrandt, K.; Zozoulenko, I.; Crispin, X. Poly(3,4-Ethylenedioxythiophene): Chemical Synthesis, Transport Properties, and Thermoelectric Devices. *Adv. Electron. Mater.* **2019**, *5* (11), 1–20.

(62) Brooke, R.; Cottis, P.; Talemi, P.; Fabretto, M.; Murphy, P.; Evans, D. Recent Advances in the Synthesis of Conducting Polymers from the Vapour Phase. *Prog. Mater. Sci.* **2017**, *86*, 127–146.

(63) Evans, D.; Fabretto, M.; Mueller, M.; Zuber, K.; Short, R.; Murphy, P. Structure-Directed Growth of High Conductivity PEDOT from Liquid-like Oxidant Layers during Vacuum Vapor Phase Polymerization. *J. Mater. Chem.* **2012**, *22* (30), 14889–14895.

(64) Fabretto, M. V.; Evans, D. R.; Mueller, M.; Zuber, K.; Hojati-Talemi, P.; Short, R. D.; Wallace, G. G.; Murphy, P. J. Polymeric Material with Metal-like Conductivity for next Generation Organic Electronic Devices. *Chem. Mater.* **2012**, *24* (20), 3998–4003.

(65) Fabretto, M.; Müller, M.; Zuber, K.; Murphy, P. Influence of Peg-Ran-Ppg Surfactant on Vapour Phase Polymerised PEDOT Thin Films. *Macromol. Rapid Commun.* **2009**, *30* (21), 1846–1851.

(66) Mueller, M.; Fabretto, M.; Evans, D.; Hojati-Talemi, P.; Gruber, C.; Murphy, P. Vacuum Vapour Phase Polymerization of High Conductivity PEDOT: Role of PEG-PPG-PEG, the Origin of Water, and Choice of Oxidant. *Polymer (Guildf).* **2012**, *53* (11), 2146–2151.

(67) Ouyang, L.; Jafari, M. J.; Cai, W.; Aguirre, L. E.; Wang, C.; Ederth, T.; Inganäs, O. The Contraction of PEDOT Films Formed on a Macromolecular Liquid-like Surface. *J. Mater. Chem. C* **2018**, *6* (3), 654–660.

(68) Shi, W.; Yao, Q.; Qu, S.; Chen, H.; Zhang, T.; Chen, L. Micron-Thick Highly Conductive PEDOT Films Synthesized via Self-Inhibited Polymerization: Roles of Anions. *NPG Asia Mater.* **2017**, *9* (7), e405–e405.

(69) Wang, X.; Zhang, X.; Sun, L.; Lee, D.; Lee, S.; Wang, M.; Zhao, J.; Shao-Horn, Y.; Dincă, M.; Palacios, T.; et al. High Electrical Conductivity and Carrier Mobility in OCVD PEDOT Thin Films by Engineered Crystallization and Acid Treatment. *Sci. Adv.* **2018**, *4* (9), 1–10.

(70) Gueye, M. N.; Carella, A.; Massonnet, N.; Yvenou, E.; Brenet, S.; Faure-Vincent, J.; Pouget, S.; Rieutord, F.; Okuno, H.; Benayad, A.; et al. Structure and Dopant Engineering in PEDOT Thin Films: Practical Tools for a Dramatic Conductivity Enhancement. *Chem. Mater.* **2016**, *28* (10), 3462–3468.

(71) Cho, B.; Park, K. S.; Baek, J.; Oh, H. S.; Koo Lee, Y. E.; Sung, M. M. Single-Crystal Poly(3,4-Ethylenedioxythiophene) Nanowires with Ultrahigh Conductivity. *Nano Lett.* **2014**, *14* (6), 3321–3327.

(72) Groenendaal, L.; Jonas, F.; Freitag, D.; Pielartzik, H.; Reynolds, J. R. Poly(3,4-Ethylenedioxythiophene) and Its Derivatives: Past, Present, and Future. *Adv. Mater.* **2000**, *12* (7), 481–494.

(73) Xia, Y.; Ouyang, J. Significant Different Conductivities of the Two Grades of Poly(3,4-Ethylenedioxythiophene):Poly(Styrenesulfonate), Clevios P and Clevios PH1000, Arising from Different Molecular Weights. *ACS Appl. Mater. Interfaces* **2012**, *4* (8), 4131–4140.

(74) Kim, N.; Lee, B. H.; Choi, D.; Kim, G.; Kim, H.; Kim, J. R.; Lee, J.; Kahng, Y. H.; Lee, K. Role of Interchain Coupling in the Metallic State of Conducting Polymers. *Phys. Rev. Lett.* **2012**, *109* (10), 1–5.

(75) Rivnay, J.; Inal, S.; Collins, B. A.; Sessolo, M.; Stavrinidou, E.; Strakosas, X.; Tassone, C.; Delongchamp, D. M.; Malliaras, G. G. Structural Control of Mixed Ionic and Electronic Transport in Conducting Polymers. *Nat. Commun.* **2016**, *7*, 1–9.

(76) Kim, G. H.; Shao, L.; Zhang, K.; Pipe, K. P. Engineered Doping of Organic Semiconductors for Enhanced Thermoelectric Efficiency. *Nat. Mater.* **2013**, *12* (8), 719–723.

(77) Li, Z.; Ma, G.; Ge, R.; Qin, F.; Dong, X.; Meng, W.; Liu, T.; Tong, J.; Jiang, F.; Zhou, Y.; et al. Free-Standing Conducting Polymer Films for High-Performance Energy Devices. *Angew. Chemie* **2016**, *128* (3), 991–994.

(78) Taroni, P. J.; Santagiuliana, G.; Wan, K.; Calado, P.; Qiu, M.; Zhang, H.; Pugno, N. M.; Palma, M.; Stingelin-Stutzman, N.; Heeney, M.; et al. Toward Stretchable Self-Powered Sensors Based on the Thermoelectric Response of PEDOT:PSS/Polyurethane Blends. *Adv. Funct. Mater.* **2018**, *28* (15), 1–7.

(79) Yuk, H.; Lu, B.; Lin, S.; Qu, K.; Xu, J.; Luo, J.; Zhao, X. 3D Printing of Conducting Polymers. *Nat. Commun.* **2020**, *11* (1), 4–11.

(80) Worfolk, B. J.; Andrews, S. C.; Park, S.; Reinspach, J.; Liu, N.; Toney, M. F.; Mannsfeld, S. C. B.; Bao, Z. Ultrahigh Electrical Conductivity in Solution-Sheared Polymeric Transparent Films. *Proc. Natl. Acad. Sci. U. S. A.* **2015**, *112* (46), 14138–14143.

(81) Yeon, C.; Yun, S. J.; Kim, J.; Lim, J. W. PEDOT:PSS Films with Greatly Enhanced Conductivity via Nitric Acid Treatment at Room Temperature and Their Application as Pt/TCO-Free Counter Electrodes in Dye-Sensitized Solar Cells. *Adv. Electron. Mater.* **2015**, *1* (10), 1–8.

(82) Kumar, A.; Reynolds, J. R. Soluble Alkyl-Substituted Poly(Ethylenedioxythiophenes) as Electrochromic Materials. *Macromolecules* **1996**, *29* (23), 7629–7630.

(83) Ponder, J. F.; Österholm, A. M.; Reynolds, J. R. Designing a Soluble PEDOT Analogue without Surfactants or Dispersants. *Macromolecules* **2016**, *49* (6), 2106–2111.

(84) Reeves, B. D. PROCESSABLE DISUBSTITUTED POLY(PROPYLENEDIOXYTHIOPHENES), University of Florida, 2005.

(85) Walczak, R. M.; Reynolds, J. R. Poly(3,4-Alkylenedioxypyrroles): The PXDOPs as Versatile yet Underutilized Electroactive and Conducting Polymers. *Adv. Mater.* **2006**, *18* (9), 1121–1131.

(86) Noriega, R.; Rivnay, J.; Vandewal, K.; Koch, F. P. V.; Stingelin, N.; Smith, P.; Toney, M. F.; Salleo, A. A General Relationship between Disorder, Aggregation and Charge Transport in Conjugated Polymers. *Nat. Mater.* **2013**, *12* (11), 1038–1044.

(87) Treat, N. D.; Westacott, P.; Stingelin, N. Organic Semiconductors: Manipulation and Control of the Microstructure of Active Layers. In *The WSPC Reference on Organic Electronics: Organic Semiconductors*; 2016; Vol. 2, pp 159–193.

(88) Salleo, A. Impact of Organic Semiconductor Microstructure on Transport: Basic Concepts. *WSPC Ref. Org. Electron. Org. Semicond.* **2016**, *1*, 293–323.

(89) Brédas, J.-L.; Marder, S. R.; André, J.-M. An Introduction to the Electronic Structure of π -Conjugated Molecules and Polymers, and to the Concept of Electronic Bands. In *WSPC Reference on Organic Electronics: Organic Semiconductors*; Brédas, J.-L., Marder, S., Eds.; World Scientific Publishing Co., 2016; pp 1–18.

(90) Patil, A. O.; Heeger, A. J.; Wudl, F. Optical Properties of Conducting Polymers. *Chem. Rev.* **1988**, *88* (1), 183–200.

(91) Wudl, F.; Kobayashi, M.; Heeger, A. J. Poly(Isothianaphthene). *J. Org. Chem.* **1984**, *49* (18), 3382–3384.

(92) Spano, F. C.; Silva, C. H- and J-Aggregate Behavior in Polymeric Semiconductors. *Annu. Rev. Phys. Chem.* **2014**, *65* (1), 477–500.

(93) Naarmann, H.; Theophilou, N. New Process for the Production of Metal-like, Stable Polyacetylene. *Synth. Met.* **1987**, *22* (1), 1–8.

(94) Zozoulenko, I.; Singh, A.; Singh, S. K.; Gueskine, V.; Crispin, X.; Berggren, M. Polarons, Bipolarons, And Absorption Spectroscopy of PEDOT. *ACS Appl. Polym. Mater.* **2019**, *1* (1), 83–94.

(95) Heimel, G. The Optical Signature of Charges in Conjugated Polymers. *ACS Cent. Sci.* **2016**, *2* (5), 309–315.

(96) Aoki, K. Stochastic Property in the Propagation of a Conductive Zone in Electroactive Conducting Polymers. *J. Electroanal. Chem.* **1990**, *292* (1–2), 53–62.

(97) Albery, W. J.; Doblhofer, K.; Lyons, M. E. G.; Mount, A. R.; Vorotyntsev, M. *Electroactive Polymer Electrochemistry*; Lyons, M. E. G., Ed.; Springer Science + Business Media, LLC: New York, 1994.

(98) Kittlesen, G. P.; White, H. S.; Wrighton, M. S. Chemical Derivatization of Microelectrode Arrays by Oxidation of Pyrrole and N-Methylpyrrole: Fabrication of Molecule-Based Electronic Devices. *J. Am. Chem. Soc.* **1984**, *106* (24), 7389–7396.

(99) Kumar, A.; Welsh, D. M.; Morvant, M. C.; Piroux, F.; Abboud, K. A.; Reynolds, J. R. Conducting Poly(3,4-Alkylenedioxythiophene) Derivatives as Fast Electrochromics with High-Contrast Ratios. *Chem. Mater.* **1998**, *10* (3), 896–902.

(100) Morvant, M. C.; Reynolds, J. R. In Situ Conductivity Studies of Poly(3,4-Ethylenedioxythiophene). *Synth. Met.* **1998**, *92* (1), 57–61.

(101) Johansson, T.; Persson, N.-K.; Inganäs, O. Moving Redox Fronts in Conjugated Polymers Studies from Lateral Electrochemistry in Polythiophenes. *J. Electrochem. Soc.* **2004**, *151* (4), E119.

(102) Stavrinidou, E.; Leleux, P.; Rajaona, H.; Khodagholy, D.; Rivnay, J.; Lindau, M.; Sanaur, S.; Malliaras, G. G. Direct Measurement of Ion Mobility in a Conducting Polymer. *Adv. Mater.* **2013**, *25* (32), 4488–4493.

(103) Österholm, A. M.; Ponder, J. F.; De Keersmaecker, M.; Shen, D. E.; Reynolds, J. R. Disentangling Redox Properties and Capacitance in Solution-Processed Conjugated Polymers. *Chem. Mater.* **2019**, *31* (8), 2971–2982.

(104) Kerszulis, J. A.; Bulloch, R. H.; Teran, N. B.; Wolfe, R. M. W.; Reynolds, J. R.

Relax: A Sterically Relaxed Donor-Acceptor Approach for Color Tuning in Broadly Absorbing, High Contrast Electrochromic Polymers. *Macromolecules* **2016**, *49* (17), 6350–6359.

(105) Volkov, A. V.; Wijeratne, K.; Mitraka, E.; Ail, U.; Zhao, D.; Tybrandt, K.; Andreasen, J. W.; Berggren, M.; Crispin, X.; Zozoulenko, I. V. Understanding the Capacitance of PEDOT:PSS. *Adv. Funct. Mater.* **2017**, *27* (28), 1–10.

(106) Amb, C. M.; Dyer, A. L.; Reynolds, J. R. Navigating the Color Palette of Solution-Processable Electrochromic Polymers. *Chem. Mater.* **2011**, *23* (3), 397–415.

(107) Kerszulis, J. A.; Johnson, K. E.; Kuepfert, M.; Khoshabo, D.; Dyer, A. L.; Reynolds, J. R. Tuning the Painter's Palette: Subtle Steric Effects on Spectra and Colour in Conjugated Electrochromic Polymers. *J. Mater. Chem. C* **2015**, *3* (13), 3211–3218.

(108) Österholm, A. M.; Shen, D. E.; Kerszulis, J. A.; Bulloch, R. H.; Kuepfert, M.; Dyer, A. L.; Reynolds, J. R. Four Shades of Brown: Tuning of Electrochromic Polymer Blends toward High-Contrast Eyewear. *ACS Appl. Mater. Interfaces* **2015**, *7* (3), 1413–1421.

(109) Eric Shen, D.; Österholm, A. M.; Reynolds, J. R. Out of Sight but Not out of Mind: The Role of Counter Electrodes in Polymer-Based Solid-State Electrochromic Devices. *J. Mater. Chem. C* **2015**, *3* (37), 9715–9725.

(110) Kim, J. W.; Myoung, J. M. Flexible and Transparent Electrochromic Displays with Simultaneously Implementable Subpixelated Ion Gel-Based Viologens by Multiple Patterning. *Adv. Funct. Mater.* **2019**, *29* (13), 1–9.

(111) Bulloch, R. H.; Reynolds, J. R. Photostability in Dioxyheterocycle Electrochromic Polymers. *J. Mater. Chem. C* **2016**, *4* (3), 603–610.

(112) Manceau, M.; Bundgaard, E.; Carlé, J. E.; Hagemann, O.; Helgesen, M.; Søndergaard, R.; Jørgensen, M.; Krebs, F. C. Photochemical Stability of π-Conjugated Polymers for Polymer Solar Cells: A Rule of Thumb. *J. Mater. Chem.* **2011**, *21* (12), 4132–4141.

(113) Manceau, M.; Gaume, J.; Rivaton, A.; Gardette, J. L.; Monier, G.; Bideux, L. Further Insights into the Photodegradation of Poly(3-Hexylthiophene) by Means of X-Ray Photoelectron Spectroscopy. *Thin Solid Films* **2010**, *518* (23), 7113–7118.

(114) Hintz, H.; Egelhaaf, H. J.; Lüer, L.; Hauch, J.; Peisert, H.; Chassé, T. Photodegradation of P3HT - A Systematic Study of Environmental Factors. *Chem. Mater.* **2011**, *23* (2), 145–154.

(115) Simard, S. W.; Perry, D. A.; Jones, M. D.; Myrold, D. D.; Durall, D. M.; Molina, R. Net Transfer of Carbon between Ectomycorrhizal Tree Species in the Field. *Nature* **1997**, *388* (6642), 579–582.

(116) Peter Wohlleben. *The Hidden Life of Trees: What They Feel, How They Communicate: Discoveries from a Secret World*; Greystone Books: Vancouver, 2016.

(117) Gardner, K. H.; Blackwell, J. The Structure of Native Cellulose. *Biopolymers* **1974**, *13* (10), 1975–2001.

(118) McNamara, J. T.; Morgan, J. L. W.; Zimmer, J. A Molecular Description of Cellulose Biosynthesis. *Annu. Rev. Bio* **2018**, *176* (1), 139–148.

(119) Chen, C.; Kuang, Y.; Zhu, S.; Burgert, I.; Keplinger, T.; Gong, A.; Li, T.; Berglund, L.; Eichhhorn, S. J.; Hu, L. Structure–Property–Function Relationships of Natural and Engineered Wood. *Nat. Rev. Mater.* **2020**, 19–21.

(120) Li, Y.; Fu, Q.; Yu, S.; Yan, M.; Berglund, L. Optically Transparent Wood from a Nanoporous Cellulosic Template: Combining Functional and Structural Performance. *Biomacromolecules* **2016**, *17* (4), 1358–1364.

(121) Chen, C.; Zhang, Y.; Li, Y.; Dai, J.; Song, J.; Yao, Y.; Gong, Y.; Kierzewski, I.; Xie, J.; Hu, L. All-Wood, Low Tortuosity, Aqueous, Biodegradable Supercapacitors with Ultra-High Capacitance. *Energy Environ. Sci.* **2017**, *10* (2), 538–545.

(122) Huang, W.; Hu, G.; Tian, C.; Wang, X.; Tu, J.; Cao, Y.; Zhang, K. Nature-Inspired Salt Resistant Polypyrrole-Wood for Highly Efficient Solar Steam Generation. *Sustain. Energy Fuels* **2019**, *3* (11), 3000–3008.

(123) Gan, W.; Chen, C.; Giroux, M.; Zhong, G.; Goyal, M. M.; Wang, Y.; Ping, W.; Song, J.; Xu, S.; He, S.; et al. Conductive Wood for High-Performance Structural Electromagnetic Interference Shielding. *Chem. Mater.* **2020**.

(124) Trey, S.; Jafarzadeh, S.; Johansson, M. In Situ Polymerization of Polyaniline in Wood Veneers. *ACS Appl. Mater. Interfaces* **2012**, *4* (3), 1760–1769.

(125) Fu, Q.; Yan, M.; Jungstedt, E.; Yang, X.; Li, Y.; Berglund, L. A. Transparent Plywood as a Load-Bearing and Luminescent Biocomposite. *Compos. Sci. Technol.* **2018**, *164* (June), 296–303.

(126) Vasileva, E.; Li, Y.; Sychugov, I.; Mensi, M.; Berglund, L.; Popov, S. Lasing from Organic Dye Molecules Embedded in Transparent Wood. *Adv. Opt. Mater.* **2017**, *5* (10), 1–6.

(127) Kong, W.; Wang, C.; Jia, C.; Kuang, Y.; Pastel, G.; Chen, C.; Chen, G.; He, S.; Huang, H.; Zhang, J.; et al. Muscle-Inspired Highly Anisotropic, Strong, Ion-Conductive Hydrogels. *Adv. Mater.* **2018**, *30* (39), 1–7.

(128) Garemark, J.; Yang, X.; Sheng, X.; Cheung, O.; Sun, L.; Berglund, L. A.; Li, Y. Top-Down Approach Making Anisotropic Cellulose Aerogels as Universal Substrates for Multifunctionalization. *ACS Nano* **2020**, *14* (6), 7111–7120.

(129) Moon, R. J.; Martini, A.; Nairn, J.; Simonsen, J.; Youngblood, J. *Cellulose Nanomaterials Review: Structure, Properties and Nanocomposites*; 2011; Vol. 40.

(130) Saito, T.; Kimura, S.; Nishiyama, Y.; Isogai, A. Cellulose Nanofibers Prepared by TEMPO-Mediated Oxidation of Native Cellulose. *Biomacromolecules* **2007**, *8* (8), 2485–2491.

(131) Ifuku, S.; Nogi, M.; Abe, K.; Handa, K.; Nakatsubo, F.; Yano, H. Surface Modification of Bacterial Cellulose Nanofibers for Property Enhancement of Optically Transparent Composites: Dependence on Acetyl-Group DS. *Biomacromolecules* **2007**, *8* (6), 1973–1978.

(132) Lizundia, E.; Nguyen, T. D.; Vilas, J. L.; Hamad, W. Y.; MacLachlan, M. J. Chiroptical, Morphological and Conducting Properties of Chiral Nematic Mesoporous Cellulose/Polypyrrole Composite Films. *J. Mater. Chem. A* **2017**, *5* (36), 19184–19194.

(133) Chowdhury, R. A.; Nuruddin, M.; Clarkson, C.; Montes, F.; Howarter, J.; Youngblood, J. P. Cellulose Nanocrystal (CNC) Coatings with Controlled Anisotropy as High-Performance Gas Barrier Films. *ACS Appl. Mater. Interfaces* **2019**, *11* (1), 1376–1383.

(134) Xia, J.; Zhang, Z.; Liu, W.; Li, V. C. F.; Cao, Y.; Zhang, W.; Deng, Y. Highly Transparent 100% Cellulose Nanofibril Films with Extremely High Oxygen Barriers in High Relative Humidity. *Cellulose* **2018**, *25* (7), 4057–4066.

(135) Liu, A.; Walther, A.; Ikkala, O.; Belova, L.; Berglund, L. A. Clay Nanopaper with Tough Cellulose Nanofiber Matrix for Fire Retardancy and Gas Barrier Functions. *Biomacromolecules* **2011**, *12* (3), 633–641.

(136) De France, K. J.; Hoare, T.; Cranston, E. D. Review of Hydrogels and Aerogels Containing Nanocellulose. *Chem. Mater.* **2017**, *29* (11), 4609–4631.

(137) Foster, E. J.; Moon, R. J.; Agarwal, U. P.; Bortner, M. J.; Bras, J.; Camarero-Espinosa, S.; Chan, K. J.; Clift, M. J. D.; Cranston, E. D.; Eichhorn, S. J.; et al. Current Characterization Methods for Cellulose Nanomaterials. *Chem. Soc. Rev.* **2018**, *47* (8), 2609–2679.

(138) Anothumakkool, B.; Soni, R.; Bhange, S. N.; Kurungot, S. Novel Scalable Synthesis of Highly Conducting and Robust PEDOT Paper for a High Performance Flexible Solid Supercapacitor. *Energy Environ. Sci.* **2015**, *8* (4), 1339–1347.

(139) Guo, Y.; Otley, M. T.; Li, M.; Zhang, X.; Sinha, S. K.; Treich, G. M.; Sotzing, G. A. PEDOT:PSS "Wires" Printed on Textile for Wearable Electronics. *ACS Appl. Mater. Interfaces* **2016**, *8* (40), 26998–27005.

(140) Wang, Z.; Lee, Y. H.; Kim, S. W.; Seo, J. Y.; Lee, S. Y.; Nyholm, L. Why Cellulose-Based Electrochemical Energy Storage Devices? *Adv. Mater.* **2020**, *2000892*, 1–18.

(141) Nyström, G.; Mihranyan, A.; Razaq, A.; Lindström, T.; Nyholm, L.; Strømme, M. A Nanocellulose Polypyrrole Composite Based on Microfibrillated Cellulose from Wood. *J. Phys. Chem. B* **2010**, *114* (12), 4178–4182.

(142) Malti, A.; Edberg, J.; Granberg, H.; Khan, Z. U.; Andreasen, J. W.; Liu, X.; Zhao, D.; Zhang, H.; Yao, Y.; Brill, J. W.; et al. An Organic Mixed Ion-Electron Conductor for Power Electronics. *Adv. Sci.* **2015**, *3* (2), 1–9.

(143) Wang, Z.; Tammela, P.; Huo, J.; Zhang, P.; Strømme, M.; Nyholm, L. Solution-Processed Poly(3,4-Ethylenedioxythiophene) Nanocomposite Paper Electrodes for High-Capacitance Flexible Supercapacitors. *J. Mater. Chem. A* **2016**, *4* (5), 1714–1722.

(144) Belaineh, D.; Andreasen, J. W.; Palisaitis, J.; Malti, A.; Håkansson, K.; Wågberg, L.; Crispin, X.; Engquist, I.; Berggren, M. Controlling the Organization of PEDOT:PSS on Cellulose Structures. *ACS Appl. Polym. Mater.* **2019**, *1* (9), 2342–2351.

(145) Risteen, B. E.; Blake, A.; McBride, M. A.; Rosu, C.; Park, J. O.; Srinivasarao, M.; Russo, P. S.; Reichmanis, E. Enhanced Alignment of Water-Soluble Polythiophene Using Cellulose Nanocrystals as a Liquid Crystal Template. *Biomacromolecules* **2017**, *18* (5), 1556–1562.

(146) Hamedi, M.; Karabulut, E.; Marais, A.; Herland, A.; Nyström, G. Nanocellulose Aerogels Functionalized by Rapid Layer-by-Layer Assembly for High Charge Storage and Beyond. *Angew. Chemie - Int. Ed.* **2013**, *52* (46), 12038–12042.

(147) Zhou, S.; Qiu, Z.; Strømme, M.; Wang, Z. Highly Crystalline PEDOT Nanofiber Templated by Highly Crystalline Nanocellulose. **2020**, *2005757*, 1–9.

(148) Unuma, T.; Kobayashi, O.; Kotaka, S.; Koppolu, R.; Toivakka, M.; Saarinen, J. J. Terahertz Complex Conductivity of Cellulose Nanocrystal Based Composite Films Controlled with PEDOT:PSS Blending Ratio. *Cellulose* **2020**, *4*.

(149) Mantione, D.; del Agua, I.; Sanchez-Sanchez, A.; Mecerreyes, D. Poly(3,4-Ethylenedioxythiophene) (PEDOT) Derivatives: Innovative Conductive Polymers for Bioelectronics. *Polymers (Basel).* **2017**, *9* (8).

(150) Hulvat, J. F.; Stupp, S. I. Liquid-Crystal Templating of Conducting Polymers. *Angew. Chemie - Int. Ed.* **2003**, *42* (7), 778–781.

(151) Nyström, G.; Marais, A.; Karabulut, E.; Wågberg, L.; Cui, Y.; Hamedi, M. M. Self-Assembled Three-Dimensional and Compressible Interdigitated Thin-Film Supercapacitors and Batteries. *Nat. Commun.* **2015**, *6* (May), 1–8.

(152) Park, H. S.; Ko, S. J.; Park, J. S.; Kim, J. Y.; Song, H. K. Redox-Active Charge Carriers of Conducting Polymers as a Tuner of Conductivity and Its Potential Window. *Sci. Rep.* **2013**, *3*, 1–6.

(153) Singh, R.; Tharion, J.; Murugan, S.; Kumar, A. ITO-Free Solution-Processed Flexible Electrochromic Devices Based on PEDOT:PSS as Transparent Conducting Electrode. *ACS Appl. Mater. Interfaces* **2017**, *9* (23), 19427–19435.

(154) Jensen, J.; Madsen, M. V.; Krebs, F. C. Photochemical Stability of Electrochromic Polymers and Devices. *J. Mater. Chem. C* **2013**, *1* (32), 4826–4835.

(155) Lang, A. W.; Li, Y.; De Keersmaecker, M.; Shen, D. E.; Österholm, A. M.; Berglund, L.; Reynolds, J. R. Transparent Wood Smart Windows: Polymer Electrochromic Devices Based on Poly(3,4-Ethylenedioxythiophene):Poly(Styrene Sulfonate) Electrodes. *ChemSusChem* **2018**, *11* (5), 854–863.

(156) Brinker, C. J.; Frye, G. C.; Hurd, A. J.; Ashley, C. S. Fundaments of Sol-Gel Dip Coating. *Thin Solid Films* **1991**, *201*, 97–108.

(157) Wu, D.; Kaplan, M.; Ro, H. W.; Engmann, S.; Fischer, D. A.; DeLongchamp, D. M.; Richter, L. J.; Gann, E.; Thomsen, L.; McNeill, C. R.; et al. Blade Coating Aligned, High-Performance, Semiconducting-Polymer Transistors. *Chem. Mater.* **2018**, *30* (6), 1924–1936.

(158) Kim, N.; Kee, S.; Lee, S. H.; Lee, B. H.; Kahng, Y. H.; Jo, Y. R.; Kim, B. J.; Lee, K. Highly Conductive PEDOT:PSS Nanofibrils Induced by Solution-Processed Crystallization. *Adv. Mater.* **2014**, *26* (14), 2268–2272.

(159) Palumbiny, C. M.; Liu, F.; Russell, T. P.; Hexemer, A.; Wang, C.; Müller-Buschbaum, P. The Crystallization of PEDOT:PSS Polymeric Electrodes Probed in Situ during Printing. *Adv. Mater.* **2015**, *27* (22), 3391–3397.

(160) Kim, S. M.; Kim, C. H.; Kim, Y.; Kim, N.; Lee, W. J.; Lee, E. H.; Kim, D.; Park, S.; Lee, K.; Rivnay, J.; et al. Influence of PEDOT:PSS Crystallinity and Composition on Electrochemical Transistor Performance and Long-Term Stability. *Nat. Commun.* **2018**, *9* (1).

(161) Rivnay, J.; Mannsfeld, S. C. B.; Miller, C. E.; Salleo, A.; Toney, M. F. Quantitative Determination of Organic Semiconductor Microstructure from the Molecular to Device Scale. *Chem. Rev.* **2012**, *112* (10), 5488–5519.

(162) Watts, B.; Ade, H. NEXAFS Imaging of Synthetic Organic Materials. *Mater. Today* **2012**, *15* (4), 148–157.

(163) Knott, E. P.; Craig, M. R.; Liu, D. Y.; Babiarz, J. E.; Dyer, A. L.; Reynolds, J. R. A Minimally Coloured Dioxypyrrole Polymer as a Counter Electrode Material in Polymeric Electrochromic Window Devices. *J. Mater. Chem.* **2012**, *22* (11), 4953–4962.

(164) Shi, P.; Amb, C. M.; Knott, E. P.; Thompson, E. J.; Liu, D. Y.; Mei, J.; Dyer, A. L.; Reynolds, J. R. Broadly Absorbing Black to Transmissive Switching Electrochromic Polymers. *Adv. Mater.* **2010**, *22* (44), 4949–4953.

(165) Padilla, J.; Österholm, A. M.; Dyer, A. L.; Reynolds, J. R. Process Controlled Performance for Soluble Electrochromic Polymers. *Sol. Energy Mater. Sol. Cells* **2015**, *140*, 54–60.

(166) Satam, C. C.; Irvin, C. W.; Lang, A. W.; Jallorina, J. C. R.; Shofner, M. L.; Reynolds, J. R.; Meredith, J. C. Spray-Coated Multilayer Cellulose Nanocrystal - Chitin Nanofiber Films for Barrier Applications. *ACS Sustain. Chem. Eng.* **2018**, *6* (8), 10637–10644.

(167) Moulder, J. F.; Stickle, W. F.; Sobol, P. E.; Bomban, K. D. *Handbook of X-Ray Photoelectron Spectroscopy*; 1995.

(168) Hassab, S.; Shen, D. E.; Österholm, A. M.; Da Rocha, M.; Song, G.; Alesanco, Y.; Viñuales, A.; Rougier, A.; Reynolds, J. R.; Padilla, J. A New Standard Method to Calculate Electrochromic Switching Time. *Sol. Energy Mater. Sol. Cells* **2018**, *185* (March), 54–60.

(169) *ASTM Standard D1003-13. "Standard Test Method for Haze and Luminous Transmittance of Transparent Plastics";* West Conshohocken, PA, 2013.

(170) *CIE Technical Report: Colorimetry*; Vienna, Austria, 2004.

(171) Van der Pauw, L. J. A Method of Measuring Specific Resistivity and Hall Effect of Discs of Arbitray Shape. *Philips Research Reports*. 1958, pp 1–9.

(172) Chwang, R.; Smith, B. J.; Crowell, C. R. Contact Size Effects on the van Der Pauw Method for Resistivity and Hall Coefficient Measurement. *Solid State Electron.* **1974**, *17* (12), 1217–1227.

(173) Haacke, G. New Figure of Merit for Transparent Conductors. *J. Appl. Phys.* **1976**, *47* (9), 4086–4089.

(174) Chen, R.; Das, S. R.; Jeong, C.; Khan, M. R.; Janes, D. B.; Alam, M. A. Co-Percolating Graphene-Wrapped Silver Nanowire Network for High Performance, Highly Stable, Transparent Conducting Electrodes. *Adv. Funct. Mater.* **2013**, *23* (41), 5150–5158.

(175) Ponder, J. F.; Reynolds, J. R. Conducting Polymers: Redox States in Conjugated Systems. *WSPC Ref. Org. Electron. Org. Semicond.* **2016**, *2*, 1–18.

(176) Groenendaal, L.; Zotti, G.; Aubert, P. H.; Waybright, S. M.; Reynolds, J. R. Electrochemistry of Poly(3,4-Alkylenedioxythiophene) Derivatives. *Adv. Mater.* **2003**, *15* (11), 855–879.

(177) Elgrishi, N.; Rountree, K. J.; McCarthy, B. D.; Rountree, E. S.; Eisenhart, T. T.; Dempsey, J. L. A Practical Beginner's Guide to Cyclic Voltammetry. *J. Chem. Educ.* **2018**, *95* (2), 197–206.

(178) Lang, A. W.; Ponder, J. F.; Österholm, A. M.; Kennard, N. J.; Bulloch, R. H.; Reynolds, J. R. Flexible, Aqueous-Electrolyte Supercapacitors Based on Water-Processable Dioxythiophene Polymer/Carbon Nanotube Textile Electrodes. *J. Mater. Chem. A* **2017**, *5* (45), 23887–23897.

(179) Musiani, M. M. Characterization of Electroactive Polymer Layers by Electrochemical Impedance Spectroscopy (EIS). *Electrochim. Acta* **1990**, *35* (10), 1665–1670.

(180) Ates, M. Review Study of Electrochemical Impedance Spectroscopy and Equivalent Electrical Circuits of Conducting Polymers on Carbon Surfaces. *Prog. Org. Coatings* **2011**, *71* (1), 1–10.

(181) Hernández-Labrado, G. R.; Contreras-Donayre, R. E.; Collazos-Castro, J. E.; Polo, J. L. Subdiffusion Behavior in Poly(3,4-Ethylenedioxythiophene): Polystyrene Sulfonate (PEDOT:PSS) Evidenced by Electrochemical Impedance Spectroscopy. *J. Electroanal. Chem.* **2011**, *659* (2), 201–204.

(182) Thackeray, J. W.; White, H. S.; Wrighton, M. S. Poly(3-Methylthiophene)-Coated Electrodes: Optical and Electrical Properties as a Function of Redox Potential and Amplification of Electrical and Chemical Signals Using Poly(3-Methylthiophene)-Based Microelectrochemical Transistors. *J. Phys. Chem.* **1985**, *89* (23), 5133–5140.

(183) Aubert, P. H.; Groenendaal, L.; Louwet, F.; Lutsen, L.; Vanderzande, D.; Zotti, G. In Situ Conductivity Measurements on Polyethylenedioxythiophene Derivatives with Different Counter Ions. *Synth. Met.* **2002**, *126* (2–3), 193–198.

(184) Salinas, G.; Frontana-Uribe, B. A. Analysis of Conjugated Polymers Conductivity by in Situ Electrochemical-Conductance Method. *ChemElectroChem* **2019**, *6* (16), 4105–4117.

(185) Li, Z.; Chen, C.; Mi, R.; Gan, W.; Dai, J.; Jiao, M.; Xie, H.; Yao, Y.; Xiao, S.; Hu, L. A Strong, Tough, and Scalable Structural Material from Fast-Growing Bamboo. *Adv. Mater.* **2020**, *1906308*, 1–8.

(186) Li, Y.; Yang, X.; Fu, Q.; Rojas, R.; Yan, M.; Berglund, L. Towards Centimeter Thick Transparent Wood through Interface Manipulation. *J. Mater. Chem. A* **2018**, *6* (3), 1094–1101.

(187) Li, T.; Zhu, M.; Yang, Z.; Song, J.; Dai, J.; Yao, Y.; Luo, W.; Pastel, G.; Yang, B.; Hu, L. Wood Composite as an Energy Efficient Building Material: Guided Sunlight Transmittance and Effective Thermal Insulation. *Adv. Energy Mater.* **2016**, *6* (22).

(188) Mi, R.; Li, T.; Dalgo, D.; Chen, C.; Kuang, Y.; He, S.; Zhao, X.; Xie, W.; Gan, W.; Zhu, J.; et al. A Clear, Strong, and Thermally Insulated Transparent Wood for Energy Efficient Windows. *Adv. Funct. Mater.* **2020**, *30* (1), 1–8.

(189) Zhu, M.; Song, J.; Li, T.; Gong, A.; Wang, Y.; Dai, J.; Yao, Y.; Luo, W.; Henderson,

D.; Hu, L. Highly Anisotropic, Highly Transparent Wood Composites. *Adv. Mater.* **2016**, *28* (26), 5181–5187.

(190) Zhu, M.; Song, J.; Li, T.; Gong, A.; Wang, Y.; Dai, J.; Yao, Y.; Luo, W.; Henderson, D.; Hu, L. Highly Anisotropic, Highly Transparent Wood Composites. *Adv. Mater.* **2016**.

(191) Vasileva, E.; Baitenov, A.; Chen, H.; Li, Y.; Sychugov, I.; Yan, M.; Berglund, L.; Popov, S. Effect of Transparent Wood on the Polarization Degree of Light. *Opt. Lett.* **2019**, *44* (12), 2962.

(192) Granqvist, C. G. Electrochromics for Smart Windows: Oxide-Based Thin Films and Devices. *Thin Solid Films* **2014**, *564*, 1–38.

(193) Dyer, A. L.; Thompson, E. J.; Reynolds, J. R. Completing the Color Palette with Spray-Processable Polymer Electrochromics. *ACS Appl. Mater. Interfaces* **2011**, *3* (6), 1787–1795.

(194) Bulloch, R. H.; Kerszulis, J. A.; Dyer, A. L.; Reynolds, J. R. An Electrochromic Painter's Palette: Color Mixing via Solution Co-Processing. *ACS Appl. Mater. Interfaces* **2015**, *7* (3), 1406–1412.

(195) Savagian, L. R.; Österholm, A. M.; Shen, D. E.; Christiansen, D. T.; Kuepfert, M.; Reynolds, J. R. Conjugated Polymer Blends for High Contrast Black-to-Transmissive Electrochromism. *Adv. Opt. Mater.* **2018**, *6* (19), 1–9.

(196) Argun, A. A.; Aubert, P. H.; Thompson, B. C.; Schwendeman, I.; Gaupp, C. L.; Hwang, J.; Pinto, N. J.; Tanner, D. B.; MacDiarmid, A. G.; Reynolds, J. R. Multicolored Electrochromisin in Polymers: Structures and Devices. *Chem. Mater.* **2004**, *16* (23), 4401–4412.

(197) Mukherjee, S.; Singh, R.; Gopinathan, S.; Murugan, S.; Gawali, S.; Saha, B.; Biswas, J.; Lodha, S.; Kumar, A. Solution-Processed Poly(3,4-Ethylenedioxythiophene) Thin Films as Transparent Conductors: Effect of p-Toluenesulfonic Acid in Dimethyl Sulfoxide. *ACS Appl. Mater. Interfaces* **2014**, *6* (20), 17792–17803.

(198) Xia, Y.; Sun, K.; Ouyang, J. Solution-Processed Metallic Conducting Polymer Films as Transparent Electrode of Optoelectronic Devices. *Adv. Mater.* **2012**, *24* (18), 2436–2440.

(199) Bobacka, J.; Lewenstam, A.; Ivaska, A.; Fin, A. <Electrochemical-Impedance-Spectroscopy-of-Oxidized-Poly-3-4-Ethylenedioxythiophene-Film-Electrodes-in-Aqueous-Solutions_2000_Journal-of-Electroanalyti.Pdf>. **2000**, *489*, 17–27.

(200) Otero, T. F.; Boyano, I. Comparative Study of Conducting Polymers by the ESCR Model. *J. Phys. Chem. B* **2003**, *107* (28), 6730–6738.

(201) Lessing, J.; Glavan, A. C.; Walker, S. B.; Keplinger, C.; Lewis, J. A.; Whitesides, G. M. Inkjet Printing of Conductive Inks with High Lateral Resolution on Omniphobic "RF Paper" for Paper-Based Electronics and MEMS. *Adv. Mater.* **2014**, *26* (27), 4677–4682.

(202) Perelaer, J.; Smith, P. J.; Mager, D.; Soltman, D.; Volkman, S. K.; Subramanian, V.; Korvink, J. G.; Schubert, U. S. Printed Electronics: The Challenges Involved in Printing Devices, Interconnects, and Contacts Based on Inorganic Materials. *J. Mater. Chem.* **2010**, *20* (39), 8446–8453.

(203) Liu, H.; Crooks, R. M. Paper-Based Electrochemical Sensing Platform with Integral Battery and Electrochromic Read-Out. *Anal. Chem.* **2012**, *84* (5), 2528–2532.

(204) Zhang, F.; Cai, T.; Ma, L.; Zhan, L.; Liu, H. A Paper-Based Electrochromic Array for Visualized Electrochemical Sensing. *Sensors (Switzerland)* **2017**, *17* (2), 1–10.

(205) Bollström, R.; Määttänen, A.; Tobjörk, D.; Ihalainen, P.; Kaihovirta, N.; Österbacka, R.; Peltonen, J.; Toivakka, M. A Multilayer Coated Fiber-Based Substrate Suitable for Printed Functionality. *Org. Electron.* **2009**, *10* (5), 1020–1023.

(206) Bollström, R.; Tobjörk, D.; Dolietis, P.; Salminen, P.; Preston, J.; Österbacka, R.; Toivakka, M. Printability of Functional Inks on Multilayer Curtain Coated Paper. *Chem. Eng. Process. Process Intensif.* **2013**, *68*, 13–20.

(207) Asadpoordarvish, A.; Sandström, A.; Larsen, C.; Bollström, R.; Toivakka, M.; Österbacka, R.; Edman, L. Light-Emitting Paper. *Adv. Funct. Mater.* **2015**, *25* (21), 3238–3245.

(208) Nogi, M.; Iwamoto, S.; Nakagaito, A. N.; Yano, H. Optically Transparent Nanofiber Paper. *Adv. Mater.* **2009**, *21* (16), 1595–1598.

(209) Nogi, M.; Karakawa, M.; Komoda, N.; Yagyu, H.; Nge, T. T. Transparent Conductive Nanofiber Paper for Foldable Solar Cells. *Sci. Rep.* **2015**, *5*, 1–7.

(210) Wang, C. Y.; Fuentes-Hernandez, C.; Liu, J. C.; Dindar, A.; Choi, S.; Youngblood, J. P.; Moon, R. J.; Kippelen, B. Stable Low-Voltage Operation Top-Gate Organic Field-Effect Transistors on Cellulose Nanocrystal Substrates. *ACS Appl. Mater. Interfaces* **2015**, *7* (8), 4804–4808.

(211) Celano, U.; Nagashima, K.; Koga, H.; Nogi, M.; Zhuge, F.; Meng, G.; He, Y.; De Boeck, J.; Jurczak, M.; Vandervorst, W.; et al. All-Nanocellulose Nonvolatile Resistive Memory. *NPG Asia Mater.* **2016**, *8* (9), e310.

(212) Ji, S.; Jang, J.; Cho, E.; Kim, S. H.; Kang, E. S.; Kim, J.; Kim, H. K.; Kong, H.; Kim, S. K.; Kim, J. Y.; et al. High Dielectric Performances of Flexible and Transparent Cellulose Hybrid Films Controlled by Multidimensional Metal Nanostructures. *Adv. Mater.* **2017**, *29* (24).

(213) Malti, A.; Brooke, R.; Liu, X.; Zhao, D.; Andersson Ersman, P.; Fahlman, M.; Jonsson, M. P.; Berggren, M.; Crispin, X. Freestanding Electrochromic Paper. *J. Mater. Chem. C* **2016**, *4* (41), 9680–9686.

(214) Cai, G.; Darmawan, P.; Cheng, X.; Lee, P. S. Inkjet Printed Large Area Multifunctional Smart Windows. *Adv. Energy Mater.* **2017**, *7* (14).

(215) Mortimer, R. J. Electrochromic Materials. *Annu. Rev. Mater. Res.* **2011**, *41* (1), 241–268.

(216) Danine, A.; Cojocaru, L.; Faure, C.; Olivier, C.; Toupance, T.; Campet, G.; Rougier, A. Room Temperature UV Treated WO3 Thin Films for Electrochromic Devices on Paper Substrate. *Electrochim. Acta* **2014**, *129*, 113–119.

(217) Kang, W.; Yan, C.; Foo, C. Y.; Lee, P. S. Foldable Electrochromics Enabled by Nanopaper Transfer Method. *Adv. Funct. Mater.* **2015**, *25* (27), 4203–4210.

(218) Su, Y.; Yang, F.; Zhou, L.; Geng, Y.; Zhang, J.; Jiang, M. Flexible and Tailorable Alkylviologen/Cellulose Nanocrystals Composite Films for Sustainable Applications in Electrochromic Devices. *ChemElectroChem* **2018**, *5* (10), 1407–1414.

(219) Viñuales, A.; Alesanco, Y.; Cabañero, G.; Sobrado, J.; Tena-Zaera, R. Incorporating Paper Matrix into Flexible Devices Based on Liquid Electrochromic Mixtures: Enhanced Robustness, Durability and Multi-Color Versatility. *Sol. Energy Mater. Sol. Cells* **2017**, *167* (January), 22–27.

(220) Andersson Ersman, P.; Kawahara, J.; Berggren, M. Printed Passive Matrix Addressed Electrochromic Displays. *Org. Electron.* **2013**, *14* (12), 3371–3378.

(221) Tehrani, P.; Hennerdal, L. O.; Dyer, A. L.; Reynolds, J. R.; Berggren, M. Improving the Contrast of All-Printed Electrochromic Polymer on Paper Displays. *J. Mater. Chem.* **2009**, *19* (13), 1799–1802.

(222) Tehrani, P.; Isaksson, J.; Mammo, W.; Andersson, M. R.; Robinson, N. D.; Berggren, M. Evaluation of Active Materials Designed for Use in Printable Electrochromic Polymer Displays. *Thin Solid Films* **2006**, *515* (4), 2485–2492.

(223) Ko, Y.; Kwon, M.; Bae, W. K.; Lee, B.; Lee, S. W.; Cho, J. Flexible Supercapacitor Electrodes Based on Real Metal-like Cellulose Papers/639/4077/4079/4105/639/301/299/1013 Article. *Nat. Commun.* **2017**, *8* (1), 1–10.

(224) Wang, Z.; Malti, A.; Ouyang, L.; Tu, D.; Tian, W.; Wågberg, L.; Hamedi, M. M. Copper-Plated Paper for High-Performance Lithium-Ion Batteries. *Small* **2018**, *14* (48), 1–8.

(225) Koga, H.; Nogi, M.; Komoda, N.; Nge, T. T.; Sugahara, T.; Suganuma, K.

Uniformly Connected Conductive Networks on Cellulose Nanofiber Paper for Transparent Paper Electronics. *NPG Asia Mater.* **2014**, *6* (3), e93-8.

(226) Toivonen, M. S.; Kaskela, A.; Rojas, O. J.; Kauppinen, E. I.; Ikkala, O. Ambient-Dried Cellulose Nanofibril Aerogel Membranes with High Tensile Strength and Their Use for Aerosol Collection and Templates for Transparent, Flexible Devices. *Adv. Funct. Mater.* **2015**, *25* (42), 6618–6626.

(227) Layani, M.; Darmawan, P.; Foo, W. L.; Liu, L.; Kamyshny, A.; Mandler, D.; Magdassi, S.; Lee, P. S. Nanostructured Electrochromic Films by Inkjet Printing on Large Area and Flexible Transparent Silver Electrodes. *Nanoscale* **2014**, *6* (9), 4572–4576.

(228) Wang, J. L.; Lu, Y. R.; Li, H. H.; Liu, J. W.; Yu, S. H. Large Area Co-Assembly of Nanowires for Flexible Transparent Smart Windows. *J. Am. Chem. Soc.* **2017**, *139* (29), 9921–9926.

(229) Song, J.; Chen, C.; Wang, C.; Kuang, Y.; Li, Y.; Jiang, F.; Li, Y.; Hitz, E.; Zhang, Y.; Liu, B.; et al. Superflexible Wood. *ACS Appl. Mater. Interfaces* **2017**, *9* (28), 23520–23527.

(230) Jensen, J.; Krebs, F. C. From the Bottom Up - Flexible Solid State Electrochromic Devices. *Adv. Mater.* **2014**, *26* (42), 7231–7234.

(231) De Keersmaecker, M.; Lang, A. W.; Österholm, A. M.; Reynolds, J. R. All Polymer Solution Processed Electrochromic Devices: A Future without Indium Tin Oxide? *ACS Appl. Mater. Interfaces* **2018**, *10* (37), 31568–31579.

(232) Andersson, P.; Forchheimer, R.; Tehrani, P.; Berggren, M. Printable All-Organic Electrochromic Active-Matrix Displays. *Adv. Funct. Mater.* **2007**, *17* (16), 3074–3082.

(233) Kawahara, J.; Andersson Ersman, P.; Wang, X.; Gustafsson, G.; Granberg, H.; Berggren, M. Reconfigurable Sticker Label Electronics Manufactured from Nanofibrillated Cellulose-Based Self-Adhesive Organic Electronic Materials. *Org. Electron.* **2013**, *14* (11), 3061–3069.

(234) Hassab, S.; Shen, D. E.; Österholm, A. M.; Reynolds, J. R.; Padilla, J. Exploring Unbalanced Electrode Configurations for Electrochromic Devices. *J. Mater. Chem. C* **2018**, *6* (2), 393–400.

(235) Zhang, S.; Lee, K. H.; Frisbie, C. D.; Lodge, T. P. Ionic Conductivity, Capacitance, and Viscoelastic Properties of Block Copolymer-Based Ion Gels. *Macromolecules* **2011**, *44* (4), 940–949.

(236) Collier, G. S.; Pelse, I.; Reynolds, J. R. Aqueous Electrolyte Compatible Electrochromic Polymers Processed from an Environmentally Sustainable Solvent. *ACS Macro Lett.* **2018**, *7* (10), 1208–1214.

(237) Savagian, L. R.; Österholm, A. M.; Ponder, J. F.; Barth, K. J.; Rivnay, J.; Reynolds, J. R. Balancing Charge Storage and Mobility in an Oligo(Ether) Functionalized Dioxythiophene Copolymer for Organic- and Aqueous- Based Electrochemical Devices and Transistors. *Adv. Mater.* **2018**, *30* (50), 1–6.

(238) Jensen, J.; Hösel, M.; Dyer, A. L.; Krebs, F. C. Development and Manufacture of Polymer-Based Electrochromic Devices. *Adv. Funct. Mater.* **2015**, *25* (14), 2073–2090.

(239) Burrell, A. K.; Del Sesto, R. E.; Baker, S. N.; McCleskey, T. M.; Baker, G. A. The Large Scale Synthesis of Pure Imidazolium and Pyrrolidinium Ionic Liquids. *Green Chem.* **2007**, *9* (5), 449–45.

(240) Geyer, R.; Jambeck, J. R.; Law, K. L. Production, Use, and Fate of All Plastics Ever Made. *Sci. Adv.* **2017**, No. July, 25–29.

(241) Raamsdonk, L. W. D. Van; Zande, M. Van Der; Koelmans, A. A.; Ron L. A. P. Hoogenboom, R. J. B. P.; Groot, M. J.; Peijnenburg, A. A. C. M.; Weesepoel, Y. J. A. Current Insights into Monitoring, Bioaccumulation and Potential Health Effects of Microplastics Present in the Food Chain. *Foods* **2020**, *9* (72).

(242) Mülhaupt, R. Green Polymer Chemistry and Bio-Based Plastics: Dreams and Reality. *Macromol. Chem. Phys.* **2013**, *214* (2), 159–174.

(243) Coates, G. W.; Getzler, Y. D. Y. L. Chemical Recycling to Monomer for an Ideal, Circular Polymer Economy. *Nat. Rev. Mater.* **2020**.

(244) Wang, J.; Gardner, D. J.; Stark, N. M.; Bousfield, D. W.; Tajvidi, M.; Cai, Z. Moisture and Oxygen Barrier Properties of Cellulose Nanomaterial-Based Films. *ACS Sustain. Chem. Eng.* **2018**, *6* (1), 49–70.

(245) Nair, S. S.; Zhu, J.; Deng, Y.; Ragauskas, A. J. High Performance Green Barriers Based on Nanocellulose. *Sustain. Chem. Process.* **2014**, *2* (1), 1–7.

(246) Wu, J.; Zhang, K.; Girouard, N.; Meredith, J. C. Facile Route to Produce Chitin Nanofibers as Precursors for Flexible and Transparent Gas Barrier Materials. *Biomacromolecules* **2014**, *15* (12), 4614–4620.

(247) Shamshina, J. L.; Berton, P.; Rogers, R. D. Advances in Functional Chitin Materials: A Review. *ACS Sustain. Chem. Eng.* **2019**, *7* (7), 6444–6457.

(248) Yadav, M.; Goswami, P.; Paritosh, K.; Kumar, M.; Pareek, N.; Vivekanand, V. Seafood Waste: A Source for Preparation of Commercially Employable Chitin/Chitosan Materials. *Bioresour. Bioprocess.* **2019**, *6* (1).

(249) Wu, Q.; Mushi, N. E.; Berglund, L. A. High-Strength Nanostructured Films Based on Well-Preserved α-Chitin Nanofibrils Disintegrated from Insect Cuticles. *Biomacromolecules* **2020**, *21* (2), 604–612.

(250) Ifuku, S.; Nogi, M.; Abe, K.; Yoshioka, M.; Morimoto, M.; Saimoto, H.; Yano, H. Preparation of Chitin Nanofibers with a Uniform Width as α-Chitin from Crab Shells. *Biomacromolecules* **2009**, *10* (6), 1584–1588.

(251) Yan, N.; Chen, X. Don't Waste Seafood Waste: Turning Cast-off Shells into Nitrogen-Rich Chemicals Would Benefit Economies and the Environment. *Nature* **2015**, *524*, 155–157.

(252) Tuck, C. O. Valorization of Biomass: Deriving More Value from Waste (Science (695)). *Science (80-.).* **2012**, *338* (6107), 604.

(253) Lenardon, M. D.; Munro, C. A.; Gow, N. A. R. Chitin Synthesis and Fungal Pathogenesis. *Curr. Opin. Microbiol.* **2010**, *13* (4), 416–423.

(254) Yildirim, S.; Röcker, B.; Pettersen, M. K.; Nilsen-Nygaard, J.; Ayhan, Z.; Rutkaite, R.; Radusin, T.; Suminska, P.; Marcos, B.; Coma, V. Active Packaging Applications for Food. *Compr. Rev. Food Sci. Food Saf.* **2018**, *17* (1), 165–199.

(255) Mehta, M. J.; Kumar, A. Ionic Liquid Assisted Gelatin Films: Green, UV Shielding, Antioxidant, and Antibacterial Food Packaging Materials. *ACS Sustain. Chem. Eng.* **2019**, *7* (9), 8631–8636.

(256) Papadopoulou, E. L.; Paul, U. C.; Tran, T. N.; Suarato, G.; Ceseracciu, L.; Marras, S.; D'arcy, R.; Athanassiou, A. Sustainable Active Food Packaging from Poly(Lactic Acid) and Cocoa Bean Shells. *ACS Appl. Mater. Interfaces* **2019**, *11* (34), 31317–31327.

(257) Zimmermann, J.; Jürgensen, N.; Morfa, A. J.; Wang, B.; Tekoglu, S.; Hernandez-Sosa, G. Poly(Lactic-Co-Glycolic Acid) (PLGA) as Ion-Conducting Polymer for Biodegradable Light-Emitting Electrochemical Cells. *ACS Sustain. Chem. Eng.* **2016**, *4* (12), 7050–7055.

(258) Smyth, E.; Skinner, G. A.; Allen, D. INDICATOR DEVICE. 0253252 A1, 2015.

(259) Kang, H.; Park, H.; Park, Y.; Jung, M.; Kim, B. C.; Wallace, G.; Cho, G. Fully Roll-to-Roll Gravure Printable Wireless (13.56 MHz) Sensor-Signage Tags for Smart Packaging. *Sci. Rep.* **2014**, *4*, 2–8.

(260) Hintz, H.; Egelhaaf, H. J.; Peisert, H.; Chassé, T. Photo-Oxidation and Ozonization of Poly(3-Hexylthiophene) Thin Films as Studied by UV/VIS and Photoelectron Spectroscopy. *Polym. Degrad. Stab.* **2010**, *95* (5), 818–825.

(261) Dupuis, A.; Wong-Wah-Chung, P.; Rivaton, A.; Gardette, J. L. Influence of the Microstructure on the Photooxidative Degradation of Poly(3-Hexylthiophene). *Polym. Degrad. Stab.* **2012**, *97* (3), 366–374.

(262) Yamilova, O. R.; Martynov, I. V.; Brandvold, A. S.; Klimovich, I. V.; Balzer, A. H.; Akkuratov, A. V.; Kusnetsov, I. E.; Stingelin, N.; Troshin, P. A. What Is Killing

Organic Photovoltaics: Light-Induced Crosslinking as a General Degradation Pathway of Organic Conjugated Molecules. *Adv. Energy Mater.* **2020**, *10* (7).

(263) Mizukado, J.; Sato, H.; Chen, L.; Suzuki, Y.; Yamane, S.; Aoyama, Y.; Suda, H. High-Resolution MALDI-TOF MS Study on Analysis of Low-Molecular-Weight Products from Photo-Oxidation of Poly(3-Hexylthiophene). *J. Mass Spectrom.* **2015**, *50* (8), 1006–1012.

(264) Lang, A. W.; Österholm, A. M.; Reynolds, J. R. Paper-Based Electrochromic Devices Enabled by Nanocellulose-Coated Substrates. *Adv. Funct. Mater.* **2019**, *29* (39), 1–11.

(265) Marciniak, S.; Crispin, X.; Uvdal, K.; Trzcinski, M.; Birgerson, J.; Groenendaal, L.; Louwet, F.; Salaneck, W. R. Light Induced Damage in Poly(3,4-Ethylenedioxythiophene) and Its Derivatives Studied by Photoelectron Spectroscopy. *Synth. Met.* **2004**, *141* (1–2), 67–73.

(266) Luke, J.; Speller, E. M.; Wadsworth, A.; Wyatt, M. F.; Dimitrov, S.; Lee, H. K. H.; Li, Z.; Tsoi, W. C.; McCulloch, I.; Bagnis, D.; et al. Twist and Degrade—Impact of Molecular Structure on the Photostability of Nonfullerene Acceptors and Their Photovoltaic Blends. *Adv. Energy Mater.* **2019**, *9* (15), 1–14.

(267) Abdou, M. S. A.; Holdcroft, S. Mechanisms of Photodegradation of Poly(3-Alkylthiophenes) in Solution. *Macromolecules* **1993**, *26* (11), 2954–2962.

(268) Lee, H. S.; Song, H. G.; Jung, H.; Kim, M. H.; Cho, C.; Lee, J. Y.; Park, S.; Son, H. J.; Yun, H. J.; Kwon, S. K.; et al. Effects of Backbone Planarity and Tightly Packed Alkyl Chains in the Donor-Acceptor Polymers for High Photostability. *Macromolecules* **2016**, *49* (20), 7844–7856.

(269) Du, X.; Heumueller, T.; Gruber, W.; Almora, O.; Classen, A.; Qu, J.; He, F.; Unruh, T.; Li, N.; Brabec, C. J. Unraveling the Microstructure-Related Device Stability for Polymer Solar Cells Based on Nonfullerene Small-Molecular Acceptors. *Adv. Mater.* **2020**, *32* (16).

(270) Crispin, X.; Marciniak, S.; Osikowicz, W.; Zotti, G.; Gon, a W. D. V. a N. D. E. R.; Louwet, F.; Fahlman, M.; Groenendaal, L.; Schryver, F. D. E.; Salaneck, W. R. Conductivity, Morphology, Interfacial Chemistry, and Stability of Poly(3,4-Ethylene Dioxythiophene)–Poly(Styrene Sulfonate): A Photoelectron Spectroscopy Study. *Polymer (Guildf).* **2003**, *41* (21), 2561–2583.

(271) Irimia-Vladu, M.; Kanbur, Y.; Camaioni, F.; Coppola, M. E.; Yumusak, C.; Irimia, C. V.; Vlad, A.; Operamolla, A.; Farinola, G. M.; Suranna, G. P.; et al. Stability of Selected Hydrogen Bonded Semiconductors in Organic Electronic Devices. *Chem. Mater.* **2019**, *31* (17), 6315–6346.

(272) Körzdörfer, T.; Brédas, J.-L. DFT 101 and Applications To π-Conjugated Systems. In *WSPC Reference on Organic Electronics: Organic Semiconductors*; Brédas, J.-

L., Marder, S. R., Eds.; CRC Press: Boca Raton, FL, 2016; Vol. 1, pp 1–43.

(273) Körzdörfer, T.; Brédas, J. L. Organic Electronic Materials: Recent Advances in the Dft Description of the Ground and Excited States Using Tuned Range-Separated Hybrid Functionals. *Acc. Chem. Res.* **2014**, *47* (11), 3284–3291.

(274) Manceau, M.; Rivaton, A.; Gardette, J. L.; Guillerez, S.; Lemaître, N. The Mechanism of Photo- and Thermooxidation of Poly(3-Hexylthiophene) (P3HT) Reconsidered. *Polym. Degrad. Stab.* **2009**, *94* (6), 898–907.

(275) Ljungqvist, N.; Hjertberg, T. Oxidative Degradation of Poly(3-Octylthiophene). *Macromolecules* **1995**, *28* (18), 5993–5999.

(276) Kim, S.; Rashid, M. A. M.; Ko, T.; Ahn, K.; Shin, Y.; Nah, S.; Kim, M. H.; Kim, B. S.; Kwak, K.; Cho, M. New Insights into the Photodegradation Mechanism of the PTB7-Th Film: Photooxidation of π-Conjugated Backbone upon Sunlight Illumination. *J. Phys. Chem. C* **2020**, *124* (5), 2762–2770.

(277) Holliday, S.; Luscombe, C. K. Low Boiling Point Solvent Additives for Improved Photooxidative Stability in Organic Photovoltaics. *Adv. Electron. Mater.* **2018**, *4* (10), 1–9.

(278) Shi, J.; Xu, X.; Xia, Y.; Chen, R.; Hawash, Z.; Deribew, D.; Moons, E.; Inganäs, O.; Scheblykin, I. G. Photo-Oxidation Reveals H-Aggregates Hidden in Spin-Cast-Conjugated Polymer Films as Observed by Two-Dimensional Polarization Imaging. *Chem. Mater.* **2019**.

(279) Zhong, J.; Zhu, H.; Zhong, Q.; Dai, J.; Li, W.; Jang, S. H.; Yao, Y.; Henderson, D.; Hu, Q.; Hu, L.; et al. Self-Powered Human-Interactive Transparent Nanopaper Systems. *ACS Nano* **2015**, *9* (7), 7399–7406.

(280) Yamada, K.; Shibata, H.; Suzuki, K.; Citterio, D. Toward Practical Application of Paper-Based Microfluidics for Medical Diagnostics: State-of-the-Art and Challenges. *Lab Chip* **2017**, *17* (7), 1206–1249.

(281) Nie, Z.; Nijhuis, C. A.; Gong, J.; Chen, X.; Kumachev, A.; Martinez, A. W.; Narovlyansky, M.; Whitesides, G. M. Electrochemical Sensing in Paper-Based Microfluidic Devices. *Lab Chip* **2010**, *10* (4), 477–483.

(282) Solazzo, M.; Krukiewicz, K.; Zhussupbekova, A.; Fleischer, K.; Biggs, M. J.; Monaghan, M. G. PEDOT:PSS Interfaces Stabilised Using a PEGylated Crosslinker Yield Improved Conductivity and Biocompatibility. *J. Mater. Chem. B* **2019**, *7* (31), 4811–4820.

(283) del Agua, I.; Mantione, D.; Ismailov, U.; Sanchez-Sanchez, A.; Aramburu, N.; Malliaras, G. G.; Mecerreyes, D.; Ismailova, E. DVS-Crosslinked PEDOT:PSS Free-Standing and Textile Electrodes toward Wearable Health Monitoring. *Adv. Mater. Technol.* **2018**, *3* (10), 1–8.

(284) Kim, Y.; Kim, H.; Graham, S.; Dyer, A.; Reynolds, J. R. Durable Polyisobutylene Edge Sealants for Organic Electronics and Electrochemical Devices. *Sol. Energy Mater. Sol. Cells* **2012**, *100*, 120–125.

(285) Shimizu, M.; Saito, T.; Isogai, A. Water-Resistant and High Oxygen-Barrier Nanocellulose Films with Interfibrillar Cross-Linkages Formed through Multivalent Metal Ions. *J. Memb. Sci.* **2016**, *500*, 1–7.

(286) Toivonen, M. S.; Kurki-Suonio, S.; Schacher, F. H.; Hietala, S.; Rojas, O. J.; Ikkala, O. Water-Resistant, Transparent Hybrid Nanopaper by Physical Cross-Linking with Chitosan. *Biomacromolecules* **2015**, *16* (3), 1062–1071.

(287) Kinlen, P. J.; Liu, J.; Ding, Y.; Graham, C. R.; Remsen, E. E. Emulsion Polymerization Process for Organically Soluble and Electrically Conducting Polyaniline. *Macromolecules* **1998**, *31* (6), 1735–1744.

(288) Jakešová, M.; Apaydin, D. H.; Sytnyk, M.; Oppelt, K.; Heiss, W.; Sariciftci, N. S.; Głowacki, E. D. Hydrogen-Bonded Organic Semiconductors as Stable Photoelectrocatalysts for Efficient Hydrogen Peroxide Photosynthesis. *Adv. Funct. Mater.* **2016**, *26* (29), 5248–5254.

(289) Amdursky, N.; Głowacki, E. D.; Meredith, P. Macroscale Biomolecular Electronics and Ionics. *Adv. Mater.* **2019**, *31* (3), 1–28.

(290) Bhamla, M. S.; Benson, B.; Chai, C.; Katsikis, G.; Johri, A.; Prakash, M. Hand-Powered Ultralow-Cost Paper Centrifuge. *Nat. Biomed. Eng.* **2017**, *1* (1), 9.

(291) Sinha, S.; Irani, U. D.; Manchaiah, V.; Bhamla, M. S. Addressing Age Related Hearing Loss through Engineering Accessible and Affordable Hearing Technology. *bioRxiv* **2019**, 1–12.

(292) Cybulski, J. S.; Clements, J.; Prakash, M. Foldscope: Origami-Based Paper Microscope. *PLoS One* **2014**, *9* (6).

(293) Berglund, L. A.; Burgert, I. Bioinspired Wood Nanotechnology for Functional Materials. *Adv. Mater.* **2018**, *30* (19), 1–15.

(294) Stavrinidou, E.; Gabrielsson, R.; Nilsson, K. P. R.; Singh, S. K.; Franco-Gonzalez, J. F.; Volkov, A. V.; Jonsson, M. P.; Grimoldi, A.; Elgland, M.; Zozoulenko, I. V.; et al. In Vivo Polymerization and Manufacturing of Wires and Supercapacitors in Plants. *Proc. Natl. Acad. Sci. U. S. A.* **2017**, *114* (11), 2807–2812.

(295) Dufil, G.; Parker, D.; Gerasimov, J. Y.; Nguyen, T. Q.; Berggren, M.; Stavrinidou, E. Enzyme-Assistedin Vivopolymerisation of Conjugated Oligomer Based Conductors. *J. Mater. Chem. B* **2020**, *8* (19), 4221–4227.

(296) Liu, J.; Kim, Y. S.; Richardson, C. E.; Tom, A.; Ramakrishnan, C.; Birey, F.; Katsumata, T.; Chen, S.; Wang, C.; Wang, X.; et al. Genetically Targeted Chemical

Assembly of Functional Materials in Living Cells, Tissues, and Animals. *Science (80-.).* **2020**, *367* (6484), 1372–1376.

(297) Matta, M.; Wu, R.; Paulsen, B. D.; Petty, A.; Sheelamanthula, R.; Mcculloch, I.; Schatz, G. C.; Rivnay, J. Ion Coordination and Chelation in a Glycolated Polymer Semiconductor : Molecular Dynamics and X-Ray Fluorescence Study Ion Coordination and Chelation in a Glycolated Polymer Semiconductor : Molecular Dynamics and X-Ray Fluorescence Study. **2020**.

(298) Bischak, C. G.; Flagg, L. Q.; Yan, K.; Rehman, T.; Davies, D. W.; Quezada, R. J.; Onorato, J. W.; Luscombe, C. K.; Diao, Y.; Li, C.-Z.; et al. A Reversible Structural Phase Transition by Electrochemically-Driven Ion Injection into a Conjugated Polymer. *J. Am. Chem. Soc.* **2020**.

(299) Melianas, A.; Quill, T. J.; LeCroy, G.; Tuchman, Y.; Loo, H. v.; Keene, S. T.; Giovannitti, A.; Lee, H. R.; Maria, I. P.; McCulloch, I.; et al. Temperature-Resilient Solid-State Organic Artificial Synapses for Neuromorphic Computing. *Sci. Adv.* **2020**, *6* (27), eabb2958.

(300) Porada, S.; Zhao, R.; Van Der Wal, A.; Presser, V.; Biesheuvel, P. M. Review on the Science and Technology of Water Desalination by Capacitive Deionization. *Prog. Mater. Sci.* **2013**, *58* (8), 1388–1442.

(301) Srimuk, P.; Su, X.; Yoon, J.; Aurbach, D.; Presser, V. Charge-Transfer Materials for Electrochemical Water Desalination, Ion Separation and the Recovery of Elements. *Nat. Rev. Mater.* **2020**.

(302) Chowdhury, R. A.; Clarkson, C.; Apalangya, V. A.; Islam, S. M. N.; Youngblood, J. P. Roll-to-Roll Fabrication of Cellulose Nanocrystal-Poly(Vinyl Alcohol) Composite Coatings with Controlled Anisotropy. *Cellulose* **2018**, *25* (11), 6547–6560.

(303) Zhou, J.; Jeon, J. W.; Ponder, J. F.; Geldmeier, J. A.; Mahmoud, M. A.; El-Sayed, M.; Reynolds, J. R.; Tsukruk, V. V. Electrochromic Tuning of Transparent Gold Nanorods with Poly[(3,4-Propylenedioxy)Pyrrole] Shells in the near-Infrared Region. *J. Mater. Chem. C* **2017**, *5* (47), 12571–12584.

(304) Schermelleh, L.; Ferrand, A.; Huser, T.; Eggeling, C.; Sauer, M.; Biehlmaier, O.; Drummen, G. P. C. Super-Resolution Microscopy Demystified. *Nat. Cell Biol.* **2019**, *21* (1), 72–84.

(305) Persson, N. E.; Engmann, S.; Richter, L. J.; Delongchamp, D. M. In Situ Observation of Alignment Templating by Seed Crystals in Highly Anisotropic Polymer Transistors. *Chem. Mater.* **2019**, *31*, 4133–4147.

(306) Zhang, X.; Bronstein, H.; Kronemeijer, A. J.; Smith, J.; Kim, Y.; Kline, R. J.; Richter, L. J.; Anthopoulos, T. D.; Sirringhaus, H.; Song, K.; et al. Molecular Origin of High Field-Effect Mobility in an Indacenodithiophene- Benzothiadiazole

Copolymer. *Nat. Commun.* **2013**, *4*, 1–9.

VITA

Gus Lang was born and raised in Denver, Colorado. He earned his bachelor's degree in Mechanical Engineering from the University of Southern California where he minored in chemistry. It was through this chemistry minor that he was first exposed to relevant organic chemistry and inorganic chemistry concepts under pining conjugated organic materials. His undergraduate research focused on studying polymer composite materials in Prof. Steven Nutt's lab as part of the M.C. Gill Composites Center. His summer internship as part of the E3S program at UC Berkeley cemented his interest in electronic materials which led him to Prof. John Reynolds' group at Georgia Tech. He joined the Reynolds group in 2015 supported by funding from the Renewable Bioproducts Institute to study how cellulose might be incorporated into electrochemical devices.